

POLITECNICO DI MILANO

Facoltà di Ingegneria Industriale e dell'Informazione

Corso di Laurea Magistrale in

Materials Engineering and Nanotechnology

Dipartimento di Chimica, Materiali e Ingegneria Chimica "Giulio Natta"



DEVELOPMENT OF ENGINEERED NANOPARTICLES AS CANCER THERANOSTIC SYSTEMS.

Relatore: Prof. Francesca BALDELLI BOMBELLI

Co-relatori: Dott. Claudia PIGLIACELLI

Dott. Ilaria TIROTTA

Dott. Marco MACCARINI

Tesi di Laurea di:

Simone CARSANA Matr. 801284

Umberto MARTINO Matr. 799190

Anno Accademico 2014 – 2015

Ringraziamenti

Per prima cosa desideriamo ringraziare la professoressa Francesca Baldelli Bombelli per l'opportunità di studio dataci, per la sua pazienza e per le numerose ore che ha dedicato alla nostra tesi. Inoltre ringraziamo sentitamente le dottoresse Claudia Pigliacelli e Ilaria Tirota per essere sempre state disponibili a insegnarci, dirimere i nostri dubbi e seguirci durante tutto il periodo di stesura della tesi. Intendiamo poi ringraziare l'intero gruppo di ricerca NFM lab e in particolare il professor Metrangolo, il professor Resnati, la professoressa Gabriella Cavallo, Daniele Maiolo, Arianna Bertolani e Paola Sanchez Moreno, per l'aiuto e la disponibilità mostrataci in questi mesi. Vogliamo ringraziare vivamente Marco Maccarini, Giovanna Fragneto e l'intero gruppo di ricerca "Soft Matter Science and Support group" presso l'Institut Laue-Langevin per l'enorme possibilità offertaci, per l'aiuto e gli insegnamenti forniti durante i tre mesi di stage svolti. Infine, desideriamo dedicare un ringraziamento speciale alle persone a noi più care, i nostri genitori, le nostre famiglie e i nostri amici per il loro supporto e il loro sostegno incondizionato durante questi mesi di lavoro e, soprattutto, durante questi cinque anni di studi.

Milano, 8 Aprile 2015

Table of contents:

Sommario.....	14
Abstract.....	16
Chapter 1 - Introduction.....	18
1.1. Imaging for diagnostic medicine.....	19
1.1.1. Optical Imaging.....	20
1.1.2. Magnetic resonance imaging (MRI).....	21
¹⁹ F MRI.....	22
1.2. Drug delivery.....	24
1.2.1. Nanomedicine in drug delivery for cancer therapies.....	25
1.3. Theranostic nanomedicine.....	27
1.4. Different types of NPs used in nanomedicine.....	29
1.4.1. Polymer-based nanostructures.....	29
Polymeric NPs.....	30
Dendrimers.....	31
Micelles.....	32
1.4.2. Liposomes.....	32
1.4.3. Carbon nanotubes.....	34
1.4.4. Metal-based NPs.....	35
Metallic NPs.....	35
Magnetic NPs.....	36
1.5. SPIONs in nanomedicine.....	37
1.5.1. Characteristics.....	37
1.5.2. Synthesis.....	38
1.5.3. Colloidal stability by surface stabilization.....	39
1.5.4. Coating.....	39
1.5.5. SPIONs in drug delivery.....	42
1.5.6. SPIONs in MRI diagnostic.....	43
1.6. Gold nanoparticles.....	45
1.6.1 Characteristics.....	45
1.6.2. Imaging with Gold NRs and NPs.....	50
1.6.3. Fluorinated Gold NPs.....	52
1.6.4 Gold NPs Toxicity.....	54
1.7. Aim of the project.....	55
i) Development of Magnetite NPs as possible theranostic agents.....	56
ii) Synthesis of fluorinated Au NPs as ¹⁹ F MRI probes.....	56
iii) Analysis of Neutron Reflectometry experiments to study Au NPs interaction with cell membranes.....	57
Chapter 2 - Materials and methods.....	59
2.1. Materials.....	59
2.2. Methods.....	60
2.2.1. Size measurement and colloidal stability.....	60
Dynamic Light Scattering (DLS).....	60

Zeta-Potential	61
Transmission Electron Microscopy (TEM).....	62
2.2.2. Physical-Chemical analysis	63
UV-Vis Absorption	63
FT-IR spectroscopy	64
Fluorescence Emission Spectroscopy	65
Circular Dichroism Spectroscopy (CD)	65
Inductively Coupled Plasma Atomic Emission spectroscopy (ICP-AES)	66
2.2.3. NPs Interaction with cell membranes	66
Neutron reflectometry	66
Chapter 3 – Development of SPION-based theranostic nanostructures.....	69
3.1. Introduction.....	69
3.1.1. Nanoparticle synthesis.....	69
3.1.2. Nanoparticle surface coating	70
3.1.3. Hydrophobin proteins.....	72
3.2. Experimental	75
3.2.1. Procedure.....	75
3.3 Results and discussion	79
3.3.1 Coating protocol optimization	79
3.3.2. Physical-chemical Characterization	81
3.3.2.1. Size, colloidal stability and concentration.....	81
3.3.2.2 Qualitative/quantitative analysis	91
3.4 Conclusions.....	102
Chapter 4 - Development of fluorinated gold nanoparticles	104
4.1. Introduction.....	104
4.2. Synthesis procedures	107
4.3. Results and discussion	112
4.4. Conclusions.....	140
Chapter 5 - Nanoparticles interaction with cell membranes models.....	142
5.1. Introduction.....	142
5.2. Neutron reflectometry	145
5.3. D17 Reflectometer	148
5.4. Motofit.....	150
5.5. Procedures	152
5.5.1 Gold nanoparticles synthesis	152
5.5.2 Cell membrane model.....	153
5.5.3. Membrane model preparation.....	155
5.6. Results and discussion	158
5.7. Conclusions.....	172
Chapter 6 - Conclusions.....	174
Bibliography	178

Table of figures:

Figure 1.1. Graphic representation of the surface-to-volume ratio for different shape particles vs. particle side length. [3]	18
Figure 1.2. Cancer death incidence worldwide in 2008 divided by type. [44].....	26
Figure 1.3. Schematic representation of the possible diagnostic and therapeutic medical functions of a NP used for nanomedicine. [58].....	28
Figure 1.4. Ideal multifunctional NPs for theranostic purposes. They combine a specific targeting agent (usually with an antibody or peptide) with NPs for imaging, a cell-penetrating agent, a stimulus-selective element for drug release, a stabilizing polymer to ensure biocompatibility (typically polyethylene glycol), and the therapeutic compound. [12].....	29
Figure 1.5. Schematic representation of the main polymer-based nanostructures used in nanomedicine: a) Polymeric NP [61] ; b) Dendrimer [62]; c) Polymeric micelle. [63].....	30
Figure 1.6. a) Schematic [72] and b) 3D representation of a liposome. [73]	33
Figure 1.7. 3D representation of a single-walled and a multi-walled carbon nanotubes. [78].....	35
Figure 1.8. Schematic representation of a SPION stabilized by oleic acid ligands and soluble in non-polar solvents.. [9].....	39
Figure 1.9. Passive vs active targeting. NPs tend to passively (by their biophysicochemical properties) pass through the inflamed vasculature. On the right passive targeting mechanism is shown compared to the active targeting on the left. Once NPs have passed in the target tissue, the presence of targeting ligands on the NP surface can result in active recognizing of NPs by receptors that are present on target cell or tissue. This resulting in enhanced accumulation and cell uptake through receptor-mediated endocytosis. [14].....	40
Figure 1.10. Schematic representation of a) a single particle coated by a thermally cross-linked polymer. [104] b) Non-covalent functionalization of single SPIONs with peptide amphiphile molecules. [105] c) Oleosin coated SPIONs supraparticle functionalized by targeting ligands for a specific type of cells. [83]	42
Figure 1.11. schematic representation of thiolate stabilized AuNP and its synthesis according to Burst method. [119].....	46
Figure 1.12. Thiolate monolayer-protected gold nanoparticles. [124]	47
Figure 1.13. Surface plasmon resonance of 9, 22, 48, and 99 nm spherical gold nanoparticles. [132]	48
Figure 1.14. Normalized optical absorption spectra for dilute solutions of several purified fractions of nanocrystal gold molecules passivated by (a) hexyl-thiolates and (b) dodecyl-thiolates. The spectra are compared to an aqueous solution of commercial colloidal Au particles (dotted lines) of 9 nm mean size. The plasmon peak amplitude (near 2.5 eV) diminish with the metallic core diameters: (a) 3.2, 2.5, 2.4, 2.2, 2.0, and 1.7 nm (SC ₆ passivant); (b) 2.5, 2.4, 2.2, 2.1, 2.0, and 1.7 nm (SC ₁₂ passivant). [135].....	49
Figure 1.15. UV-Vis-NIR spectrum of gold NRs of increasing aspect ratio. [136].....	50
Figure 1.16. Representation of hydrocarbon–fluorocarbon exchange reactions on gold NPs. In this example Perfluorodecanethiols (PFDT) ligands replace Decanethiol (DT). [37]	53
Figure 2.1. Schematic representation of the ion double layer which provides the Zeta-potential values. [158]	62

Figure 2.2. Schematic of surface plasmonic resonance where the free conduction electrons in the metal nanoparticle are driven into oscillation due to coupling with incident light. [161].....	64
Figure 3.1. Schematic representation of the hydrophobic (oleic acid stabilized) SPIONs synthesis process.[92]	70
Figure 3.2. Schematic representation of a HPB coated SPIONs supraparticle. It must be noticed that every single SPION inside the coating is still stabilized by hydrophobic ligands (oleic acid).....	72
Figure 3.3. A) Linear representation of HPB II amino acids sequence. Polar (blue) and non-polar (red) amino acids and cysteine residues (black) are shown. Plus and minus signs indicate charged amino acids. Black lines indicate the disulphide bridges. [180] B) Explicit list of all the aminoacids componing HPB II protein. [177].....	73
Figure 3.4. A) Schematic topology of HFBII. The arrows mark strands and the rectangle the α -helix. B) 3D structure of HPBII. [177].....	74
Figure 3.5. Comparison between HPB I and HPB II 3D structures [178] It is appreciable the more globular structure of HPB II.	74
Figure 3.6. Comparison between an average of the two hydrophobic SPIONs batches and an average of the three measurements of the water-dissolved HPB coated supraparticles reference sample A. The results are given in terms of A) Correlation functions and B). Intensity-weighted size distribution obtained by CONTIN.....	84
Figure 3.7. Comparison between an average of the three runs for the water-dissolved HPB coated supraparticles reference sample A and for the buffer-dissolved HPB coated supraparticles reference sample B. The results are given in terms of A) Correlation functions and B) Intensity-weighted size distribution obtained by CONTIN.....	86
Figure 3.8. visual comparison between water-dissolved HPB coated supraparticles reference sample A (left) and the Nile red encapsulated HPB coated supraparticles reference sample C (right). It appreciable a colour variation from light clear brown for water-dissolved sample (left) to a more purple shade for the Nile red sample (right).....	88
Figure 3.9. Comparison between an average of the three runs for the water-dissolved HPB coated supraparticles reference sample A supraparticles for the Nile red-encapsulated HPB coated supraparticles reference sample C. The results are given in terms of A) Intensity-weighted size distribution obtained by CONTIN and B) Correlation functions.	89
Figure 3.10. Comparison a comparison between the reference samples chosen for the three different types of protocols The results are given in terms of A) Correlation functions and B) Intensity-weighted size distribution obtained by CONTIN.....	90
Figure 3.11. FT-IR spectra comparison between Oleic acid (green) and hydrophobic SPIONs batch (red).	91
Figure 3.12. FT-IR spectra comparison between hydrophobic SPIONs (red), HPB II 0.1 mg/mL aqueous solution (blue) and water-dissolved HPB coated supraparticles reference sample A (green).	92
Figure 3.13. FT-IR spectra comparison between an HPB 0.1 mg/mL aqueous solution (red), HPB 0.1 mg/mL buffer solution at pH 4.5 (green) and the buffer-dissolved HPB coated supraparticles reference sample B (blue).....	93
Figure 3.14. FT-IR spectra of Nile Red (purple), Nile red encapsulated HPB coated supraparticles reference sample C (red) and the water-dissolved HPB coated supraparticles reference sample A (blue).....	95
Figure 3.15. Nile red molecule.....	95

Figure 3.16. UV-Vis absorbance spectra of the three reference samples at stock concentration for the three types of coating protocols.....	98
Figure 3.17. UV-Vis normalized absorbance spectra comparison between the Nile red-encapsulated HPB coated supraparticles reference sample C and a Nile red/CHCl ₃ solution.	99
Figure 3.18. UV-Vis absorbance spectra comparison between the water-dissolved HPB coated supraparticles reference sample A and a HPB II aqueous 0.1 mg/mL solution.	99
Figure 3.19. CD spectra comparison between HPB-II solution in mQw and Acetate buffer.....	100
Figure 3.20. Normalized fluorescence emission spectra comparison between Nile red HPB coated supraparticles reference sample C, water-dissolved HPB coated supraparticles reference sample A and a Nile Red/CHCl ₃ solution.....	101
Figure 4.1. Schematic illustration of a generic exchange reaction. The new molecules establish a stronger bond with the NPs than those present on the surface. [201].....	104
Figure 4.2. UV-Vis spectra of: partially fluorinated AuNPs, obtained by ligands-exchange reaction treated with PFDT in toluene (sample 1) and solkane (sample 2).....	113
Figure 4.3. TEM images and corresponding size distribution of partially fluorinated AuNPs, obtained by ligands-exchange reaction performed before the start of this work.	114
Figure 4.4. TEM images and corresponding size distribution of sample 1 (b) and sample 2 (c)..	115
Figure 4.5. Correlation function (average of the three DLS runs) of gold nanoparticles stabilized by oleylamine	116
Figure 4.6. Intensity-weighted size distribution obtained by CONTIN (average of the three DLS runs) of gold nanoparticles stabilized by oleylamine and DLS values table.....	117
Figure 4.7. TEM image and corresponding size distribution (obtained by size analysis of several TEM images of particles) of gold nanoparticles stabilized by oleylamine.....	117
Figure 4.8. UV-Vis spectrum of gold nanoparticles stabilized by oleylamine.....	118
Figure 4.9. FT-IR spectra of Au NPs stabilized by oleylamine (yellow line) and free oleylamine (red line).	119
Figure 4.10. UV-Vis spectrum of gold nanoparticles stabilized by DT.....	119
Figure 4.11. TEM image and corresponding size distribution (obtained by size analysis of several TEM images of particles) of gold nanoparticles stabilized by DT.	120
Figure 4.12. FT-IR spectra comparison between gold nanoparticle stabilized by DT and DT molecule.	121
Figure 4.13. UV-Vis spectra of: original batch of oleylamine stabilized AuNPs (sample 3) and partially fluorinated AuNPs, obtained through 3h ligand exchange with PFDT (sample 5).	122
Figure 4.14. TEM images and corresponding size distribution (obtained by size analysis of several TEM images) of partially fluorinated AuNPs obtained through 3h ligand exchange with PFDT.	123
Figure 4.15. FT-IR spectra comparison between the original batch of oleylamine stabilized AuNPs (upper spectrum), partially fluorinated AuNPs obtained through 3h ligand exchange with PFDT (in the middle) and PFDT molecule (bottom spectrum).....	124
Figure 4.16. FT-IR spectra comparison between the original batch of oleylamine stabilized AuNPs (upper spectrum), partially fluorinated AuNPs obtained through 18h ligand exchange with PFDT (in the middle) and PFDT molecule (bottom spectrum).....	125
Figure 4.17. UV-Vis spectra of: original batch of oleylamine stabilized AuNPs (sample 3) compared to the partially fluorinated AuNPs obtained through 18h ligand exchange with PFDT (sample 6).	126

Figure 4.18. TEM images and corresponding size distribution (obtained by size analysis of several TEM images) of partially fluorinated AuNPs obtained through 18h ligand exchange with PFDT.	127
Figure 4.19. Correlation function (average of the three DLS runs) of DT exchanged oleylamine-stabilized AuNPs.	128
Figure 4.20. Intensity-weighted size distribution obtained by CONTIN (average of the three DLS runs) of DT exchanged oleylamine-stabilized AuNPs.	128
Figure 4.21. UV-Vis spectra of: original batch of oleylamine stabilized AuNPs (sample 3) compared to the partially DT substituted AuNPs obtained through 18h ligand exchange with DT (sample 7).	129
Figure 4.22. TEM images and corresponding size distribution (obtained by size analysis of several TEM images) of DT exchanged oleylamine-stabilized AuNPs.	129
Figure 4.23. FT-IR spectra comparison between the original batch of oleylamine stabilized AuNPs (upper spectrum), DT substituted AuNPs obtained through 18h ligand exchange with DT (in the middle) and DT molecule (bottom spectrum).	130
Figure 4.24. UV-Vis spectra of: original batch of oleylamine stabilized AuNPs (sample 3) compared to the partially fluorinated AuNPs obtained through 18h ligand exchange with triple amount of PFDT (sample 8).	131
Figure 4.25. FT-IR spectra comparison between the original batch of oleylamine stabilized AuNPs (upper spectrum), partially fluorinated AuNPs obtained through 18h ligand exchange with triple amount of PFDT (in the middle) and PFDT molecule (bottom spectrum).	132
Figure 4.26. UV-Vis spectra of: original batch of DT stabilized AuNPs (sample 4) compared to the partially fluorinated AuNPs obtained through 18h ligand exchange with PFDT (sample 9).	133
Figure 4.27. TEM images and corresponding size distribution (obtained by size analysis of several TEM images) of partially fluorinated AuNPs obtained through 18h ligand exchange with PFDT.	133
Figure 4.28. FT-IR spectra comparison between the original batch of DT stabilized AuNPs (upper spectrum), totally fluorinated AuNPs obtained through 18h ligand exchange with PFDT (in the middle) and PFDT molecule (bottom spectrum).	134
Figure 4.29. UV-Vis spectra of totally fluorinated AuNPs obtained via direct Brust method.	136
Figure 4.30. TEM images and corresponding size distribution (obtained by size analysis of several TEM images) of totally fluorinated AuNPs obtained via direct Brust method.	137
Figure 4.31. FT-IR spectra comparison between totally fluorinated AuNPs obtained via direct Brust method (upper spectrum) and PFDT molecule (lower spectrum).	138
Figure 4.32. Correlation function (average of the three DLS runs) of totally fluorinated AuNPs coated with HPBII.	139
Figure 4.33. Intensity-weighted size distribution obtained by CONTIN (average of the three DLS runs) of totally fluorinated AuNPs coated with HPBII and DLS values table.	139
Figure 5.1. Schematic interaction of a cell membrane and one NPs. [231]	142
Figure 5.2. Schematic representation of cationic AuNPs interacting with membrane model at high concentration (a) and low concentration (b). [165]	144
Figure 5.3. Schematic illustration of the geometrical configuration in a reflectivity measurement. [246]	146
Figure 5.4. From left to right: a) overhead view of D17 reflectometer with its detector (big cylinder on the left) and b) view of sample holder	148
Figure 5.5. Top view of the two operating modes of D17.	149

Figure 5.6. Interface model represented by a series of parallel layers.	150
Figure 5.7. Representation of a) single lipid bilayer adsorbed onto the surface, b) fluctuating mono-lipid double bilayer and c) fluctuating mixed-lipid double bilayer.....	153
Figure 5.8. Schematic representation of DSPC (left) molecule and DSPG molecule (right).....	154
Figure 5.9. Schematic representation and related parameters of the molecule on the right and its approximation to a cylinder on the left.....	155
Figure 5.10. Representation of double bilayer formation with a) Langmuir-Blodgett method for the first three layers and b) Langmuir-Schaefer method for the last layer.	156
Figure 5.11. Reflectivity profiles of the pristine lipid double bilayer composed by 10% DSPG and 90% DSPC at four different contrasts: (<i>green curve</i>) pure D ₂ O, (<i>blue curve</i>) a mixture of D ₂ O and H ₂ O having the same SLD of the silicon, silicon matched water (SMW), (<i>red curve</i>) a mixture of D ₂ O and H ₂ O having SLD = 4 (×10 ⁻⁶ Å ⁻²), 4 matched water (4MW), (<i>orange curve</i>) pure H ₂ O. The reflectivity profiles are offset in order to better appreciate the curves behavior.	158
Figure 5.12. SLD profile of the pristine lipid double bilayer composed by 10% DSPG and 90% DSPC at four different contrasts: (<i>green curve</i>) pure D ₂ O, (<i>blue curve</i>) a mixture of D ₂ O and H ₂ O having the same SLD of the silicon, silicon matched water (SMW), (<i>red curve</i>) a mixture of D ₂ O and H ₂ O having SLD = 4 (×10 ⁻⁶ Å ⁻²), 4 matched water (4MW), (<i>orange curve</i>) pure H ₂ O.	159
Figure 5.13. Reflectivity profiles of the lipid double bilayer composed by 10% DSPG and 90% DSPC + cationic AuNPs at three different contrasts: (<i>green curve</i>) pure D ₂ O, (<i>blue curve</i>) a mixture of D ₂ O and H ₂ O having the same SLD of the silicon, silicon matched water (SMW), (<i>red curve</i>) a mixture of D ₂ O and H ₂ O having SLD = 4 (×10 ⁻⁶ Å ⁻²), 4 matched water (4MW). The reflectivity profiles are offset in order to better appreciate the curves behavior.	160
Figure 5.14. SLD profile of the lipid double bilayer composed by 10% DSPG and 90% DSPC + cationic AuNPs at three different contrasts: (<i>green curve</i>) pure D ₂ O, (<i>blue curve</i>) a mixture of D ₂ O and H ₂ O having the same SLD of the silicon, silicon matched water (SMW), (<i>red curve</i>) a mixture of D ₂ O and H ₂ O having SLD = 4 (×10 ⁻⁶ Å ⁻²), 4 matched water (4MW).....	160
Figure 5.15. Reflectivity profiles of the pristine lipid double bilayer composed by 25% DSPG and 75% DSPC at three different contrasts: (<i>green curve</i>) pure D ₂ O, (<i>blue curve</i>) a mixture of D ₂ O and H ₂ O having the same SLD of the silicon, silicon matched water (SMW), (<i>red curve</i>) a mixture of D ₂ O and H ₂ O having SLD = 4 (×10 ⁻⁶ Å ⁻²), 4 matched water (4MW). The reflectivity profiles are offset in order to better appreciate the curves behavior.	162
Figure 5.16. SLD profile of the pristine lipid double bilayer composed by 25% DSPG and 75% DSPC at three different contrasts: (<i>green curve</i>) pure D ₂ O, (<i>blue curve</i>) a mixture of D ₂ O and H ₂ O having the same SLD of the silicon, silicon matched water (SMW), (<i>red curve</i>) a mixture of D ₂ O and H ₂ O having SLD = 4 (×10 ⁻⁶ Å ⁻²), 4 matched water (4MW).....	163
Figure 5.17. Reflectivity profiles of an ideal double bilayer [purple curve], an ideal supported bilayer [yellow] and the lipid double bilayer composed by 25% DSPG and 75% DSPC + cationic AuNPs [green] The reflectivity profiles are offset in order to better appreciate the curves behavior.....	164
Figure 5.18. Reflectivity profiles of the lipid double bilayer composed by 25% DSPG and 75% DSPC + cationic AuNPs measured at two different contrasts: (<i>blue curve</i>) a mixture of D ₂ O and H ₂ O having the same SLD of the silicon, silicon matched water (SMW) and (<i>orange curve</i>) pure H ₂ O. The reflectivity profiles are offset in order to better appreciate the curves behavior.	165

- Figure 5.19.** Reflectivity profiles of the lipid double bilayer composed by 25% DSPG and 75% DSPC + cationic AuNPs measured at two different contrasts: : (*green curve*) pure D₂O, and (*red curve*) a mixture of D₂O and H₂O having SLD = 4 ($\times 10^{-6} \text{ \AA}^{-2}$), 4 matched water (4MW). The reflectivity profiles are offset in order to better appreciate the curves behavior..... 166
- Figure 5.20.** SLD profile of the lipid double bilayer composed by 25% DSPG and 75% DSPC + cationic AuNPs measured at four different contrasts: H₂O and SMW (a) and 4MW and D₂O (b). 166
- Figure 5.21.** Reflectivity profiles of the pristine lipid double bilayer composed by 25% DSPG and 75% dDSPC at four different contrasts: (*green curve*) pure D₂O, (*blue curve*) a mixture of D₂O and H₂O having the same SLD of the silicon, silicon matched water (SMW), (*red curve*) a mixture of D₂O and H₂O having SLD = 4 ($\times 10^{-6} \text{ \AA}^{-2}$), 4 matched water (4MW), (*orange curve*) pure H₂O. The reflectivity profiles are offset in order to better appreciate the curves behavior. 168
- Figure 5.22.** SLD profile of the pristine lipid double bilayer composed by 25% DSPG and 75% dDSPC at four different contrasts: (*green curve*) pure D₂O, (*blue curve*) a mixture of D₂O and H₂O having the same SLD of the silicon, silicon matched water (SMW), (*red curve*) a mixture of D₂O and H₂O having SLD = 4 ($\times 10^{-6} \text{ \AA}^{-2}$), 4 matched water (4MW), (*orange curve*) pure H₂O. 168
- Figure 5.23.** Reflectivity profiles of the lipid double bilayer composed by 25% DSPG and 75% dDSPC + cationic AuNPs at four different contrasts: (*green curve*) pure D₂O, (*blue curve*) a mixture of D₂O and H₂O having the same SLD of the silicon, silicon matched water (SMW), (*red curve*) a mixture of D₂O and H₂O having SLD = 4 ($\times 10^{-6} \text{ \AA}^{-2}$), 4 matched water (4MW), (*orange curve*) pure H₂O. The reflectivity profiles are offset in order to better appreciate the curves behavior..... 170
- Figure 5.24.** SLD profile of the lipid double bilayer composed by 25% DSPG and 75% dDSPC + cationic AuNPs at four different contrasts: (*green curve*) pure D₂O, (*blue curve*) a mixture of D₂O and H₂O having the same SLD of the silicon, silicon matched water (SMW), (*red curve*) a mixture of D₂O and H₂O having SLD = 4 ($\times 10^{-6} \text{ \AA}^{-2}$), 4 matched water (4MW), (*orange curve*) pure H₂O..... 170

Table of tables:

Table 3-1. List of the reagents and solvents used for the synthesis with stoichiometric ratios of chemicals, their weights and their volumes.....	75
Table 3-2. ICP data about hydrophobic SPIONs concentrations.....	79
Table 3-3. List of coating procedures tested showing chemical molar ratios, volumes, purification method and the protocol type. Samples labelled in red are the chosen reference samples for water-dissolved, buffer-dissolved and Nile red-encapsulated HPB coated supraparticles.....	80
Table 3-4. Reference samples for water-dissolved (A), buffer-dissolved (B) and Nile red-containing (C) HPB coated supraparticles, with molar ratios and the volumes of HPB II, Nile Red and hydrophobic NPs and the purification method used.....	80
Table 3-5. Size results (with units) from the two hydrophobic SPIONs batches. D_H is the hydrodynamic diameter, and only the CONTIN algorithm values are reported. PDI is the polydispersity index.....	81
Table 3-6. Size and Zeta-potential results (with units) from all the water-dissolved HPB coated supraparticles samples. D_H is the hydrodynamic diameter, and only the CONTIN algorithm values are reported. PDI is the polydispersity index.	82
Table 3-7. Size and Zeta-potential results (with units) from all the buffer-dissolved HPB coated supraparticles samples and a sample produced by supraparticles dissolution in acidic pH aqueous solution. D_H is the hydrodynamic diameter, and only the CONTIN algorithm values are reported. PDI is the polydispersity index.	85
Table 3-8. Size and Zeta-potential results (with units) from all the Nile red encapsulate HPB coated supraparticles samples. D_H is the hydrodynamic diameter, and only the CONTIN algorithm values are reported. PDI is the polydispersity index.....	87
Table 4-1. List of the amounts of reagents and solvents used for the synthesis. In the AuNPs column (a) indicates oleylamine-stabilized AuNPs whereas (b) indicates DT-stabilized AuNPs.	109
Table 4-2. List of the amounts of reagents used for the synthesis of samples 10-14.	110
Table 4-3. List of the amounts of reagents and solvents used for the synthesis. In the AuNPs column (a) indicates oleylamine-stabilized AuNPs whereas (b) indicates DT-stabilized AuNPs.	121
Table 5-1. Percentage amount of different molecules used in the three experiments.	154
Table 5-2. Percentage amount of different molecules used in the three experiments.	157
Table 5-3. Structural parameters of the pristine double lipid bilayer composed by 10% DSPG and 90% DSPC.....	159
Table 5-4. Structural parameters of the double lipid bilayer composed by 10% DSPG and 90% DSPC + cationic AuNPs.....	161
Table 5-5. Structural parameters of the pristine double lipid bilayer composed by 25% DSPG and 75% DSPC.....	164
Table 5-6. Structural parameters of the structure composed by 25% DSPG and 75% DSPC + cationic AuNPs coupled by different contrasts: a) H_2O and SMW, b) 4MW and D_2O	167
Table 5-7. Structural parameters of the pristine double lipid bilayer composed by 25% DSPG and 75% dDSPC.....	169
Table 5-8. Structural parameters of the double lipid bilayer composed by 25% DSPG and 75% dDSPC + cationic AuNPs.....	171

Sommario

La nanomedicina è un nuovo settore della medicina volto all'applicazione di nanomateriali per la diagnostica e la cura delle più diffuse patologie umane. In questa direzione, le nanoparticelle (NPs) sono una delle tecnologie più innovative e versatili per la veicolazione di farmaci e per la diagnostica. In particolare, negli ultimi anni, l'attenzione si è concentrata su NPs che possano combinare proprietà diagnostiche e terapeutiche in una singola nanostruttura teranostica. Tra tutti i tipi di NPs studiati in nanomedicina, questa tesi si è focalizzata sulla produzione, sviluppo e ottimizzazione di NPs di magnetite (SPIONs), idrosolubili e teranostiche e di NPs d'oro fluorurate che possano essere usate come agenti di contrasto per la ^{19}F MRI.

SPIONs idrofobiche sono state sintetizzate e poi stabilizzate grazie all'utilizzo di una proteina anfifilica, creando quindi dei cluster di SPIONs idrosolubili. La procedura di rivestimento è stata proposta e ottimizzata dal gruppo di ricerca del NFM lab. Essa consiste nell'utilizzare come agente di rivestimento una "proteina tensioattiva" chiamato Idrofobina (HPB) di tipo II. Il processo è in grado di produrre NP rivestite di proteina che siano stabili, con dimensioni variabili secondo le condizioni sperimentali. Inoltre, è stata studiata la possibilità di incapsulare molecole idrofobiche all'interno dei cluster di SPION rivestiti con HPB; i risultati in tal senso sono stati incoraggianti ma necessitano un ulteriore approfondimento. Le AuNPs fluorurate sono state sintetizzate con successo tramite una modifica del metodo diretto di Brust e tramite reazioni di scambio. Il procedimento sviluppato ha prodotto NPs fluorurate con dimensione e funzionalizzazione superficiale riproducibili. In alcuni casi si è riscontrato un processo di frammentazione non del tutto compreso, probabilmente causato dall'eccesso di ligandi fluorurati.

La caratterizzazione qualitativa e quantitativa è stata condotta tramite Dynamic light scattering (DLS), Zeta-potential, microscopia elettronica a trasmissione (TEM) e tramite tecniche di spettroscopia quali la Inductively coupled plasma emission (ICP-AES), spettroscopia UV-Vis, spettroscopia infrarossa (FT-IR), fluorescenza e dicroismo circolare (CD).

Questo lavoro si è anche concentrato sullo studio delle interazioni delle Au NPs con modelli di membrane cellulari tramite esperimenti di riflettometria a neutroni. Questo è

stato fatto per una migliore comprensione dell'effetto delle NPs, in base alle loro caratteristiche, sulle loro proprietà biologiche. Gli esperimenti sono stati condotti dal “Soft matter Science and Support” group presso l’Institut Laue-Langevin (Grenoble, Francia).

Abstract

Nanomedicine is a new branch of medicine that focuses on the application of nanomaterials for detection and treatment of human diseases. Nanoparticles (NPs) are one of the most versatile drug delivery and diagnostic devices. In particular, in last decades, the attention has been posed on NPs that combine diagnosis and therapy ability into one single theranostic nanostructure. Among all the possible types of NPs studied in nanomedicine, this work focused on the production, development and optimization of water-soluble magnetite NPs as possible theranostic agents and fluorinated Au NPs as ^{19}F MRI probes.

Hydrophobic SPIONs have been synthesized and then stabilized with an amphiphilic protein with the formation of water-soluble SPIOs supraparticles. The coating protocol has been proposed and optimized by NFMLab research group; it involves the use of the “surfactant protein” class II Hydrophobin as coating agent. The optimized process produces colloidal stable protein coated supraparticles of different sizes depending on the experimental conditions. Validation of HPB II coated SPION to encapsulate a hydrophobic molecule has been tested with encouraging results, which need further investigation. Fluorinated AuNPs have been successfully synthesized by a modification of the Brust direct method and also by exchange reactions. The developed processes produce reproducible fluorinated NPs in terms of size and surface functionalization. In some cases, a fragmentation process occurred probably induced by the excess of fluorinated ligands, but still not completely understood.

Qualitative and quantitative characterization has been performed by Dynamic light scattering (DLS), Zeta-potential, Transmission electron microscopy (TEM) and by spectroscopic techniques as Inductively coupled plasma emission (ICP-AES), UV-Vis, Fourier transform infrared (FT-IR), fluorescence and circular dichroism (CD).

This work also investigated the interaction of AuNPs with model cell membranes through neutron reflectometry measurements, performed by the “Soft matter Science and Support” group at ILL (Grenoble, France), to better understand how the NPs properties affect their biological behaviour.

Chapter 1 - Introduction

The advent of nanomaterials was forecast in 1959 by Richard P. Feynman. [1] In the last few decades, nanotechnology has been applied to different research fields and has emerged as a rapidly growing area with numerous applications, especially for the purpose of manufacturing new materials. Nanotechnology is essentially defined as the ability to fabricate, measure, manipulate and make predictions about materials at the scale of nanometers. [2] The nanoscale is where materials start to lose their bulk physicochemical properties and exhibit novel ones due to the higher surface-to-volume ratio and the few number of atoms composing the material (Figure 1.1). These properties depend largely on the size of the particles and can be grasped in order to create new structures and systems with specific new functions.

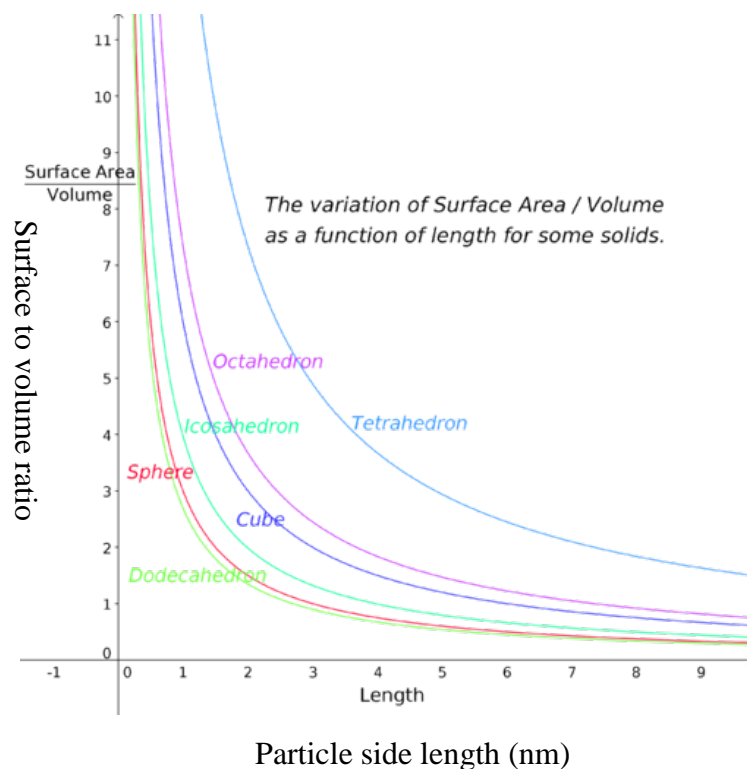


Figure 1.1. Graphic representation of the surface-to-volume ratio for different shape particles vs. particle side length [3].

Nanotechnology has been exploited also in the field of medicine establishing the new discipline of “Nanomedicine”, which is defined as the application of nanotechnology to disease treatments, diagnosis, monitoring, and to the control of biological systems. Nanostructured materials often show novel properties that make them excellent candidates for medicine and biomedical applications [4]. The advent of nanomedicine has mostly brought novel findings, for improving the pharmacokinetic and pharmacodynamic properties of existing molecules combining them with nanoplatforms. [5], [6] In particular, many biological molecules (e.g., viruses, organelles, proteins, DNA) involved in biological events can specifically interact with structures of the same size enhancing their functionality. [7]–[9] Nanomedicine thus offers new solutions for treating untreatable diseases and improving diagnosis. [6] Particularly, impressive achievements using novel nanomaterials have been made in the field of diagnosis and detection, for example by MRI-sensitive and fluorescent labeled structures, of targeted and controlled drug/gene delivery as well as in cancer treatment for example by hyperthermia. [1], [6], [7], [10]–[13] Finally, the impact of nanotechnology on medicine can mainly be seen in four principal fields: diagnostic methods, therapy, cell therapy/tracking and regenerative medicine. [1], [14]–[16] This work focused principally on diagnosis and therapy, which can be also combined in a way that has been called “Theranostic”.

1.1. Imaging for diagnostic medicine

Molecular imaging allows the characterization of biological processes at cellular and subcellular levels in intact organisms. [17] By exploiting specific molecular probes or contrast agents, this powerful technique can detect and characterize early stage diseases and provide a rapid method for evaluating treatment. Currently used molecular imaging modalities include magnetic resonance imaging (MRI), computed tomography (CT), ultrasound (US), optical imaging (OI) (bioluminescence [18] and fluorescence), single photon emission computed tomography (SPECT) and positron emission tomography (PET). [17] All of these modalities require marker molecules in a certain quantity in order to accumulate in the region of interest (ROI). Due to the different chemical nature of marker molecules and intrinsic sensitivity of each technology, the tissue concentration required to

achieve signal varies considerably between the modalities and must be considered very carefully in order to avoid toxicity problems. [17]

On this line, nanostructures have been studied in order to improve the mentioned imaging/diagnostic techniques. Nanotechnology is applied to molecular imaging in the form of imaging nanoprobe capable of enhancing the sensitivity of the image and the specificity toward the target tissue. Usually, the imaging probe consists of NPs conjugated with active targeting ligands. [19] Nanostructures can be surface-functionalized with one or more targeting molecules to increase their concentration in the ROI and the so-obtained contrast agents can be taken up at predetermined ratios either in the interior or on the surfaces of the cells. In addition, it is important to evaluate their body permanence time, that can be tuned by their physicochemical properties. [17], [20]–[22]

For a further in-depth analysis of this topic, the focus is posed on two of the most used imaging modalities: Optical Imaging (OI) and magnetic resonance imaging (MRI).

1.1.1. Optical Imaging

Optical Imaging (OI) is one of the most common modalities used for *in vitro* and *in vivo* imaging. OI utilizes photons emitted from bioluminescent or fluorescent probes. One advantage of this imaging technique is its relatively inexpensive cost. It is also used as complementary technique of microcomputed tomography/single photon emission computed tomography (micro-CT/SPECT) and magnetic resonance imaging (MRI). [17], [20]

OI exploits the wavelength spectrum from visible to near-infrared (NIR) light. This spectrum provides good spatial resolution, without exposure to ionizing radiation. However, in living tissues, OI usually suffers from the attenuation of photon propagation and poor signal to noise ratio due to tissue autofluorescence. [17], [20], [21]

The use of near-infrared (NIR) contrast agents is thus desired for *in vivo* OI. OI can be performed by NPs bringing several advantages over conventional fluorescence. On this line, different types of nanofabricated NIR contrast agents have been developed for *in vivo* OI. The Signal-to-noise ratio and detection sensitivity are improved because autofluorescence is reduced and *in vivo* imaging is facilitated by deep penetration of

noninvasive NIR excitation. Furthermore photodamage to living organisms is very low. [23]

Examples of promising nanostructures used in OI are quantum dots (QDs) and fluorescently-labeled polymeric NPs. These NPs have size and composition-tunable fluorescence emission with high quantum yields and photostability. They have been used for *in vivo* cancer targeting and imaging, and imaging-guided surgery. [20], [21], [24] In addition, OI technique by using persistent luminescence (afterglow emission) was implemented with rare earth ion-based NPs (emission at 690 nm) for *in vivo* imaging. [25]

1.1.2. Magnetic resonance imaging (MRI)

Magnetic resonance imaging (MRI) has become one of the most used and powerful tools for non-invasive clinical diagnosis due to its high soft tissue contrast, spatial resolution, and penetration depth. [10] Because MRI methods are non-invasive, they can be applied repeatedly to monitor targeted cells and cellular processes *in vivo* in real time. For cells to be visualized by MRI, they generally must be labelled to enable their discrimination from surrounding tissue. [15] MRI employs a strong magnetic field that aligns the magnetic moments of protons in a material (typically water in body tissues) producing an equilibrium magnetization along one direction (z) with a magnitude of M_0 . A radio frequency (RF) pulse, at a resonant frequency capable of transferring energy to protons, is applied in order to align their magnetic moments in phase to an angle called the flip angle. The choice of flip angle depends on the imaging sequence applied, but it is generally the transverse plane (xy-plane), causing a net magnetization of M_{xy} . Upon removal of RF pulse the magnetic moments of the protons relax to equilibrium. The time required for the magnetic moments to relax to the equilibrium state, which is broadly termed the relaxation time, is tissue-dependent. [10], [17], [26]

MRI contrast in soft tissue is due to differences in the proton density, spin-lattice relaxation time (T_1) and spin-spin relaxation time (T_2) of the protons. T_1 is the time constant of the exponential recovery process of M_0 along the z-axis after the RF pulse. Protons that relax rapidly (short T_1) recover full magnetization along the z-axis and produce high signal intensities. For protons that relax more slowly (long T_1), full magnetization is not recovered before subsequent field application, and so they inherently

produce fewer signals and result in the so-called “saturation effect”. T_1 weighted images well-illustrate anatomy and are preferred when a clear image of the structure is required. [10], [27] T_2 is the time constant of the exponential decay of the transverse magnetization (M_{xy}) after the application of the magnetic field. T_2 is related to the amount of time for the precession of the magnetic moments of the protons to return randomly aligned. T_2 weighted images produce good pathological information since collections of abnormal fluid appear bright against the normal tissue background. [10], [26]

In most tissue, intrinsic variations of T_1 and T_2 are not sufficiently strong; therefore exogenous materials are employed clinically to enhance the contrast between the tissue of interest and the surrounding tissue. While nearly all MRI contrast agents affect both T_1 and T_2 , usually the effects of contrast agents are more pronounced for either T_1 or T_2 , leading to the categorization of these probes as T_1 or T_2 contrast agents. T_1 contrast agents are used to increase signal intensity providing positive contrast enhancement in T_1 weighted images, whereas, T_2 contrast agents decrease signal intensity resulting in a negative contrast enhancement in T_2 weighted images. MRI signal typically lack of sensitivity and MRI contrast agents need to be the most concentrated as possible in the ROI. This often brings to health problems that must be carefully taken into account. [17]

^{19}F MRI

The first and most used MRI systems were based on ^1H nuclei relaxation, but shortly after the introduction of ^1H MRI, fluorinated molecules were tested as MR-detectable tracers. Many nontoxic and chemically inert fluorinated compounds are now being used in a broad range of biomedical applications. These compounds can be monitored via fluorine (^{19}F) MRI, providing a non-invasive way to investigate different organ tissues and monitor their biological functions. ^{19}F MRI exploits the advantages of the fluorine nucleus, which possesses a gyromagnetic ratio very close to that of ^1H , spin $\frac{1}{2}$, 100% natural abundance and resonates at a frequency that is 94% of that of ^1H . [15] The similarity of ^{19}F and ^1H nuclei can be exploited also in measurements: ^{19}F -MRI experiments can often be performed with the same MRI scanner as used for conventional ^1H MRI, with the same receiver electronics but re-tuned radiofrequency coils. [28] Moreover, fluorine agents and ^{19}F imaging represent an opportunity for cell-labelling with

minimal effects on cell proliferation, function and maturation, whilst permitting ^{19}F label-based quantification. [15] Endogenous ^{19}F MRI signal from the body is quite low because fluorine is present only in bones and teeth, where it is immobilized in the solid phase. Thus, the physiological concentration of detectable mobile fluorine is below the detection limit. [15], [28] This lack of background signal makes fluorinated molecules promising contrast agents, providing a signal with a potentially extremely high signal-to-noise ratio and specificity. [15] However, in order to produce an image quality similar to that of ^1H MRI, whose signal derives from nearly two-thirds of all nuclei present in the body, the fluorinated agent requires a very high density of ^{19}F nuclei and a high tissue concentration. As it was already anticipated, the use of large quantities of fluorinated compounds can yield high-quality ^{19}F images, but high doses may be limited in humans by safety concerns. [15], [17]

^{19}F MRI diagnostic applications can be divided in two groups: the first is based on the study of the relaxivity properties of small fluorinated molecules (for example liquid C_6F_6) that show high sensitivity to oxygen concentration in body tissues. [28] The second group is based on the detection of different fluorinated probes, such as gaseous SF_6 , C_2F_6 , CF_4 , C_6F_6 , C_3F_8 , perfluorocarbons (PFCs) or fluorinated drugs, in order to monitor their behaviour and position in the organism. [15], [28] An example of this second type of applications is the evaluation of the biodistribution of 5-fluorouracil (5-FU), a chemotherapeutic agent. Measuring the effectiveness of targeting *in vivo* would thus provide insights on the mechanism of action of the drug. [28], [29]

Nanostructured materials are currently under extensive development for improved MRI diagnosis of a wide range of diseases, including cancer [30], cardiovascular diseases [31], and neurological diseases. [32] The nanoscale dimensions of such devices give rise to unique properties and the ability to function on a cellular and molecular level. [10], [11], [33], [34] Currently, for ^1H MRI, superparamagnetic iron oxides (SPIOs) are the most widely used clinical MRI contrast agents. [6], [10], [35] and also metallic NPs stabilized with PFC ligands have been studied as ^{19}F MRI imaging tools. [36] In particular, water-soluble superparamagnetic iron oxide NPs (SPIONs) and fluorocarbons stabilized gold NPs have attracted considerable interest due to their excellent magnetic properties, biocompatibility and biodegradability. [11], [28], [34], [37], [38] A deep focus on the

advantages and disadvantages in the use of such NPs in medicine will be provided in a following section.

1.2. Drug delivery

The biological activity of a therapeutically active substance (drug) depends on the nature of the interaction with the target tissue or organ. When the interaction occurs, the drug should be in the region of interest (ROI) and at the required concentration to achieve the desired response. This means that the therapeutic agent should be released at the ROI at a controlled rate.

Typically drugs are orally taken, because oral is the most convenient route and usually the safest and least expensive, but a large number of drugs cannot be administered by this route because the amount adsorbed through the gastrointestinal membrane is often too small to produce the therapeutic effect. This is the reason why a lot of medicines must be taken with alternative routes such as parenteral or inhaled. Parenteral route is particularly interesting and useful in everyday medicine. But it must be said that intravenous injection of poorly soluble drugs may cause serious problems such as embolization of blood vessels and local toxicity as a result of high drug concentration at the site of deposition. Furthermore, often drugs require repeated doses to reach the necessary concentration in the blood to ensure the therapeutical effect. [22], [39]

The advent of nanotechnology and nanomedicine has brought to new possibilities in drug delivery routes. Controlled delivery devices that respond to environmental stimuli or release drugs via a triggered mechanism has been explored extensively for the past decade.

Nanostructures seem to be able to overcome many traditional problems of conventional drug delivery systems including therapeutic index, controlled release, drug targeting, and unwanted side effects. [4], [7], [12], [34], [40], [41]

In more detail the advantages of using nanostructures in drug delivery includes the following: i) particle size and surface characteristics of NPs can be easily manipulated to achieve both passive and active drug targeting. ii) Controlled and sustained release of a drug during the transport to the site of localization to achieve increased therapeutic

efficacy and reduced side effects. iii) Drug loading can be relatively high and drugs can be incorporated into systems without any chemical reaction. iv) Site-specific targeting can be achieved by attaching targeting ligands to surface of particles or use of magnetic guidance. v) The system can be used for various routes of administration including oral, nasal and parenteral. [4], [12], [42]

Nanotechnology-driven drugs delivery presents some drawbacks too. For example, their small size and large surface area can lead to particle-particle aggregation, making physical handling of NPs difficult in liquid and dry forms. In addition, small particles size and large surface area readily result in limited drug loading and burst release. These practical problems have to be overcome before NPs can be used clinically or made commercially available. [42]

1.2.1. Nanomedicine in drug delivery for cancer therapies

Cancer is among the top three “killers” in modern society (see Figure 1.2 for the cancer death incidence in 2008 worldwide). In the last 50 years research and therapies have made huge headways leading to numerous lives saved. [4] Regarding the present therapy methods there are numerous anticancer agents available in the clinic and are administered with some methodologies. They include surgery, chemotherapy, and radiation therapy; many forms of cancer are treatable by these therapies. However, these kinds of therapies show significant toxicities for the whole body with serious side effects (anemia, vomiting, diarrhea, nausea, decreased infection resistance, increased hemorrhage, hair loss) and are often used in combination. [4], [7] Because of the not selectiveness and high quantity of the used drugs, patients are compelled to tolerate such heavy side effects, decreased life quality and repeated treatments. [4], [39], [43]

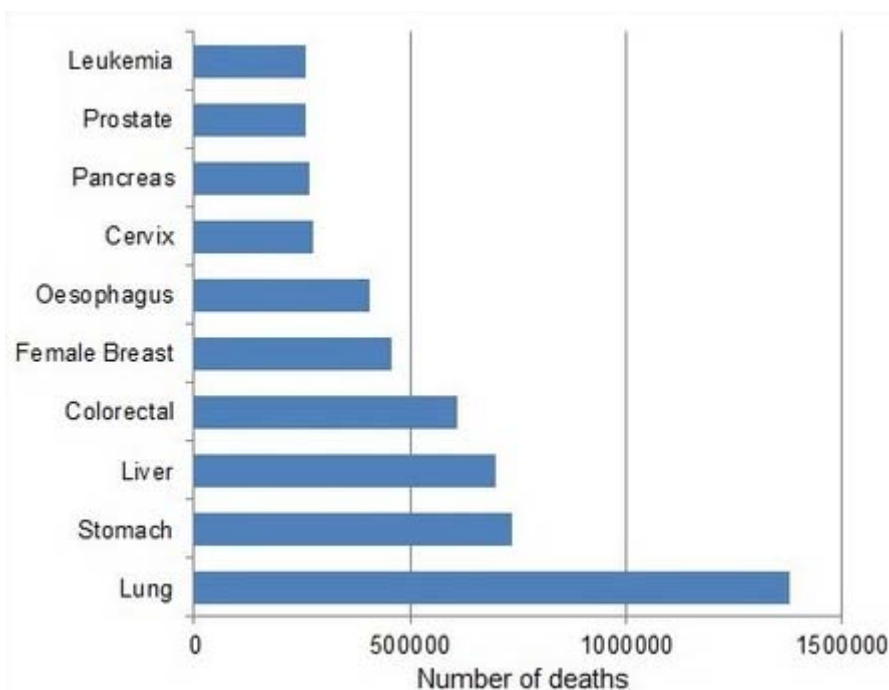


Figure 1.2. Cancer death incidence worldwide in 2008 divided by type [44].

Nanotherapeutics where drugs are either encapsulated in the NP or chemically linked to it show remarkable advantages such as reduction in dosage and toxicity, optimization of the pharmaceutical effects minimizing the associated side effects, protection of the drug against degradation and consequent drug stability enhancement. [4], [42], [43], [45], [46]

For example some drugs, like Paclitaxel, have been found to be a potent anticancer drug against a wide range of cancers, including head and neck, ovarian, lung, breast, and colon cancers. However, the practical chemotherapeutic application of these molecules has been limited by their high hydrophobicity and poor water-solubility of the typical formulation (known as Taxol and also including ethanol). Delivery problem of this drug seems to be overcome by using thermodynamically stable polymeric micelles able to carry poorly water-soluble drugs. [12], [39], [46]

Abraxane[®] is another example of the first FDA-approved nanomedicines as Paclitaxel drug delivery system. Abraxane[®] (also commonly referred to as nab-Paclitaxel) was approved by the FDA in 2005 for the treatment of breast cancer. [47] This is a NP-based cancer treatment that utilizes albumin nanoparticles as carrier of the active agent.

Albumin is an ideal natural carrier of hydrophobic molecules such as vitamins and hormones with favourable non-covalent binding interactions. [48] The active agent in Abraxane[®] is Paclitaxel. Paclitaxel original formulation includes the solvent Cremophor, which itself caused a number of adverse side reactions, including acute hypersensitivity. [49] Because of paclitaxel's hydrophobic nature, it needs a nonpolar carrier to make it clinically viable. Paclitaxel is easily complexed with human serum albumin in order to form protein stabilized nanoparticles in the size range of 100 nm-200 nm which are soluble in aqueous solvents. These are synthesized by mixing the drug and albumin in an aqueous solvent and passing the solution through a high-pressure jet. [50] Upon injection into biological systems, the nanoparticles rapidly dissolve into smaller 10 nm complexes consisting of albumin molecules with bound paclitaxel. [47], [51] Abraxane[®] has been shown to not only decrease the toxicity of traditional paclitaxel formulations, but to actually increase the efficacy of the drug in clinical trials involving patients with an advanced breast cancer. [47] Several other indications are currently being pursued through aggressive clinical trials, including Pancreas adenocarcinoma treatment. [51], [52]

1.3. Theranostic nanomedicine

The term “Theranostic” is simply the combination of “therapy” and “diagnosis”, which refers properly to the integration of both concepts. [17] This is achieved typically by creating multifunctional nanostructures offering the opportunities to combine targeting, environmentally responsive drug release, molecular imaging, and other therapeutic functions into a single platform providing to simultaneously monitor and treat disease. [12], [17], [53]–[55] Theranostic nano-tools can simultaneously detect cancer cells, and visualize their location in the body, kill cells, and monitor therapeutic responses. [12] These are generally divided into the following categories: polymer-based, lipid-based, carbon nanotubes and metal-based NPs. [4], [22], [34], [54] Some typical examples of inorganic NPs have been already mentioned and consist in gold and superparamagnetic (iron oxide) NPs, whose physical properties are involved in both the photodiagnostics and photothermal therapy of cancers and other main diseases. [34], [56] Unfortunately, most existing studies in the fields of imaging or therapy focus more on single modality and do not necessarily encourage comprehensive theranostic studies. Only few publications refer already to theranostic biotechnology and nanomedicine. [12], [17], [53], [55] Theranostic

nanomedicine present of course some difficult topic and drawbacks since optimal therapeutics and diagnostics are two very different fields to be fully investigated. The development of effective theranostic NPs for medicine will require some give and take between imaging sensitivity, accuracy of targeting, and controlled drug release. [17] The body normally treats NPs as foreign particles, so it is possible they become easily removed from the circulation before completion of their function. Thus, one of the most important properties of any pharmaceutical nanocarrier loaded with any contrast molecule and/or drug is its longevity. Long-circulating pharmaceuticals and pharmaceutical carriers are currently an important and still growing area of biomedical research. [57]

To summarize, Figure 1.3 shows a schematic review of the different medical abilities that a NP can present with proper functionalization. Figure 1.4 shows a simple diagram of an ideal typical theranostic NP.

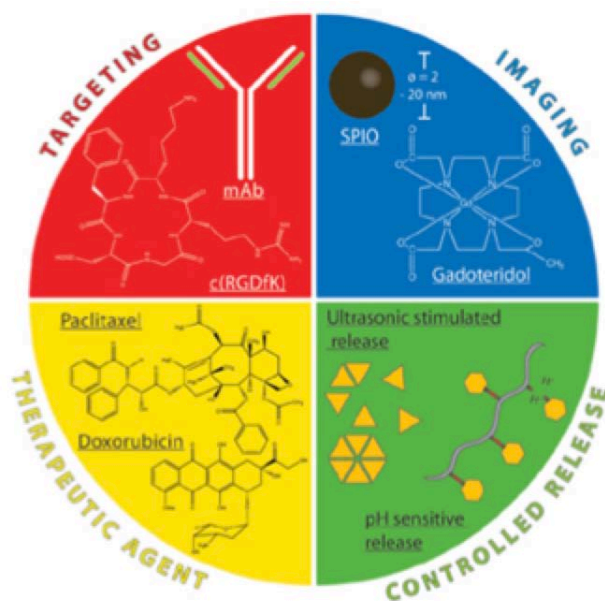


Figure 1.3. Schematic representation of the possible diagnostic and therapeutic medical functions of a NP used for nanomedicine [58].

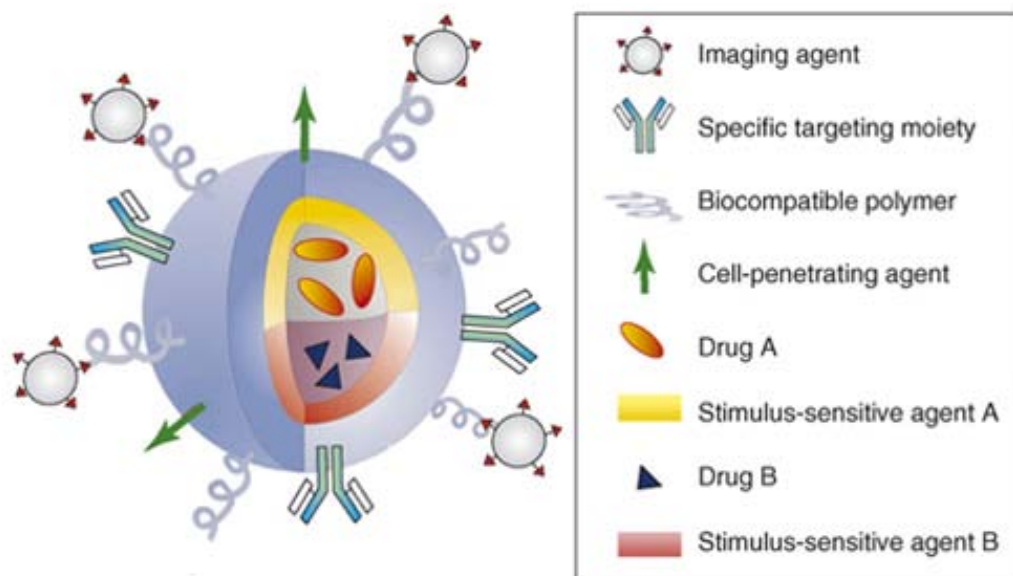


Figure 1.4. Ideal multifunctional NPs for theranostic purposes. They combine a specific targeting agent (usually with an antibody or peptide) with NPs for imaging, a cell-penetrating agent, a stimulus-selective element for drug release, a stabilizing polymer to ensure biocompatibility (typically polyethylene glycol), and the therapeutic compound. [12]

1.4. Different types of NPs used in nanomedicine

1.4.1. Polymer-based nanostructures

Polymer-based nanostructures have been extensively investigated as therapeutic carriers and diagnostic novel tools. Many polymers have been proposed and studied for these purposes but only a few of them have been accepted into clinical practice. [17], [22], [59] Biodegradable polymers are highly preferred due to their bioavailability, better encapsulation ability, controlled release and less toxic properties. [60] Among the studied types of polymeric-based cancer therapies the attention is posed on polymeric NPs, dendrimers and micelles. [12] All these structures are commonly used both in therapeutics (drug delivery) and diagnostics (imaging) also combined into theranostic NPs.

Generally, polymers are conjugated to a drug forming a pro-drug that has an increased circulation time, a lower toxicity, and higher tumor accumulation with respect to

the free drug. The incorporation of additional functionalities, such as an active targeting moiety or contrast agent are also desired. [17], [59] The major bottlenecks of pro-drugs are related to reach an efficient drug loading and the complexity of the synthesis in order to control production cost and reproducibility. In addition the toxicity of these NPs circulating in the blood must be also taken into account. [17]

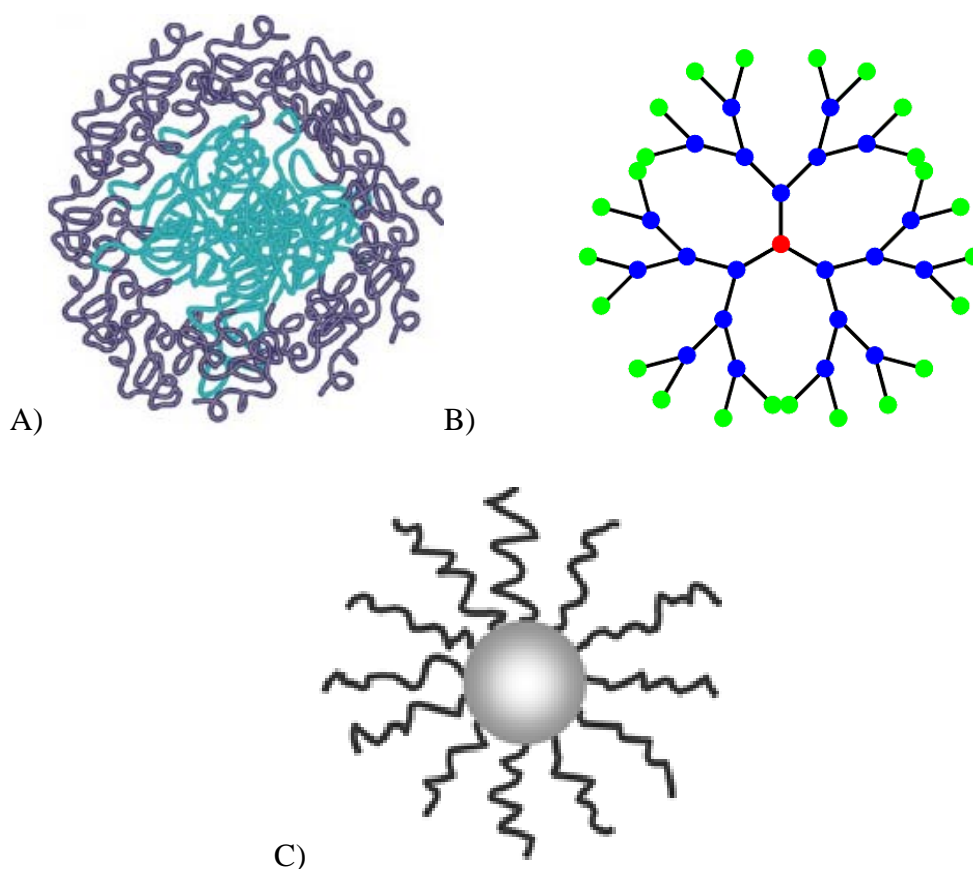


Figure 1.5. Schematic representation of the main polymer-based nanostructures used in nanomedicine: a) Polymeric NP [61] ; b) Dendrimer [62]; c) Polymeric micelle. [63]

Polymeric NPs

Polymeric NPs used as carriers of anticancer drugs often consist of a polymeric matrix in which the drug is dispersed within the particle or conjugated to the polymeric backbone. [12], [43], [46], [64] This structure can be used for transporting small-molecule

drugs, peptides, proteins, and nucleic acids. [12] This is due to the fact that chemotherapeutic agents that are lipophilic in nature, may be solubilize in the polymeric matrix, while hydrophilic biomolecules used for targeting the cancer site may be adsorbed onto the particle surface. [46]

This results in potent therapeutic effects. [12] Polymer-based NPs are also used as imaging probes. [12], [43] A schematic representation of different type of polymer based is shown in Figure 1.5.

Dendrimers

Dendrimers are highly branched synthetic polymers which can be synthesized in different chemical structures and functional groups. [17], [22], [40] They are constructed through a set of repeating chemical synthesis on the core. As polymerization progresses, a small, planar molecule transforms into a spherical nanostructure, with cavities and potentially active surfaces. [17], [40] Due to this peculiar molecular structure, drugs can be encapsulated into the interior of the dendrimers, chemically attached or physically adsorbed on the surface. [65] The described synthesis method is able to produce dendrimers with very uniform and extremely low polydispersity, with the size ranging from 1–10 nm. This control over size, polydispersity, shape, and surface functionality make dendrimers a very interesting application in nanomedicine. [40], [65]

Dendrimers have proven to be successful drug and imaging agent carriers in a number of preclinical studies, including, cancer regression, gene delivery, and molecular imaging. [17], [66] These are used also for diagnostic issues; for example PAMAM dendrimers have been widely used substrates for creating macromolecular MRI contrast agents due to their defined structure and large number of available surface amino groups. [17], [40], [66], [67]

Drawbacks in using such nanostructures for theranostic purpose include toxicity of the NP, its polymeric component, as well as the off-target effects of the contrast and therapeutic agent. [17]

Micelles

Micellar NPs are attractive structures for carriers of drug and contrast agents because they can form relatively uniform size structures and are prepared from a variety of amphiphilic materials. Among these possible materials, biocompatible block copolymers are one of the most interesting. [68] These copolymers assemble into a core-shell structure in aqueous environment. Hydrophobic blocks form the core while the hydrophilic ones form the shell. This structure increases solubility of hydrophobic molecules, and incorporates multiple functionalities into a single structure. Due to ease of formation, stability, ability to encapsulate hydrophobic molecules, and therapeutic success in preclinical and clinical studies, polymeric micelles are widely accepted as viable drug and imaging agent delivery systems. [17], [22]

1.4.2. Liposomes

Liposomes are spherical lipid vesicles which consist in an aqueous volume entrapped by one or more lipidic bilayers of natural or synthetic amphiphilic lipid molecules, which size can vary from 50 nm to 1000 nm (see figure 1.6). [22], [57] Liposomes have been widely used in the pharmaceutical industry, again, both for therapeutic and imaging functions. [40] They are biologically inert and completely biocompatible, and they cause practically no toxic or antigenic reactions; moreover drugs included in liposomes are protected from the destructive action of external media. [57] Delivering hydrophobic and hydrophilic drugs in vesicles can evade the immune systems, target cells, and reduce drug cytotoxicities. In addition, liposomes can easily be surface modified and grafted with different targeting moieties including various antibodies or bioresponsive components such as biosensitive lipids or polymers. Both hydrophobic and hydrophilic drugs can be encapsulated inside liposomes by tuning the amphiphilic behavior of the selected lipid molecules. [22]

Liposomes characteristics have led to their use as vectors for imaging agents as well. These liposomal-mediated contrast agents can be divided into two main categories: liposomes encapsulating the contrast agent within the core and liposomes in which the contrast agent is dispersed within the lipid bilayer. [40]

As example of FDA-approved liposome-based drug Doxil[®] is reported. It is considered the first approved “nanodrug” available on the market and has been successful since its introduction, with over \$600 million USD in annual world sales. [51], [69] Doxil[®] consist of a single lipid bilayer membrane liposomes composed of hydrogenated soy phosphatidylcholine (HSPC) and cholesterol with the antitumoral drug doxorubicin encapsulated in the internal compartment. [51] Mean size of the vesicles is in the range of 80–90 nm and because doxorubicin is a small-molecule therapeutic, each vesicle can hold a payload of up to 15,000 molecules. [51] In order to mitigate the stability and early release issues that traditional liposomal encapsulations of doxorubicin have, 2000 Da segments of poly(ethylene glycol) (PEG) are grafted to the liposome surface. [70] Doxil[®] vesicles rely on a simple passive targeting mechanism in order to accumulate at tumor sites. [69]

Furthermore, Doxil[®] presents a very little uptake of the liposomes by healthy tissue. Consequently, many studies have indicated that Doxil[®] efficacy is substantially higher than that of free doxorubicin and has dramatically different, and less severe, side effects than the free drug. [71]

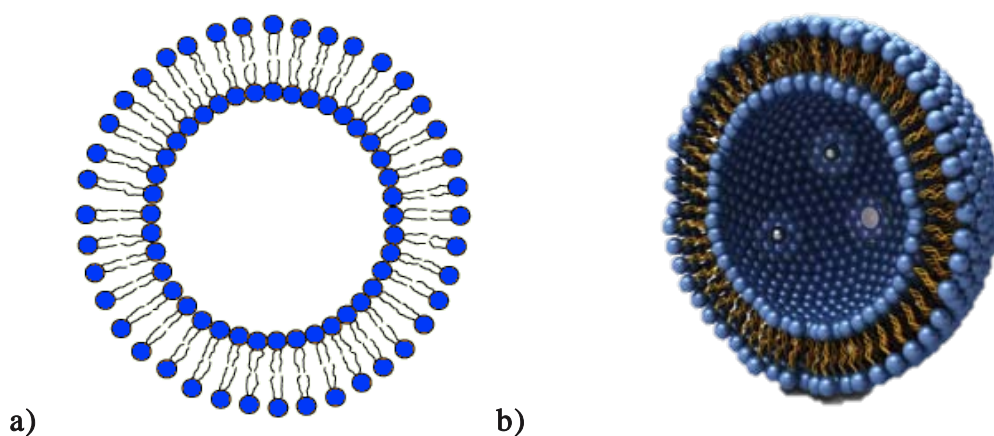


Figure 1.6. a) Schematic [72] and b) 3D representation of a liposome. [73]

1.4.3. Carbon nanotubes

Carbon nanotubes (CNTs) are tubular objects with a length-to-diameter ratio of up to 28000: 1 and a diameter in the nanometer range. CNTs can be single-walled carbon nanotubes (SWNTs) or multiwalled carbon nanotubes (MWNTs). SWNTs consist of a single layer of sp^2 hybridized carbon atoms (graphene) sheet rolled into a cylindrical tube. On the other hand, MWNTs are formed from multiple layers of concentric cylinders. [74] Both the CNT types are shown in Figure 1.7. In general, as the tips are open, CNTs can also be considered as nanocontainers. [22] Many molecules, ions, or metals can be inserted into the interior, giving to CNT the ability of delivering both drugs and imaging molecules. [75] This is the reason why CNTs are being investigated as TNPs because of their tunable properties and ability to incorporate multiple functionalities. [17]

Medical imaging agents derived from US-tubes are very promising as intracellular contrast agents; and even if CNTs provide poor MRI contrast, they can be functionalized to be made detectable [40][76]. For example NIR and Raman signals from CNTs have been detected in mice by using appropriate molecules. [76] The advantages of using CTNs for drug delivery is attributed to their exclusive ability of crossing various biological barriers without generating an immunogenic response. [22]

Although CNT have several unique properties, non-functionalized CNT are poorly soluble and highly cytotoxicity. This problem seems to be possibly faced by functionalization with more soluble and biocompatible materials; some study has demonstrated this functionalization that allows enhancing solubility in water, which bring them to an improved biocompatibility. [77] Moreover it must be mentioned that the main problems, which arise by using CNT, concern biodegradation and reduction of off-target toxicity. [17]

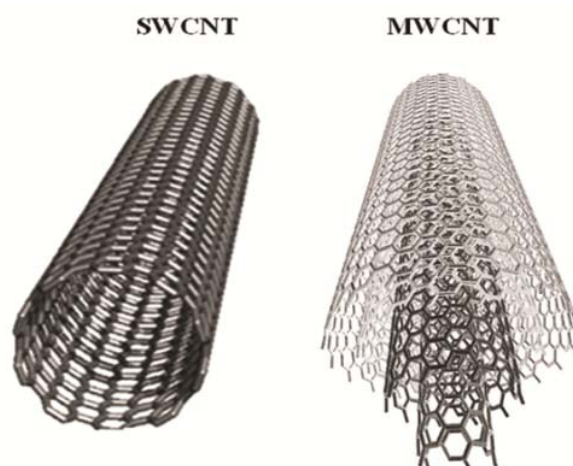


Figure 1.7. 3D representation of a single-walled and a multi-walled carbon nanotubes. [78]

1.4.4. Metal-based NPs

Metallic NPs

Metallic nanomaterials have been extensively studied for potential applications in nanotechnology and, thus, in the emerging field of nanomedicine. They can be synthesized in extremely small size, which range starts from 5 nm up to several hundreds of nm. Their properties can be tuned in a very various arrays, leading to interesting kind of different nanostructures. [12], [22], [79], [80] Metal-based nanomaterials have several attractive characteristics for nanomedicine applications, including biocompatibility and stability, unique tunable optical properties, and easy conjugation of biomolecules to the surface for tumor specific targeting. [12], [37] Thus, many diagnostic applications have been developed exploiting this type of NPs. The typical example are gold NPs (AuNPs). Large (420 nm) gold NPs (AuNPs) can be imaged using an optical microscope in phase contrast or differential interference contrast mode. Small AuNPs only absorb light, causing heat that can be detected by photothermal imaging. Furthermore the possibility of functionalize AuNPs with a wide range of chemicals, in particular carbon alkane and fluorocarbon ligands allow to use AuNPs for MRI imaging. [34], [37], [79] The presence of surface plasmon resonance (SPR) bands is responsible for their large absorption and scattering cross-section, which are 4 to 5 order of magnitude larger than that of conventional dyes and are not affected by photobleaching. [12], [22], [81]

Dealing with therapy issues, metal-based NPs are used and studied for therapy in deep tissues; once they are highly accumulated at the target site, are activated via the absorption of irradiation of an appropriate wavelength, and thereby can cause the irreversible thermal cellular destruction. [12]

Magnetic NPs

A variety of magnetic NPs have been developed for biomedical applications and the optimization of these carriers is one of the main fields of modern nanomedicine. [13], [82]

These particles consist of a metal or metallic oxide core coated with some organic macromolecules [83] or inorganic polymers in order to increase their stability and biocompatibility. [84] Various cell-specific targeting, imaging, and therapeutic functions can be incorporated into a single magnetic NP that is designed for simultaneous diagnostic and therapeutic use, without losing the individual properties of each component. [53] Magnetic NPs are thought to be optimal for the application in theranostic nanomedicine because of their unique properties which include uniform size, biocompatibility, superior imaging characteristics, and facile surface modification. [53] These structures can be used for cancer therapy as thermal release trigger when irradiated with infrared light or excited by an alternating magnetic field. In magnetic drug targeting, magnetic carrier particles with surface-bound or encapsulated drugs are injected into vascular system and then captured at the cancer site by an alternating magnetic field.

For example biocompatible superparamagnetic iron oxide NPs (SPIONs) are used in magnetic resonance imaging (MRI) contrast enhancement, tissue specific release of therapeutic agents, hyperthermia, and magnetic field assisted radionuclide therapy. [10], [13] In addition, many others metal-based NPs, with various surface functionalization, are being studied and used in nanomedicine applications. These include platinum [85], silver [80], and palladium NPs. [86]

1.5. SPIONs in nanomedicine

1.5.1. Characteristics

SPIONs consist of cores made of iron oxides NPs that can be targeted to the required area through external magnets. They show interesting properties such as superparamagnetism, high field irreversibility, high saturation field and extra anisotropy contributions. Biocompatible SPIONs have been widely used for *in vivo* biomedical applications including magnetic resonance imaging (MRI), contrast enhancement tissue-specific release of therapeutic agents and hyperthermia. [82] The main reason superparamagnetic particles are studied for application in the previous applications is due to the fact they do not retain any magnetism after removal of magnetic field. [13], [30], [82], [87] SPIONs are usually made of maghemite ($\gamma\text{-Fe}_2\text{O}_3$) and magnetite (Fe_3O_4) single domains of about 5–20 nm in diameter. [82][83] Magnetite, Fe_3O_4 , is a common magnetic iron oxide that has a cubic inverse spinel structure with oxygen forming an FCC closed packing structure with Fe cations occupying interstitial tetrahedral sites and octahedral sites [82][88]. Quantum size effects and the large surface area of magnetic NPs dramatically change some of the magnetic properties and exhibit superparamagnetic phenomena and quantum tunneling of magnetization, because each particle can be considered as a single magnetic domain. [89] Characteristics of SPIONs such as core and shell chemical composition, size (and its distribution), shape, crystallinity, roughness, surface hydrophobicity/hydrophilicity are important for their *in vivo* applications and must be well known and precisely controlled. [13]

From the practical point of view, these NPs are dispersed into suitable solvents by coating them with a lot of different molecules forming homogeneous suspensions, called ferrofluids. [90] Such a suspension can interact with an external magnetic field and be positioned to a specific area, facilitating magnetic resonance imaging for medical diagnosis and AC magnetic field-assisted cancer therapy; in other words these NPs are prone to be guided to the desired target area using an external magnetic field while simultaneously tracking their biodistribution. This approach truly makes them theranostic. [91] Moreover, SPIONs application in biology, medical diagnosis and therapy require that the SPIONs be stable in water at neutral pH and physiological salinity. Such colloidal stability depends on

various factors as the surface NPs chemistry, charge and the dimensions of the particles. [13]

1.5.2. Synthesis

The synthesis of magnetite NPs with controlled size has promoted scientific and technological interest for many years. [82] Most technological and medical applications require that these NPs possess sizes smaller than 20 nm with a narrow distribution in order to obtain uniform physical and chemical properties. However, producing magnetite NPs with the desired size and polydispersity without particle aggregation has been hard. [92] Magnetite NPs can be produced by the following different procedures such as co-precipitation of ferrous (Fe^{2+}) and ferric (Fe^{3+}) ions by a base in an aqueous solution [93], thermal decomposition of alkaline solution of Fe^{3+} chelate in the presence of hydrazine or chemical decomposition of hydrolysed Fe(II) salt followed by thermal treatment. [94] The disadvantage of these aqueous solution syntheses is that the pH value of the reaction mixture has to be adjusted in both the synthesis and purification steps, and the possibility to obtain smaller monodisperse NPs has only very limited success. [95] In order to overcome these problems, an organic solution-phase decomposition of the iron precursor at high temperatures has been widely used in last years for synthesizing small, monodisperse and stable SPIONs. [92] A schematic representation NPs obtained following this protocol is shown in Figure 1.8.

Different experimental conditions influence the size, the polydispersity and the stability of the produced SPIONs, which are important parameters related to their biological applications. Particles of sizes in the 10-20 nm range are preferable since show higher effective surface areas (easier attachment of ligands), lower sedimentation rates (i.e. high stability in suspension) and improved tissue diffusion and clearance. [13] Particles should be small enough to escape from the reticuloendothelial system (RES) in in-vivo applications, but not below 10 nm as they would selectively filtered by renal systems and eliminated from the body. [64], [82]

1.5.3. Colloidal stability by surface stabilization

The stability of SPIONs in suspension is controlled by (a) electrostatic, (b) van der Waals and (c) magnetic interactions. Due to all these three forces, SPIONs tend to aggregate to micron size supraparticles in suspension and such aggregation can hamper the efficacy of SPIONs in drug delivery (less drug loading) due to their low surface area and larger sizes. This can be avoided by a proper chemical-physical stabilization. [96], [97] Stabilization of SPIONs is typically performed using capping agents adsorbing onto the NPs surface. Most common molecules used for SPIONs stabilization employed during the synthesis are oleic acid, lauric acid, alkane sulphonic acids, and alkane phosphonic acids. [98] Such ligands confer optimal stability by steric repulsion but are not able to produce water soluble NPs. [92] Hence, the stabilization of SPIONs in suspension by modifying their surface with some coating is an important issue in the context of medical application.

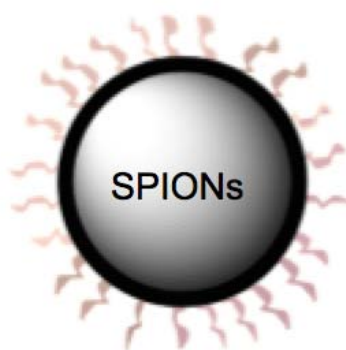


Figure 1.8. Schematic representation of a SPION stabilized by oleic acid ligands and soluble in non-polar solvents. [9]

1.5.4. Coating

The control of the surface properties of SPIONs is performed using coatings made by different materials such as surfactants, biocompatible polymers and biomolecules (typically peptides or proteins). [83], [99], [100] The coating makes SPIONs soluble in water or polar solvents, provides colloidal stability and act also as shielding agent for the magnetic interactions. It can also be further functionalized in order to produce active

targeting nanostructures (targeting ligands studied includes proteins, peptides, antibodies, polymers, carbohydrates, aptamers, DNA, RNA and oligosaccharides). [38] The biomolecules are the active part that provides the NP with a theranostic function; they must be chosen very carefully according to the specific application. For example, the attachment of targeting ligands onto the coating produces theranostic NPs with enhanced ability to accumulate in the ROI (Figure 1.9). [38], [101] It must be taken also into account that the capping ligands chemistry and the hydrophilicity of the coating layer have significant effect on SPIONs magnetic properties. [10]

In addition, the surface charge of coated SPIONs play a significant role in colloidal stability since it confers the possibility to produce reliable pharmaceutical products. [13] It can be qualitatively described as the nature and behavior of the surface groups in solution at a certain pH in the presence of an electrolyte. Quantitatively, it can be measured as an electrical potential in the interfacial double layer on the surface of NPs in suspension. A high Zeta-potential (+ or -) value is an indication of the dispersion stability of SPIONs due to the electrostatic interaction. [13]

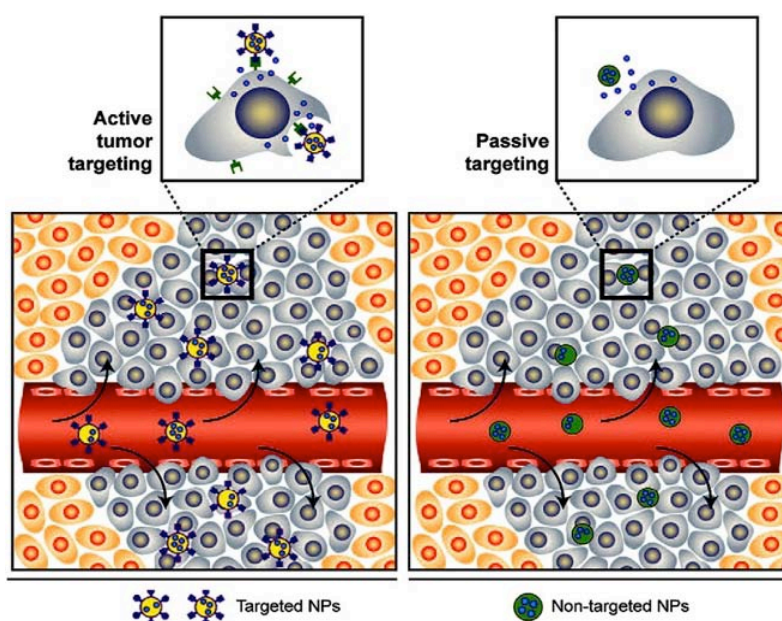


Figure 1.9. Passive vs active targeting. NPs tend to passively (by their biophysicochemical properties) pass through the inflamed vasculature. On the right passive targeting mechanism is shown compared to the active targeting on the left. Once NPs have passed in the target tissue, the presence of targeting ligands on the NP surface can result in active recognizing of NPs by receptors that are present on target cell or tissue. This resulting in enhanced accumulation and cell uptake through receptor-mediated endocytosis [14].

Many coating materials and coating procedures have been studied and used for surface modification of SPIONs. The chosen materials must not be toxic and, on this line, a lot of studies have been performed. Typically the coating procedure consists in the use of various biocompatible polymers or natural biomolecules. [102], [103] Biocompatible polymers and peptides can be classified as hydrophilic or amphiphilic, neutral or charged. [10], [38] Polymers include typically dextran and polyethylene glycols (PEGs) known to be biocompatible and promote good dispersion of SPIONs in aqueous media. [104] Dextran is a branched polysaccharide consisting of glucose subunits and PEG is a neutral linear polymer and can be prepared with a variety of terminal functional groups. Their neutral nature helps SPIONs to escape from phagocytes providing a longer blood circulation time. Although PEG and dextran increase blood circulation time of SPIONs, they do not offer any biological targeting. This is the reason why proteins and peptides for targeted have found large use to provide biological surface functionalization of the SPIONs. [83], [105] Attention should be posed on the fact that some of polymeric materials that are used for surface modification may be the cause of unwanted high uptake in the liver and spleen possibly showing toxic effects in the site of accumulation. [98], [102]

Two main coating protocols were investigated in the literature: i) Replacement of a stabilizing hydrophobic capping ligand producing single NP coated with molecules possibly conjugated with drugs and targeting moieties. [104]–[107] ii) coating of supraparticles of hydrophobic SPIONs in order to be able to encapsulate hydrophobic molecules inside the supraparticles. [30], [38], [83] Some examples of single NP and supraparticle coating results are reported in Figure 1.10. Surface modification of SPIONs can be carried out either during their synthesis or in a post-synthesis process. [13], [83]

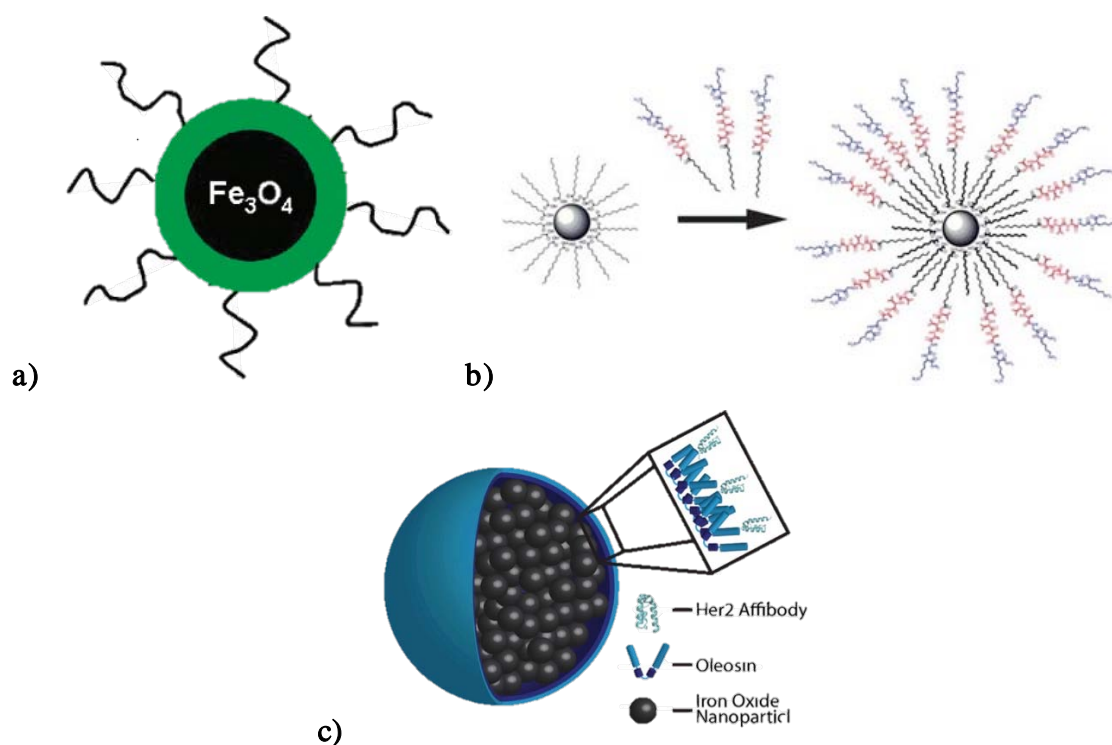


Figure 1.10. Schematic representation of a) a single particle coated by a thermally cross-linked polymer. [104] b) Non-covalent functionalization of single SPIONs with peptide amphiphile molecules. [105] c) Oleosin coated SPIONs supraparticle functionalized by targeting ligands for a specific type of cells. [83]

1.5.5. SPIONs in drug delivery

SPIONs-assisted drug delivery is a very promising research field and some systems have been designed to deliver peptides, DNA molecules, and chemotherapeutic, radioactive and hyperthermic drugs. [82], [108] The process of drug localization using SPIONs is based on the competition between forces exerted on the particles by the blood compartment and magnetic forces generated from the applied magnetic field. [13] In most cases, the magnetic field gradient is generated by a strong permanent magnet, fixed outside the body over the target site. The biocompatible surface engineered SPIONs, usually in the form of a biocompatible ferrofluid, are injected into the patient parenteral. Then magnetic particles are retained at the target site by external, high-gradient magnetic fields. Once the drug/carrier is concentrated at the target, the drug can be released either via enzymatic activity or changes in physiological conditions such as pH or temperature, and may be internalized by the endothelial cells of the target tissue or be taken up by the tumor cells.

Such a system has the potential to minimize the side effects and the required dosage of the drugs. [109] However, once such NPs reach cells interior, the coating is very probably digested leaving the bare particles exposed to other cellular components thereby potentially influencing the overall integrity of the cells. [110] It is hypothesized that rigid coatings such as crosslinked PEG could postpone this shortcoming. [111]

1.5.6. SPIONs in MRI diagnostic

SPIONs have been extensively studied and used as contrast agents for MR imaging of tumors as targeting probes eventually up to microscopic resolution. [38]

SPIONs exhibit a high magnetization when an external magnetic field is applied. Along this line the most interesting characteristic of these particles compared to traditional magnetic materials, is the fact that they no longer show magnetic interaction after the external magnetic field is removed. Such NPs primarily act to short T_2 values of the water protons surrounding the particle. More precisely, when SPIONs present in tissue are subject to an external magnetic field the large magnetic moments of the particles align to create large heterogeneous field gradients through which water protons diffuse. The dipolar coupling between the magnetic moments of water protons and the magnetic moments of particles cause efficient spin dephasing and T_2 relaxation leading to a decrease in signal intensity [112]. The contrast provided by SPIONs in a T_2 weighted image is termed negative contrast enhancement since areas with high concentrations of SPIONs that appear dark on MR images. [10] In addition, surface coating and functionality is essential for SPIONs as MRI applications. The good water solubility of SPIONs is important to avoid the aggregation. It is also important to modulate the water soluble SPIONs and the coating thickness for T_1/T_2 relaxations in MRI. Different thickness of coating materials will affect T_2 relaxivity of water protons from magnetic field. [38] Another approach that has recently been investigated is the addition of a traditionally MRI used gadolinium chelate on the polymer coating of SPIONs. [113] This dual contrast agent efficiently reduces both T_1 and T_2 relaxation times and achieves good contrast in mice for both T_1 and T_2 weighted images. This unique combination allows for the acquisition of both highly detailed T_1 weighted anatomical images and pathologically relevant T_2 weighted images with a single imaging nanoprobe. [10]

SPIONs have been already approved for some clinical use as a blood agent for MRI [82], but further studies have been performed in the last years. More specific understanding of the various interactions of SPIONs with biomolecules in the body lead to the development of particles with optimum surface properties; that could overcome the problem of “rejection of magnetic NPs by the human body”.

1.6. Gold nanoparticles

1.6.1 Characteristics

One of the most commonly used metal-based nanoparticles in nanomedicine are the gold nanoparticles (AuNPs). These are available in the range from 1 to more than 120 nm and they disclose considerable applications in optics, catalysis, materials science and nanotechnology also including biology and nanomedicine. [34] While there is a large number of ways to synthesize AuNPs, the most common is to start from HAuCl_4 . The first reported synthesis was performed by Michael Faraday in 1857 where he described the formation of deep red solutions of colloidal gold (the so called "activated gold") by reduction of an aqueous solution of chloroaurate (AuCl_4^-) using phosphorus in CS_2 (a two-phase system) [114], [115]. Through the years many other methods were investigated in order to obtain colloidal gold suspensions: one of the most important was the Turkevich method, introduced in 1951, where the reduction of Au^{III} to Au^0 , obtained with a small amount of sodium citrate, evolved in a single water phase [116]. In this synthesis the growth of the NPs is controlled by varying the citrate/gold ratios: the citrate ions form a double layer around the particles, stabilizing them electrostatically. Generally, smaller amount of citrate yields larger nanospheres. Even if it is possible to produce nearly monodisperse gold nanospheres, the major limitations of this method are the low yield and the restriction of using water as solvent. [117] To overcome these problems, in 1993, Giersig and Mulvaney reported a method inspired to Faraday's two phase procedure capable of producing thermally and air stable gold nanospheres of reduced size-dispersion and well-controlled size (below 10 nm) [118]. After some years, in 1994, Brust and coworkers improved this methodology through the introduction of a phase transfer catalyst and stabilizing agent (tetraoctylammonium bromide) that brought to even higher yield and size monodispersity. In order to guarantee long stability to the particles, dodecanethiol was added: thanks to the strong thiol-Au bond these NPs are stable and do not aggregate even after drying and re-dissolution in other organic solvents. [119]

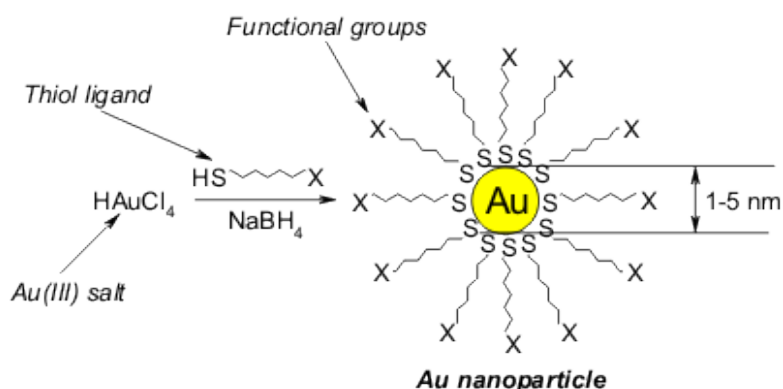


Figure 1.11. schematic representation of thiolate stabilized AuNP and its synthesis according to Brust method [119].

Still nowadays, the Brust direct synthesis method is one of the most used to produce functionalized gold NPs. The main drawback that this method presents is the contamination of the NPs shell with residual TOAB [120]. Brust himself developed a new single-phase method to overcome this problem [121], but also many other scientists tried to find new ways to synthesize gold NPs with a monophasic reaction. The Turkevich's experiments have been improved and new procedures have been fine-tuned not just in aqueous phase but also in organic environment [122]–[125]. Thanks to these new chemical methods, gold NPs have been synthesized and stabilized by a large variety of stabilizers (ligands, surfactants, polymers, dendrimers, biomolecules) and the terminal end of such ligands can be also modified with various functional groups. One interesting synthesis was performed by Zhichuan Xu *et al.* who used oleylamine both as capping and reducing agent in a single organic phase. [126] In fact, the choice of the stabilizer molecule is of paramount importance, because it determines the size and size distributions, dispersion media, activity, solubility and therefore the application of the obtained AuNPs [34], [79], [115], [127].

As already mentioned, every nanostructure used for medical purposes needs to be water-soluble and biocompatible, and gold NPs are not an exception. They are turned to water-soluble NPs typically by using water soluble thiol ligands, which can be divided into three groups: (i) thiols terminated with a polyethylene glycol (PEG) moiety that are

employed to form “inert surfaces” which resist to nonspecific adsorption of biomolecules; (ii) simple alkyl-thiols with a polar end group such as a carboxylate or an ammonium ion; (iii) biomolecules such as peptides, glycosides, DNA sequences, containing a thiol group or linked to a short alkyl thiol. In particular, the last two categories may display some possibilities of functional groups at the interface and can be exploited to create medical diagnostic and therapeutic nanostructures. [36], [128], [129]

Moreover, it is possible to synthesize not only spherical AuNPs but also different shaped AuNPs such as gold nanorods gold nanoshells, gold nanostars and so on. [130], [131]

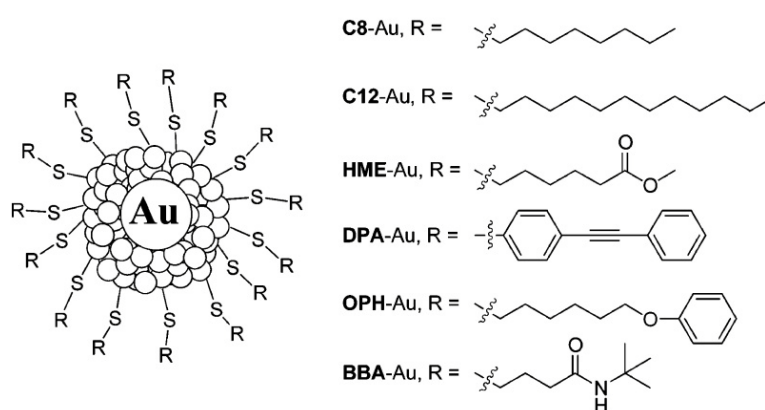


Figure 1.12. Thiolate monolayer-protected gold nanoparticles [124].

Another way to functionalize gold NPs surface with specific organic molecules is through ligand-exchange reactions. [37] Ligand-exchange reactions are mainly used for two reasons: achieving more monodisperse, homogeneously coated NPs and obtaining multi-functionalized gold NPs, in such a way the final NPs are characterized by various properties deriving from a mixed ligand shell. [37] This pathway is particularly interesting when trying to synthesize NPs functionalized with molecules that are not suitable in a direct synthesis, for chemical or physical reasons [28]. For example, short chain hydrocarbon ligands can be replaced with long chain hydrocarbons or plain hydrocarbon chains can be replaced with molecules bearing end-groups such as Br, CN, OH, CO₂H. [37]

Between all the advantages, offered by differently functionalized AuNPs, the most interesting property derives from the Au core. In fact, the great interest to Au NPs is due to the electronic properties of Au: according to the Mie theory, an electromagnetic frequency induces a resonant coherent oscillation of the free electrons on the surface of a spherical NP, called surface plasmon resonance (SPR), only if the particle size is much smaller than the light wavelength. [132] This absorption lies in the visible region for Au, Ag and Cu. For metal nanoparticles, the localized surface plasmon resonance results in an enhanced electromagnetic field at the metal nanoparticle surface. [133] For AuNPs the plasmon resonance is observed down to 3 nm diameters, below which the NP can no longer be considered as a “normal metal” with a conduction band. [34] As a result, an enhanced electromagnetic field appears at the AuNP surface above this size allowing surface-enhanced optical properties revealed using spectroscopic techniques. Thus, the signal intensity of the SPR bands is several orders of magnitude larger than those of all the organic dyes. [132]

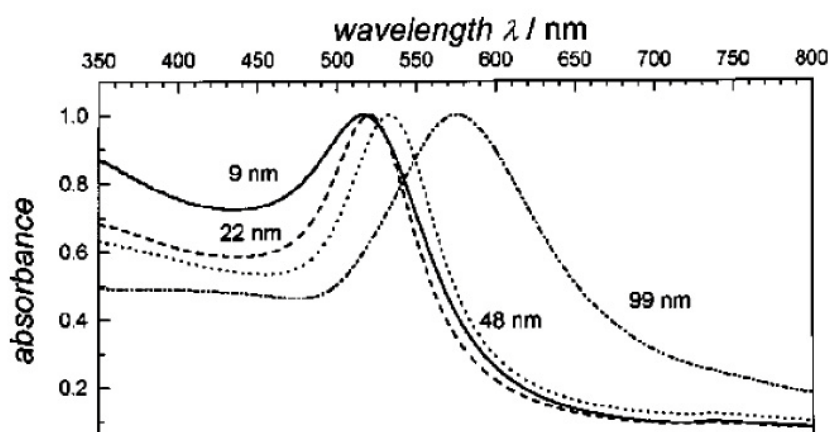


Figure 1.13. Surface plasmon resonance of 9, 22, 48, and 99 nm spherical gold nanoparticles [132]

For spherical AuNPs the surface plasmon band is very sensitive to the composition, size, shape, inter-particle distance and environment (dielectric properties) of the AuNPs. It is the high sensitivity to these factors that makes the basis of their use for biological labeling, detection, diagnostic and sensing. For instance, with AuNRs, two plasmon bands are observed, one corresponding to oscillations along the length of the AuNR (longitudinal plasmon band) and the other along the width of the AuNR (transverse plasmon band). The positions of these two bands vary with the AuNR aspect ratio. Thus AuNRs exhibit

plasmon bands with two maxima and since the ratio influences the position of the plasmon band absorption, the syntheses of AuNRs can be adjusted with suitable ratio. [34] AuNPs with a diameter smaller than 20 nm essentially show absorption, but when size increases up to 80 nm also increases the ratio of scattering to absorption. A high scattering cross section is indeed required for biological imaging based on light scattering. [34], [133]

Therefore, from a biomedical point of view, plasmon absorbance is an important feature for gold nanoparticles, although it is not always present. Gold exhibits size-tunable plasmon absorption due to electrons confinement, in both the ground and excited state, to dimensions smaller than the electron mean free path (≈ 20 nm for gold). If the nanoparticle size is further reduced, confinement of the free electrons reaches a second critical size scale called the electron Fermi wavelength. This starts to happen at a size lower than 3 nm and should result in discrete, quantum-confined electronic transitions that heavily affect the plasmon absorption properties. [134], [135] Generally, with decreasing cluster size, the broad absorption band centred at 2.4 eV decreases its intensity until the spectrum is a nearly featureless straight line stretching from the near-infrared through the near-ultraviolet (see Figure 1.14). [135]

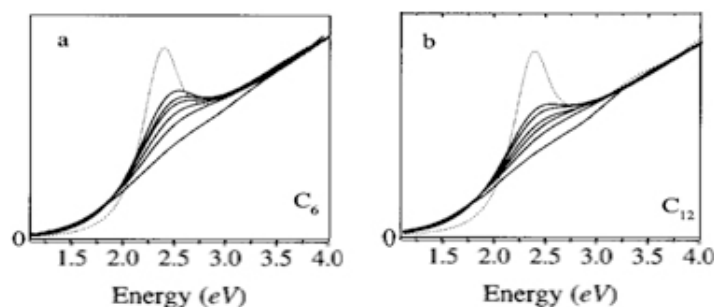


Figure 1.14. Normalized optical absorption spectra for dilute solutions of several purified fractions of nanocrystal gold molecules passivated by (a) hexyl-thiolates and (b) dodecyl-thiolates. The spectra are compared to an aqueous solution of commercial colloidal Au particles (dotted lines) of 9 nm mean size. The plasmon peak amplitude (near 2.5 eV) diminish with the metallic core diameters: (a) 3.2, 2.5, 2.4, 2.2, 2.0, and 1.7 nm (SC₆ passivant); (b) 2.5, 2.4, 2.2, 2.1, 2.0, and 1.7 nm (SC₁₂ passivant) [135].

1.6.2. Imaging with Gold NRs and NPs

Gold nanostructures could be the perfect tool for diagnostic and therapy, due to their versatility. Some techniques, as NIR fluorescence imaging and photothermal therapy, take advantage of the specific signals given by tailored shapes of gold complexes. Nanorods, as said before, present two characteristic plasmonic peaks in the UV-Vis-NIR spectrum. These techniques employ longitudinal oscillation of electrons, which gives rise to a strong long wavelength band in the NIR part of the spectrum. These peaks can be tuned properly to have the maximum of longitudinal absorption peak of the surface plasmon resonance in the range of 700 - 900 nm. As it can be seen from figure 1.10, the longitudinal absorption band shifts from the visible to the NIR region increasing the rod's aspect ratio. Thus, since long-wavelength laser irradiation around these lengths can penetrate tissues *in vivo* and excite the SPR of these structures, a double advantage is gained. This property in fact allows to have a molecular imaging tool using simple dark-field microscopy, where nanorods act like a novel contrast reagent, and a selective photothermal therapy tool using a near-infrared low energy continuous wave laser [20], [21], [24], [136]–[138].

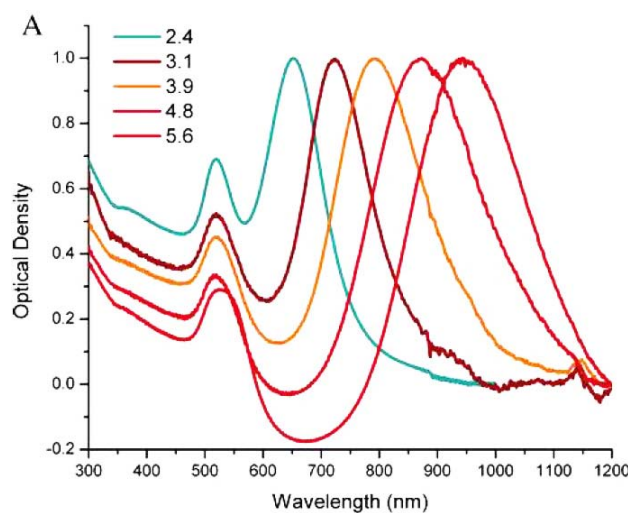


Figure 1.15. UV-Vis-NIR spectrum of gold NRs of increasing aspect ratio [136].

Despite nanorods, gold nanoparticles present just one characteristic surface plasmon resonance peak in the UV-Vis spectra, around 520-540 nm depending on their

dimension and shape. [132] Also with NPs, SPR can be used to have a very peculiar signal for imaging. It is possible, for example, to enhance a signal due to the very intense electric field that is created around the AuNPs. This is the case of surface enhanced Raman spectroscopy (SERS), which takes advantage of Raman effect: when a photon is scattered by an atom or a molecule, it could be scattered elastically (Rayleigh scattering) or inelastically (Raman scattering). In the first case the scattered photon has the same frequency and wavelength as the incident photons, whereas in the second case the emitted one has a different energy. This depends from the possible polarization modes that the molecules can assume after the photon absorption. Because of the complexity of the phenomenon (compared to elastic scattering), only 1 in 10 million photons are scattered with Raman scattering. [139] Thanks to SPR, SERS has been developed and has brought new way to investigate very detailed structures as molecules. In fact, this imaging technique can enhance the weak Raman scattering signal up to 10^{10} to 10^{15} times. [140]–[142] Even if the exact mechanisms of enhancement are not completely understood, the only theory that seems to fulfill the phenomenon is the electromagnetic theory. According to this theory, the increase of the Raman signal is caused by a strong enhancement of the electric field in proximity of the surface. This electric field induces a SPR on the surface and so on the molecules or NPs that lie on the surface: the field enhancement is greatest when the plasmon frequency, ω_p , is in resonance with the incident radiation. Since the SPR peak of gold NPs is located in the visible region of the UV-Vis spectra, a visible light laser should be used for this kind of detection technique [143], [144]. This allows to have a very strong signal coming from a single NP, that, if binds to a molecules or a specific target, could reveal the presence of single complexes on the surface. These are the reasons why this technique is widely used and promising for detection and diagnostic with nanostructured sensors. [145]

Another important technique that could take advantage of AuNPs is Computed Tomography (CT). This tool provides an accurate 3D imaging of the internal tissues of human body thanks to different scattering and X-Ray absorption of the elements in human body. Different tissues present very different composition, and so X-Ray interacting with these structures will be more attenuated the higher will be the atomic number of the elements inside the tissue. [146] Properly functionalized gold NPs, could be conjugated to

a wide range of tissues or molecule inside the human body, they could give rise to a strong attenuation of the X-Ray in proximity of the desired target yielding a tunable contrast that allows recognition of specific tissues. This technique has been widely used for imaging of tumors and the use of AuNPs is a very promising tool for the detection of very small targets. [147]–[149] Another tomography technique that gives several information about functional processes in the human body is the Positron Emission Tomography (PET). This nuclear medicine and functional imaging technique produces a three-dimensional image of functional processes in the body. The signal is produced by the introduction in the human body of a radionuclide with a well-known decay time. While decaying, the nuclide will emit a positron that can be detected and measured. It is possible then to go back up to the origin of the emission and to build up the area of emission and so the tissue volume. The main difficulty in this process is the insertion of the radionuclide in the right place inside the human body, conjugating the emitting atoms to those structures that have to be measured. [150], [151] One of the most promising emitting agents is ^{18}F , widely used for this kind of diagnostic, but the targeting to specific molecules is still today a great field of research. A new solution for this application could be the labeling of ^{18}F in fluorinated gold NPs. In this way the nuclide could bind to the target structure and emit from the area of interest. [152] PET and CT are very often combined together to provide a complete analysis of the part under study: PET with the functional processes whereas CT with very accurate 3D imaging. [151]

1.6.3. Fluorinated Gold NPs

It is possible to replace the typically used alkyl thiol ligands, used in Au NPs and/or nanoclusters stabilization, with fluorinated ligands. This offers several advantages such as: (i) tunability of size and shape of the NPs and their optical properties; (ii) possibility of multimodal detection; (iii) possibility of encapsulation of a drug in the hydrophobic moiety formed by the fluorine corona. [36]

Among all the possible stabilizing ligands, perfluorocarbons (PFCs) are one of the most interesting molecules because of their unique properties. [153] These compounds, in which all the hydrogen atoms are replaced with fluorine, show highly hydrophobic and

significantly lipophobic behaviour. In addition, thanks to the strength of the C–F bond and the high electronegativity and low polarizability of fluorine, PFCs exhibit high thermal, chemical, and oxidative stability, low polarity, weak intermolecular interactions, high vapour pressure, and small surface tension. [28] These properties confer to PFCs the role of one of the most used probes in ^{19}F MRI. [28] However, even if PFCs show such unique properties, their application as stabilizing ligands for gold NPs is still a quite new field of research. [37]

The production of fluorinated gold NPs is more difficult because of the PFCs particular chemo-physical properties. For example, due to their low solubility in common organic solvents, PFCs require the use of fluorinated solvents more difficult to handle than their non-fluorinated counterparts.

Functionalization of AuNPs with perfluorinated ligands has been reported only in very few works so far. Some of them exploit variations of the Brust method, for example using thiolates rather than thiols to overcome the reduced nucleophilicity typical of sulfur atoms close to a perfluorinated chain. Alternatively, a ligands-exchange reaction can be used. [28]

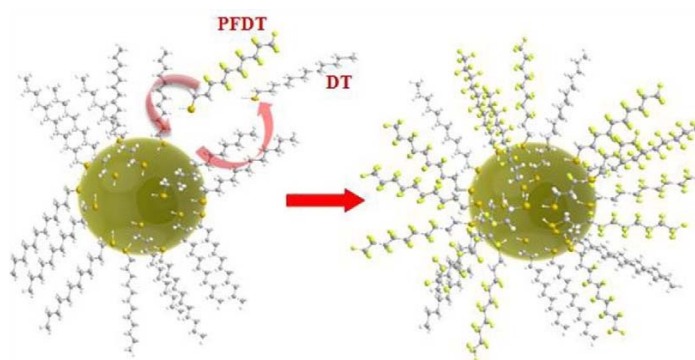


Figure 1.16. Representation of hydrocarbon–fluorocarbon exchange reactions on gold NPs. In this example Perfluorodechanethiol (PFDT) ligands replace Dechanethiol (DT). [37]

The obtained NPs are generally hydrophobic, given the poor hydrophilicity of perfluorinated chains and their attitude to give strong fluorofluorous interactions.

Further functionalization with hydrophilic groups and/or amphiphilic coating agents is therefore necessary to disperse them into aqueous solutions. [28] For example, water-soluble fluorinated AuNPs were obtained using thiols containing a perfluorinated portion and a short polyethylene glycol unit. [36], [37]

Despite the complications involved in the use of fluorinated ligands to stabilize gold NPs, it is an interesting and “hot” topic with promising advancements and results. PFCs combined with gold NPs are envisaged to produce innovative theranostic nanostructures that can bear multimodal diagnostic modalities such as ^{19}F MRI, ^{18}F -PET, SERS (Surface enhanced Raman Spectroscopy) and NIR fluorescence. [37]

1.6.4 Gold NPs Toxicity

The long history of gold colloid use for therapeutic purposes suggests that AuNPs should be biocompatible. In order to apply AuNPs to nanomedicine, their toxicity needs to be thoroughly examined. Since, in principle, everything is toxic at high dose, the important issue is whether AuNPs are toxic at the concentration at which they will be used (believed to be in the range of 1–100 AuNPs per cell). In addition, it must taken into account that *in vivo* conditions are different from the ones that can be studied *in vitro*, therefore more *in vivo* studies are required in order to achieve a better comprehension. The cytotoxicity of AuNPs has been studied by several research groups and some of these efforts have been reviewed. [34], [154]

Moreover, it is essential to distinguish between the toxicity of the AuNP core and that due to the ligands. [11], [37] PFCs are very inert compounds: they tend to be non-toxic *in vivo*, in most cases are not degraded at physiological pH values, are generally not metabolized by enzymes and tend to be cleared via the reticuloendothelial system. [28], [34], [153] However, prolonged retention in the organism of PFCs increases rapidly when the F-chain exceeds eight carbon atoms. [153]

Indeed, it has been suggested that AuNPs could be taken as reference nanoparticles for low toxicity in the set-up of a nanoparticle toxicity scale, given the higher toxicity of carbon nanotubes and quantum dots. [34] To better study the interaction of gold NPs with the cell membrane structure, new techniques as neutron reflectometry can be used to investigate

the effect in the bilayer structure of the cell membrane (see Chapter 5).

1.7. Aim of the project

Within the scenario offered by all the possible modalities studied in theranostic nanomedicine field, this work focus in particular on diagnostic nanostructures with some potential applications also as theranostic tools. More specifically, attention has been posed in the production, development and optimization of water-soluble SPIONs as MRI enhancing contrast agents and fluorinated Au NPs used as ^{19}F MRI probes. As mentioned before, these two types of NPs are interesting because of their biocompatibility and their peculiar physical-chemical properties that can be tuned changing size, shape and coating. They are ideal candidates to be used as theranostic agents since they can be used as imaging tools, exploiting the intrinsic properties of their core and work as targeting nanocarriers through functionalization of their surface with different ligands. Moreover, they enable also the encapsulation of hydrophobic molecules (drugs) thanks to their structural features that offer a hydrophobic pocket.

Moreover, a key issue in making use of NPs for biomedical purposes is understanding their interaction with cells beyond their designated functions; the first contact that nanomaterials have with any living organism is through the cell membrane. Therefore, this work also investigates on the interaction of AuNPs with model cell membranes through neutron reflectometry measurements. The attention was mostly posed on cell membrane integrity when it is posed in contact with Au NPs. Given the complexity of the methodology, this study has been first done on model NPs that has been well-characterized. In particular, in this thesis has been carried out an advanced analysis of these data by software analysis of neutron reflectometry experiments on zwitterionic lipid double bilayers in the presence of Au NPs functionalized with cationic and anionic head groups; experiments that have been performed by the “Soft matter Science and Support” group at ILL.

In more detail, the objects of the work are the following. They are reported divided in the three main experimental field of the project.

i) Development of Magnetite NPs as possible theranostic agents

- Synthesis and characterization of hydrophobic SPIONs (Super Paramagnetic Iron Oxide NPs) by following a synthesis protocol known in literature.
- Development, optimization and characterization (both in water and in water-based buffer) of a novel coating protocol to produce water-soluble SPIOs supraparticles coated by a “surfactant” protein called type II Hydrophobin (HPB II).
- Validation of HPB II coated SPION to encapsulate a hydrophobic molecule (as model systems of cytotoxic drugs).

ii) Synthesis of fluorinated Au NPs as ¹⁹F MRI probes

- Synthesis and characterization of hydrophobic fluorinated Au NPs by following two different synthesis protocols: modification of Brust method and ligands exchange reaction.
- Optimization of the ligand exchange reaction protocol. This was performed studying the influence of the amount of PFDT and the reaction time.
- Validity of the possibility to coat fluorinated Au NPs synthesized by Brust modified method by adapting the same HPB II coating proposed for SPION.

It is appropriate to state that the trials concentrating Au NPs were performed almost at the end of this project and were not examined in depth. They give only a direction for future studies.

iii) Analysis of Neutron Reflectometry experiments to study Au NPs interaction with cell membranes

Neutron reflectometry data were analysed by Motofit software. More precisely neutron reflectometry data of AuNPs interacting with a double bilayer membrane model have been fitted in order to obtain the best match between experimental points and the numerical simulated curve. The main point of the experiment was the increase of complexity of the membrane model that was tuned properly for a better investigation of the problem.

Chapter 2 - Materials and methods

2.1. Materials

Reagents:

Iron (III) acetylacetonate [$\text{Fe}(\text{acac})_3$, $\text{Fe}(\text{C}_5\text{H}_7\text{O}_2)_3$], Gold(III) chloride trihydrate [$\text{HAuCl}_4 \cdot 3\text{H}_2\text{O}$, $\geq 99.9\%$]; Sodium Borohydride [NaBH_4 , 98%]; Oleic acid [*cis*-9-Octadecenoic acid; $\text{CH}_3(\text{CH}_2)_7\text{CH}=\text{CH}(\text{CH}_2)_7\text{COOH}$];

Oleylamine [*cis*-1-Amino-9-octadecene; $\text{CH}_3(\text{CH}_2)_7\text{CH}=\text{CH}(\text{CH}_2)_7\text{CH}_2\text{NH}_2$, 70%], 1,2-tetradecanediol ($\text{CH}_3(\text{CH}_2)_{11}\text{CH}(\text{OH})\text{CH}_2\text{OH}$, $\geq 97\%$); Tetraoctylammonium bromide (TOAB) [$[\text{CH}_3(\text{CH}_2)_7]_4\text{N}(\text{Br})$, 98%]; Acetic acid ($\text{C}_2\text{H}_4\text{O}_2$, 99-100%) and 1*H*,1*H*,2*H*,2*H*-Perfluorodecanethiol [$\text{CF}_3(\text{CF}_2)_7\text{CH}_2\text{CH}_2\text{SH}$, 97%] were purchased by Sigma-Aldrich®.

Sodium Acetate (CH_3COONa , 99% anhydrous) was purchased by Farmitalia Carlo Erba®.

Hydrophobin class II protein (HPB-II) is provided by VTT Technical Research Centre of Finland.

Solvents:

Benzyl ether [$(\text{C}_6\text{H}_5\text{CH}_2)_2$, 98%]; Toluene [$\text{C}_6\text{H}_5\text{CH}_3$, $\geq 99.7\%$]; α,α,α -Trifluorotoluene [$\text{C}_6\text{H}_5\text{CF}_3$, $\geq 99\%$]; Ethanol (EtOH, $\text{CH}_3\text{CH}_2\text{OH}$, 99.8%) and Chloroform (CHCl_3 , $\geq 99.8\%$) were purchased by Sigma-Aldrich®. The water used during the entire experimental phase was a deionized Milli-Q water (mQw) (18.2 m Ω /cm) provided by a Simplicity® water purification system.

The fluorophore molecule used is Nile Red [9-diethylamino-5-benzo- α -phenoxazinone; $\text{C}_{20}\text{H}_{18}\text{N}_2\text{O}_2$] purchased by Sigma-Aldrich®.

All of them have been used as received, HPB was stocked under vacuum in a Falcon sealed using Parafilm® in order to avoid contact with air humidity, Nile red was stocked in a dark room in order to avoid fluorescence degradation.

2.2. Methods

2.2.1. Size measurement and colloidal stability

The hydrodynamic diameter (D_H) size of the obtained samples has been measured by Dynamic Light Scattering (DLS) and by Transmission Electron Microscopy (TEM). Colloidal stability has been measured by Zeta-Potential analysis.

Dynamic Light Scattering (DLS)

In DLS technique a monochromatic and coherent light allows the observation of time-dependent fluctuations of the scattering intensity when passing through a particle suspension. The distance between the particles is always changing since they are subjected to Brownian motion and constructive and destructive interferences occur, so the time-dependent scattering fluctuations contains the information about the dynamics of the particle, and then about their hydrodynamic size. [155]

During an experiment, the dynamic information on particles is derived from the autocorrelation function of the intensity of the scattered that typically shows an exponential time decay:

$$g_2(q; \tau) = A \exp(-\tau/\tau_c) + B \quad 1)$$

Where A and B are constants and τ_c (in seconds) is the relaxation time which is related to the hydrodynamic diameter of the dispersed particles. By measuring such time correlation decay, τ_c , and knowing the diffusion coefficient of the solvent, it is possible to measure the nanoparticles D_H through the Stoke-Einstein equation (3):

$$\tau_c = \frac{1}{2Dq^2} \quad 2)$$

$$D = \frac{K_B T}{6\pi\eta r_H} \quad 3)$$

Where q is the scattering vector, D is the diffusion coefficient, K_b is the Boltzmann constant, T is the temperature (K), η is the solvent viscosity and r_h is the hydrodynamic radius of the particle. This formula is valid only for spherical particles, if the DLS analysis is performed on non-spherical NPs (rodlets, discs, ecc...), the measured radius is the hydrodynamic radius of the equivalent sphere. When the dispersion is not monodispersed and contain different distributions more advanced algorithms are used in order to achieve a better interpretation of the autocorrelation data and distinguish different size populations' contribution to the signal. [156]

Zeta-Potential

Zeta-potential analysis gives information on the colloidal stability through the evaluation of the NPs net surface charge. If NPs are particularly negative or positive charged they repel each other avoiding flocculation. It is important to state that NPs functionalized with coating agents could also be stabilized by steric interactions, bearing sometime Zeta-Potential close to zero. A net charge on NPs surface will affect the distribution of the ions in the solution at the interface, causing an increase in the counterion concentration close to the NPs surface. It means that an electrical double layer is formed around the NPs. The two layers are an inner region called Stern Layer, where ions are strongly bound to the surface, and an outer part of diffuse ions that are bound weakly (called diffuse layer). The potential at the interface between the Stern and the diffuse layer is the Zeta Potential (see Figure 2.1). When an electric field is applied, charged NPs tend to move toward the electrode with opposite charge and their velocity become constant when the equilibrium with viscous forces is reached. This velocity is measured and can be related to Z-potential value. [157] It is important to consider that the magnitude of the charge on the nanoparticle surface depends on the solution pH. In fact, the surface charge can be reduced to zero at a specific pH referred to as the isoelectric point. [158]

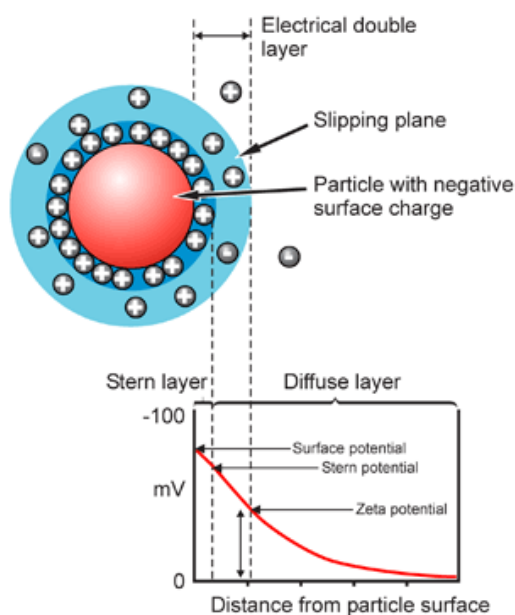


Figure 2.1. Schematic representation of the ion double layer which provides the Zeta-potential values [158].

A Malvern® Nano-zetasizer has been used for both DLS and Zeta-Potential measurements. For DLS measurements 450 μL of solution were transferred in a ZEN0112 plastic cuvette, for Zeta-Potential measurements 1 mL of solution was transferred in a DTS1060C plastic cuvette. Samples were tip-sonicated on ice (3 x 30'' cycles) before analysis. DLS analysis consisted on 3 runs of 8 measurements each at 25°C after 2 minutes of sample equilibration. Data reported are averaged over the 3 runs results. Zeta-Potential analysis consists in 1 run of 100 measurements (the system stops automatically after 12 measurements) after 2 minutes of sample equilibration.

Transmission Electron Microscopy (TEM)

TEM is a high magnification measurement technique that is able to produce images starting from a beam of electrons passing through the sample. Amplitude and phase variations in the transmitted beam provide imaging contrast that is a function of the sample thickness and the sample material (heavier atoms scatter more electrons and therefore have a smaller electron mean free path than lighter atoms). Because this technique uses electrons rather than light to illuminate the sample, TEM imaging has significantly higher resolution than light-based imaging techniques. [158], [159]

TEM measurements have been performed with Philips® CM200 Field Emission Gun with an electrons acceleration tension of 200 kV. 10-20 μ L of NPs solutions have been posed on carbon coated copper grids (200 mesh). The samples got dried overnight before be measured. The obtained images have been analysed by Image-J software in order to obtain the size distribution statistics.

2.2.2. Physical-Chemical analysis

Physical-chemical analysis of the metallic NPs core, hydrophobic/fluorinated stabilizing ligands, HPB coating and Nile red fluorescence has been performed. These were done by ultraviolet-visible (UV-Vis) absorption, Fourier-transform infrared (FT-IR), fluorescence and circular dichroism (CD) spectroscopic techniques. Metal concentration was measured by Inductively Coupled Plasma Atomic Emission Spectroscopy (ICP-AES).

UV-Vis Absorption

UV/Visible spectroscopy is a technique used to quantify the light that is absorbed by a sample in the spectrum region of visible (Vis) and ultraviolet (UV). The absorption is able to produce some energetic transitions in the sample outer electrons. The positions of the absorption peaks are related to the molecule type and the intensities of the absorption peaks are related to the concentration by the Lambert-Beer law. [160]

Dealing with metallic NPs, Gold NPs usually show a plasmonic absorbance. According to the Mie theory, an electromagnetic frequency induces a resonant coherent oscillation of the free electrons on the surface of a spherical NP, called surface plasmon resonance (SPR), only if the particle size is much smaller than the light wavelength. [132] This absorption lies in the visible region for Au, Ag and Cu. As a result, an enhanced electromagnetic field appears at the AuNPs surface allowing surface-enhanced optical properties revealed using spectroscopic techniques. In particular, the study of the plasmonic peak can give information about size, shape, concentration, agglomeration state, and refractive index near the nanoparticle surface. On the other hand, non-plasmonic

nanoparticles (as Magnetite) also have size and concentration dependent optical properties, however, their spectrum is not as sensitive to the dispersion properties as plasmonic nanoparticles. [158]

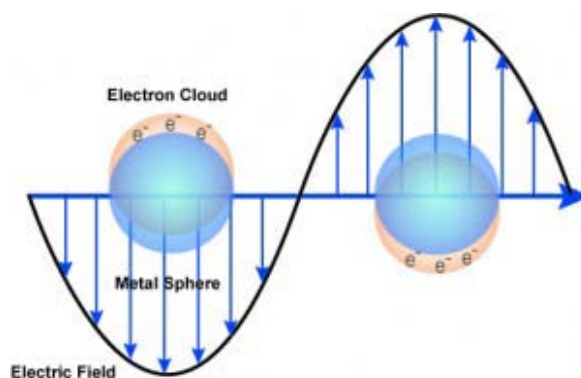


Figure 2.2. Schematic of surface plasmon resonance where the free conduction electrons in the metal nanoparticle are driven into oscillation due to coupling with incident light [161].

In this work, UV-Vis analysis has been performed by a Jasco® V-630 spectrophotometer; the explored wavelength range is 210-850 nm at 400 nm/min using a baseline data correction. The absorbing sample consists in a NPs solution that is transferred into quartz cuvettes (1 mm optic length, 700 μ L capacity).

FT-IR spectroscopy

Infrared spectroscopy is the study of interactions between matter and electromagnetic fields in the IR region. IR spectral region is the region where molecules absorb specific frequencies that are characteristic of their structure. The probability of a particular IR frequency being absorbed depends on the actual interaction between this frequency and the molecule. In general, a frequency will be strongly absorbed if its photon energy coincides with the vibrational energy levels of the molecule. IR spectroscopy is therefore a very powerful technique, which provides very precise information on the chemical composition of the sample. FT-IR exploits the Fourier transform in order to distinguish the different wavelength contributions to the signal.

NICOLET® iS50 FT-IR spectrophotometer has been used. This possesses KBr windows and a KBr beam splitter and the explored wavenumber range is 400-4000 cm^{-1} . Liquid samples are analysed by evaporating some small drops of the NPs solution on the KBr plate, 128 scans were collected for each sample at a resolution value of 1 cm^{-1} . Background signal has been measured after sample spectrum collection.

Fluorescence Emission Spectroscopy

Fluorescence spectroscopy is based on the same UV-Vis physic phenomena, but it exploits the ability of some molecules (fluorophores) to absorb radiation at a specific wavelength providing electron excitation and emit a radiation in a higher wavelength (compared to the absorption wavelength) when the electrons decay at lower energies.

In this work a Jasco® FP-8500 spectrofluorometer has been used in order to evaluate the emission of Nile red fluorescent dye. Wavelength spectrum explored range is from 200 nm to 900 nm. The instrument emits radiations by a Xe lamp at 150 W with a 5 nm precision. The scan speed is set 50 nm/min. Sample are analysed by transferring into quartz cuvettes (1 mm optic length, 700 μL capacity). Data correction needs a baseline measure.

Circular Dichroism Spectroscopy (CD)

CD is a spectroscopic technique used extensively to study chiral molecules of all types and sizes, and it is based on the samples different absorption properties in absorbing left and right circularly polarised radiation, according to its chirality. CD finds one of its most important applications in the study of large biological molecules; it is used in order to give the content of regular secondary structural features such as α -helix and/or β -sheet. Proteins can give rise to CD signals thank to their chiral functional groups typically in the far UV region (240-180 nm).

In addition, is possible to use CD spectrometry to observe how secondary structure changes with environmental conditions or on interaction with other molecules. [162]

Circular Dichroism (CD) analysis is performed by a Jasco® j-815 CD spectrometer. The wavelength range explored is 180 nm-300 nm; the scanning speed is set at 100 nm/min with a 1 nm resolution. Data correction requires a baseline measurement. CD measurements consist in 10 acquisition runs averaged in only one spectrum.

Inductively Coupled Plasma Atomic Emission spectroscopy (ICP-AES)

Concentration of the obtained samples has been measured by ICP-AES analysis. ICP is a spectroscopic technique used to determine sample composition and concentration. It is based upon the spontaneous emission of photons from atoms and ions that have been excited. The sample solution is converted to an aerosol and directed into the central channel of the plasma, where is quickly vaporized. Analyte elements are liberated as free atoms in the gaseous state. Further collisional excitation within the plasma imparts additional energy to the atoms, promoting them to excited states. These atomic transitions are characteristic for a particular element and their intensity is related to the concentration of the specie through a calibration curve. [163]

2.2.3. NPs Interaction with cell membranes

Neutron reflectometry

The technique involves the use of a highly collimated beam of neutrons incident on a flat smooth surface. The neutrons are reflected at the surface with a potential, which depends on the number density of the atoms in the surface and their average coherent scattering length. The calculation of the reflectivity intensity provides information on the sample and it can be carried out by standard optical methods, using Fresnel coefficients for the transmitted and reflected amplitudes at each interface. [164] Neutrons are used because have a weak interaction with matter due to their neutral charge and perturb soft matter systems very little. Neutrons are therefore deeply penetrating, making them ideal probes for buried interfaces. Last, but not least, with the use of isotopic substitution, we can vary the contrast between different regions of the system, highlighting the scattering of each component of the system. This greatly aids structural determination. [165]

Reflectivity measurements were performed on the D17 reflectometer at the ILL

centre, Grenoble (France) by the research group of Dr Giovanna Fragneto and Marco Maccarini. Variable resolution is 1–10%, wavelength range between 2 Å and 20 Å, with two incoming angles of 0.7° and 3°. The cell was oriented vertically and kept in position while changing solvents and temperature. [165] Data were analysed using Motofit, a software package that uses IGOR Pro for co-refinement of neutron and X-ray reflectivity data allowing simultaneous fitting of data sets from the same sample under different contrast conditions.

Chapter 3 – Development of SPION-based theranostic nanostructures.

3.1. Introduction

Theranostic nanomedicine exploits the peculiar features of a variety of nanodevices in order to achieve improved diagnosis results, site-specific delivery of drugs and combine them in a unique nanostructure, [12], [54], [55] SPIONs have been widely studied for their potential application in nanomedicine during the last decades. As reported by Etheridge et al., using “nanomedicine” as keyword for search in literature, clinical trial registries and Web, 66 results (over 247) related to SPIONs study and application are obtained. [166]

SPIONs intrinsic properties have made their application possible and particularly promising as contrast agents for magnetic resonance imaging (MRI) of tumors, targeting probes as well as drug carriers. [38] Their surface can be easily modified byfunctionalization with various targeting ligands, dyes, and drugs providing multimodal nanoparticles with excellent magnetic properties, biocompatibility and biodegradability. [82], [92], [107], [108], [167] These structures can be also retained at the target site by external intense magnetic fields. Once the SPIONs reach the target thanks to the MRI signal they are visible and the carried drug can be released through different triggering mechanisms near the region of interest (ROI). [109]

The present work focused on the development and optimization of SPIOs supraparticles, coated by a “surfactant” protein called class II Hydrophobin (II HPB), which represent a novel theranostic system. Such a protein can, in theory, be applied to coat a variety nanoparticles stabilized by hydrophobic ligands. HPB coatings of other type of metallic nanoparticles (Au NPs) have been performed in the NFMIlab of Politecnico of Milan with appreciable success.

3.1.1. Nanoparticle synthesis

As first step to develop this new theranostic nanosystem stabilized by class II HPB,

the synthesis of monodispersed iron oxide NPs was performed. Magnetite (Fe_3O_4) NPs stabilized by oleic acid were synthesised according to a slight modified procedure reported by Sun et al. [92] The SPIONs synthesis consists of a high-temperature reaction of iron (III) acetylacetonate ($\text{Fe}(\text{acac})_3$), in benzylether and in the presence of long chain molecules such as oleic acid and oleylamine. The details on the synthesis mechanism are still not well understood. However, this procedure with a controlled temperature increase generally allows a better control on the size distribution of the NPs (see Figure 3.1). [95] The process does not require a size selection procedure and is readily scaled up for mass production. [92], [95]

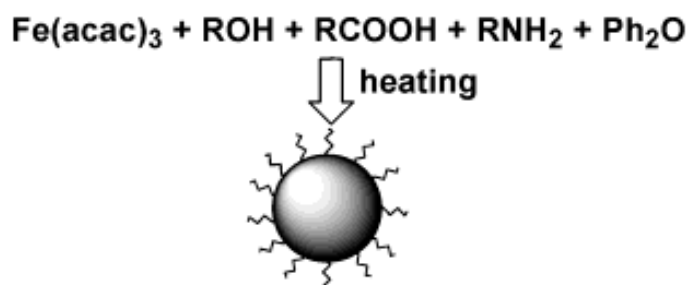


Figure 3.1. Schematic representation of the hydrophobic (oleic acid stabilized) SPIONs synthesis process.[92]

3.1.2. Nanoparticle surface coating

In order to transfer the so-formed hydrophobic SPIONs into a stable dispersion in water for biological applications, the use of biocompatible stabilizing agents was required. [90]. As possible biocompatible agents surfactants, biopolymers and more generally biomolecules (proteins) can be used. [83], [99], [100] Colloidal stability in water is influenced by several factors such as the surface NPs chemistry, surface charge and size. [13] Typically the stabilizing coatings give to the NPs colloidal stability as well as possibility of easy surface functionalization with bioactive molecules (drugs, dyes, peptides) by covalent bonding or adsorption. [101], [168] [87]

A significant number of coating protocols, based on the use of different coating agents, have been reported in the literature during last years. [83], [104], [105], [169] In this study, the coating procedure has been performed by a drop-wise addition of a HPB

water solution to a dispersion of SPIONs in chloroform under moderate stirring at 50°C. This was followed by evaporation of both solvents and further dissolution of the dry film either in water or in acetate buffer (pH 4.5, 10 mM). Fifteen coating procedures with different combination of the experimental parameters have been performed in order to optimize the procedure.

Moreover, the coated SPIONs dispersed in aqueous solutions were tested for their ability to encapsulate a hydrophobic molecule (i.e. a cytotoxic drug). Unfortunately, the works in literature reporting on the encapsulation of a dye in SPIONs based nanomaterials are not many, given the SPION quenching effect on the fluorophore emission. [170]–[172] For example Lee, Smith et al. proposed the production of fluorescent SPIONs by conjugating Texas Red dye dextran directly to hydrophobic SPION and coat them with a peptide complex. [41] Other dyes used reported in literature are typically Cy 5.5 and Fluorescein isothiocyanate (FTIC). It is important to consider that this two molecules have been studied often associated to polymer SPIONs coating. Therefore, it could be possible that their use in combination with a protein coating could be challenging. [169], [173]

In this work Nile Red, a benzophenoxazone hydrophobic fluorophore, was used. Nile Red is characterised by an absorption wavelength at 485 nm and emission range between 500 and 600 nm depending on the nature of the solvent. [174], [175] Nile red has been used as model molecule, which simulates the behaviour of a hydrophobic drug molecule but can also be easily detected thanks to its fluorescence properties. Nile red has been chosen as it is a well-known fluorescent dye for *in vitro* cell labelling and has already been employed in previous SPIONs based theranostic systems studies. [170]

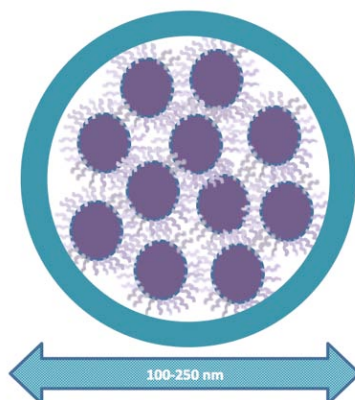


Figure 3.2. Schematic representation of a HPB coated SPIONs supraparticle. It must be noticed that every single SPION inside the coating is still stabilized by hydrophobic ligands (oleic acid).

With regard to the possible functionalization of protein coating with some targeting moieties, it has been not investigated in this work but it could be an additional step in the HPB coated supraparticles optimization. Some studies are reported which concern this point and focus, in particular, on SPIONs coated with protein or peptide coatings. Sulek et al. exploited amphiphilic peptide molecules as surfactants for the functionalization of SPIONs and they modified this peptide coating by various ending peptide sequences. This seems to permit to target only desired cell types and/or molecules. [105]. Furthermore, Vargo et. al. focused on the use of amphiphilic recombinant proteins that can assemble on the surface of SPIONs in a defined orientation with the possibility to be functionalized with particular targeting ligands. This is done by fusing a specific affibody onto the protein side exposed to the environment, leading to the formation of protein stabilized targeting supraparticles for enhanced MRI. This produces a peptide-based coating for NPs biological applications as in the case of this work. [83]

3.1.3. Hydrophobin proteins

Hydrophobins are short proteins produced by filamentous fungi and are among the most surface-active proteins known. [176] HPBs have some important roles in fungi nature such as in adhesion and formation of protective surface coatings essential for the fungi lifecycle. [177], [178] Since HPB shows amphiphilic properties; it means that one side of the molecule is easily solvated by water, whereas the other tries to escape it. Such proteins can be exploited to produce self-assembled nanosystems that possess interesting properties

for biomedical and nanomedicine applications. [177] HPB have a size of about 100 amino acids (see Figure 3.3) and molecular weights lower than 20 KDa, are also remarkably stable and can withstand temperatures near the boiling point of water. [179] They are divided in two classes (HPB I and HPB II) according to their secondary structure as well as the solubility of the aggregates that they form. [177] Both classes present eight cysteine residues at fixed places along the chain of the amino acids strongly affecting their secondary structure. [177], [178], [180] HPB I class often form rodlet-like supramolecular assemblies that hinder their water solubility and therefore their application in nanomedicine and biotechnology. [178] The monolayers formed on interfaces by class II hydrophobins lack the fibrillar rodlet morphology and can be solubilized well in water (or water-based) solvents. [178], [181] In HPB II, the hydrophobic part consists mainly of amino acid residues near the loops of two β -sheets.

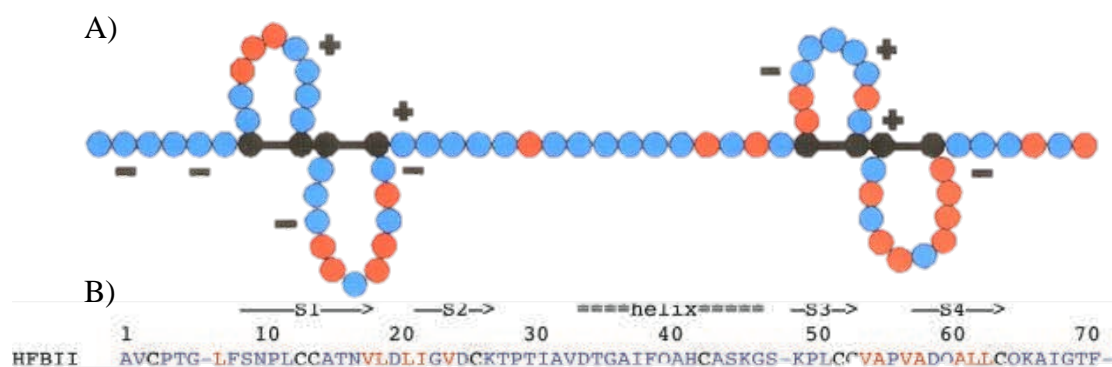


Figure 3.3. A) Linear representation of HPB II amino acids sequence. Polar (blue) and non-polar (red) amino acids and cysteine residues (black) are shown. Plus and minus signs indicate charged amino acids. Black lines indicate the disulfide bridges. [180] B) Explicit list of all the amino acids composing HPB II protein.

[177]

The hydrophilic part contains one α -helix. [181] HPB II in water presents, then, a globular structure that is stabilized by a network of disulfide bonds between eight cysteine residues. [29] [182] The assembly of class II hydrophobins at the water-air interface is accompanied by a not dramatic change in the secondary structure and/or ultrastructure. [29] The globular structure and the low conformational change after the self-assembling process may explain why class II hydrophobins reduce the water surface tension more rapidly. [178], [181], [183] From a quantitative point of view, HPB II is able to reduce the

surface tension of water from 72 mJ/m^2 to 28 mJ/m^2 at a concentration of 20 mg/ml . [177]

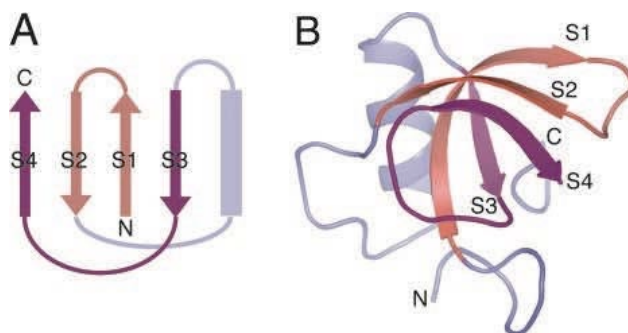


Figure 3.4. A) Schematic topology of HFBII. The arrows mark strands and the rectangle the α -helix. B) 3D structure of HPBII [177].

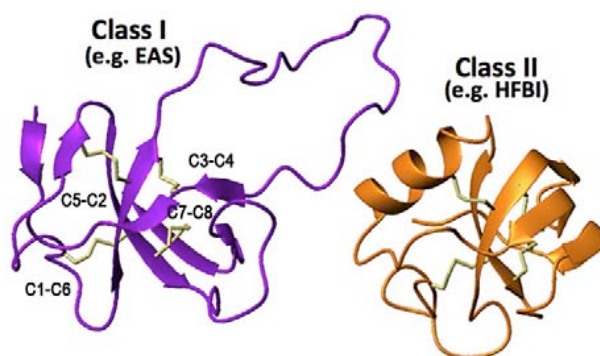


Figure 3.5. Comparison between HPB I and HPB II 3D structures [178] It is appreciable the more globular structure of HPB II.

Quite surprisingly, the rigidity of the HPB II molecule may assist them in keeping the side chains of the hydrophobic patch exposed to solvent. The natural evolution made such fungi able to produce a surfactant protein that, differs from typical surfactants for both its structure and its self-assembling behaviour. A possible explanation of this is related to the thermodynamics of adsorption but it is still not completely clear how the protein structure affects its surfactants properties. [177], [184] Some studies have been carried out on this subject by investigating features of the hydrophilic region of the protein, which is characterized by charged residues that are located in two different areas of the hydrophilic region of the protein. [185], [186]

3.2. Experimental

3.2.1. Procedure

Hydrophobic SPIONs synthesis

The procedure is based on that from Sun. et al. proposed in 2002. [92] This is a high temperature iron salt reaction carried out in a N₂ not dry atmosphere. Some chemicals used by Sun et al. have been changed such as Benzyl-ether is used instead of phenyl-ether as solvent and 1,2-tetradecanethiole is used to replace 1,2-hexadecanediol. This variation is known to not modify the results by appreciable values. [95] The used stoichiometric ratios of chemicals, their weights and their volumes are listed in Table 1.

Table 3-1. List of the reagents and solvents used for the synthesis with stoichiometric ratios of chemicals, their weights and their volumes.

Chemicals	Stoichiometric ratio	mMol	Weight [g]	Volume [mL]	Molecular weight [g/Mol]	Density [g/cm ³]
Fe(acac) ₃	1	7	2,471	/	353	/
Oleic acid	3	21	5,93	6,7	282,46	0,89
Oleylamine	3	21	5,617	6,9	267,49	0,813
1,2-Tetradecanediol	5	35	8,064	/	280,39	/
Benzyl ether	10	/	/	70	/	/

Accurately weighed solid reagents were first placed in a 2 neck round-bottomed flask and subsequently liquid reagents and solvent were added. A condenser was connected to the 2-neck flask and attached to a trap chilled by liquid Nitrogen. Temperature was gradually increased from room temperature (RT) to 300 °C, following a temperature ramp. Stirring speed was constant at 1000 rpm for the whole process.

In detail the temperature ramp consisted of the following steps:

1. RT → 100 °C in 45 minutes (1.7 °C/min).
2. Maintaining at 100 °C for 45 minutes.
3. 100 °C → 200 °C in 45 minutes (2.2 °C/min).
4. Maintained at 200 °C for 2 hours.
5. Manually set at 300°C for 1 hour. Since the probe does not withstand temperatures above 250°C, the temperature is set manually. The temperature indicated is now the plate temperature and not the temperature inside flask.
6. 300 °C → RT and maintained at RT overnight.

Work-up: the liquid was transferred in a Falcon tube and centrifuged (MPW®-352 centrifuge, REF 11457 rotor) at 4000 rpm for 10 minutes. The supernatant have been collected and the aggregated residues are conserved for eventual further pellet collection. EtOH was added in each Falcon tube up to completely fill them. Centrifugation at 8500 rpm for 30 minutes was performed and the residue is collected. Purification was repeated twice on the supernatant.

All the residues were dried by N₂ and dissolved in the minimum amount of Toluene. The obtained solution was filtered using a syringe 0,22 µm filter for organic solutions and then centrifuged at 1500 rpm for 10 minutes. The final supernatant was collected (residues were not found after this centrifugation). The solution obtained has been filtered three times by a syringe 0,22 µm filter for organic solutions. The final solution has been transferred in glass vials and stocked sealing with Parafilm® in order to avoid solvent evaporation.

Coating protocol

The coating protocol has been proposed and optimized by NFM Lab research group at Politecnico di Milano. A solution (ranging from 0.05 mg/mL to 0.1 mg/mL) of HPB II in milli-Q deionized water (mQw) has been prepared dissolving weighed HPB and sonicated for 15 minutes (FALC® sonicator bath at 59 KHz, 100%). A volume (ranging from 0.6 to 1.8 mL) of hydrophobic SPIONs in toluene was transferred into a Falcon and EtOH was added up to fill the Falcon; and then centrifuged at 8000 rpm for 20 minutes.

The supernatant was gently discarded and the residue has been collected, dried and dissolved in Chloroform. The Chloroform SPIONs dispersion was transferred into a round-bottomed flask (100 mL) and placed at a 50 °C under moderate stirring. 30 mL of HPB/water solution were added dropwise. The sample was then left at 50 C for 1 hour under stirring. The obtained two-phase sample has been slowly evaporated by Rotavapor (BÜCHI® ROTAVAPOR II, chilled by a Julabo® FL300 chiller using ethilenglycol refrigerant. Pressure has been controlled by a KNF LAB® SC-920 pump) set on a specific pressure/time function. After the solvents completed evaporation, the dry film was left for 1 hour under vacuum (5 mbar) in order to remove every eventual residual solvent. The film was then dissolved in 20 mL of solvent (mQw or Acetate buffer (pH 4.5, 10 mM)) and sonicated for 15 minutes. The film dissolution in the solvent indicates that SPIONs turned successfully into water-soluble supraparticles.

Purification

The obtained solutions have been purified in order to eliminate the possible excess of HPB protein present in solution. Purification was performed following three different procedures: Amicon filter purification, dialysis purification and magnetic purification.

Amicon filter purification consists in the use of Amicon filters during 3 cycles of centrifugation at 3500 rpm for 10 minutes. Dialysis purification has been carried out by transferring the not-purified solution into 100 KDa dialysis membranes and left diffuse through the membrane against 2L of mQw (or Acetate buffer pH 4.5, 10 mM) for 24 hours. Magnetic purification was performed exploiting SPIONs magnetic properties. Due to the application of a magnetic field, when placed close to a magnet, the dissolved HPB coated SPIONs were deposited on the bottom of the stocking vial. Supernatant was discarded and the obtained pellet was re-dissolved in the solvent (mQw or buffer). The procedure has been repeated at least 3 times until the supernatant was completely clear.

Both not-purified and purified samples were tip-sonicated on ice (3x1 minute cycles) by a SONICS® Vibracell (130 W, 20 KHz, 80%) before stocking.

Fluorophore encapsulation procedures

In order to encapsulate a fluorescent dye in the supraparticles, the coating protocol was modified. A volume (ranging from 12 µL to 1mL) of a Nile Red in Chloroform 0.34

mg/mL solution was added to the Chloroform dissolved SPIONs before adding the HPB/mQw solution. The whole procedure has been carried out by covering the flask with aluminium paper in order to avoid that light could degrade the Nile Red emission characteristics.

3.3 Results and discussion

3.3.1 Coating protocol optimization

Several hydrophobic SPIONs synthesis and coating protocols have been performed in order to optimize the results in terms of NPs size, stability and Nile Red encapsulation efficiency. The list of all the experiments performed is reported in Table 3-2, Table 3-3. Table 3-2 shows the concentrations values for the hydrophobic SPIONs obtained by ICP analysis.

Table 3-2. ICP data about hydrophobic SPIONs concentrations.

Hydrophobic SPIONs Batch	Fe Concentration (mg/l)	NPs concentration (NPs/ml)	Fe Molarity (mol/L)
1	7566	7.045×10^{14}	0.134
2	7743	4.87×10^{14}	0.138

Table 3-3 shows the concentrations and molar ratios of HPB II, Nile Red and hydrophobic NPs and the purification method used in each coating procedure. Since the majority of the samples are prepared starting from the same hydrophobic SPIONs batch, the effect of stoichiometric have been investigated by modifying the relative volumes instead of molarity. The concentrations of HPB in the aqueous solutions are 0.1 mg/mL and 0.05 mg/mL, while the volumes of hydrophobic NPs are 0.6 mL, 1.2 mL and 1.8 mL. Different combinations of these parameters have been investigated as it is shown in Table 3-3. All the samples have been produced by following the same procedure, which has been explained in the experimental section 3.2.

Table 3-3. List of coating procedures tested showing chemical molar ratios, volumes, purification method and the protocol type. Samples labelled in red are the chosen reference samples for water-dissolved, buffer-dissolved and Nile red-encapsulated HPB coated supraparticles.

Sample	HPB (mg/mL)	NPs/mL	Molar ratio (NPs/HPB)	Molar ratio (dye/NPs)	Purification Method	Protocol type
1	0.1	7.0×10^{14}	584.46		Dialysis	Water-dissolved
2	0.05	7.0×10^{14}	389.64		Dialysis	Water-dissolved
3	0.1	7.0×10^{14}	194.82		Dialysis	Water-dissolved
4	0.1	7.0×10^{14}	389.64		Dialysis	Water-dissolved
5	0.05	7.0×10^{14}	779.28		Dialysis	Water-dissolved
6	0.1	7.0×10^{14}	584.46		Magnetic	Water-dissolved
7 (A)	0.1	7.0×10^{14}	584.46		Magnetic	Water-dissolved
8	0.1	7.0×10^{14}	584.46		Dialysis	Buffer-dissolved
9 (B)	0.1	7.0×10^{14}	584.46		Magnetic	Buffer-dissolved
10	0.1	7.0×10^{14}	584.46		Magnetic	Buffer-dissolved
11	0.1	7.0×10^{14}	598.27		Magnetic	Buffer-dissolved
12	0.05	7.0×10^{14}	389.84	8.0×10^{-5}	Dialysis	Nile red encapsulate
13	0.05	7.0×10^{14}	779.28	6.6×10^{-3}	Magnetic	Nile red encapsulate
14 (C)	0.1	4.9×10^{14}	398.84	6.4×10^{-3}	Amicon filter	Nile red encapsulate

Three samples have been taken as reference for reasons that will be explained in the following section. One for water-dissolved, one for buffer-dissolved and one for Nile red-containing HPB coated supraparticles. The reference samples are listed in Table 3-4. Hereafter the reference sample for water-dissolved HPB coated supraparticles will be called sample A, the reference sample for buffer-dissolved HPB coated supraparticles will be called sample B and the reference sample for Nile red containing HPB coated supraparticles will be called sample C.

Table 3-4. Reference samples for water-dissolved (A), buffer-dissolved (B) and Nile red-containing (C) HPB coated supraparticles, with molar ratios and the volumes of HPB II, Nile Red and hydrophobic NPs and the purification method used.

Reference sample	HPB (mg/mL)	NPs/mL	Molar ratio (NPs/HPB)	Molar ratio (dye/NPs)	Purification Method
A	0.1	1.8	584.46		Magnetic
B	0.1	1.8	584.46		Magnetic
C	0.1	1.2	398.84	6.4×10^{-3}	Amicon filter

3.3.2. Physical-chemical Characterization

3.3.2.1. Size, colloidal stability and concentration

The hydrophobic cores and the coated nanoparticles reported in Tables 3-2 and 3-3 were characterized by DLS and Zeta-potential in terms of size, surface charge and colloidal stability, the results are reported in Table 3-5. The averaged DLS hydrodynamic diameters were extracted from the size distributions obtained by fitting the auto-correlation functions with CONTIN algorithm. This was done because, differently from the CUMULANT, CONTIN algorithm takes into account contributions to the autocorrelation function from different populations.

Hydrophobic SPIONs

Size results for the hydrophobic core NPs are reported in Table 3-5, they are in agreement with the literature [92]. DLS measurements met the software quality criteria in terms of correlation functions and data fit. This type of synthesis is a well-known procedure and it is appreciable its reproducibility. The size results presented an average hydrodynamic size of 16.9 ± 0.5 nm.

Table 3-5. Size results (with units) from the two hydrophobic SPIONs batches. D_H is the hydrodynamic diameter, and only the CONTIN algorithm values are reported. PDI is the polydispersity index.

Sample	Size $\langle D_H \rangle$ (nm)	PDI
Hydrophobic SPIONs batch 1	16 ± 0.4	0.29 ± 0.03
Hydrophobic SPIONs batch 2	18 ± 0.6	0.32 ± 0.01

Water-dissolved HPB coated supraparticles

As shown in Table 3-6, the coating procedure produced NPs with an average hydrodynamic size varying from about 230 nm to about 350 nm with a relatively low PDI. This size compared to those of the SPION cores suggested the formation of HPB coated supraparticles rather than single coated NPs. [187]

Table 3-6. Size and Zeta-potential results (with units) from all the water-dissolved HPB coated supraparticles samples. D_H is the hydrodynamic diameter, and only the CONTIN algorithm values are reported. PDI is the polydispersity index.

Sample	Size $\langle D_H \rangle$ (nm)	PDI	Z-pot (mV)	Molar ratio (NPs/HPB)
1	254 ± 20	0.14 ± 0.01	-24.6	584.46
2	270 ± 3.6	0.21 ± 0.01	-36	389.64
3	354 ± 22	0.26 ± 0.02	-16.1	194.82
4	283 ± 9	0.17 ± 0.03	-9.4	389.64
5	336 ± 22	0.21 ± 0.03	-21.8	779.28
6	230 ± 8	0.19 ± 0.03	-35.0	584.46
7 (A)	263 ± 8	0.17 ± 0.01	-28.3	584.46

Samples 2, 3 and 4 in Table 3-6 presented the lowest NP/HPB molar ratios and showed some aggregation that was reduced by tip-sonication. The NP concentration was very low indicating that the transfer into the aqueous solution was not optimal. Magnetic purification was chosen as best purification procedure being faster and more effective than dialysis (Samples 6 and 7 in Table 3-6). DLS measurements showed that the samples are sufficiently monodispersed. The best size results are obtained for the samples produced starting from a 584.46 NPs/HPB molar ratio (i.e samples 1, 6, and 7 in Table 3-6)

Nanostructures bearing a high surface charge (high Zeta-Potential) are stabilized by electrostatic repulsions and are generally stable. The produced samples showed Zeta-potential values ranging between -9 mV and -36 mV with five samples (over seven) showing values lower than -20 mV. This suggests the coated supraparticles may be stable in aqueous solution.

Concentration results are provided by ICP analysis and have been performed only on samples 5 (779.28 NPs/HPB molar ratio) and 7 (584.46 NPs/HPB molar ratio) because they were the only samples produced, possessing different molar ratios, at the time the analysis was performed. Sample 7 presents a concentration of $4,62 \times 10^8$ supraparticles/mL or $1,85 \times 10^{11}$ SPIONs/mL. Sample 5 shows a concentration of $1,37 \times 10^8$ supraparticles/mL or $1,28 \times 10^{11}$ SPIONs/mL. The last, even if it is produced with the higher NPs/HPB molar ratio, it contains quite big supraparticles.

According to the reported results, the protocol that brought to the best sample in terms of size, stability and concentration was the 7th in Table 6. This sample will then be used as reference for the characterization in the following sections and will be called sample “A”. A comparison between the water-dissolved HPB coated supraparticles in sample 7 and the starting hydrophobic SPIONs in terms of size distribution and correlation function are reported in Figure 3.6.

The results suggest that the protocol has a quite good reproducibility and produces supraparticles with an average hydrodynamic diameter of 249.3 ± 12.05 nm and an average Zeta-potential of -29.3 mV.

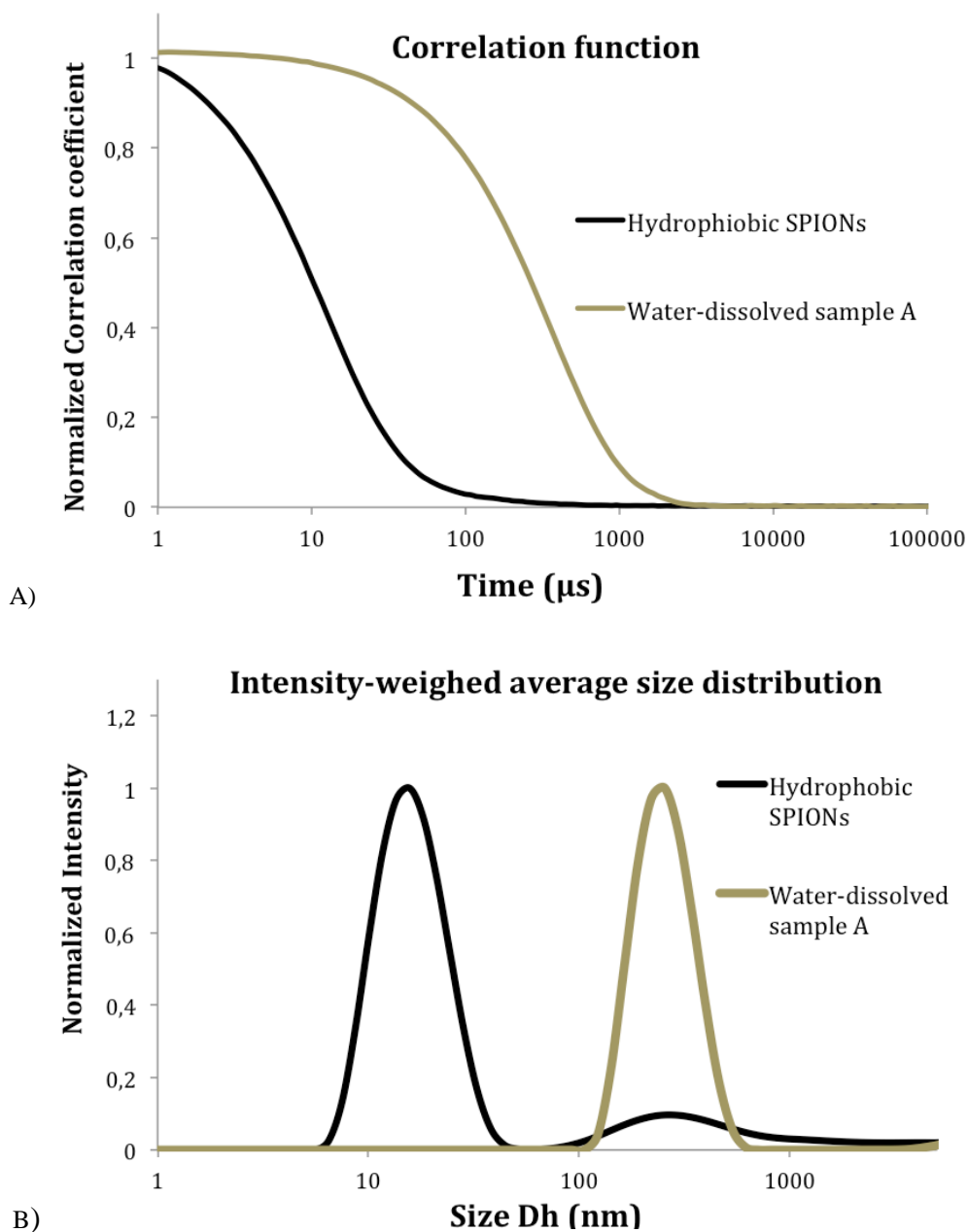


Figure 3.6. Comparison between an average of the two hydrophobic SPIONs batches and an average of the three measurements of the water-dissolved HPB coated supraparticles reference sample A. The results are given in terms of A) Correlation functions and B). Intensity-weighted size distribution obtained by CONTIN.

Acetate buffer-dissolved samples

Table 3-7. Size and Zeta-potential results (with units) from all the buffer-dissolved HPB coated supraparticles samples and a sample produced by supraparticles dissolution in acidic pH aqueous solution.

D_H is the hydrodynamic diameter, and only the CONTIN algorithm values are reported. PDI is the polydispersity index.

Sample	Size $\langle D_H \rangle$ (nm)	PDI	Z-pot (mV)	Molar ratio (NPs/HPB)
8	657 ± 104	0.28 ± 0.05	-7.8	584.46
9 (B)	390 ± 41	0.22 ± 0.03	-18.5	584.46
10	287 ± 7	0.23 ± 0.01	14	584.46
11	256 ± 4	0.15 ± 0.00	18.1	598.27

A sample dissolved in an aqueous solution at acidic pH was prepared by dropwise addition of a 0.01 M HCl solution until pH = 4.0 was reached. The so-obtained sample showed extensive aggregation (sample 8 in Table 3-7).

Then, a different procedure was tested in which the dried HPB coated supraparticles, obtained following the experimental procedure (molar ratio) used for water-dissolved reference sample “A”, was re-dissolved in 10 mM acetate buffer at pH 4.5 rather than in water. DLS experiments on these batches showed hydrodynamic diameters ranging from 256 nm to 390 nm. The averaged hydrodynamic size, D_H , is 311 ± 17 nm (Table 3-7). It is appreciable an increase in the supraparticle size compared to water-dissolved samples. This indicates that an acidic pH together with an increment in the ionic strength slightly modifies the HPB II behaviour in terms of filming ability at the hydrophobic/hydrophilic interfaces, as already reported in the literature. [185] The last two samples (10 and 11 in table 3-7) reported problems during the purification protocol with extended aggregation, for this reason results on the purified samples are not reported in this thesis.

Thus, the only sample purified in acetate buffer (pH 4.5, 10 mM) was sample 9. This sample showed a quite good colloidal stability with a Zeta-potential of -18.5 mV, suggesting that the acidic pH, which should induce protonation of the free amine groups of the protein, might be compensated by a counter ion screening due to the increase in ionic

strength. ICP analysis of this sample resulted in a concentration of $7,86 \times 10^7$ supraparticles/mL or $1,14 \times 10^{11}$ SPIONs/mL, which is almost six times lower than the water-dissolved reference sample A. Sample 9 is, anyway, used as reference for Acetate buffer-dissolved sample since it is the best in terms of size and colloidal stability and has been called sample “B”. A comparison between the Water-dissolved and the buffer-dissolved reference samples, in terms of size distribution and correlation function, is shown in Figure 3.7.

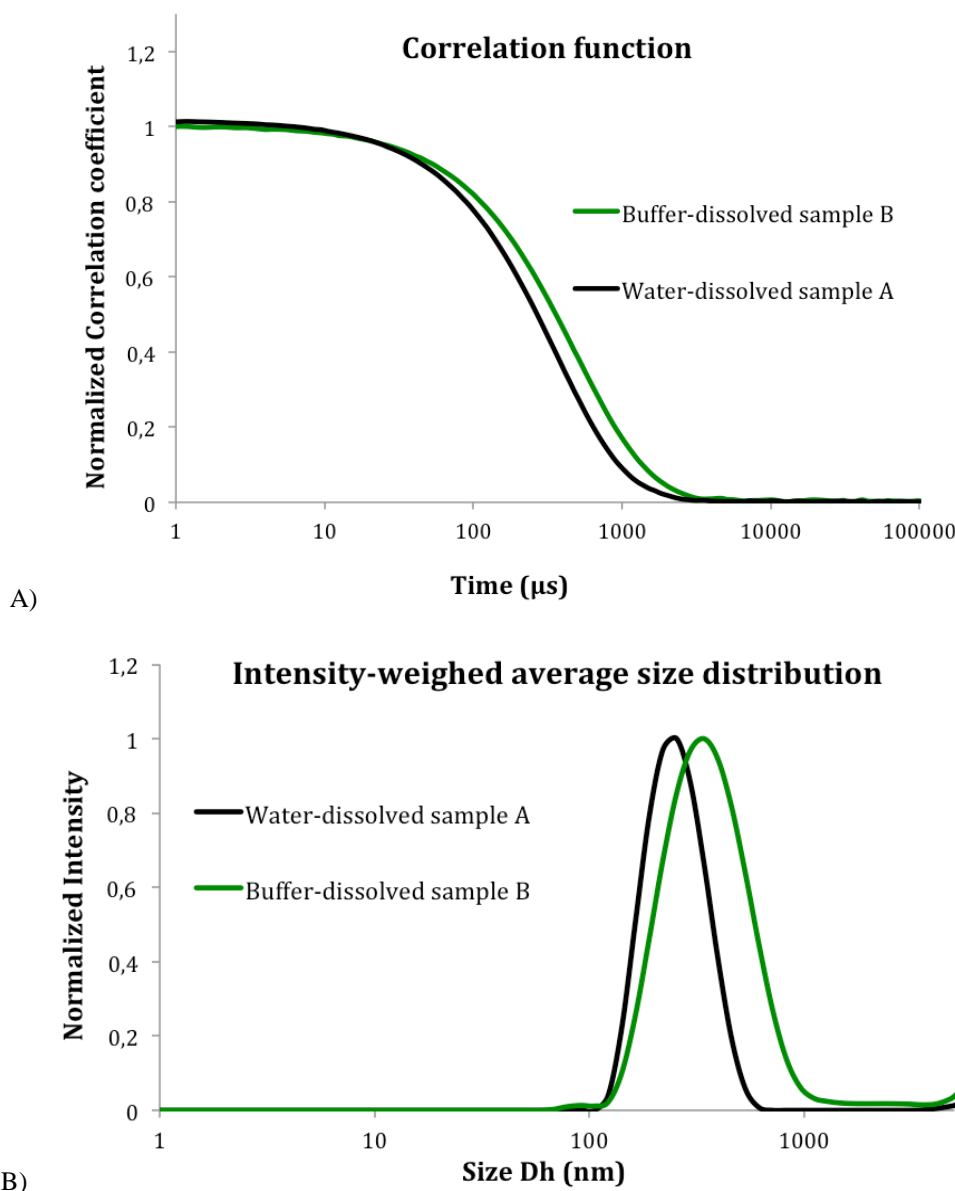


Figure 3.7. Comparison between an average of the three runs for the water-dissolved HPB coated supraparticles reference sample A and for the buffer-dissolved HPB coated supraparticles reference sample B. The results are given in terms of A) Correlation functions and B) Intensity-weighted size distribution obtained by CONTIN.

Nile Red encapsulate samples

Table 3-8. Size and Zeta-potential results (with units) from all the Nile red encapsulate HPB coated supraparticles samples. D_H is the hydrodynamic diameter, and only the CONTIN algorithm values are reported. PDI is the polydispersity index.

Sample	Size $\langle D_H \rangle$ (nm)	PDI	Z-pot (mV)	Molar ratio (NPs/HPB)	Molar ratio (dye/NPs)
12	255 ± 33	0.51 ± 0.08	-23.2	389.84	8×10^{-5}
13	349 ± 26	0.38 ± 0.02	/	779.28	6.6×10^{-3}
14 (C)	280 ± 11	0.28 ± 0.03	-25.9	398.84	6.4×10^{-3}

As said in the introduction, the so-formed supraparticles present a hydrophobic pocket where it might be possible to encapsulate a drug. To prove the ability of encapsulation of the supraparticles, the hydrophobic fluorescent dye Nile red was chosen as model system. The Nile Red was added during the coating procedure, in particular samples that contain it are listed in Table 3-8. DLS experiments on these batches produced by different experimental protocols contain supraparticles with a size ranging from 260 nm to 350 nm.

More in detail, sample 12 has been produced from the lowest dye/NP molar ratio (8.0×10^{-5}). Even if the NPs/HPB molar ratio is not the lowest, it is probably too diluted. DLS data obtained by sample 12 do not meet the software quality criteria probably due to such excessive dilution and this reflects also on the very high PDI value, which may due to the software inability to fit a very low intensity signal.

Sample 13 (779.289 NPs/HPB and 6.6×10^{-3} dye/NPs molar ratios) has been purified magnetically as the dialysis did not work well. Then, it has been possible to purify magnetically only a small amount of the dispersion (hydrodynamic diameter $D_H > 350$ nm).

Sample 14 (398.84 NPs/HPB and 6.4×10^{-3} dye/NPs molar ratio) has been purified both magnetically and by successively using Amicon filters. It showed the best hydrodynamic size values among those samples and also it appeared light brown but with a

low intense purple shade (Figure 3.8).



Figure 3.8. visual comparison between water-dissolved HPB coated supraparticles reference sample A (left) and the Nile red encapsulated HPB coated supraparticles reference sample C (right). It appreciable a colour variation from light clear brown for water-dissolved sample (left) to a more purple shade for the Nile red sample (right).

In terms of colloidal stability all the Nile Red samples show quite good properties with Zeta-potential values lower than -17.0 mV. Again, the sample 14 presents the most negative values and then the best colloidal stability. Sample 14 is chosen as reference for Nile Red coatings and named sample “C”.

It is important to state that the addition of Nile red in the coating protocol has been carried out principally for testing the Nile Red encapsulating ability inside the supraparticles. Therefore, it has not been done with the objective to obtain supraparticles with a specific size. This is the reason why such results are quite encouraging even if the reproducibility seems to need further optimization.

A comparison between the samples chosen as reference for water-dissolved (A) and Nile Red-encapsulating (C) HPB coated supraparticles is shown in Figure 3.9. Finally, a comparison between the reference samples chosen for the three different types of protocols is reported in Figure 3.10. Both the comparisons are in terms of size distribution and correlation function.

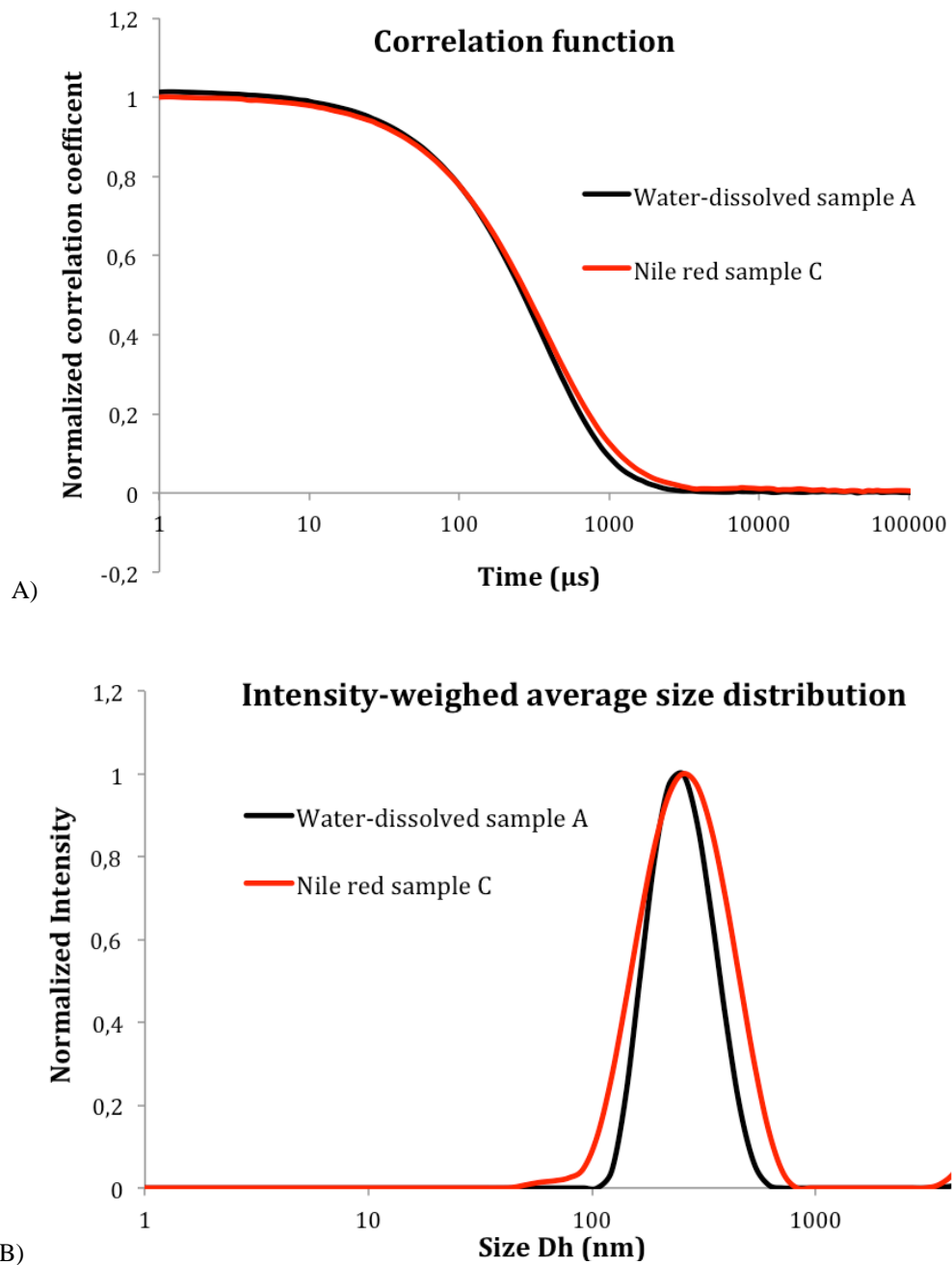


Figure 3.9. Comparison between an average of the three runs for the water-dissolved HPB coated supraparticles reference sample A supraparticles for the Nile red-encapsulated HPB coated supraparticles reference sample C. The results are given in terms of A) Intensity-weighted size distribution obtained by CONTIN and B) Correlation functions.

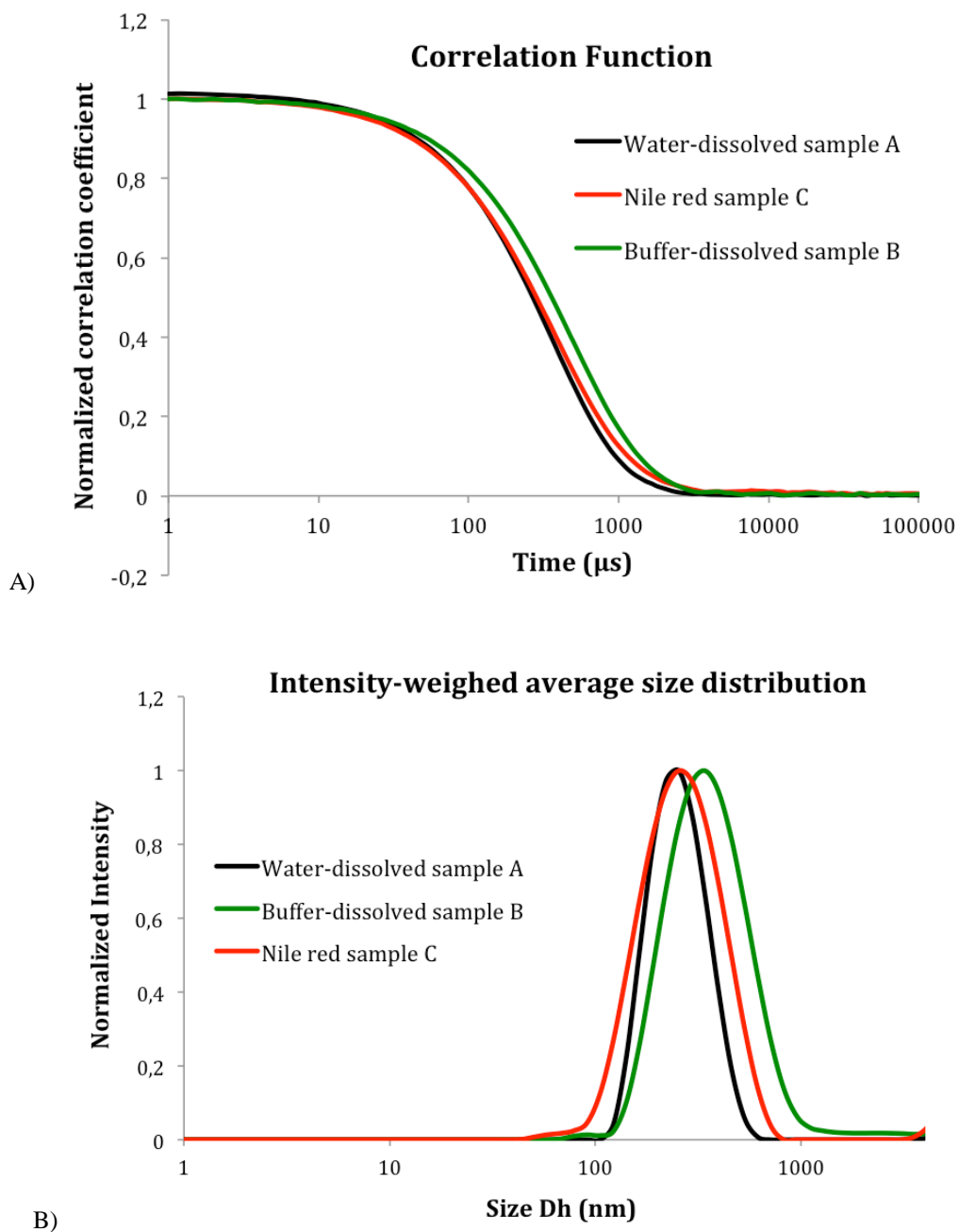


Figure 3.10. Comparison a comparison between the reference samples chosen for the three different types of protocols The results are given in terms of A) Correlation functions and B) Intensity-weighted size distribution obtained by CONTIN.

3.3.2.2 Qualitative/quantitative analysis

FT-IR

Fourier transform infrared spectra (FT-IR) have been collected for all the reference samples and for hydrophobic SPIONs dissolved in toluene. They are reported in the following figures compared also with the reference spectra of oleic acid, HPB II and Nile red.

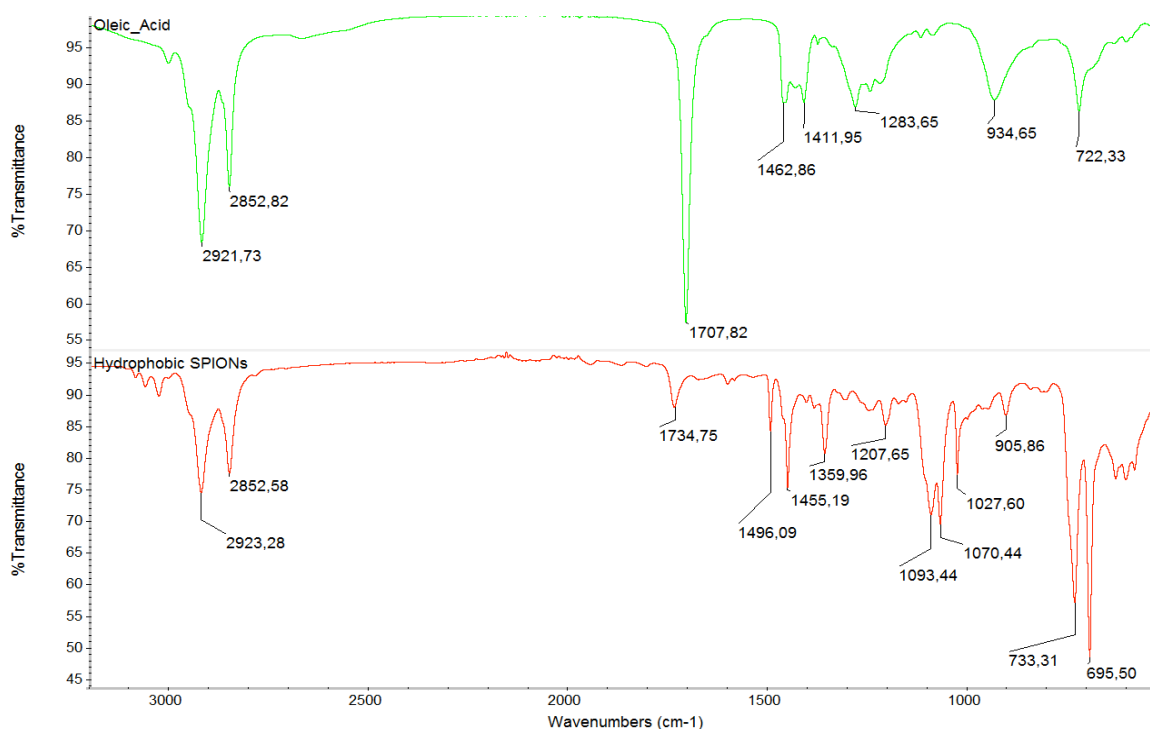


Figure 3.11. FT-IR spectra comparison between Oleic acid (green) and hydrophobic SPIONs batch (red).

In Figure 3.11 is shown the comparison between free oleic acid and hydrophobic SPIONs, which are known to contain SPIONs stabilized by oleic acid. This is confirmed by the IR analysis. The two peaks at 2921.73 cm^{-1} and 2852.82 cm^{-1} present in the oleic acid spectrum due to the C-H stretching of the alkylic chains [99] are also evident in the hydrophobic SPIONs spectrum where the first peak is slightly shifted (2923.28 cm^{-1}) suggesting that oleic acid ligands are bonded onto the NPs surface as expected. [188]. These peaks are also present in the spectrum of the HPB coated SPIONs (figure 3.12). The high intensity peak found at 1707.82 cm^{-1} is due to carboxyl C=O vibrations of the oleic acid. [189] This peak is shifted (1734.75 cm^{-1}) and less intense in the spectrum of the

hydrophobic SPIONs in agreement with the literature. [188]

In Figure 3.12 is reported the FT-IR spectrum of the HPB coated SPIONs supraparticles in the aqueous dispersion compared with the spectra of the SPIONs in toluene and of a 0.1 mg/mL HPB solution, respectively.

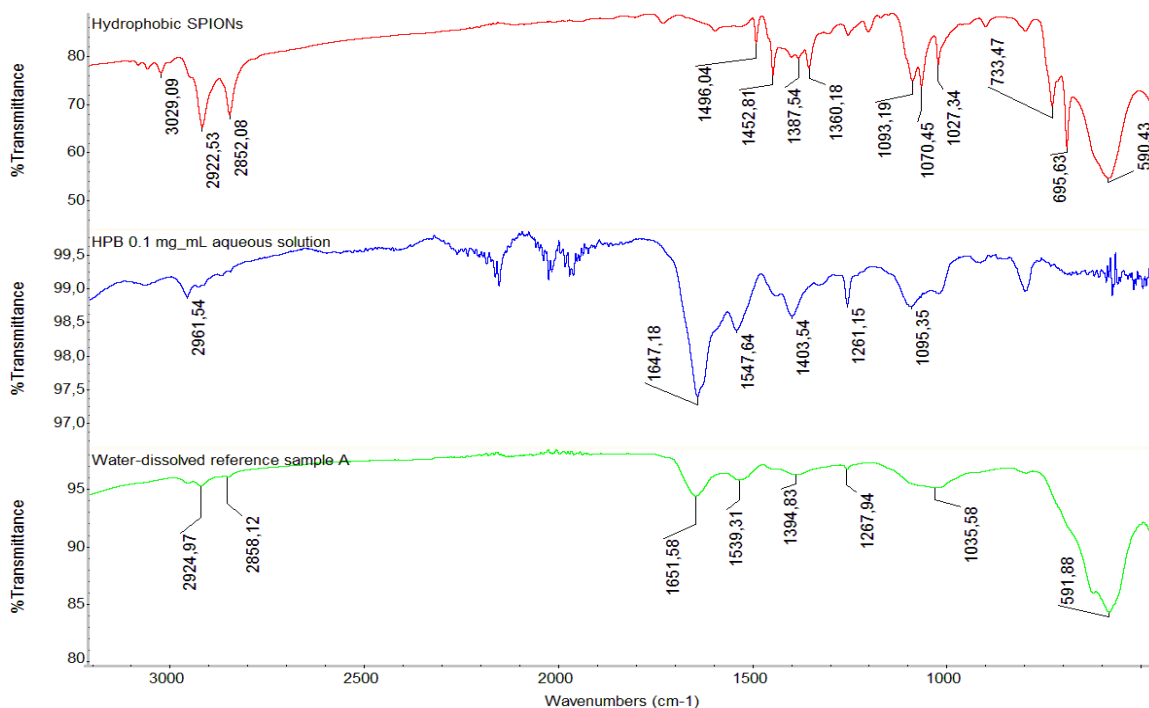


Figure 3.12. FT-IR spectra comparison between hydrophobic SPIONs (red), HPB II 0.1 mg/mL aqueous solution (blue) and water-dissolved HPB coated supraparticles reference sample A (green).

The main peak visible in the spectrum of the HPB II in solution is related to the strong amide I band (1647.18 cm^{-1}) signal, due to the C=O vibrations of the HPB II peptide bonds. [189] The exact frequency of vibration of the amide I band is determined by the substituents on the Nitrogen atom. The signal is then averaged on all the signals from the amino acids of the protein. [189] The peak at 1547.64 cm^{-1} is the amide II band, typical of amide functional groups in proteins, and due to the deformation of N-H scissoring vibrations modes. [189] Amide I and II bands positions depends on the relative amount α -helix and β -sheets in the secondary structure of the protein. The positions of the amide I and II bands in this spectrum are in agreement with a predominant β -sheet structure as expected for HPB II. [190] Finally, the low intensity peak at 1261.15 cm^{-1} can be related to the amide III band as reported in the literature [189]. For the spectrum of the HPB II

coated SPION supraparticles a broadening of the amide I band together with a shift from 1647.18 cm^{-1} to 1651.58 cm^{-1} are observed. This shift is supposed to be associated to a change in the protein secondary structure upon adsorption onto the supraparticles. This is in agreement with the increase of α -helix content described in the literature for protein assembling at water-hydrophobic interfaces. [181], [182], [190]

In Figure 3.13 are reported the spectra of HPB-II dissolved in water, in 10 mM, acetate buffer at pH 4.5 and of the HPB II coated SPION supraparticles in acetate buffer, respectively.

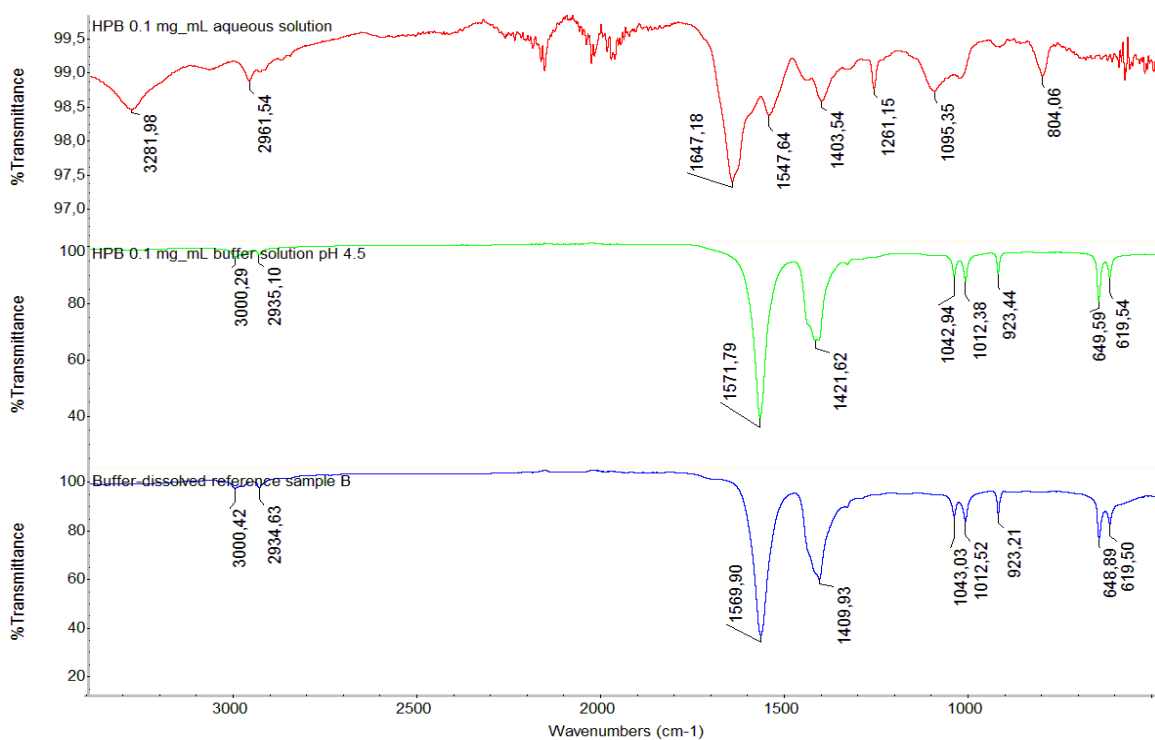


Figure 3.13. FT-IR spectra comparison between an HPB 0.1 mg/mL aqueous solution (red), HPB 0.1 mg/mL buffer solution at pH 4.5 (green) and the buffer-dissolved HPB coated supraparticles reference sample B (blue).

This comparison is reported in order to provide a better understand of the effect of an acid environment on HPB II and on the HPB II coated supraparticles. It is interesting to note the HPB II behaviour when is dissolved in Acetate buffer (dark green spectrum). It shows a different spectrum, with very shifted peaks with respect to the water dissolution case. The carbonyl C=O bond stretching peak seems shifted to $1571,79\text{ cm}^{-1}$ and this could be

associated to the carbonyl group protonation that occurs in acid environment. In addition, amino acid protonation possibly lead to the formation of hydrogen bonds both intra and intermolecular which may further affect the C=O stretching vibration frequency. [189], [191]

Finally, a gradual shift towards lower wavenumbers of the two main peaks associated to the carboxylic groups is observed passing from HPB II in water to HPB II in acetate buffer to HPB II adsorbed on the surface of the SPIONs in acidic conditions (see figure 3.13). While the adsorption of HPB II on the surface of the SPIONs in water induced an opposite shift of the two peaks (see Figure 3.12) with respect to the spectrum of the free HPB in the same conditions. It is known that shifts are possibly due to a change in the secondary protein structure upon adsorption onto the hydrophobic NPs, but they are typically to higher wavenumbers. On the other hand, the acid environment is known to lead to amino acid protonation with possible formation of hydrogen bonds both intra and intermolecularly. [190] Therefore, it is possible that secondary structure changes upon HPB adsorption at hydrophobic/hydrophilic interface sum with hydrogen bonds effects inducing variations in the FTIR spectrum.

The same analysis was performed on Nile red-encapsulated HPB coated supraparticles reference sample C and the FTIR spectrum of this sample in comparison to that of the Nile red and the empty HPB coated SPIONs are reported in Figure 3.14.

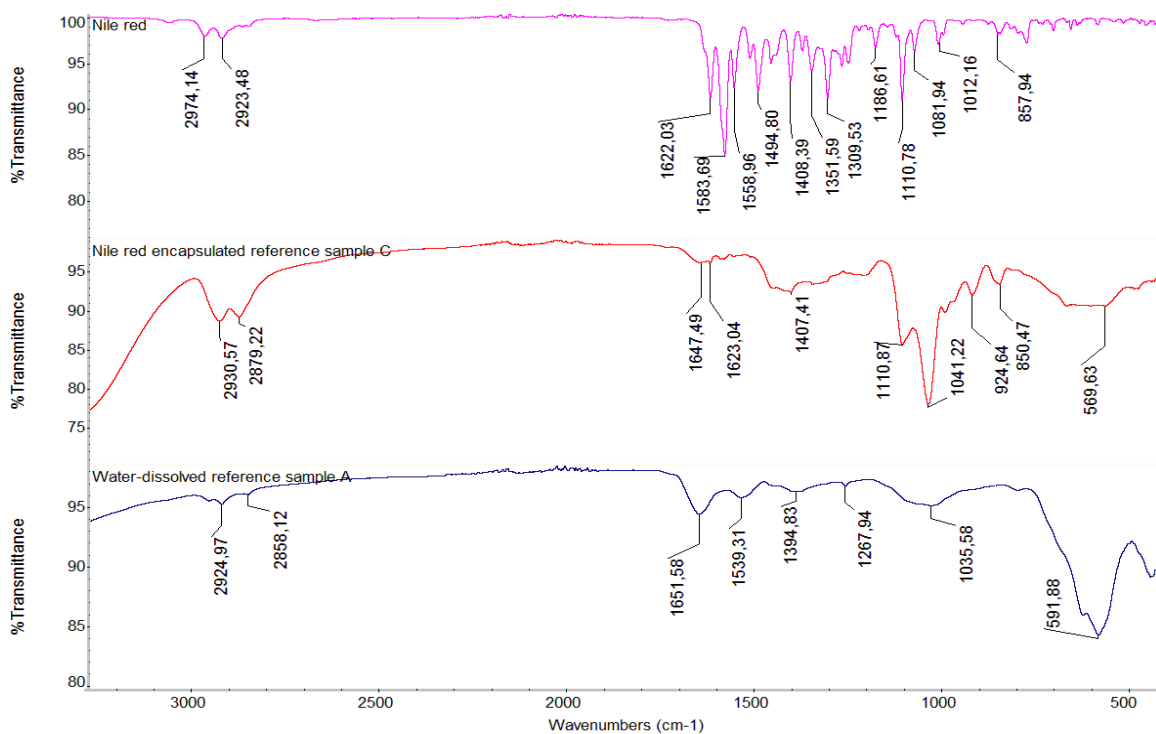


Figure 3.14. FT-IR spectra of Nile Red (purple), Nile red encapsulated HPB coated supraparticles reference sample C (red) and the water-dissolved HPB coated supraparticles reference sample A (blue).

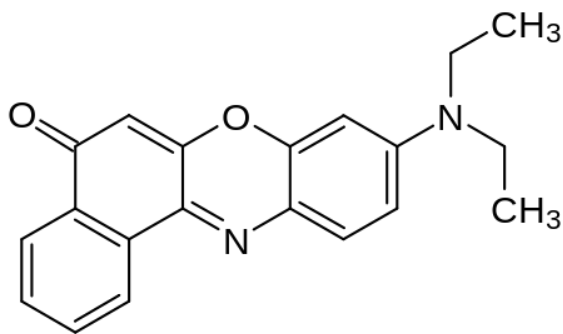


Figure 3.15. Nile red molecule

Nile red spectrum shows the absorption peaks associated to the typical four skeletal ring breathing modes of aromatic compounds in the range 1600-1450 cm⁻¹. In particular, the peak at 1622.03 cm⁻¹ is known to be associated to the first of these four modes, which is typically found near 1600 cm⁻¹ for single ring aromatic compounds, while can be shifted at higher wavenumbers for polyaromatic compounds as Nile red. The same peak is observed for the Nile red containing NPs (sample C), but it appears slightly shifted

(1623.03 cm^{-1}), much less intense as well as wider. The same peak is not present in the spectrum of the empty HPB coated SPIONs (sample A). The presence of the Nile red in the spectrum of the loaded NPs is also highlighted by the presence of the peak at 1110.78 cm^{-1} , probably associated to the C-N stretching absorption of the aliphatic amines (Figure 3.15) also evident in the dye spectrum at the same wavenumber. [189]

UV-Vis Absorption

UV-Vis absorbance spectra of the three reference samples are reported in Figure 3.16 from samples at stock concentration. The absorbance spectrum of the HPB II coated supraparticles presents a monotonic trend with a continuous decrease towards visible wavelengths. The reference water-dissolved sample A presents a very wide and low intensity peak at about 320 nm which is in agreement with theoretical values calculated by Creighton for colloidal Fe. [192], [193] Reference buffer-dissolved sample B shows a plateau starting from about 400 nm down to 200 nm. Unfortunately, the reason for this is still unknown but could be associated to the low concentration of the sample. It has been not possible obtain more concentrated samples for samples B and C because of experimental reasons.

The NP sample supposed to contain Nile red shows a very low-intensity and very wide shoulder at about 600 nm indicated in Figure 3.16 by the arrow. This shoulder is shifted if compared with the absorption peak of the free Nile red (dissolved in CHCl_3), as reported in figure 3.17. The lack of a clear peak related to Nile red absorption at 520 nm can be explained with a very low concentration of the encapsulated dye together to the scattering background effect due to the NPs [194], [195]

In Figure 3.18 is reported a comparison between the UV-Vis spectra of HPB-II dissolved in water and adsorbed at the interface (sample A). The spectrum of the free HPB has been recorded at the concentration used for the coating procedure. The lack of a sharp peak characteristic of the protein at 300 nm indicated that at this concentration the HPB UV-absorption is negligible.

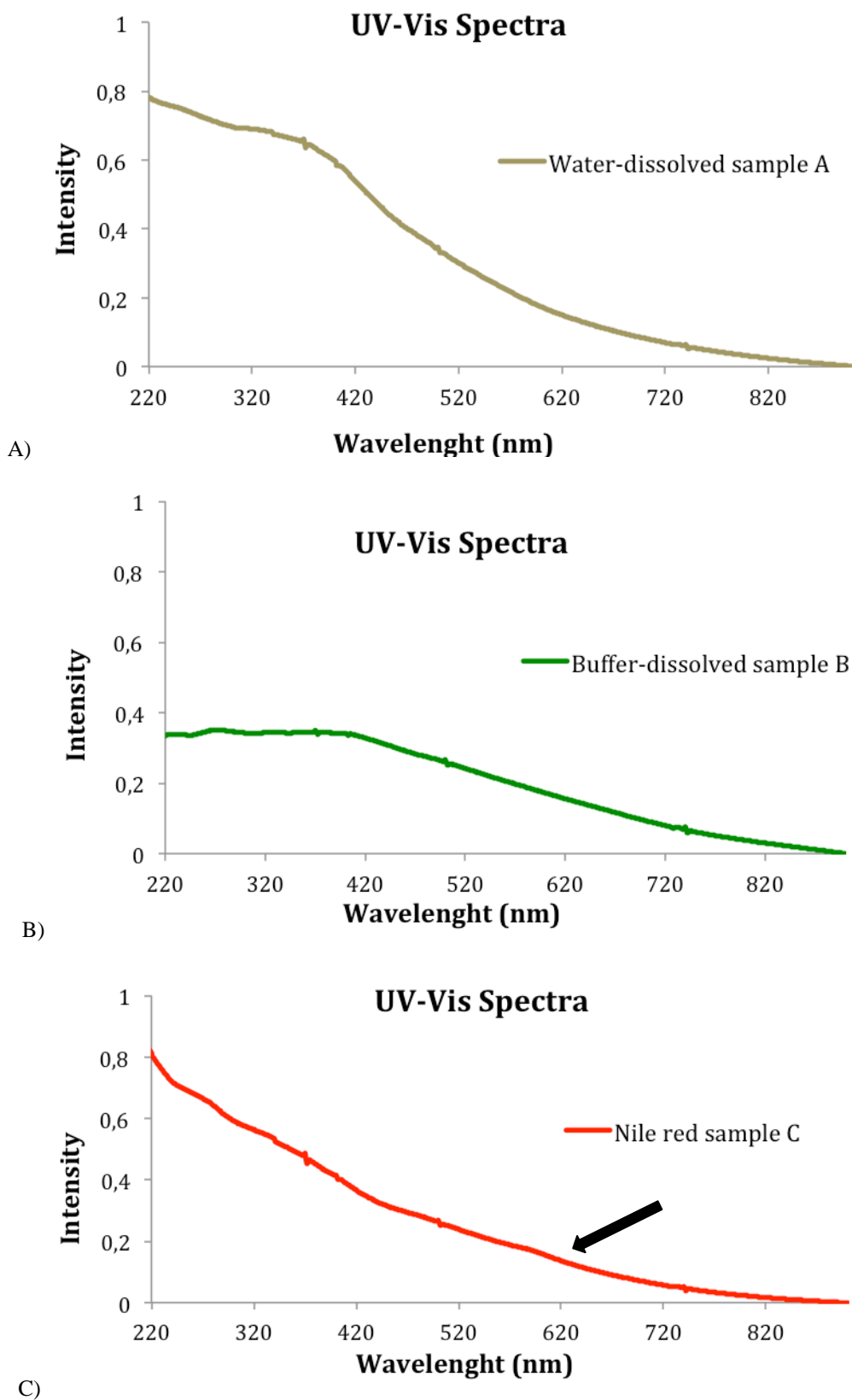


Figure 3.16. UV-Vis absorbance spectra of the three reference samples at stock concentration for the three types of coating protocols.

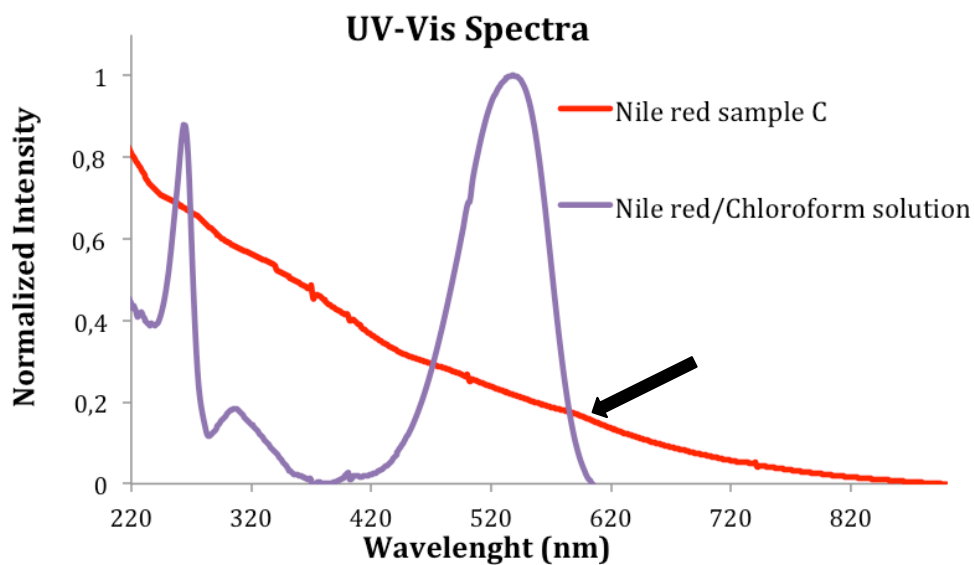


Figure 3.17. UV-Vis normalized absorbance spectra comparison between the Nile red-encapsulated HPB coated supraparticles reference sample C and a Nile red/ CHCl_3 solution.

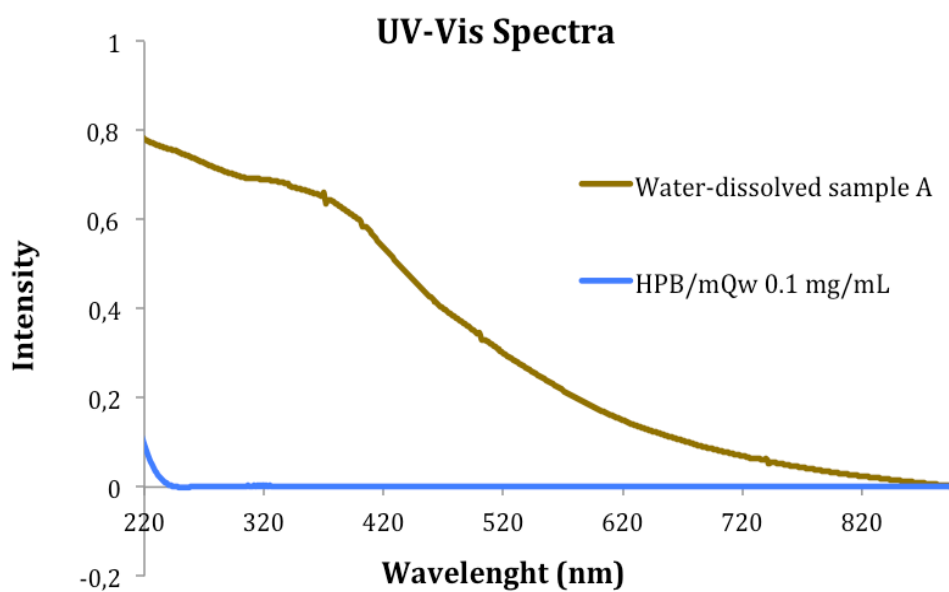


Figure 3.18. UV-Vis absorbance spectra comparison between the water-dissolved HPB coated supraparticles reference sample A and a HPB II aqueous 0.1 mg/mL solution.

Circular Dichroism (CD)

CD measurements have been performed on HPB-II 0.3 mg/mL solutions both in aqueous and acetate buffer (10mM, pH 4.5) solutions as well as on HPB coated NPs. Unfortunately, CD spectrum was not detectable for any of the NP samples. This may be due to the excessive dilution of HPB-II as already highlighted by UV-Vis absorption.

The spectra obtained from HPB-II dissolved in aqueous solution and acetate buffer are reported and compared in Figure 3.19. The minimum in molar ellipticity found in the UV zone of the CD spectrum is known to be associated to the protein secondary structure. The minimum lies at about 202 nm in both the solutions, in agreement from what reported in the literature for HPB dissolved in water, even if there is a slight change in the intensity. [181] This result suggests that the secondary structure is not modified changing the solvent from mQw to Acetate aqueous buffer.

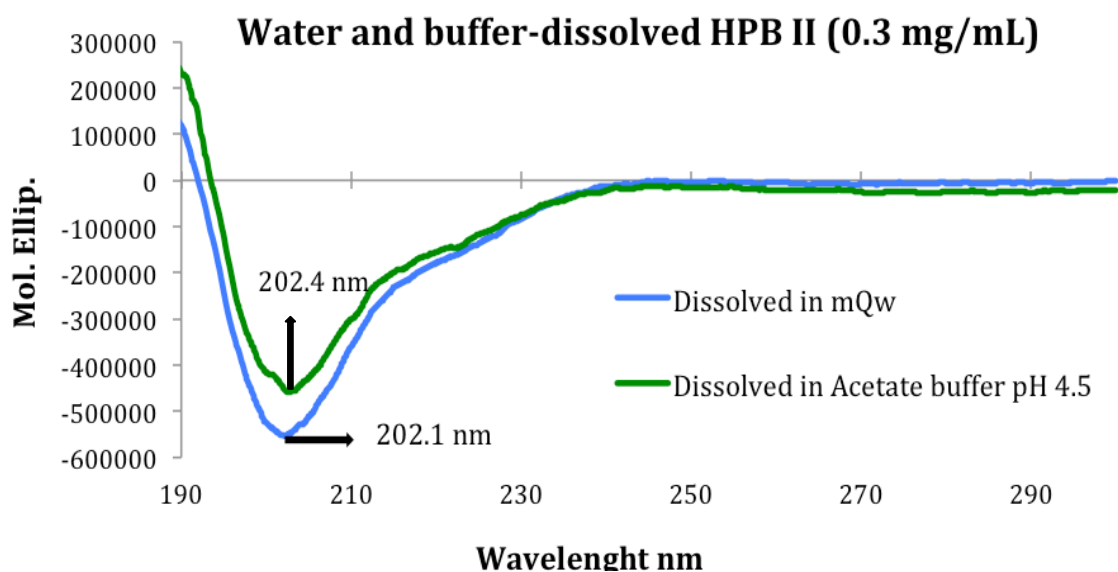


Figure 3.19. CD spectra comparison between HPB-II solution in mQw and Acetate buffer.

Fluorescence

Fluorescence measurements have been performed using 485 nm as excitation and monitoring emission in the range from 520 nm to 700 nm. In fact, the spectra of a solution of Nile red in CHCl_3 , the empty NPs and the loaded NPs are reported in Figure 3.20.

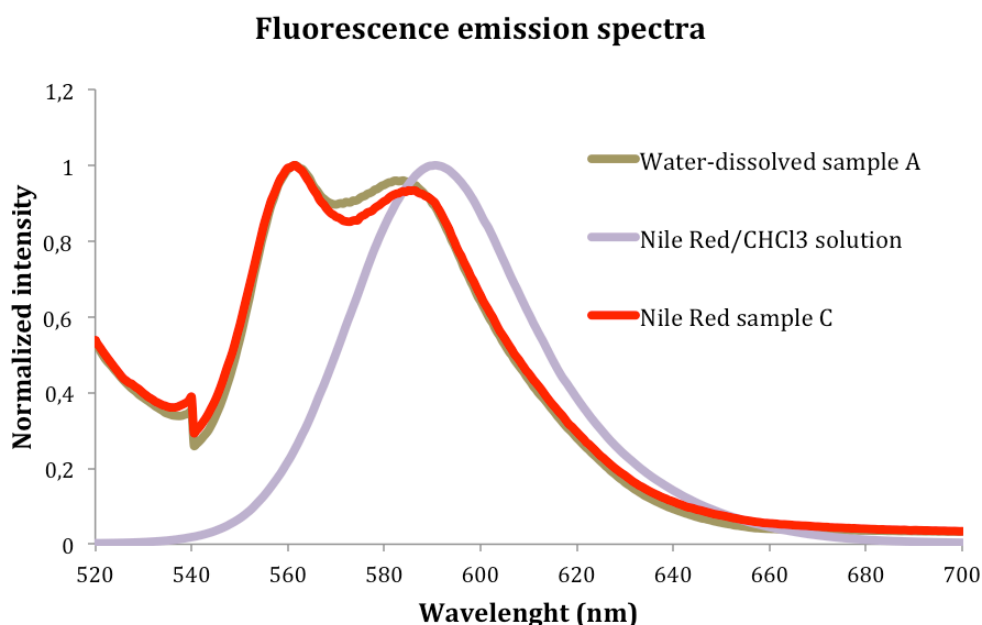


Figure 3.20. Normalized fluorescence emission spectra comparison between Nile red HPB coated supraparticles reference sample C, water-dissolved HPB coated supraparticles reference sample A and a Nile Red/ CHCl_3 solution.

The CHCl_3 solution of Nile red is characterized by a strong emission peak at 590,5 nm as expected [50], while the NP samples showed a similar emission spectra featured by a double wide peak with two maximum at 558 nm and 585 nm. These peaks cannot be related to the presence of Nile red, as they are present also in the spectrum of the empty NPs. The lack of the emission can be related to an excessive dilution of the sample C and/or to quenching effect due to the iron oxide cores. [196]

3.4 Conclusions

In this work a first approach to develop a new protocol to produce water-soluble SPIONs has been studied. The protocol has been optimized in order to obtain water-soluble SPIONs supraparticles coated by HPB-II protein to be used as theranostic nanostructures, in particular as MRI contrast agents and drug carriers.

Three different modifications of the protocol have been tested in order to produce supraparticles stable and soluble in water, in water-based acid buffer and able to produce fluorescent images by dye encapsulation.

Size and colloidal stability measurements have been performed providing size results in the range of 220-390 nm and Zeta-potential in the range of -7.0 mV and -35.0 mV. The best results are found for supraparticles dispersed in water, which show an averaged hydrodynamic diameter (Dh) of 249 ± 12 nm and an averaged Zeta-potential of -29 mV. While these samples showed a good reproducibility, the supraparticles dispersed in acetate buffer and containing the fluorescence dye need further optimization.

These NPs have been characterized by FT-IR, UV-Vis, Fluorescence and CD spectroscopy that, together with the structural characterization, indicated the formation of HPB coated SPION supraparticles rather than of single HPB coated NPs.

FTIR analysis showed the characteristic bands of the oleic acid and HPB for all the samples. UV-Vis absorption spectra presented a trend analogous to the one reported in literature for colloidal Iron for the empty NPs in water, while not conclusive results have been obtained for the other samples. In addition, CD analysis results suggested that the protein does not strongly change its secondary structure when dissolved in water or in acid water-based buffer. Therefore, the modifications in the secondary structure observed in FT-IR spectra are possibly due to the HPB II physics of adsorption on the hydrophobic/hydrophilic interface in both water and acid environment. Fluorescence experiments showed an emission for these NPs at about 558 nm and 585 nm that needs further investigation.

All the samples showed magnetic response upon magnetic forces suggesting that they can be moved by application of an external magnetic field. These NPs are promising theranostic nanovectors even if further optimization is needed.

In particular, we envisage more studies in the following areas:

- Optimization of the reproducibility of the supraparticles formed at acidic pH by testing different HPB/NPs molar ratios and a deeper investigation of the HPB-II filming behaviour in acidic environment.
- Optimization of Nile red encapsulation by testing other (higher) dye/NPs molar ratios.
- Optimization of supraparticles ability to encapsulate hydrophobic molecules.
- Cryo-TEM analysis of formed NPs.

Besides improving the experiments as proposed, it is also interesting to state that the study can be continued with further steps.

For example, it would be interesting to test possibility of functionalize HPB-II coating with some targeting moieties, in order to make the supraparticles more site-specific. Another step could be the study of the encapsulation and the release of a cytotoxic drug in order to make the supraparticles really theranostic and, then, to study their theranostic ability behaviour *in vitro*.

Chapter 4 - Development of fluorinated gold nanoparticles

4.1. Introduction

The synthesis of functionalized fluorinated gold NPs was also investigated during this master thesis project. Functionalization of AuNPs with highly fluorinated ligands is particularly interesting for the unique chemical and physical properties of these molecules. Perfluorocarbons (PFCs) are organic compounds in which all hydrogen atoms are replaced with fluorine. This makes them highly hydrophobic and lipophobic as well as thermally and chemically stable. These properties are conferred by the strength of the C-F bond and the high electronegativity and low polarizability of fluorine. Moreover, perfluorinated ligands can also confer to the NP certain permeability towards drugs, thanks to the possible affinity they have with this kind of ligands. Many drugs currently used for the treatment of a wide range of diseases, in fact, contain fluorine atoms that can display fluorine-fluorine interactions with the fluorinated shell. This peculiarity can therefore be exploited and fluorinated NPs used as drug carriers for controlled drug delivery. In fact, incorporation of F-alkyl chains into NPs can improve the diffusion across membranes and the blood-brain barrier. [1],[4]–[6]

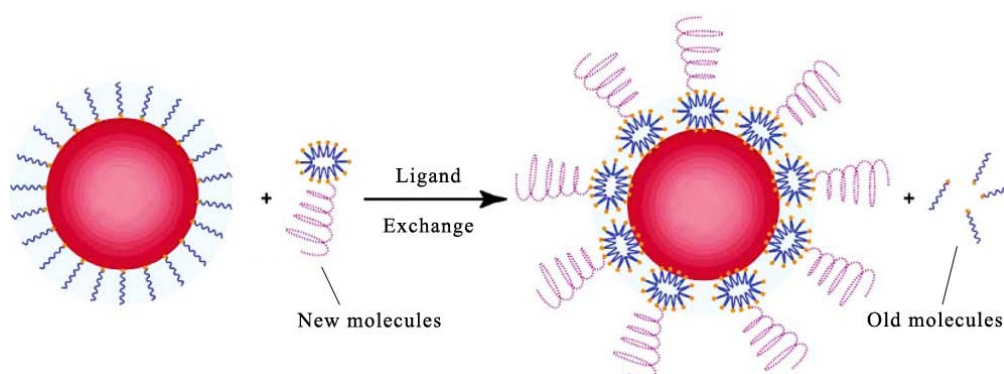


Figure 4.1. Schematic illustration of a generic exchange reaction. The new molecules establish a stronger bond with the NPs than those present on the surface. [201]

For the synthesis of these highly fluorinated NPs, two different approaches were used: direct Brust synthesis and ligand-exchange reactions; the latter mechanism is schematically represented in Figure 4.1.

The exchange with fluorinated ligands was done starting from previously synthesized oleylamine-stabilized AuNPs, partially following the work of M.L. Kraft and co-workers. [202], [203] In this synthesis oleylamine is used as both reducing and capping agent. These NPs were subsequently treated with a mixture of ligands, containing different ratios of *1H,1H,2H,2H*-perfluorodecanethiol (PFDT) and dodecanethiol (DT), to obtain a mixed shell. The bond formed by the oleylamine nitrogen with the NP gold core is quite labile, allowing complete replacement of these ligands with thiols, which form a much stronger bond with gold. [204] The PFDT:DT ratios were varied from 0:100 to 100:0 to understand the kinetics and the stoichiometry of the exchange reaction, which means to determine the minimum amount of PFDT necessary to obtain fluorinated ligands bonded to the surface of the AuNPs.

Samples with PFDT:DT ratios from 80:20 to 100:0 showed quite unexpected properties: in these batches TEM analysis showed the presence of two different populations, one of AuNPs between 5-7 nm, and one of Au nanoclusters between 0.9-1 nm, quite possibly formed by fragmentation of the bigger NPs. Furthermore, UV-Vis spectra of those samples showed, together with the expected peak around 530 nm typical of the plasmonic vibrations of AuNPs, another peak around 350 nm. [132], [133]

This unexpected peak is probably ascribable to the electronic properties of the Au nanoclusters. In fact, these aggregates are formed by few tens of atoms and thus they do not present a collective plasmon oscillation of electrons. On the contrary, the reduced dimensions of these particles causes a split in the electronic band of the structure. This bands division brings to a molecular-like electronic behaviour since the characteristic dimension is similar to the Fermi one. This explains why electrons exhibit transition just between the split electronic levels of the structures and not collective oscillation modes. [205]–[207]

The data also showed a dependence of the fragmentation on the amount of PFDT, in particular the nanoclusters population seemed to increase with the concentration of PFDT. In this regards, it has been reported in the literature how small molecules with particular electronic properties could induce the fragmentation of AuNPs. Bigger particles in the presence of electron-attracting molecules could fragment because of the interaction with the surface charges (and so of the electrons) of these structures. [208]–[212] The first two experiments (sample 1 and 2) aimed to study the effect on fragmentation of a further addition of PFDT on a batch already containing Au nanoclusters.

Aim of our work was to study how the NPs fragmentation was influenced by NPs size, amount of PFDT and reaction time. To do so, ligand-exchange reactions were performed using only PFDT, with increasing PFDT:gold ratios and varying the reaction time. The reactions were performed on bigger oleylamine-capped NPs and dodecanethiol-capped NPs. Ligand-exchange reactions using only DT were also performed. To ascertain the nature of the nanoclusters, many tests on all the reagents, solvents and ligands involved in the reactions were performed.

Another procedure tested for the synthesis of fluorinated AuNPs was a process inspired to the direct Brust method. [119], [204], [213] The NPs obtained with this method were totally fluorinated and with an average diameter of 1,7 nm, very small if compared to those obtained with exchange method. Size-tunability is very important due to the optical and electronic properties that are strongly dependent on this parameter. Plasmonic oscillations for example are affected by the size: bigger NPs show a red shift of the plasmonic peak in the UV-Vis spectrum. This is very important for imaging and diagnostics, where the NPs could be used as probes responsive to different wavelength. [132], [206], [214]

A fundamental step for the application of fluorinated AuNPs in medicine, is the ability to dissolve them in biological fluids. The only way to allow this transfer from fluorinated solvents to aqueous ones, is to coat the NPs with a hydrophilic shell. A coating was performed on the totally fluorinated NPs involving HPBII, already well known for the

SPIONs encapsulation procedure. These experiments were performed almost at the end of this project and were not examined in depth, giving only a direction for future studies.

In the following paragraphs procedures, characterizations analysis and results discussions of the experiments carried out are described.

4.2. Synthesis procedures

In this section are reported the synthetic procedures performed to obtain fluorinated NPs. If not otherwise specified the experiments were performed at room temperature. After the treatment in two different environment (sample 1 and 2) of an old partially fluorinated batch containing AuNPs and Au nanoclusters, two new batches of AuNPs were synthesized, one stabilized by oleylamine (sample 3), the other one by DT (sample 4). Exchange reactions were then performed on these batches. PFDT or DT ligands were tested to investigate the eventual condition that could promote fragmentation of NPs returning nanoclusters. The first four exchange reactions were performed on oleylamine stabilized AuNPs, whereas the last one on DT capped AuNPs. Firstly, reaction time was changed at a fixed concentration of PFDT (sample 5 and 6) to perform a kinetics study on the replacement process and on the NPs fragmentation. Then an exchange reaction with DT was tested (sample 7) to verify eventual fragmentation by another ligand with the same reaction time of sample 6. On the same line, to study the effect of ligands concentration on this phenomenon, an higher amount of PFDT was added in sample 8. PFDT replacement process was also tested on DT stabilized AuNPs to investigate the possibility of fragmentation of other kind of NPs (sample 9). Tests on the reagents involved were performed to verify the origin of the nanoclusters (samples 10-15). The last two reactions involved a different synthesis method inspired to Brust direct method (sample 16) and the coating with HPBII of the so obtained totally fluorinated AuNPs (sample 17).

Sample 1 and 2. Treatment of partially fluorinated AuNPs, obtained by ligand-exchange reaction with PFDT, already presenting nanoclusters.

1 mL of partially fluorinated AuNPs solkane solution was split in two parts and put into two vials. 500 μ L of PFDT were rapidly added with a pipette: in the first vial (sample 1) PFDT was diluted in 0,8 mL of toluene and in the second one (sample 2) in 0,8 mL of solkane. Both mixtures were left stirring for 18 hours.

Purification. The vials were sonicated for few minutes and transferred into two different falcons. The mixtures were diluted with toluene to separate the pellet from the excess ligands during the centrifugation, performed at 6500 rpm for 15 minutes. The supernatant was separated and centrifuged again at 8000 rpm for 15 minutes. The pellet obtained was recovered and combined to the first one. Toluene was used to re-suspend the NPs via sonication, in order to solubilize the excess ligands and several cycles of sonication and centrifugation were performed. For the mixture reacted in toluene environment the centrifuge was set at 4000 rpm for 15 minutes; the one reacted in solkane environment needed stronger centrifuge cycles (8000 rpm for 15 minutes) to obtain a pellet separation and an almost transparent supernatant. After the final washing cycle the obtained pellet was dried and dissolved in solkane.

Sample 3. Gold nanoparticles stabilized by oleylamine. [126], [215]

17 mL of oleylamine were dissolved in 300 mL of toluene in a round bottomed flask equipped with a condenser. The mixture was brought to a slow reflux at 110°C while stirring and a freshly prepared solution of 197 mg of $\text{HAuCl}_4 \cdot 3\text{H}_2\text{O}$ dissolved in 10 mL of oleylamine and 8 mL of toluene was rapidly added. The mixture was left stirring for 2 hours at the reflux temperature at the end of which a deep red solution was obtained. The mixture was cooled to room temperature and transferred in a flask.

Purification. 300 mL of MeOH were added in order to precipitate the NPs and eliminate the oleylamine excess. The solution was then poured in several falcons and centrifuged at 3000 RPM for 20 minutes. The supernatant was separated and the falcons were rinsed with 50 mL of MeOH several times to eliminate the oleylamine left. At the end, the minimum amount of toluene was used to solubilize the NPs. The solution was filtered through a 0,22 μm syringe filter.

Sample 4. Synthesis of gold nanoparticles stabilized by dodecanethiol. [216]

1 g of HAuCl_4 was dissolved in 83 mL of mQW and added to a solution of 7,4 g of tetraoctylammoniumbromide (TOAB) dissolved in 36 mL of toluene. The solution was stirred until the organic part turned from colourless to deep red. Separately 1,1 g of NaBH_4

were dissolved in 74,6 mL of mQW and then added dropwise to the first solution. After 1h, the mixture was washed with 83 mL HCl (0,01M), then with 83 mL of NaOH (0,01 M) and then 4 times with 40 mL of mQW. The organic phase was then left stirring overnight. Finally 33,3 mL of 1-dodecanethiol were added and left stirring vigorously for 2 hours at 65°C.

Purification. The final solution was centrifuged at 3000 rpm for 10 minutes; the pellet was then discarded and divided in several falcons. MeOH was added to each falcon until it became cloudy. Another cycle of centrifugation was performed at 8000 rpm for 10 minutes after which the supernatant was centrifuged with other MeOH to re-precipitate the left NPs. The pellet was finally dissolved with the minimum amount of toluene.

Sample 5 - 9. Ligands-exchange reactions. [37], [98], [217]–[219]

In a vial, 0.2 mmol of ligand mixture dissolved in toluene was added to 1 mL of already prepared NPs in toluene. The amounts of ligands, solvent and NPs used are reported in Table 4-1. The vials were sealed and the mixture left stirring for 18 hours except sample 5, which was left stirring for 3h.

Table 4-1. List of the amounts of reagents and solvents used for the synthesis. In the AuNPs column (a) indicates oleylamine-stabilized AuNPs whereas (b) indicates DT-stabilized AuNPs.

	AuNPs [mL]	PFDT [mol/L]	DT [mol/L]	Time [h]
Sample 5	2 (a)	0.25	/	3
Sample 6	4 (a)	0.25	/	18
Sample 7	4 (a)	/	0.25	18
Sample 8	2 (a)	0.75	/	18
Sample 9	2 (b)	0.25	/	18

Purification. Same process reported for samples 1 and 2.

Sample 10-15 Reactions between HAuCl₄, PFDT, DT and oleylamine.

In a vial, the desired amount of HAuCl₄, PFDT, DT and oleylamine (see Table 4-2) was added to 1 mL of toluene and the mixture left stirring for 18h. After a few minutes of sonication, the mixture was diluted with 5 mL of toluene and 5 mL of mQW, transferred in a separatory funnel, the phases separated and analyzed via UV-Vis.

Table 4-2. List of the amounts of reagents used for the synthesis of samples 10-14.

	HAuCl ₄ [mmol]	PFDT [mmol]	DT [mmol]	Oleylamine [mmol]
Sample 10	1.5·10 ⁻²	0.10	/	/
Sample 11	1.5·10 ⁻²	/	0.15	/
Sample 12	1.5·10 ⁻²	/	/	0.19
Sample 13	/	0.10	0.15	0.19
Sample 14	1.5·10 ⁻²	0.10	0.15	0.19

Sample 15. Treatment of gold NPs stabilized by oleylamine with TOAB and NaBH₄

3 mL of gold NPs stabilized by oleylamine were put in a round-bottomed flask and 24 mg of TOAB were added while stirring. Afterwards a freshly prepared solution of 6 mg NaBH₄ in 0,6 mL mQW was added dropwise and the mixture was left stirring for 18 hours. The solution was then diluted with 5 mL of mQW and transferred in a separatory funnel, the phases separated and the organic one was washed with mQW (x3). Both the organic and the aqueous phase were then analyzed.

Sample 16. Synthesis of gold nanoparticles stabilized by PFDT, via direct Brust method. [119], [204]

A freshly prepared solution of 0,358 g of HAuCl₄ dissolved in 2 mL of mQW was added to a mixture of 0,547 g of TOAB in 200 mL of trifluorotoluene in a round-bottomed flask. 0,88 mL of PFDT were then added and the mixture vigorously stirred for 10 minutes, during which time it became colourless. The mixture was then put at 0°C and 0,378 g of NaBH₄ in 10 mL of mQW were added dropwise. The reaction was left stirring at 0°C for 3 hours.

Purification. The solution was put in a separatory funnel and washed with 150 mL of mQW for three times. The organic phase was slowly evaporated under reduced pressure at r.t. The final product was covered with 20 mL of toluene, sonicated and centrifuged at 3000 rpm for 10 minutes. The pellet was recovered and resuspended in toluene and the process was repeated 5 times. Finally the pellet was dried with air and dissolved with solkane and filtered with a 0,22 μm syringe filter.

Sample 17. HPB-coating of totally fluorinated gold nanoparticles.

A solution of 3.8 mg of HPB in 38 mL of mQW was prepared with 10 minutes of sonication. 10 mL of solution were added dropwise to 300 μL of totally fluorinated gold nanoparticles dissolved in solkane. The reaction was left stirring for 1 hour at 50°C.

Purification. Same protocol described in Chapter 3, section 3.2.1.

4.3. Results and discussion

The following section reports the physical-chemical characterization performed on the NP samples. The samples were characterized by UV-Vis analysis, FT-IR characterization, TEM and DLS. For example, most of the samples dispersed in fluorinated solvents could not be characterized by DLS.

Sample 1 and 2. Treatment of partially fluorinated AuNPs, obtained by ligand-exchange reaction with PFDT, already presenting nanoclusters.

The reaction was performed on a previously obtained batch of NPs (Figure 4.2), characterized by a large amount of small fragments ($\sim 1,4 \pm 30,6$ nm of diameter) alongside with $6,3 \pm 2,3$ nm AuNPs. The nanoclusters produced also an unusual band around 350 nm in the UV-Vis spectra, related to the energy required by electrons to jump from one electronic band to another. In fact, the reduced dimension of the particles suppresses the collective plasmonic oscillation of electrons and gives rise to a split of electronic structure, resulting in a sharp peak in the UV region. [207], [220] This experiment was performed on this batch, that was obtained before the start of this master thesis. These first two reactions were not proper exchange reactions, but they were aimed at understanding if the further addition of PFDT could increase the amount of nanoclusters. There are some examples reported in literature in fact, where fragmentation is caused by the interaction of NPs with molecules with peculiar electronic properties. [208], [209], [211]

Half batch was reacted in toluene (sample 1) whereas the other half in solkane (sample 2). The exchange reactions were all performed in toluene, but the final product was dissolved in solkane, therefore it was important to try to understand how the solvents could influence the process. In order to get as close to the original conditions as possible, sample 1 was diluted with toluene.

After 18 hours of reaction, sample 1 looked transparent with a pale pink color, whereas sample 2 looked opaque, with a pale violet color and some deposit on the bottom of the vial.

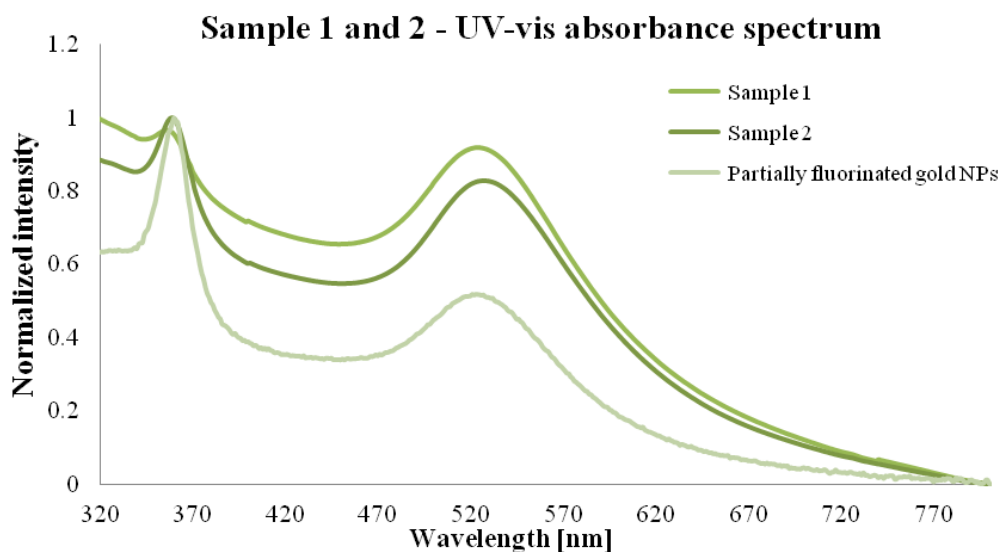
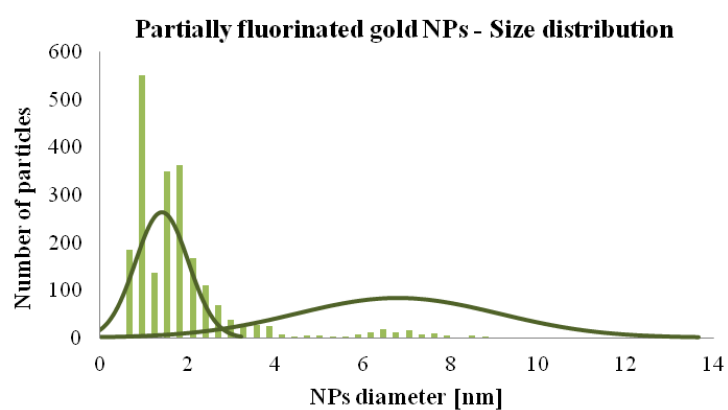
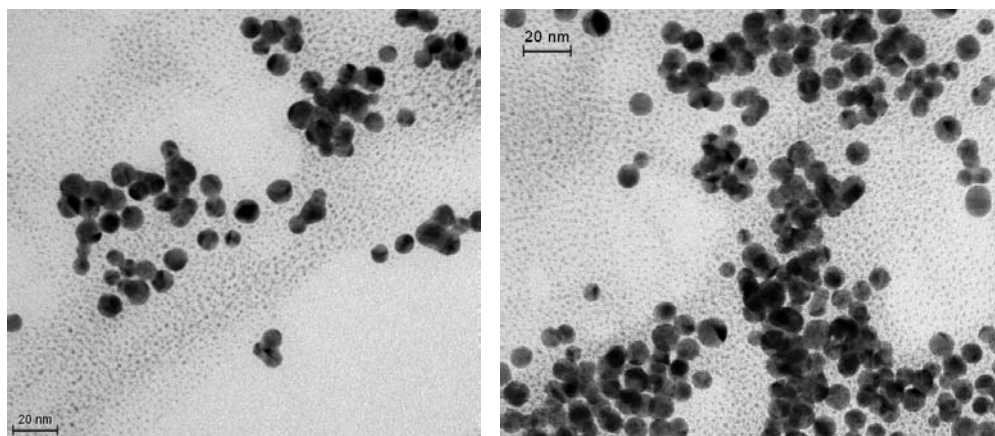


Figure 4.2. UV-Vis spectra of: partially fluorinated AuNPs, obtained by ligands-exchange reaction treated with PFDT in toluene (sample 1) and solkane (sample 2).

Figure 4.2 shows the UV-Vis spectra for sample 1 and 2 compared to that of the starting material. Since no ICP characterization was available for these samples, the spectra absorbance values were normalized in order to have a comparable intensity for the three batches that presented different concentrations. Comparing the ratio of the peaks absorbance, no significant changes were noticed, thus suggesting that the PFDT addition did not produce additional fragmentation of the bigger nanoparticles. [221]–[224] Similarly, TEM images in Figure 4.4 show no significant changes in the aggregation state and size distribution of the particles compared to the images before the reaction shown in Figure 4.3.



		Mean [nm]
Partially fluorinated gold NPs	Population 1	$1,4 \pm 0,60$
	Population 2	$6,3 \pm 2,31$

Figure 4.3. TEM images and corresponding size distribution of partially fluorinated AuNPs, obtained by ligands-exchange reaction performed before the start of this work.

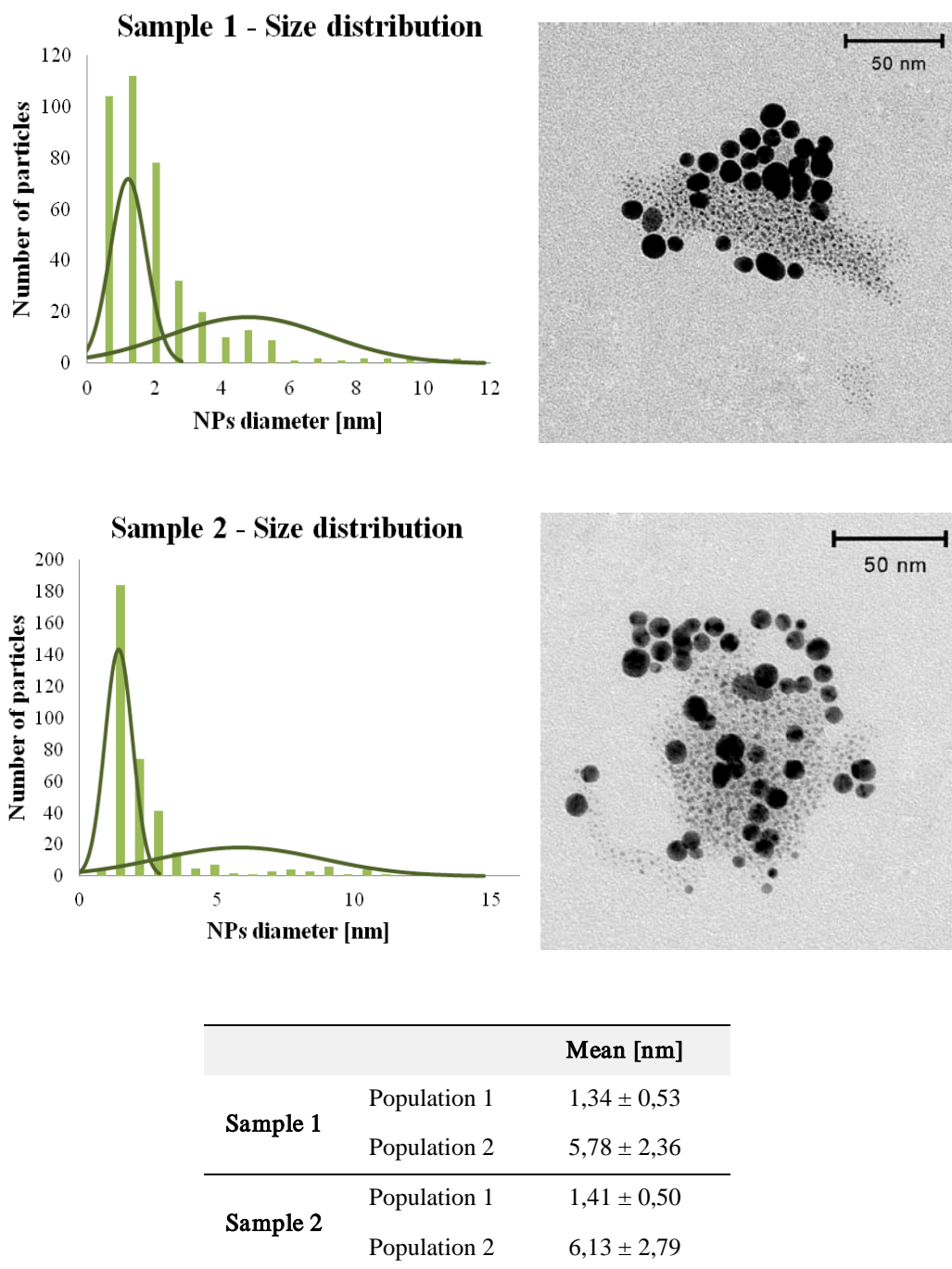


Figure 4.4. TEM images and corresponding size distribution of sample 1 (b) and sample 2 (c).

These TEM images, together with the previous UV-Vis spectra, show that the addition of PFDT to an already fragmented sample did not promote further fragmentation of bigger particles increasing the concentration of the smaller one. The analysis of several TEM images indicated that not major variations in the distribution of the two populations occurred.

Sample 3. Synthesis of gold nanoparticles stabilized by oleylamine

To study the influence of size on the fragmentation of NPs during the ligand-exchange reaction, a new batch of bigger oleylamine-AuNPs was synthesized. Changing the Au/oleylamine ratio a dispersion of 13 nm oleylamine-AuNPs was obtained.

DLS analysis of Au NPs stabilized by oleylamine is shown in figure 3 and an averaged hydrodynamic diameter of 16.0 ± 0.8 nm, with good monodispersity (PDI 0.28) was extracted from cumulant analysis (Fig. 4.5 and 4.6).

Statistical analysis of the TEM images gives an averaged core size of 12.8 ± 1.2 nm with no sign of aggregation. This is very important because it means that the NPs are well dispersed in toluene.

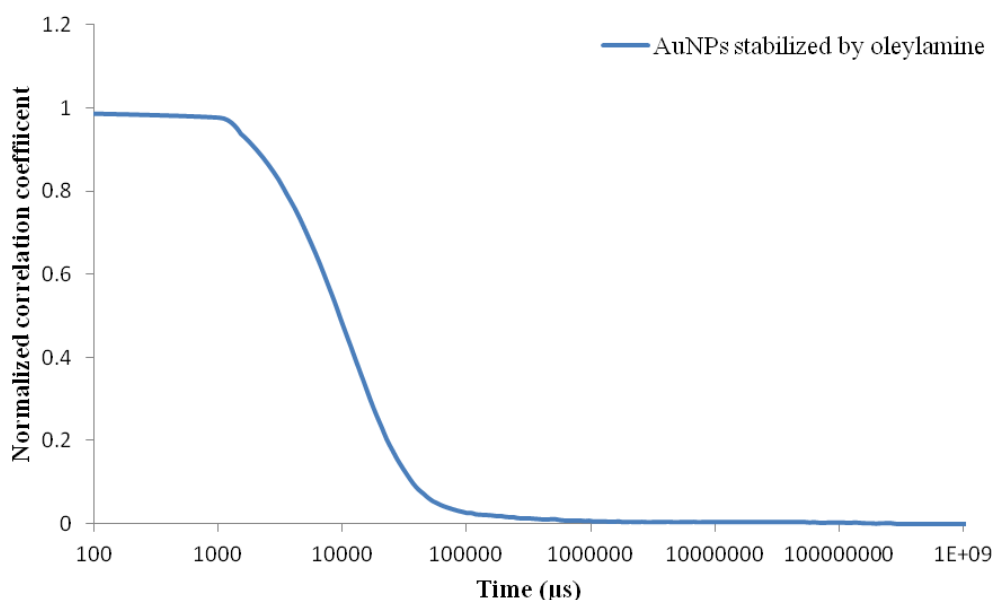
Sample 3 - correlation function

Figure 4.5. Correlation function (average of the three DLS runs) of gold nanoparticles stabilized by oleylamine

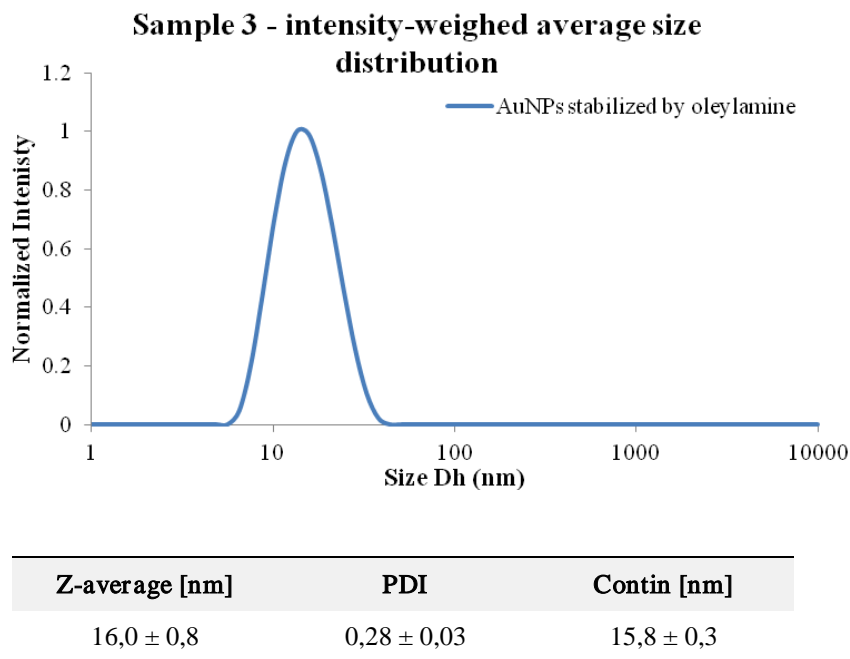


Figure 4.6. Intensity-weighted size distribution obtained by CONTIN (average of the three DLS runs) of gold nanoparticles stabilized by oleylamine and DLS values table.

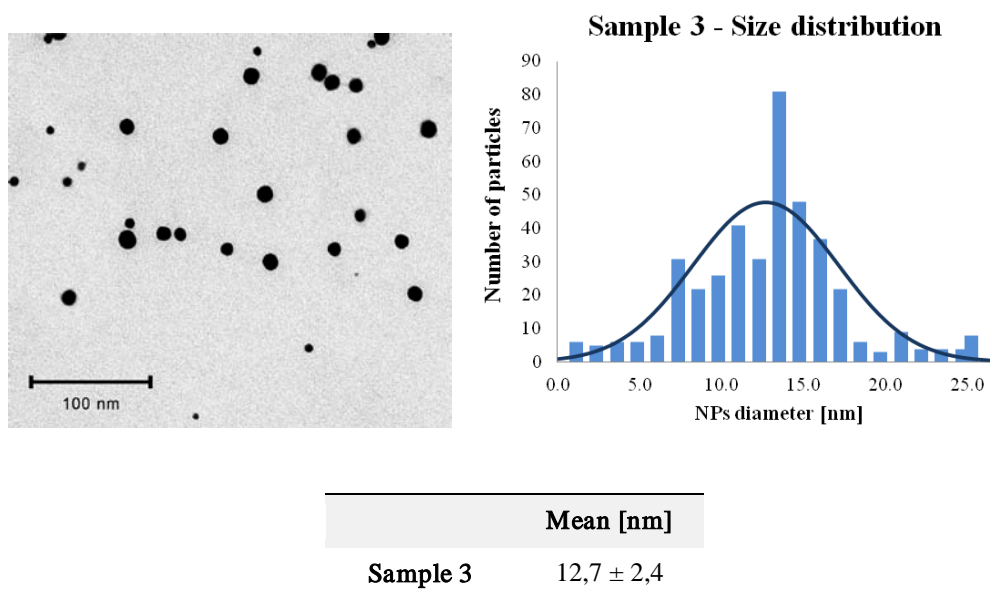


Figure 4.7. TEM image and corresponding size distribution (obtained by size analysis of several TEM images of particles) of gold nanoparticles stabilized by oleylamine.

Figure 4.8 shows the UV-Vis spectrum of sample 3 that is characterized by a sharp plasmon peak around 535 nm. The broadness of the peak in the UV-Vis spectrum strongly

depends on the polydispersity on the size of the particles contributing to the plasmonic signal and in this case it confirms a good monodispersity of the sample. [34], [132], [133], [206]

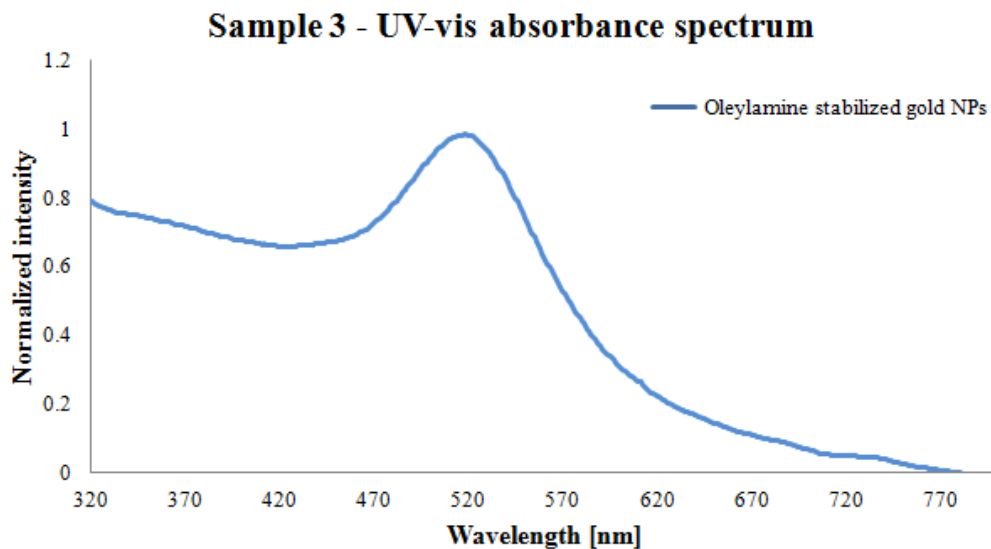


Figure 4.8. UV-Vis spectrum of gold nanoparticles stabilized by oleylamine

FT-IR analysis showed a spectrum where the peaks from the NP sample were similar to those of pure oleylamine (see Figure 4.9). It can be observed that several bands presented a significant shift, which is consistent with the ligand bound to the Au NPs. In particular, it is possible to notice a small shift for the C-H stretching bands around $2850 - 2920 \text{ cm}^{-1}$ and for the peaks at 1084 cm^{-1} and 1459 cm^{-1} , corresponding to =C-H and -C-H bending modes, respectively. [124], [126], [215], [225], [226] These shifts indicate that oleylamine ligands are covalently linked to the Au NPs.

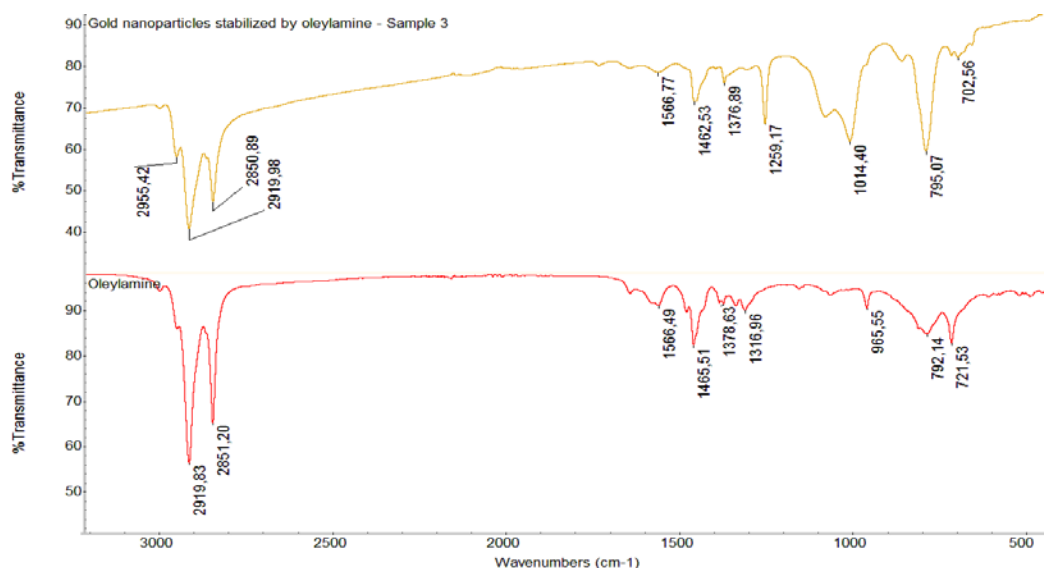


Figure 4.9. FT-IR spectra of Au NPs stabilized by oleylamine (yellow line) and free oleylamine (red line).

Sample 4. Synthesis of Au NPs stabilized by DT

To investigate the effect of NP surface functional groups on the fragmentation reaction, AuNPs capped with dodecanethiol (DT) were synthesized (sample 4). The UV-Vis spectrum in figure 4.10 shows the typical plasmonic peak around 530 nm. [132] The shape of the band is wide, meaning that the AuNPs are not well monodispersed. [133] The distribution size, obtained by statistical analysis of several TEM images of particles (about 550 NPs), shows that the mean diameter of the batch is $4,0 \pm 1,7$ nm (figure 4.11), confirming the higher polydispersity of the particles.

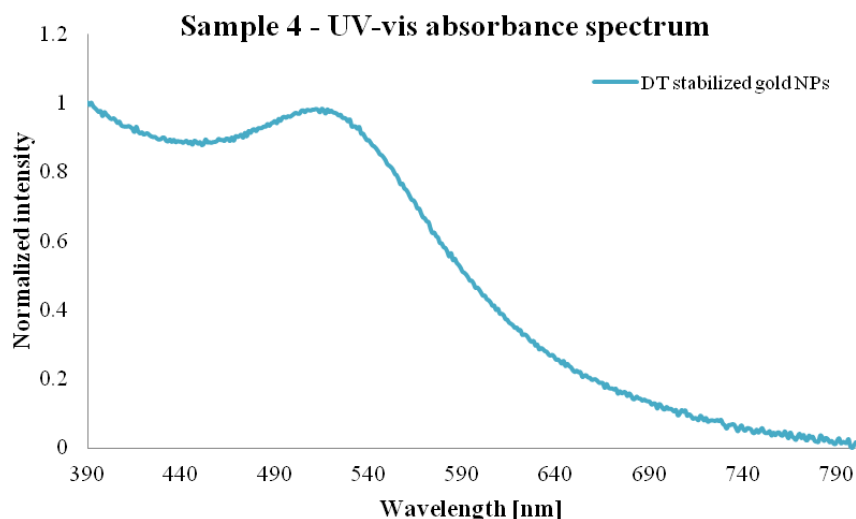
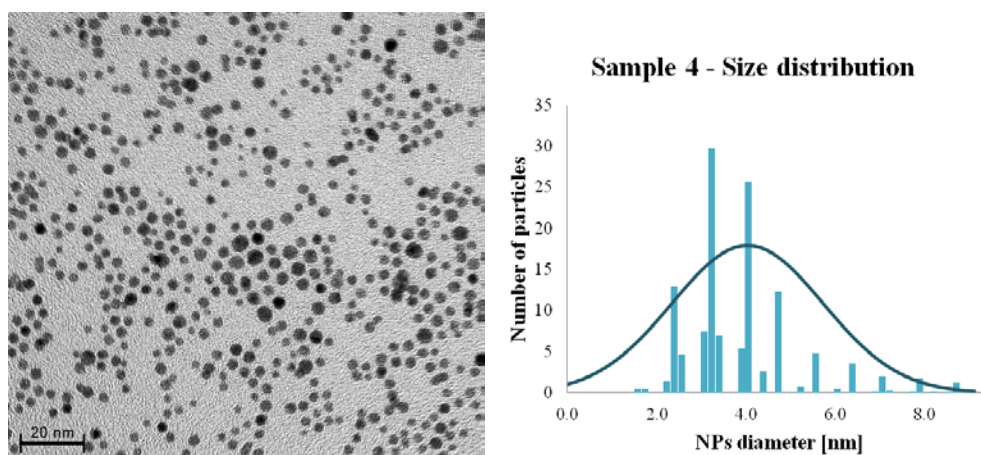


Figure 4.10. UV-Vis spectrum of gold nanoparticles stabilized by DT.



	Mean [nm]
Sample 4	$4,02 \pm 1,69$

Figure 4.11. TEM image and corresponding size distribution (obtained by size analysis of several TEM images of particles) of gold nanoparticles stabilized by DT.

FT-IR spectra of the DT functionalized NPs and free DT are shown in Figure 4.12. From the comparison of the peaks, it looks clear that the AuNPs shell is functionalized with DT. The distinctive signals are the three peaks between 2850 and 2950 cm^{-1} . [227] Also other peaks, at 720 cm^{-1} and 1465 cm^{-1} are distinctive respectively for C–H rocking and C–H bending in alkane molecules.

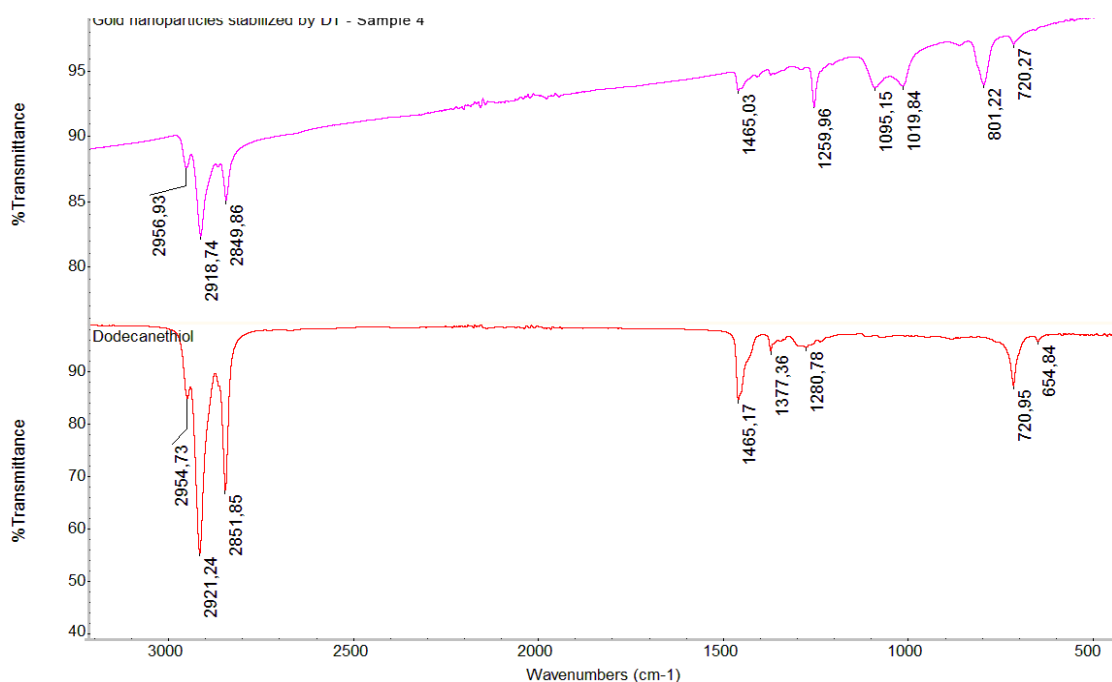


Figure 4.12. FT-IR spectra comparison between gold nanoparticle stabilized by DT and DT molecule.

Samples 5 to 9. Ligand-Exchange reactions.

This set of reactions was performed in order to understand the causes of the fragmentation and the kinetics of the substitution process.

Table 4-3. List of the amounts of reagents and solvents used for the synthesis. In the AuNPs column (a) indicates oleylamine-stabilized AuNPs whereas (b) indicates DT-stabilized AuNPs.

	AuNPs (mL)	Toluene (mL)	PFDT (μ L)	DT (μ L)	Time (h)
Sample 5	2 (a)	1,6	114	/	3
Sample 6	4 (a)	3,2	230	/	18
Sample 7	4 (a)	3,2	/	192	18
Sample 8	2 (a)	1,6	342	/	18
Sample 9	2 (b)	1,6	114	/	18

Since the further addition of PFDT to an old batch already presenting Au cluster did not showed any consequence (sample 1 and 2), other exchange reactions were performed from the beginning (and not on already fluorinated AuNPs) to investigate if fragmentation could happen during the replacement process (see Table 4-3).

Sample 5.

The first exchange reaction involved oleylamine stabilized AuNPs and PFDT. The experiment was stopped after 3 hours whereas the other samples were left for 18 hours. The UV-Vis spectrum of this sample reported in Figure 10 shows the typical plasmonic peak around 530 nm with a slight blue shift when compared with the spectrum of the starting NP dispersion stabilized with oleylamine. This could be caused by exchange of oleylamine with PFDT ligands that modify the interface environment. [228] Representative TEM images of this sample are in Figure 4.14 show that the NPs have an averaged diameter of $8,8 \pm 4,6$ nm and are more aggregated than the starting NPs. Moreover, it can be noticed that a population nanoclusters is present, indicating that fragmentation already occurred after 3h. Probably this population did not give rise to a visible peak around 350 nm in the UV-Vis spectra because of the small amount compared to the bigger ones (Figure 4.13).

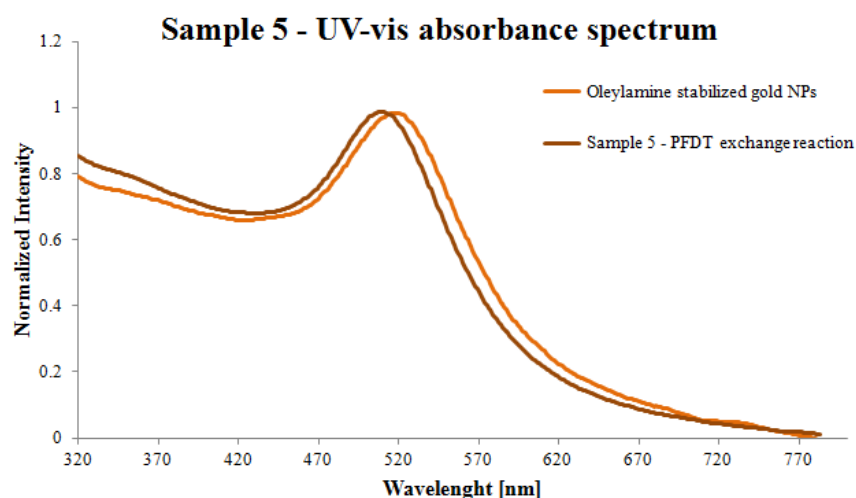
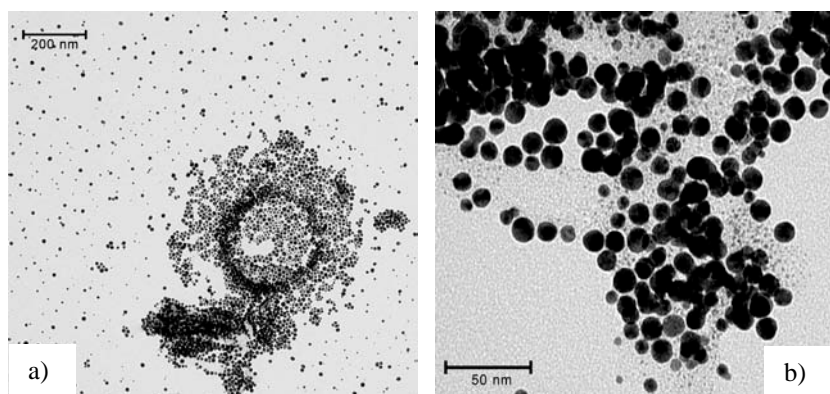
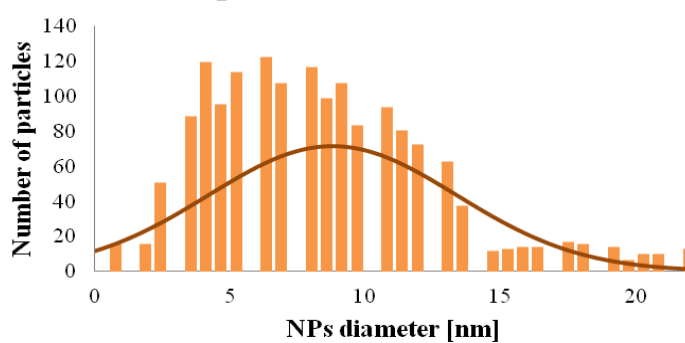


Figure 4.13. UV-Vis spectra of: original batch of oleylamine stabilized AuNPs (sample 3) and partially fluorinated AuNPs, obtained through 3h ligand exchange with PFDT (sample 5).



Sample 5 - Size distribution



	Mean [nm]
Sample 5	$8,76 \pm 4,6$

Figure 4.14. TEM images and corresponding size distribution (obtained by size analysis of several TEM images) of partially fluorinated AuNPs obtained through 3h ligand exchange with PFDT.

FT-IR characterization (figure 4.15) was crucial to understand the composition of the organic shell around the NPs. Some distinctive peaks typical of the C-F bonds were seen around 1230 cm^{-1} together with peaks attributable to oleylamine at $1330\text{-}1650\text{ cm}^{-1}$ due to -NH_2 bending mode, and the bands around 2920 cm^{-1} and 2850 cm^{-1} due to methyl stretching. This is a clear indication of the presence of both ligands in the NPs shell. [126]

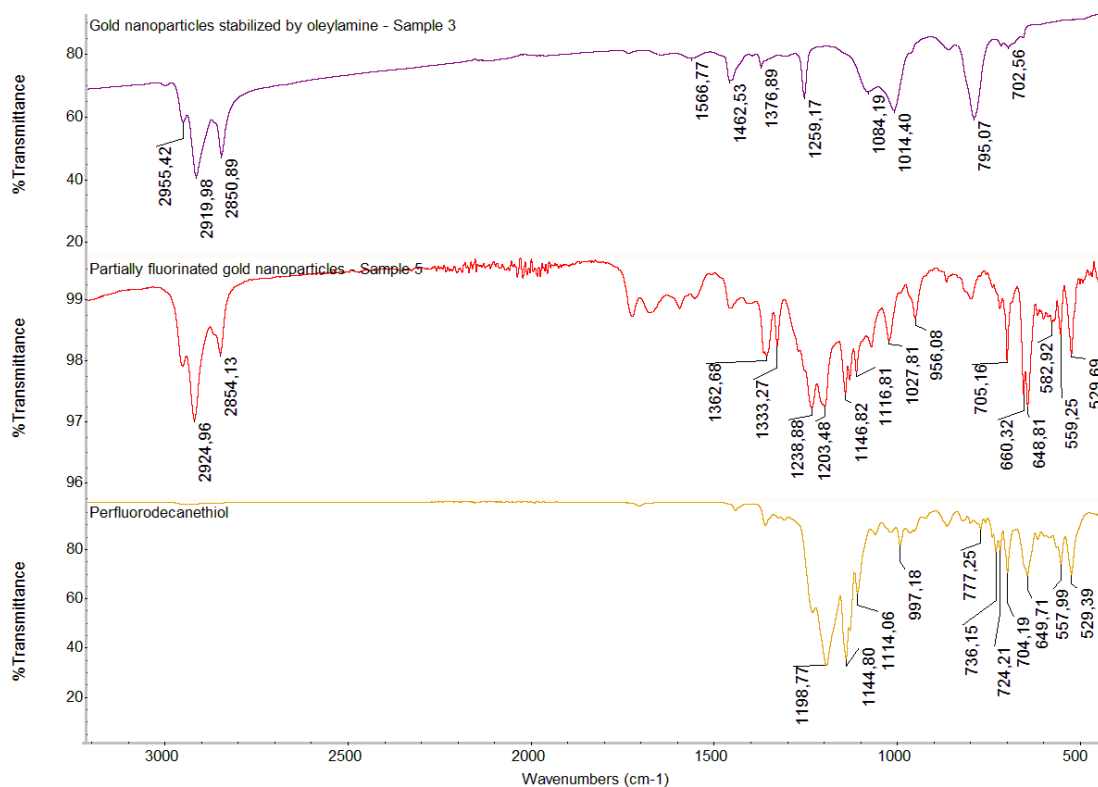


Figure 4.15. FT-IR spectra comparison between the original batch of oleylamine stabilized AuNPs (upper spectrum), partially fluorinated AuNPs obtained through 3h ligand exchange with PFDT (in the middle) and PFDT molecule (bottom spectrum).

These analyses showed that after 3 hours there was only partial replacement of oleylamine and only a small amount of NPs were fragmented, bringing to a batch composed mostly of big NPs ($8,8 \pm 4,6$ nm).

Sample 6.

The second exchange reaction was performed increasing the amount of PFDT, with a AuNPs/PFDT ratio of 1:200 instead than 1:100, to understand how the amount of PFDT is linked to the fragmentation. During the purification process of this experiment a portion of the supernatant was collected and analysed to see if the fragmented NPs remained in the supernatant during centrifugation. DLS analysis of this phase showed the presence of large aggregates with an average size of 110 nm whereas UV-Vis analysis showed a small plasmonic peak around 530 nm, consistent with the presence of a limited amount of the NPs. Finally, FT-IR analysis showed both the presence of peaks attributable to oleylamine

and to PFDT. We can infer that the supernatant analysed contained both a very limited amount of nanoparticles, probably still capped by oleylamine, and a mixture of free ligands. No evidence of nanoclusters was observed.

The purified sample was then thoroughly characterized. As can be seen from the comparison between the FT-IR spectra of sample 6 and that of PFDT, it is clear that the ligand-exchange was indeed successful (Figure 4.16). The peaks 1236 (C-F bending), 1144, 1114, 749 and 529 cm^{-1} proper of PFDT vibrating modes can also be tracked in the spectrum of exchanged NPs. [37], [126]

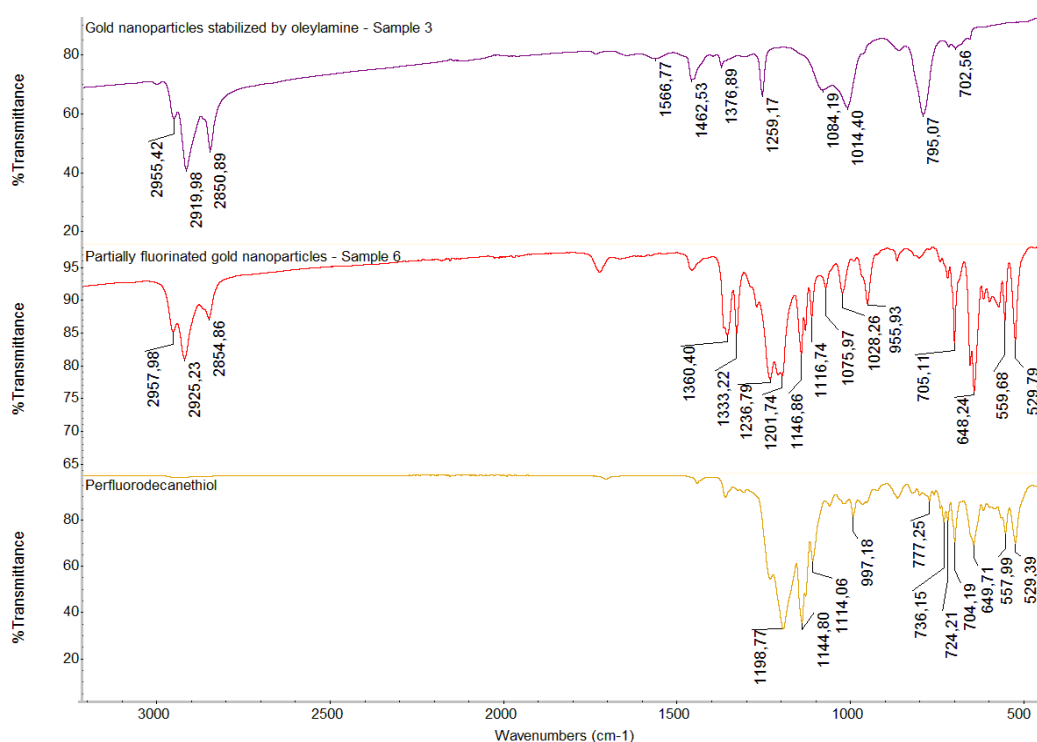


Figure 4.16. FT-IR spectra comparison between the original batch of oleylamine stabilized AuNPs (upper spectrum), partially fluorinated AuNPs obtained through 18h ligand exchange with PFDT (in the middle) and PFDT molecule (bottom spectrum).

The UV-Vis spectrum in Figure 4.17 shows the usual plasmonic peak at 530 nm typical of AuNPs, just slightly blue shifted when compared to the starting NPs spectrum. The absence of the peak at 350 nm suggests that no fragmentation occurred.

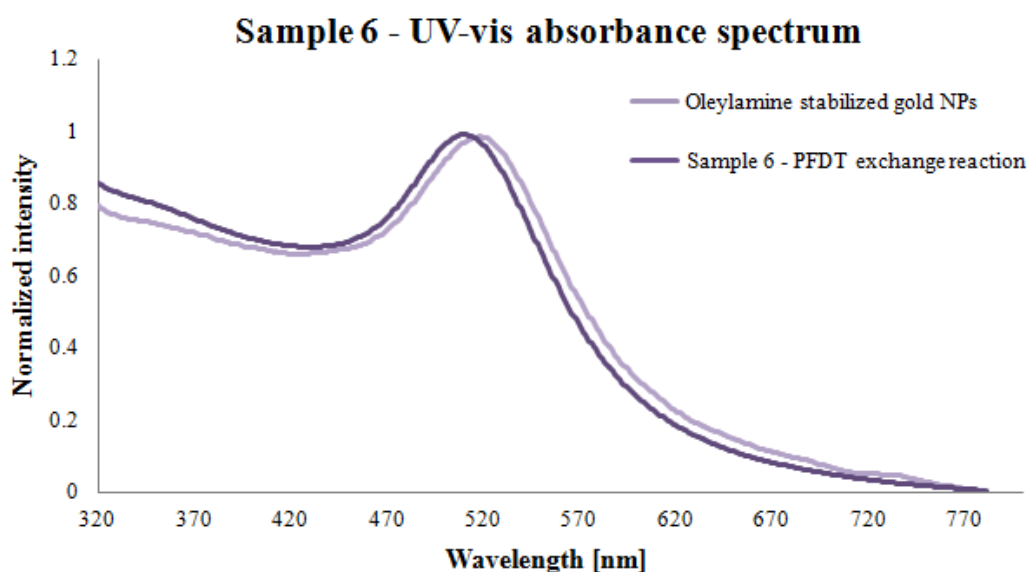


Figure 4.17. UV-Vis spectra of: original batch of oleylamine stabilized AuNPs (sample 3) compared to the partially fluorinated AuNPs obtained through 18h ligand exchange with PFDT (sample 6).

Indeed, a representative TEM image reported in Figure 4.18 shows that the batch contains very monodispersed NPs of averaged diameter of $9,1 \pm 3,4$ nm. No fragmentation was observed. Comparing the averaged size before and after the exchange reaction, the small shift observed in the UV-Vis peak is caused by substitution with PFDT ligands. [226], [228], [229] This is an evidence of the stability of the big AuNPs that do not produce any kind of fragmentation also in presence of PFDT and oleylamine for long time of reaction. Even if the reaction time is proved to be a fundamental parameter for the substitution process, it seemed not to influence the fragmentation of the NPs.

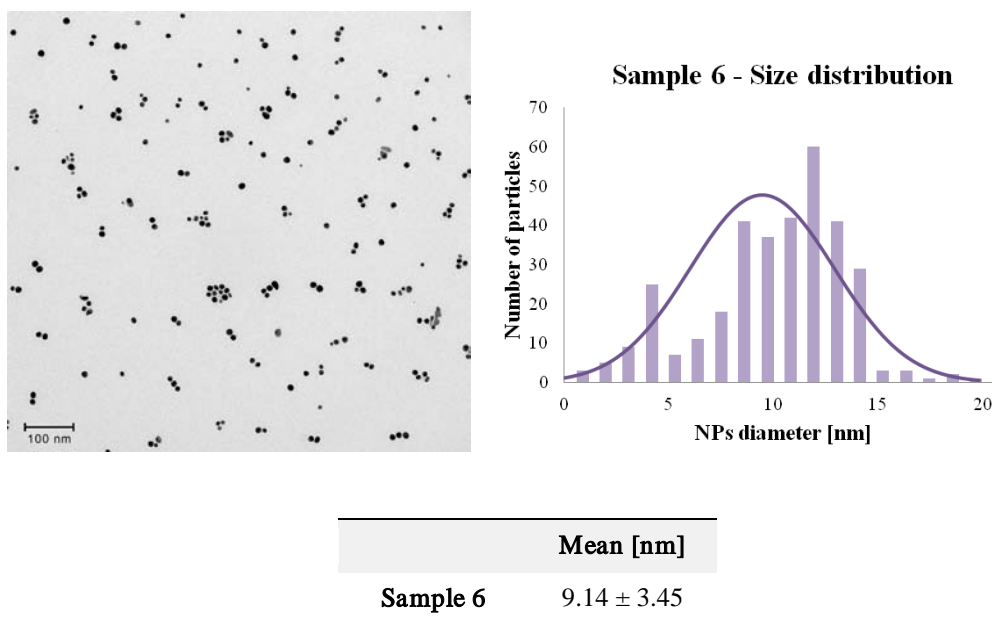


Figure 4.18. TEM images and corresponding size distribution (obtained by size analysis of several TEM images) of partially fluorinated AuNPs obtained through 18h ligand exchange with PFDT.

Sample 7.

This reaction was performed to study the link between the electronic nature of the exchange ligand, dodecanethiol (DT) was used to exchange oleylamine stabilized AuNPs. The purpose was to verify if also an hydrogenated ligand could induce fragmentation on the oleylamine stabilized AuNPs.

The solution obtained after 18 hours of reaction was pale violet coloured and showed a strong tendency to attach on the walls and bottom of the container. DLS correlation function was not well-fit by Cumulant analysis (Figure 4.19) and CONTIN size distribution is characterized by a broad peak centred at about 110-150 nm, as can be seen from the size distribution histogram reported in Figure 4.20. UV-Vis spectrum (see Figure 4.21) performed on the NP stock solution, showed a broad low absorption peak confirming DLS data.

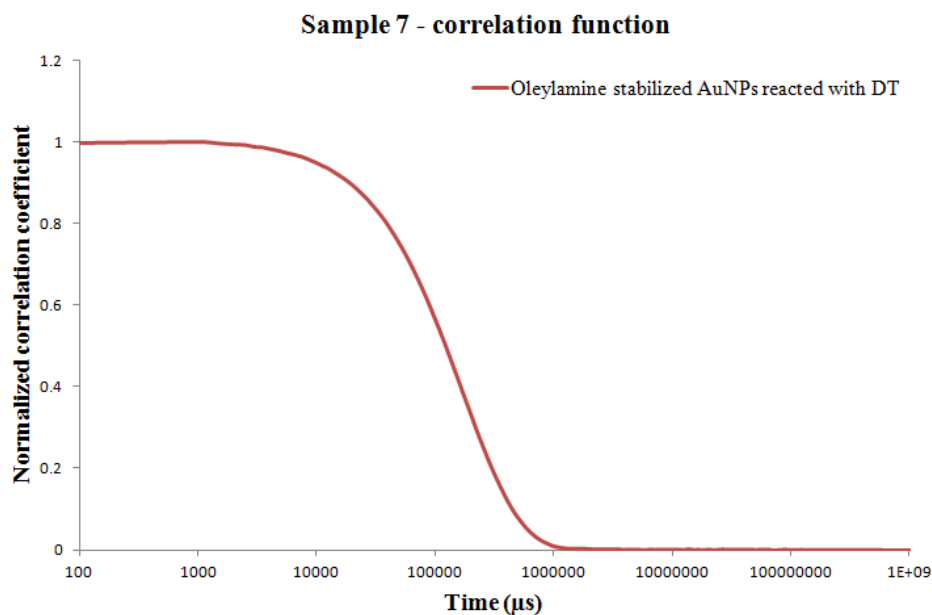
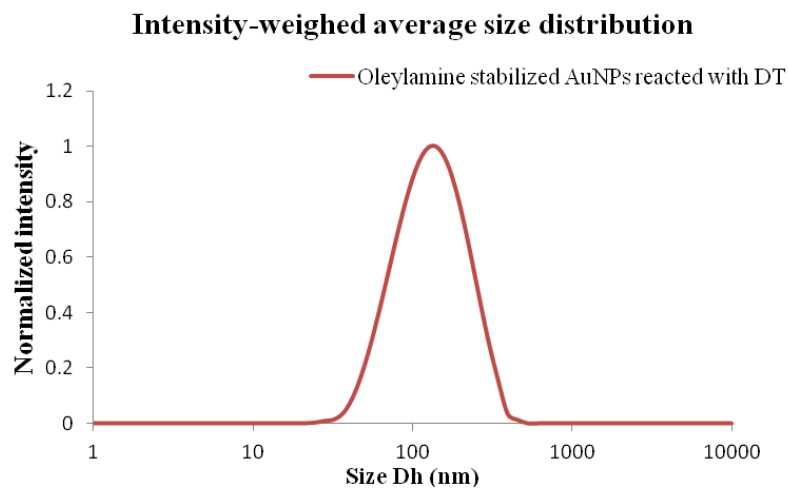


Figure 4.19. Correlation function (average of the three DLS runs) of DT exchanged oleylamine-stabilized AuNPs.



Z-average [nm]	PDI	Contn [nm]
115.3 ± 12.4	0.54 ± 0.13	119.9 ± 18.2

Figure 4.20. Intensity-weighted size distribution obtained by CONTIN (average of the three DLS runs) of DT exchanged oleylamine-stabilized AuNPs.

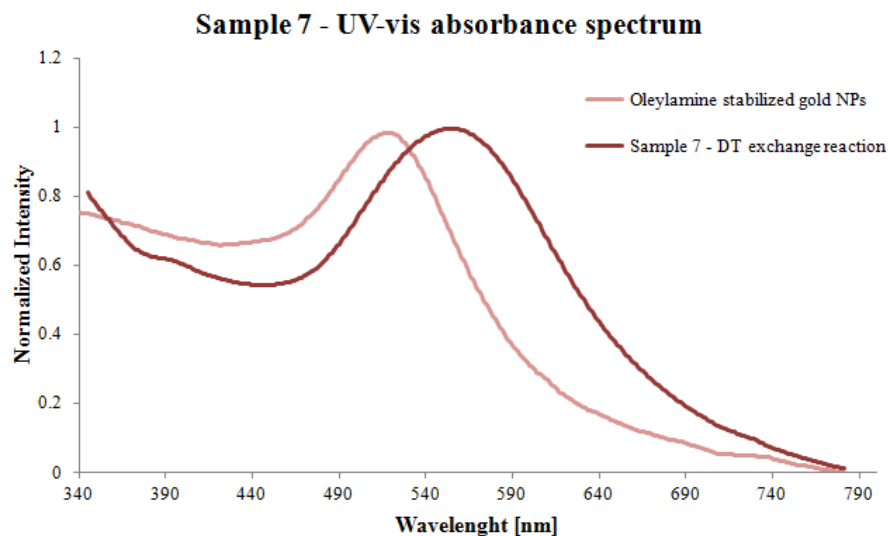
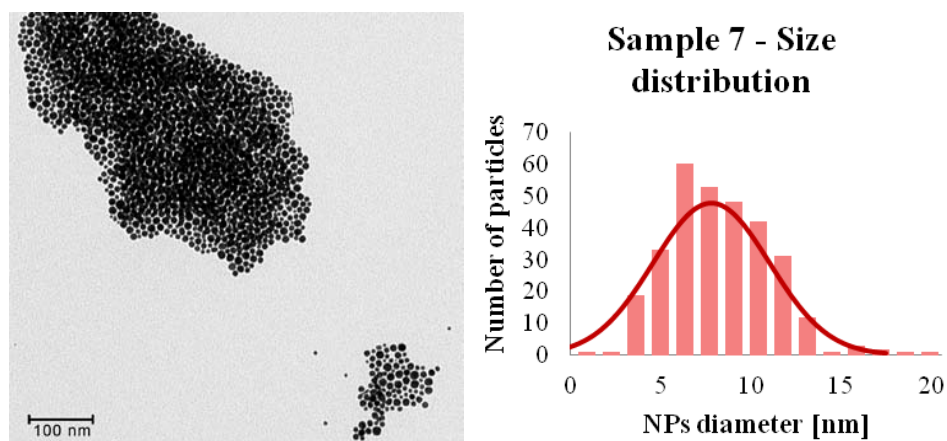


Figure 4.21. UV-Vis spectra of: original batch of oleylamine stabilized AuNPs (sample 3) compared to the partially DT substituted AuNPs obtained through 18h ligand exchange with DT (sample 7).

A representative TEM image reported in Figure 4.22 confirms DLS and UV-Vis results showing aggregation upon drying contrarily to the PFDT exchanged samples. The unit NPs forming these big aggregates have an averaged diameters of 7.9 ± 3.2 nm. FT-IR analysis is necessary to understand the nature of the ligands present on the AuNPs surface.



	Mean [nm]
Sample 7	$7,9 \pm 3,2$

Figure 4.22. TEM images and corresponding size distribution (obtained by size analysis of several TEM images) of DT exchanged oleylamine-stabilized AuNPs.

The FT-IR spectrum reported in Figure 4.23 shows that the exchange reaction did not work. The spectrum of the substituted AuNPs looks almost equal to the spectrum of the NPs before the reaction. This is a clear evidence of the failure of replacement process between DT and oleylamine even if a small amount of DT shall be present onto the NPs surface to promote aggregation as visible in the previous TEM images (figure 18).

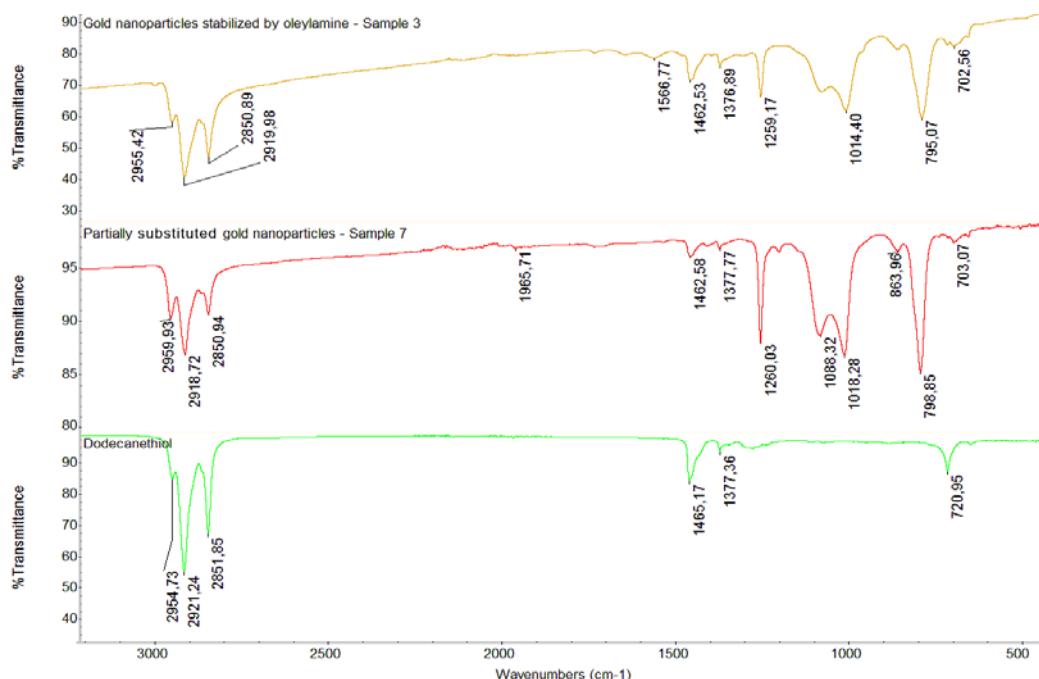


Figure 4.23. FT-IR spectra comparison between the original batch of oleylamine stabilized AuNPs (upper spectrum), DT substituted AuNPs obtained through 18h ligand exchange with DT (in the middle) and DT molecule (bottom spectrum).

Sample 8.

The exchange reaction was repeated with the same procedure but involving a triple amount of PFDT than the one used in samples 5 and 6.

The UV-Vis spectra comparison reported in Figure 4.24 shows that a higher amount of PFDT did not produce a drastic change in the electronic properties of the NPs. The broadness of the band increased with respect to the starting sample, indicating a higher polydispersity. Unfortunately, TEM images were not obtained for this sample. The lack of the peak at 350 nm suggests that fragmentation did not occur although.

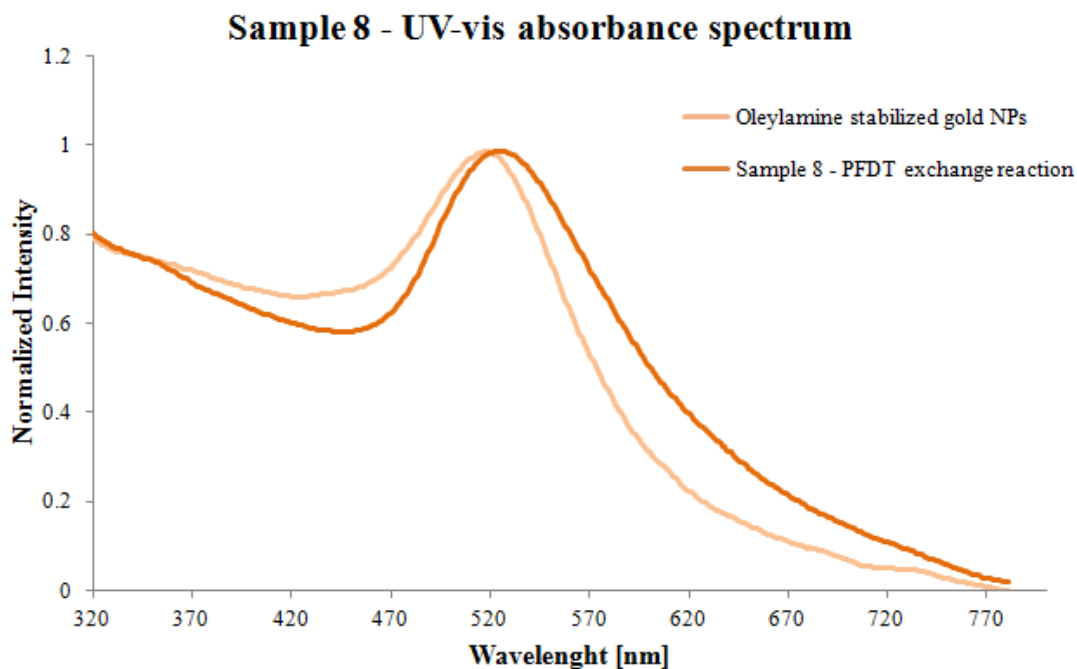


Figure 4.24. UV-Vis spectra of: original batch of oleylamine stabilized AuNPs (sample 3) compared to the partially fluorinated AuNPs obtained through 18h ligand exchange with triple amount of PFDT (sample 8).

As can be seen from FT-IR spectra reported in Figure 4.25, PFDT substituted AuNPs did not show any distinctive peak of oleylamine, whereas it is possible to observe an high resemblance with the ligand spectrum. Thus, the higher concentration of PFDT during the exchange process induced a higher level of fluorination of the NP surface, but. it did not promote fragmentation.

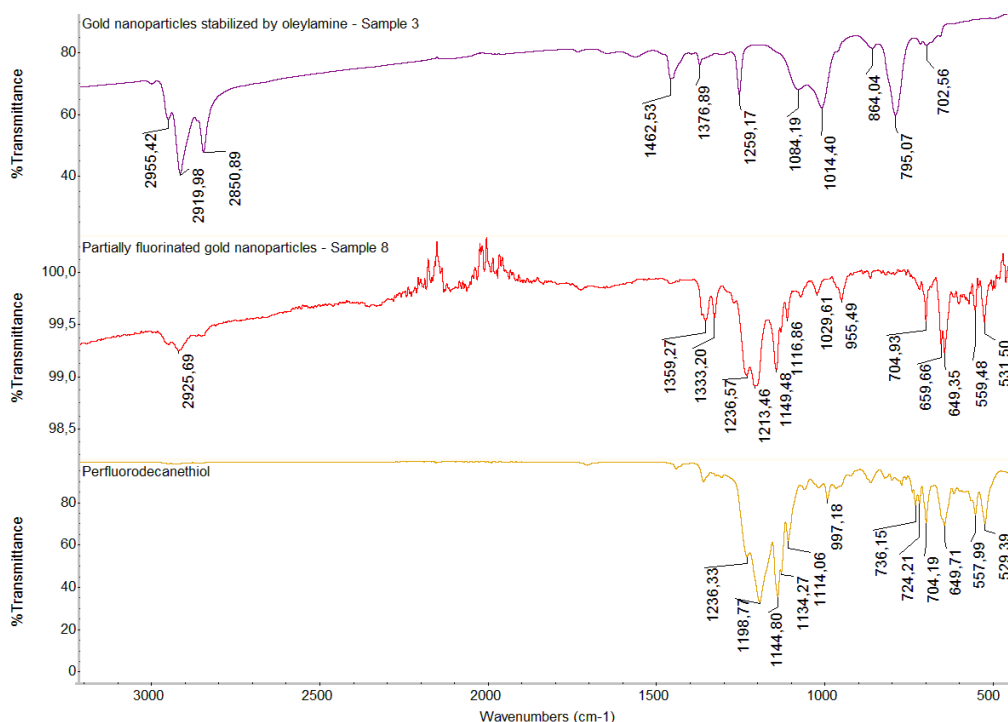


Figure 4.25. FT-IR spectra comparison between the original batch of oleylamine stabilized AuNPs (upper spectrum), partially fluorinated AuNPs obtained through 18h ligand exchange with triple amount of PFDT (in the middle) and PFDT molecule (bottom spectrum).

Sample 9.

This experiment was performed to ascertain whether PFDT could promote fragmentation of NPs functionalized by dodecanethiol, which should form a stronger bond with gold than oleylamine. [37]

The batch, after the purification procedure, appeared deep violet coloured. The UV-Vis analysis results are reported in Figure 4.26. The typical plasmonic peak is present but it is slightly shifted towards shorter wavelengths but the width of the peak is conserved. [132] This could imply no change in the size distribution of the sample, but a different shell composition. [37], [115], [230]

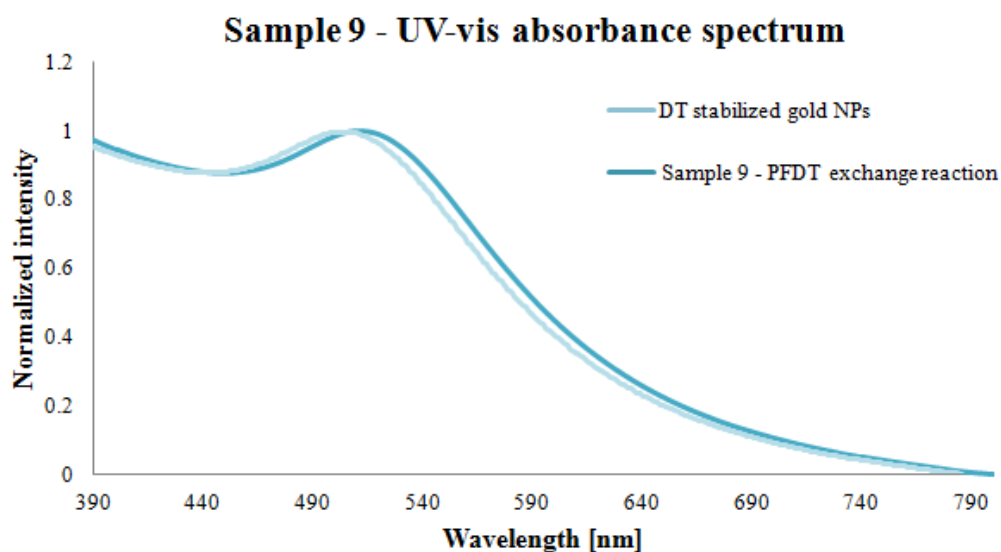
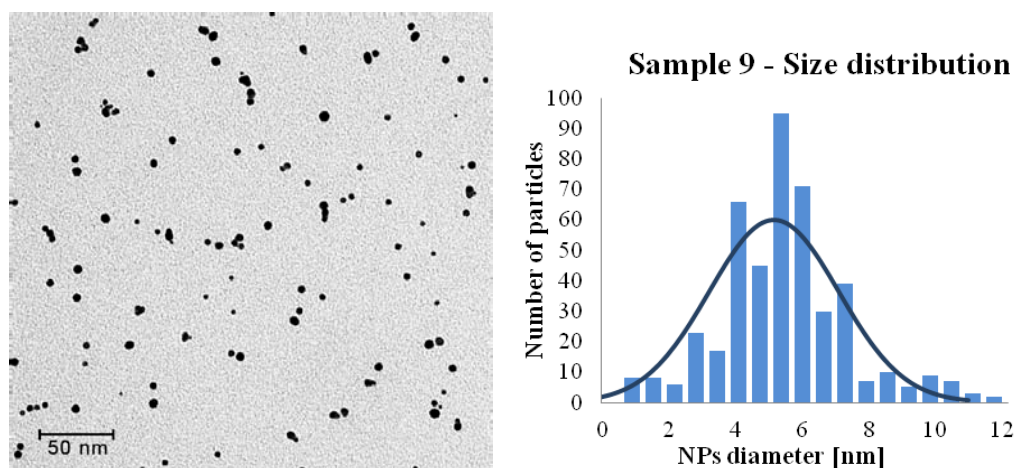


Figure 4.26. UV-Vis spectra of: original batch of DT stabilized AuNPs (sample 4) compared to the partially fluorinated AuNPs obtained through 18h ligand exchange with PFDT (sample 9).

A representative TEM image is reported in Figure 4.27 and shows that the NPs are well dispersed. The averaged size of the exchanged NPs is $5,1 \pm 1,9$ nm. The images did not show aggregation between the NPs.



	Mean [nm]
Sample 9	$5,1 \pm 1,9$

Figure 4.27. TEM images and corresponding size distribution (obtained by size analysis of several TEM images) of partially fluorinated AuNPs obtained through 18h ligand exchange with PFDT.

The FT-IR characterization of sample 9 is reported in Figure 4.28 and the comparison between the spectrum before and after replacement process indicates that the exchange occurred. As in the previous 18 hours exchange reactions, where PFDT substituted almost totally oleylamine ligands, also in this case FTIR spectrum is dominated by signals of PFDT. Thus, starting from DT NPs in this experimental condition completely fluorinated NPs were obtained without fragmentation.

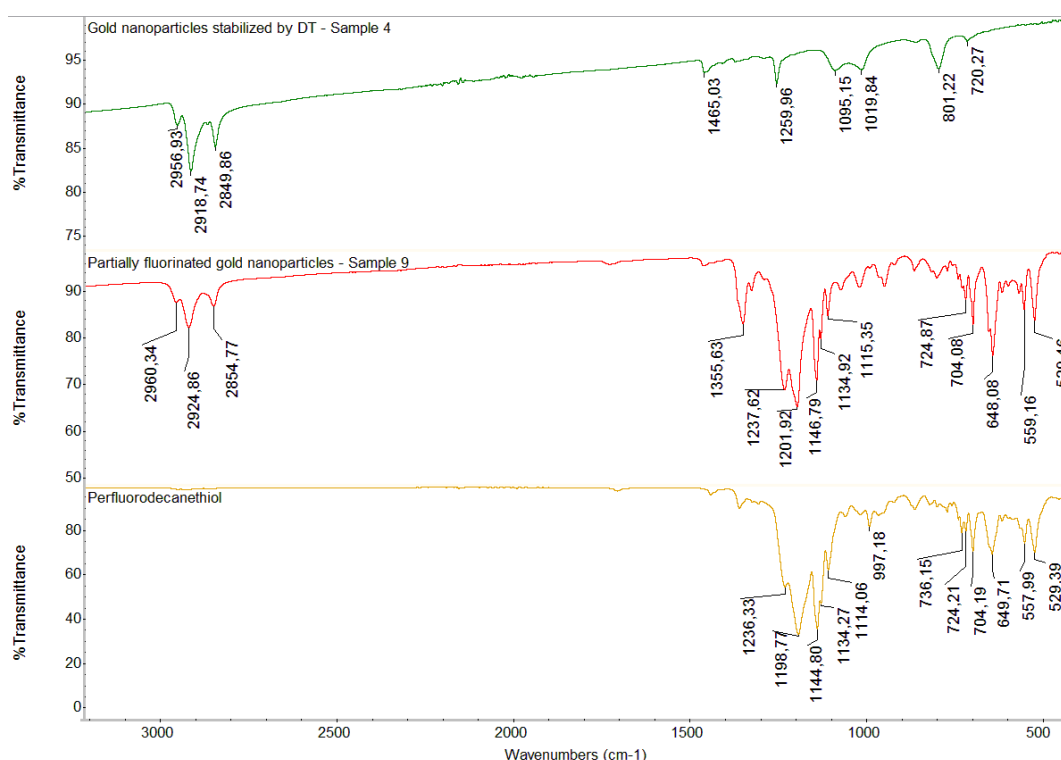


Figure 4.28. FT-IR spectra comparison between the original batch of DT stabilized AuNPs (upper spectrum), totally fluorinated AuNPs obtained through 18h ligand exchange with PFDT (in the middle) and PFDT molecule (bottom spectrum).

The exchange reaction experiments reported until here were successful in the replacement process on the NP surface from hydrogenated ligands to fluorinated ones. In some cases, fragmentation of the starting NPs occurred to form small Au nanoclusters of various sizes. Since the main objective of the project was the synthesis of fluorinated AuNPs as theranostic tool, new ways to obtain totally fluorinated AuNPs were investigated trying to form and make the NPs to grow in the presence of the fluorinated ligands.

Sample 10 to 15.

The last set of experiments was performed to study the behaviour of ligands, reagents and solvents involved in the previous reactions. Since the fragmentation of oleylamine stabilized Au NPs has not been completely understood, causes were searched in possible interactions between the reactants involved. All the tested reactions were characterized via UV-Vis and FT-IR to understand if any sort of aggregates were formed during the reaction.

The spectra are not shown since none of them reported atypical signals or any distinctive band. All the UV-Vis spectra were completely flat, meaning that the absorbance of the solutions, corrected with the solvents baseline, did not show any modification compared to the initial state of the reagents. On the other hand FT-IR spectra did not show appearance of peaks that were not attributable to the reagents involved in the reactions. The processes between Au salt and PFDT (sample 10), DT (sample 11) and oleylamine (sample 12) showed that their interaction did not give rise to any kind of products. The UV-Vis spectra proved that these solutions did not absorb in the UV-Vis range, demonstrating that the unusual band at 350 nm in the UV-Vis spectra was not produced by these molecules or by new adducts formed by their reaction. Furthermore, the process between the three ligands at the same time, with (sample 13) and without (sample 14) HAuCl_4 , did not produce any result different from those expected. This means that the molecules involved in the exchange reactions did not interact and did not give rise to any new adduct that. The importance of these reactions is fundamental for the investigation and the understanding of the processes studied.

The last experiment (sample 15) was performed to verify the hypothesis that unreacted Au salt, not completely removed during the work up process, was reduced and then trapped by oleylamine or PFDT ligands giving rise to very small aggregates. The procedure to verify the presence of Au salt left, involved the addition of an aqueous solution of NaBH_4 , TOAB as phase transfer agent to make interact the reducing agent and AuNPs stabilized by oleylamine in toluene. If still present, the excess Au salt should be reduced by NaBH_4 and a new population of fragmented NPs should be visible, in the

aqueous phase as metallic gold or in the organic one as oleylamine capped NPs. Both the final aqueous and organic phases were characterized but none of them showed a peculiar band around 350 nm. Probably no gold salt was present on the NPs surface and so the reactants did not give rise to chemical products. This last experiment demonstrates that the hypothesis of the origin of the 900 Å - 1 nm AuNPs should be treated as the result of a fragmentation process.

Sample 16. Synthesis of totally fluorinated gold nanoparticles

This reaction was performed to obtain totally fluorinated Au NPs with a nucleation reaction inspired to the direct Brust synthesis method. [121][119] The UV-Vis spectrum of sample 16, reported in Figure 4.29, represents the typical shape of very small AuNPs [132], even if on the short-wavelength region the absorbance values are higher. The peak around 530 nm is quite wide, indicating that the AuNPs are not well polydispersed. [132]

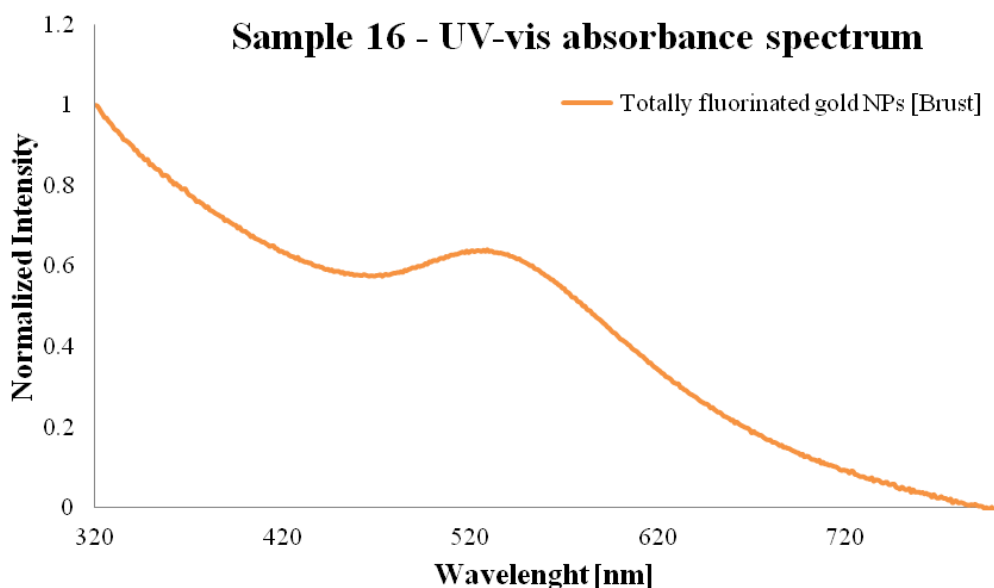
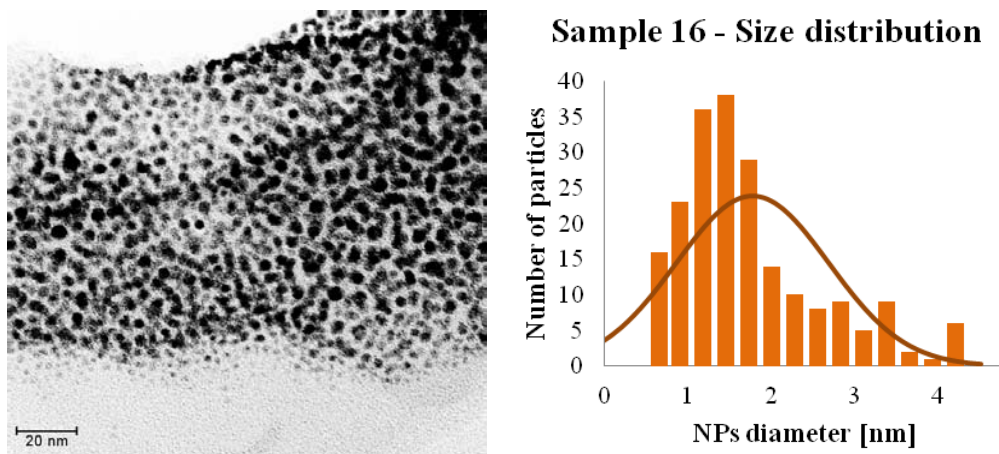


Figure 4.29. UV-Vis spectra of totally fluorinated AuNPs obtained via direct Brust method.



	Mean [nm]
Sample 16	$1,8 \pm 0,9$

Figure 4.30. TEM images and corresponding size distribution (obtained by size analysis of several TEM images) of totally fluorinated AuNPs obtained via direct Brust method.

TEM analysis was performed and brought to a size distribution with an averaged diameter size of $1,78 \pm 0,92$ nm (the images in Figure 4.30 showed a reduced resolution). FT-IR characterization confirmed the presence of a fluorinated shell, as it can be seen from the comparison between the two spectra in Figure 4.31, corresponding to the totally fluorinated AuNPs, and the PFDT molecules, respectively. All the peaks typical of the C-F vibration modes (1198 , 1114 , 704 and 557 cm^{-1} [37]) are present also in the AuNPs batch.

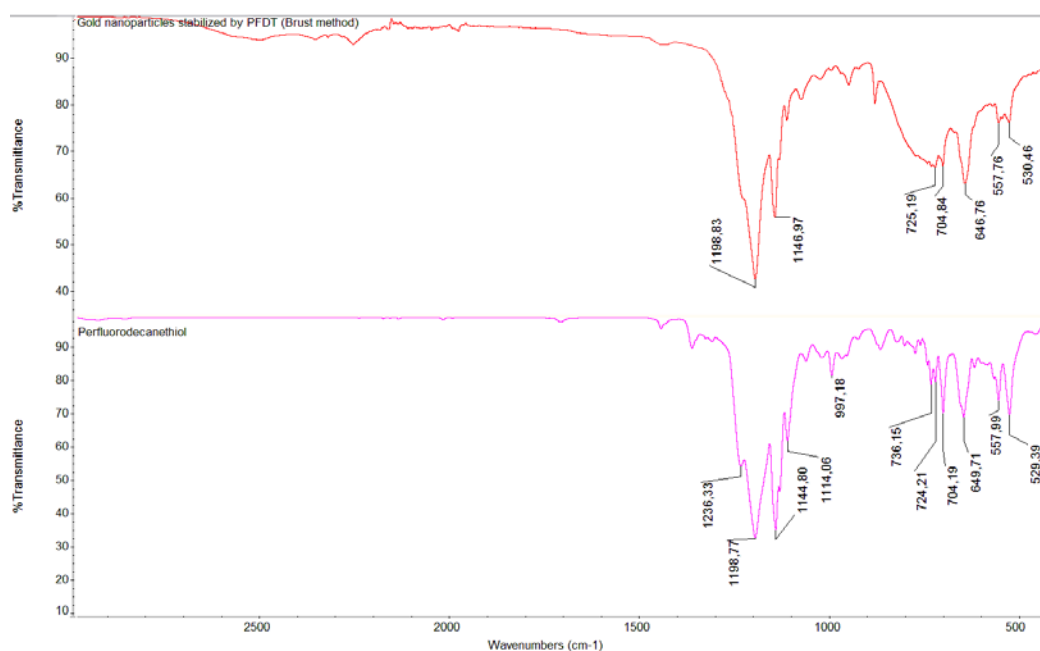


Figure 4.31. FT-IR spectra comparison between totally fluorinated AuNPs obtained via direct Brust method (upper spectrum) and PFDT molecule (lower spectrum).

Sample 17. Coating of totally fluorinated gold nanoparticles

As described in the previous chapter on the development of HPB-stabilized SPIONS, the first step to allow the application of NPs as theranostic tools is the ability to dissolve them in aqueous solvents. Since totally fluorinated AuNPs can be dissolved just in fluorinated solvents, the only way to transfer them in aqueous solvent is to coat them with water-soluble molecules. Since HPBII has been already used for coating SPIONS, it was chosen to test this protein on the fluorinated NPs. This experiment was the last step of this project and can be seen as starting point for future experiments. This process was tried only once and DLS was used to test the success of the NP transfer into the aqueous solution. The results reported in figure 4.32 and 4.33 suggest that the protocol produces supraparticles with an averaged hydrodynamic diameter of 127.1 ± 1.1 nm. The 4 nm totally fluorinated AuNPs are probably agglomerated and coated by HPBII to form supraparticle. These supraparticles are stable and well dissolved in water. Further characterization is necessary to determine the structure, composition, properties of this sample but it seems promising for further use as theranostic drug delivery system.

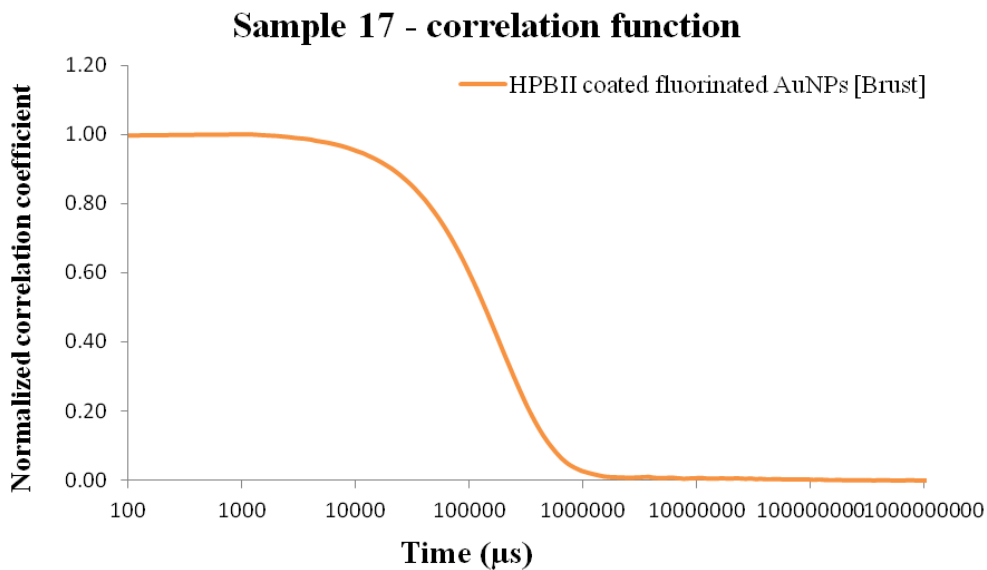
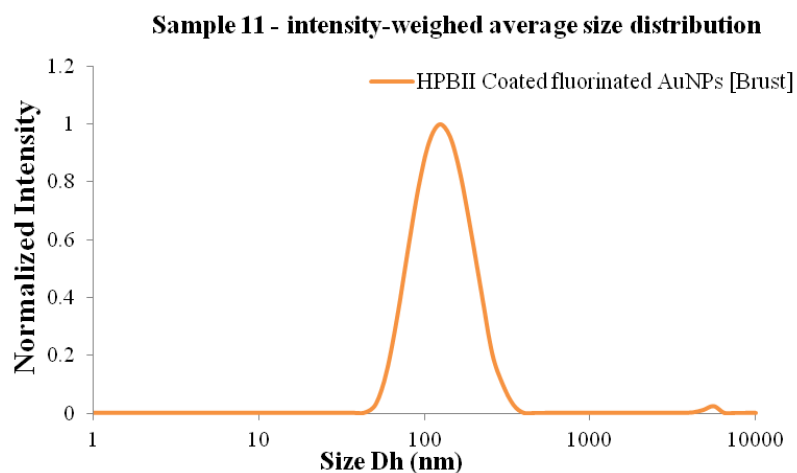


Figure 4.32. Correlation function (average of the three DLS runs) of totally fluorinated AuNPs coated with HPBII.



Z-average [nm]	PDI	Contn [nm]	Attenuator
127,1 ± 1,08	0,226 ± 0,041	136,2 ± 10,79	7

Figure 4.33. Intensity-weighted size distribution obtained by CONTIN (average of the three DLS runs) of totally fluorinated AuNPs coated with HPBII and DLS values table.

4.4. Conclusions

During this work, new ways to synthesize partially or totally fluorinated gold NPs were explored. To obtain partially fluorinated AuNPs the exchange reaction method was chosen starting from batches of oleylamine and DT stabilized AuNPs. Oleylamine stabilized AuNPs were synthesized with a bigger diameter ($12,7 \pm 2,4$ nm) compared to previous experiments to study the influence of the NPs size on the exchange process. The mean diameter of the obtained DT stabilized AuNPs was $4,0 \pm 1,7$ nm.

The replacement processes showed that it was possible to obtain partially or totally fluorinated AuNPs with a good monodispersity. The principal aim of this work was to understand the causes that brought to the formation of a fragmented NPs upon treatment with PFDT ligands. Apparently, as reported in bibliography, the 350 nm peak in UV-Vis spectrum was caused by electronic transitions of a $1,4 \pm 0,6$ nm family of NPs due to the split band structure caused by the sub nanometer dimension. [205], [207]–[212] Many different experiments were performed changing two main parameters: reaction time and ligands amount. Different reaction times could give also information about the kinetics of the substitution, whereas different concentrations of ligand could influence both final composition and fragmentation phenomena.

The first substitution process (sample 5), after 3 hours of reaction, produced partially fluorinated AuNPs, with an average dimension of $8,8 \pm 4,6$ nm. From TEM images it is clear that a very low concentration of clusters is present. Sample 6 was produced with the same protocol of the previous one, but the reaction time was extended to 18 hours. Even if there was no trace of Au nanoclusters, the obtained AuNPs ($9,1 \pm 3,4$ nm) were totally fluorinated as can be seen from FT-IR spectrum. Also DT exchange reaction (sample 7) was performed on the same oleylamine NPs batch, to understand if also other kind of ligands could promote fragmentation of bigger particles. No trace of clusters was found in DLS analysis and TEM images. Contrarily to what expected, AuNPs, with an average of $7,9 \pm 3,2$ nm, resulted to be highly aggregated and deposited onto the glass walls. This could have been caused by the displacement of the oleylamine molecules that gave time to the AuNPs to aggregate.

In order to understand if the lack of fragmentation in the previous PFDT exchanged batches was due to the too low concentration of ligands, a new test (sample 8) was done involving triple amount of PFDT compared to sample 5 and 6. No fragmentation was observed even in this case, therefore we have to deduce that the increase of PFDT concentration prevents the fragmentation process. In addition, sample 9 showed that also under other experimental condition PFDT cannot cause the fragmentation of bigger NPs. The FT-IR spectra show that in DT stabilized AuNPs exchanged successfully with PFDT, but the TEM images and statistical analysis reported that only one family of $5,15 \pm 1,94$ nm NPs was present without traces of subnanometer aggregates. Samples 10 - 15 were performed in order to understand if the reagents and solvents involved could form small aggregates. Thanks to these experiments it was showed that the nanoclusters population was not produced by the aggregation of these reactants.

The last two experiments (samples 16 and 17) were performed in order to synthesize totally fluorinated gold NPs via Brust direct method and to solubilize them in water. The fluorinated gold NPs were obtained with a small size ($1,78 \pm 0,92$ nm) and a good monodispersion. These NPs seem to be good in terms of stability and reproducibility. Also the coating with HPBII seemed to be successful, as the final coated NPs were soluble in water. These new particles were bigger sized since the protein capped aggregates of the 4 nm fluorinated AuNPs.

Even if it was not possible to give an explanation about the conditions that bring ligands to fragment bigger NPs, this chapter showed that is possible to obtain partially or totally fluorinated AuNPs and to coat them in order to make them soluble in physiologic-like solvents for future application in medicine.

Chapter 5 - Nanoparticles interaction with cell membranes models

5.1. Introduction

The experiments performed during this master thesis project aimed at the synthesis of functionalized NPs as theranostic tools in medicine, but NPs can be involved in many other branches of medicine, such as biosensing, cell therapy, gene therapy, etc. [1]–[3] Despite the great number of applications and potential uses of gold NPs as medical theranostics, many efforts are devoted on the potential NP toxicity that must be assessed before any *in vivo* applications. In fact, when interacting with living organisms, the first part of the cell met by the NPs is the membrane (Figure 5.1). One of the main challenges of using NPs in drug delivery and diagnostics, is to produce systems with an optimum balance between an efficient crossing of the biological membrane, and the possibility to destabilize it, with consequent onset of toxic effects.

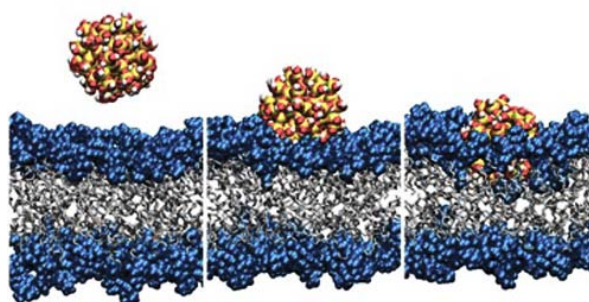


Figure 5.1. Schematic interaction of a cell membrane and one NPs [231].

Previous works in this field showed that NPs can reveal cytotoxic effects depending on their concentration, size, surface modification, and charge. [232]–[235] In particular, the formation of nanoscale holes was observed in living cell membranes, where the degree of membrane disruption was dependent on the lipid bilayer phase state. [236] Due to these

many parameters, it is difficult to understand which are those that mostly influence the toxicity threshold of NPs. [232], [237]–[240] Since the application of NPs inside human body for medicine is a quite new and still growing field, there is a lack of knowledge concerning (i) the precise molecular mechanisms regulating membrane/NPs interaction and (ii) how the interaction depends on the surface characteristics of cell membranes and NPs, (iii) how this interaction can lead to a potential cell membrane damage, cell malfunction and death. [241], [242] A recent study showed that relevant information on the interaction between model membranes and NPs can be obtained with neutron reflectometry (NR) [165], This method extends the possibility of obtaining crucial information obtained with other techniques such AFM, confocal microscopy or Brewster angle microscopy. [17], [18] Indeed, neutron scattering techniques have several advantages as a tool to study biomimetic membranes. Neutrons are not charged particles and have a weak interaction with matter allowing the study of soft matter systems with virtually no damage or alteration to the chemical behavior of the system under investigation. The weak interaction makes them strongly penetrating and this feature is ideal for buried interfaces. The use of isotopic substitution allows the contrast variation of different regions, which is ideal to highlight the structural features of each component. [165], [243] Since neutrons produced in scattering facilities have wavelengths comparable with interatomic distances, between 2 and 40 Å (cold neutrons), they are a useful tool in the characterization of materials down to the atomic scale. They are capable to provide structural information in a wide range of length scales from few Angstrom to the micrometer distances. [244] NR experiments reported in the study of [15] provides for example a proof of concept methodology to obtain insight about the fate of a model lipid membrane in the presence of anionic and cationic NPs, such as the stability of the membrane, incorporation of NPs in the membrane (in terms of average location and amount). This study provides information that might help in the understanding of the effects caused by NPs application representing an initial risk assessment and contributing to the future synthesis of new tailored NPs with higher biocompatibility.

During my thesis project there was the chance to spend three months for a stage at the Institut Laue-Langevin (ILL) in Grenoble, France, one of the world leading neutron scattering facilities accessible to external users through a ranking procedure of research

proposals. The ILL currently provides one of the most intense neutron sources with the most intense continuous neutron flux in the world in the moderator region: 1.5×10^{15} neutrons per second per cm^2 , with a thermal power of 58.3 MW.

The main objective of my stage was to analyze NR data previously taken to elucidate the role of the surface charge of model lipid membranes on the interaction with cationic NPs. These data were taken in a previous experiment performed by Dr. Marco Maccarini (Université Grenoble Alpes, Laboratoire TIMC-IMAG) and Dr. Giovanna Fragneto (Head of the Soft Matter Science and Support group at ILL). This experiment is a research study following a previous investigation described in reference [15] where differently functionalized NPs (with anionic and cationic groups) were applied on model membrane systems composed by a floating lipid bilayer deposited on another lipid bilayer adsorbed directly on Si substrate.

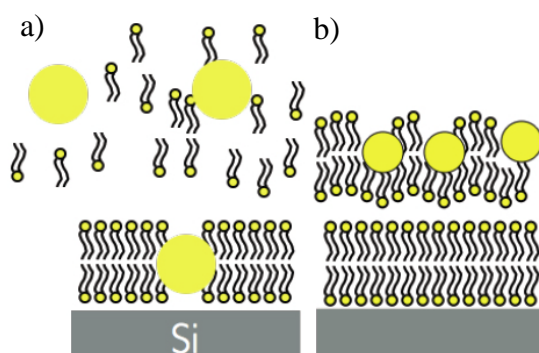


Figure 5.2. Schematic representation of cationic AuNPs interacting with membrane model at high concentration (a) and low concentration (b) [165].

These experiments highlighted the importance of the NPs surface charge: cationic AuNPs destabilized the floating bilayer at high concentration (1 mg/mL, Figure 5.2a). At lower concentration (0.01 mg/mL) they penetrated the floating bilayer and remained embedded in the hydrophobic region of the floating bilayer (Figure 5.2b). Anionic AuNPs only interacted with the surface, dehydrating it and shielding the floating bilayer from extreme alkaline pH in the fluid phase. In the new sets of experiments, the interaction between cationic AuNPs and more complex membrane models was investigated, in particular the composition and thus the surface charge of the double bilayer.

The collected data were analyzed with Motofit, a software package that runs on IGOR Pro for co-refinement of neutron and X-ray reflectivity data, allowing simultaneous fitting of data sets from the same sample under different contrast conditions.

During the stage I had also the chance to take part to an experiment performed on the reflectometer FIGARO and to deeply understand the potentialities of this technique.

5.2. Neutron reflectometry

In order to better understand the physics of a neutron reflectometry experiment, a detailed mathematical demonstration and discussion is needed. In such experiments, neutrons are scattered by atom's nuclei and the efficiency of the scattering is expressed by its bound coherent scattering length b , whose value depends on the incident neutron wavelength:

$$b^2 = \frac{d\sigma}{d\Omega} \quad 1)$$

where σ is the neutron cross section and Ω the solid angle through which the particles are scattered [245]. A neutron beam hits the sample on its surface and is reflected or transmitted depending on the incident angle and refractive index. As the neutron beam interacts with an atom, a nucleus-neutron potential can be defined as

$$V(\vec{r}) = \frac{2\pi\hbar^2}{m} b\delta(\vec{r}) \quad 2)$$

for each nucleus. The average potential inside the medium can be derived integrating on a volume:

$$\bar{V} = \frac{2\pi\hbar^2}{m} \rho \quad 3)$$

where $\rho(z) = \sum_j b_j n_j$, with n_j number of nuclei per unit volume, and b_j length of nucleus j . ρ is called Scattering Length Density (SLD) and is a key parameters in neutron reflectometry. Since the total energy of a neutron in vacuum is:

$$E = \frac{\hbar^2 k_0^2}{2m} \quad 4)$$

the total energy of a neutron inside a medium, given by the sum of kinetic energy and the potential energy is:

$$E_{tot} = \frac{\hbar^2 k^2}{2m} + \bar{V}. \quad 5)$$

Since the energy must be conserved during the interaction, the boundary condition is applied:

$$\frac{\hbar^2 k_0^2}{2m} = \frac{\hbar^2 k^2}{2m} + \bar{V} = \frac{\hbar^2 k^2}{2m} + \frac{2\pi\hbar^2}{m} \rho \quad 6)$$

or, rearranging the equation:

$$k_0^2 - k^2 = 4\pi\rho \quad 7)$$

Since by definition the refractive index can be written as $n = \frac{k}{k_0}$ and ρ assumes very small values ($\sim 10^{-6} \text{ \AA}^{-2}$), the final expression of the refractive index can be written as:

$$n = 1 - \frac{\lambda^2 \rho}{2\pi} \quad 8)$$

From Snell's law it is possible to find out the critical angle at which the incident wave is totally reflected:

$$n = \frac{n_2}{n_1} = \frac{\cos \alpha_1}{\cos \alpha_2} \quad 9)$$

Total reflection (Figure 5.3), that means $\alpha_1 = \alpha_c$, is obtained when $\alpha_2 = 0$ and so $\cos \alpha_2 = 1$.

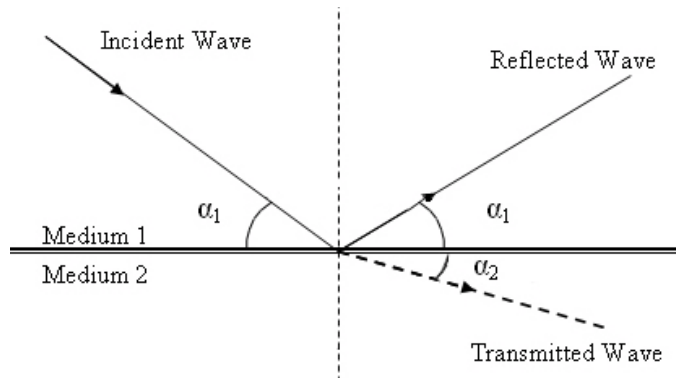


Figure 5.3. Schematic illustration of the geometrical configuration in a reflectivity measurement [246].

The critical angle α_c can be found comparing this last expression to the previous found form of n :

$$\cos \alpha_1 = \cos \alpha_c = 1 - \frac{\lambda^2 \rho}{2\pi} \quad 10)$$

$$\alpha_c = \lambda \sqrt{\frac{\rho}{\pi}} \quad 11)$$

When $\alpha < \alpha_c$ the incident beam is totally reflected from the surface ($R = 1$). For neutrons this phenomenon is observed at very small critical glancing angles. For $\alpha > \alpha_c$, the Fresnell's law describes the behavior of reflectivity:

$$R = \left| \frac{n_1 \sin \alpha_1 - n_2 \sin \alpha_2}{n_1 \sin \alpha_1 + n_2 \sin \alpha_2} \right|^2. \quad (12)$$

Considering the region of total reflection in more detail we can write:

$$n_1 \cos \alpha_1 = n_2 \cos \alpha_2 \quad (13)$$

and so

$$n_2 \cos \alpha_2 = \sqrt{(n_2^2 - n_1^2 \cos^2 \alpha_1)} \quad (14)$$

From this expression is clearly visible that

$$\text{if } \alpha > \alpha_c \rightarrow n_2^2 > n_1^2 \cos^2 \alpha_1 \rightarrow n_2 \cos \alpha_2 \text{ is real}$$

$$\text{if } \alpha < \alpha_c \rightarrow n_2^2 < n_1^2 \cos^2 \alpha_1 \rightarrow n_2 \cos \alpha_2 \text{ is imaginary}$$

The second case corresponds to an evanescent neutron wave that means

$$n_2 \cos \alpha_2 = -i \sqrt{n_1^2 \cos^2 \alpha_1 - n_2^2} \quad (15)$$

At the point of total reflection, $\alpha = \alpha_c$, $n_1 \sin \alpha_1$ is identically zero that means $n_2^2 = n_1^2 \cos^2 \alpha_1$ [247].

In a neutron reflectivity experiment, the ratio between the intensities of the reflected and incident beams, R , is measured as a function of the parameter Q_z , the momentum transfer perpendicular to the interface, defined as:

$$Q_z = \frac{4\pi}{\lambda} \sin \alpha \quad (16)$$

Reflectivity is related to the SLD across the interface by the approximate relation:

$$R(Q_z) \sim \frac{16\pi^2}{Q_z^2} |\hat{\rho}(Q_z)|^2 \quad (17)$$

valid in the Born approximation. $\hat{\rho}(Q_z)$ is the Fourier transform of the SLD profile $\rho(z)$ along the normal to the interface, giving information about the composition of each layer and about its structure. [165]

From an energetic point of view the potential acts perpendicular to the surface and it changes the normal component of the wave vector of the incident wave:

$$E_{i \perp} = \frac{(\hbar k_i \sin \alpha)^2}{2m_n} \quad (18)$$

where k_i is the wave number of the incident neutron and α is the grazing angle of incidence. So, total reflection occurs for a critical glancing angle at which E_{iL} is equal to the surface potential. For elastic scattering the momentum transfer q is normal to the surface and equal to $2k_i \sin\alpha$. This also explains why if a neutron beam is incident on a thin flat smooth surface, the neutrons interact at the top with a potential which depends on the number density of the atoms in the surface and their average coherent scattering length. Furthermore, when there is a thin uniform layer sandwiched between two bulk phases, the neutron beam is reflected at both the first and the second interfaces, giving rise to interference of the two beams and to the appearance of fringes in the reflectivity profile. The calculation of the reflectivity can be carried out by standard optical methods, using Fresnel coefficients for the transmitted and reflected amplitudes at each interface. [247] The calculated profile is compared to the measured profile, and the quality of the fit is assessed by using χ^2 in the least-squares method. The model parameters are then adjusted to minimize χ^2 . If the technique is appropriately used, it can reveal structural details down to the fraction of nanometer scale. [165]

5.3. D17 Reflectometer

D17 (Figure 5.4 on the left) is the ILL reflectometer used in the experiments. This instrument is set up to work with vertical surfaces (figure 5.4 on the right).

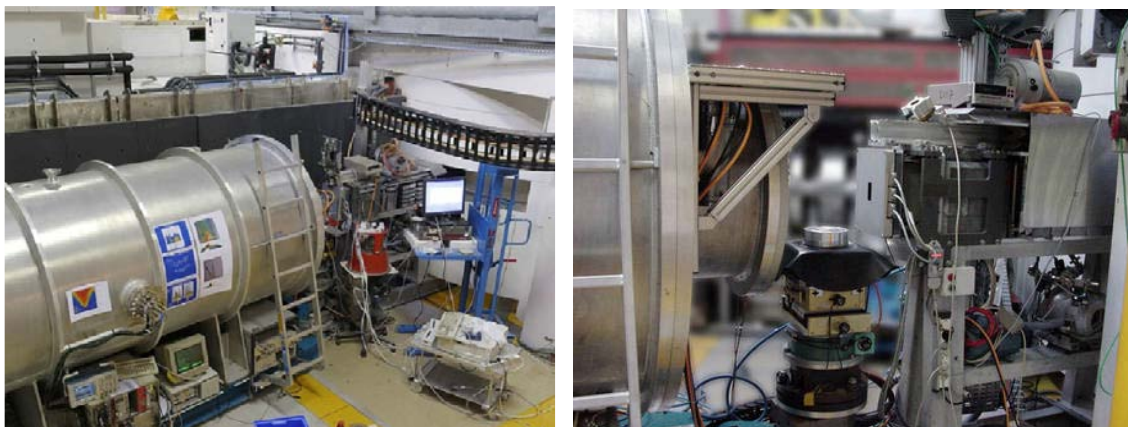


Figure 5.4. From left to right: a) overhead view of D17 reflectometer with its detector (big cylinder on the left) and b) view of sample holder

D17 can be used in two different modes (figure 5.5): monochromatic or time-of-flight (TOF) mode. The advantage of using a monochromatic beam is a higher Q resolution at the cost of longer measuring times because each angle must be measured separately. The TOF mode instead allows recording an extended range of Q at the same time, taking advantage of the fact that neutrons of different wavelengths are used. The analyzed data sets collected from experiments were collected with TOF mode. In this set up, pulses of neutrons with different wavelengths are produced by chopping the continuous neutron beam available with a double chopper system. The pulses are reflected by the sample and then are recorded by the detector. Each pulse is formed by faster and slower neutrons that arrive on the detector at slight different time (TOF spectrum). By knowing the geometry of the reflectometer (i.e. angle of the ingoing and outgoing beam, distances between choppers and samples, distances between sample and detector) the TOF (Intensity vs time of flight) signal can be transformed in the reflectivity profile (Intensity vs Q).

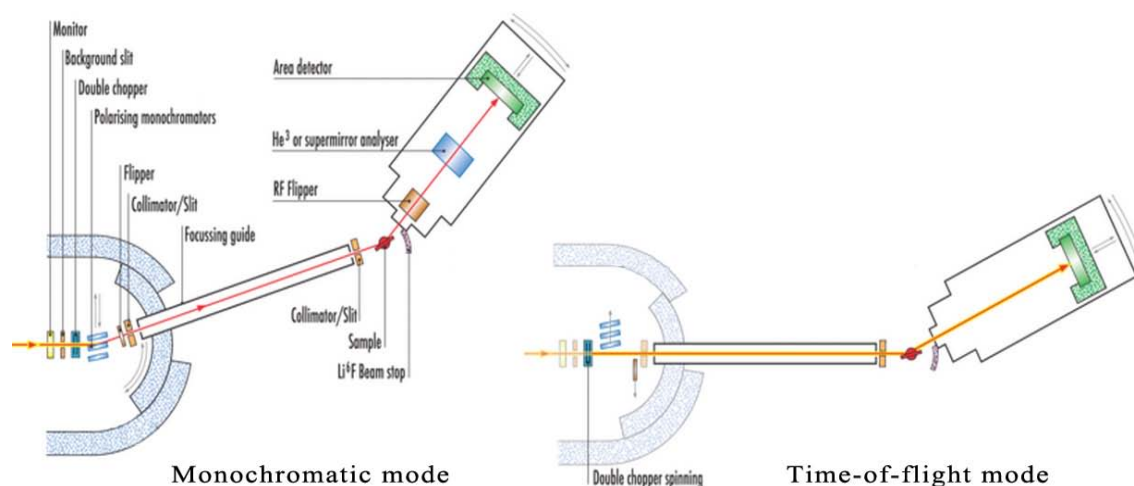


Figure 5.5. Top view of the two operating modes of D17.

A typical reflectivity measurement will involve a q -range of $0.005\text{--}0.3\text{\AA}^{-1}$ and can be completed in 1.2 hours for a 10 cm^2 sample. This can be achieved by joining the measurements at different reflection angle: at $\alpha=0,7^\circ$ the sample can be measured setting $\phi = 0$, whereas for $\alpha=3^\circ$ the projected opening is $\phi \sim 3^\circ$, which leads to only a small resolution jump in the overlap region.

5.4. Motofit

The method of analysis used by Motofit, the package within the IgorPro software chosen for the data analysis, involves the construction of a model of the interface that may be represented by a series of parallel layers of homogeneous material, as showed in figure 5.6. Each layer is characterized by an average SLD, weighted on all of its non-water components, and a thickness. These parameters are used to calculate a model reflectivity profile by means of the optical matrix method. The interfacial roughness between any two consecutive layers may also be included in the model by the Nevot-Croce method. [248]

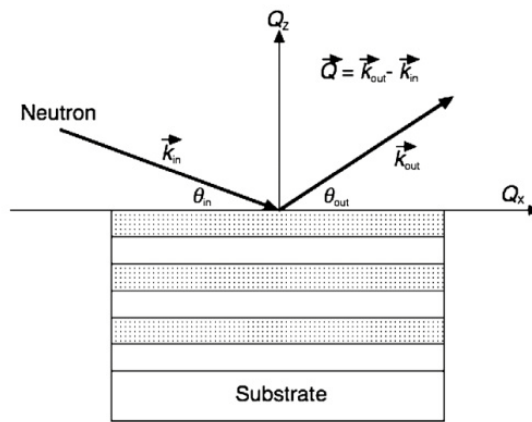


Figure 5.6. Interface model represented by a series of parallel layers.

In this description, the interface is split into n layers. Since the incident neutron beam is refracted by each of the layers, the value of the wavevector k , in layer n , is given by [249]

$$K_n = [k_0^2 - 4\pi(\rho_n - \rho_0)]^{1/2} \quad \text{where } k_0 = \frac{Q}{2} \text{ and } \rho_n = \text{SLD layer } n \quad (19)$$

The Fresnel reflection coefficient between layer n and layer $n + 1$ is then given by

$$r_{n,n+1} = \frac{k_n - k_{n+1}}{k_n + k_{n+1}}. \quad (20)$$

Since the interface between the different layer is not perfectly smooth, a roughness factor has to be introduced in order to modify the Fresnel coefficient of each interface.

This term is accounted as an exponential error function. [250]

$$r_{n,n+1} = \frac{k_n - k_{n+1}}{k_n + k_{n+1}} \exp(-2k_n k_{n+1} \sigma_{n,n+1}^2). \quad (21)$$

A phase factor, β , is introduced which accounts for the phase shift happening along the thickness d_n of each layer:

$$\beta_n = k_n d_n. \quad (22)$$

A characteristic matrix, C_n , is then calculated for each layer:

$$c_n = \begin{bmatrix} \exp \beta_n & r_n \exp (\beta_n) \\ r_n \exp (-\beta_n) & \exp (-\beta_n) \end{bmatrix} \quad (23)$$

from which the reflectivity is then calculated:

$$R = \left| \frac{M_{11}}{M_{21}} \right|^2 \quad (24)$$

In Motofit each reflectivity curve is modeled by a minimum of five variables: the instrumental scale factor, the SLDs of the super- and subphases, the sample background and the Gaussian roughness of the subphase. A further four variables are required for each layer added: the layer thickness (d), material scattering length density (ρ), solvent penetration ($\% \text{ solv}$) and roughness (σ). The total SLD of each layer is a volume-fraction-weighted addition of the material and subphase SLD [249]. The use of a combination of hydrogenated and deuterated material (contrast variation) can substantially change the reflectivity curve of a system while maintaining almost the same chemical structure. Experience on this kind of system and on similar ones suggests that the measurement of reflectivity curves from three or more contrasts, combined with standard physical hypotheses, are necessary and sufficient for extracting a unique model of the interface [165]. The model is parameterized in this way because the interfacial films are often solvated. Therefore, the co-refinement of two different contrasts allows the determination of the amount of solvent penetration, as well as the scattering length density of the material of interest.

One of the greatest advantages of MOTOFIT is the possibility to implement complex constrains between parameters. These constrains are fundamental especially when fitting those cases where fits are insensitive to some parameters or when the number of parameters is high. These effects often arise with roughness parameters, as their effects are mainly noticed in the high-Q region, where neutron data statistics are poorer. The control of these errors can be controlled by limiting the minimum and maximum value of the

parameters or by writing correlations between different parameters. These tasks can be achieved with very simple syntax as was done during this project.

5.5. Procedures

Even if not carried out personally, the experiments procedures and materials are described to give complete understanding of the measurements. The AuNPs synthesis and the double bilayer formation are performed in the same way as reported in previous work [165].

5.5.1 Gold nanoparticles synthesis

The gold NPs were produced as described by Esposito et al. [251] First, octanethiolatecapped gold NPs (C₈SAu NPs) were synthesized following the two-phase method developed by Brust et al. as previously reported. [119] The C₈SAu NPs were analyzed by TEM, UV-vis, and TGA to determine their average diameter (2 ± 0.5 nm), their surface coverage (0.59 ± 0.03 ligands per surface gold atom), and their average molecular mass (52000 ± 8000 g mol⁻¹). [165]

Cation-functionalized AuNPs were then prepared via Murray plaedisplacement reaction of the 2 nm C₈SAu NPs. [252] The cationic trimethylammonium-functionalized AuNPs were prepared by stirring 150 mg of C₈SAu NPs and 150 mg of N,N,N-trimethyl(11- mercaptoundecyl)ammonium chloride in 20 mL of degassed tetrahydrofuran under argon for two days at room temperature. The cationic thiol was synthesized according to a procedure reported by Tien et al. [253] The black precipitate of the gold NPs protected by a mixed monolayer of ω -thiol trimethylammonium chloride and octanethiol (Me₃NAu NPs) was purified by repeated suspension, centrifugation, and decantation with dichloromethane. ¹H NMR indicated an exchange of original octanethiol for the ω -thiol trimethylammonium chloride ligand by $\sim 70\%$. The Me₃NAu NPs dissolved in pure water without the need for pH adjustment. The reported SLD of AuNPs obtained with this method is approximately 4.5×10^{-6} Å⁻². [165]

5.5.2 Cell membrane model

In order to give to the reader a good comprehension of the constraints that were set during the data fitting, the model used to define the membrane structure is now described. The principal aim of this work in fact was to investigate how the membrane composition, and so the surface charge, influences the interaction with cationic AuNPs. Since it is difficult to perform scattering measurements directly on cells, and since these present a very complex membrane composition with several kind of molecules and proteins, membrane model has to be used to perform these experiments. The membrane model has to mimic as much as possible all the physical, chemical and mechanical properties of a real cell membrane. In order to reproduce the fluctuations occurring in natural membranes, a floating lipid bilayer was used. In fact, if a single lipid bilayer is directly adsorbed onto a solid (figure 5.7a), they mutually exert a strong electrostatic interaction that might change the lipid phase behavior influencing the measurements. [27]

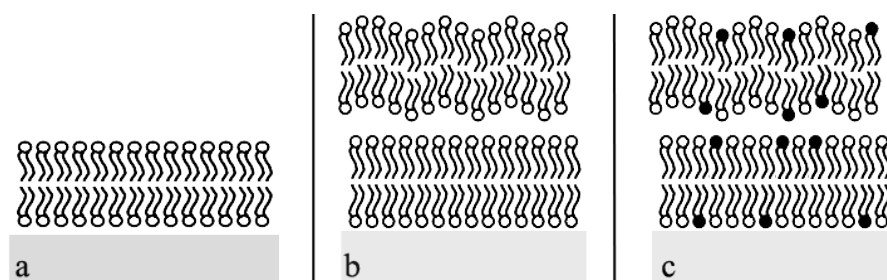


Figure 5.7. Representation of a) single lipid bilayer adsorbed onto the surface, b) fluctuating mono-lipid double bilayer and c) fluctuating mixed-lipid double bilayer.

A lipid double bilayer (figure 5.8b), in which a second bilayer floats at 20–30 Å on top of the first one, gives access to a highly hydrated, fluctuating bilayer that represents a membrane system with dynamic properties comparable to biological membranes and is greatly relevant for the examination of the influence of AuNPs on lipid membrane structure and integrity. [254]

In order to obtain a more complex membrane model compared to the one in the previous publication [165], a mixture of two different molecules, 1,2-distearoyl-sn-glycero-3-phosphocholine (DSPC) and 1,2-distearoyl-phosphatidylglycerol (DSPG), was used to create the layers, as can be seen in figure 5.8c. The composition of this solution was tuned

for different experiments as showed in Table 5-1. DSPC and DSPG were chosen and mixed before the solution was injected for the bilayer formation. These molecules present very similar properties (between the others, same gel/liquid phase transition temperature, $T_m = 55^\circ\text{C}$) and present a similar structure with many lipids contained in cell membranes. In the last sample deuterated DSPC was used instead of hydrogenated DSPC in order to have increase the contrast between the two lipid components.

Table 5-1. Percentage amount of different molecules used in the three experiments.

	DSPC	DSPG	Deuterated DSPC
Sample 1	90%	10%	/
Sample 2	75%	25%	/
Sample 3	/	25%	75%

Both the two molecules present a very similar structure as showed in figure 5.8, with a hydrophobic double tail and an hydrophilic head.



Figure 5.8. Schematic representation of DSPC (left) molecule and DSPG molecule (right).

The presence of a single head to two tail groups for molecule allows us to enforce constraints between the parameters of the two leaflets of the lipid layer. Since each head is connected to two tail groups, the SLDs of each layer and the area per molecule in the two leaflets are covariant. These features can be included in the analysis by re-parameterizing the model using physically relevant parameters. Each lipid molecule and the hydrating water molecules (Figure 5.9) are supposed to be contained in a cylinder of thickness (T_x), volume (V_x), scattering length (b_x) of the tail ($x = t$) and head ($x = h$) layers, their roughness (σ_x), and area per molecule (A). The values of the scattering lengths of each segment (head or tail) depends atomic composition, whereas their molecular volumes, V_h and V_t , are tabulated in literature. [255] The volume fraction of tails in a tail layer is given by V_t/AT_t , the volume fraction of heads in a head layer is given by V_h/AT_h . The rest of the

volume in a given layer is occupied by solvent molecules, $1 - (V_x)/(AT_x)$. The overall SLD of a head or tail layer is given by

$$\rho_x = \frac{b_x}{AT_x} + \rho_{solv} \left(1 - \frac{V_x}{AT_x} \right) \quad (25)$$

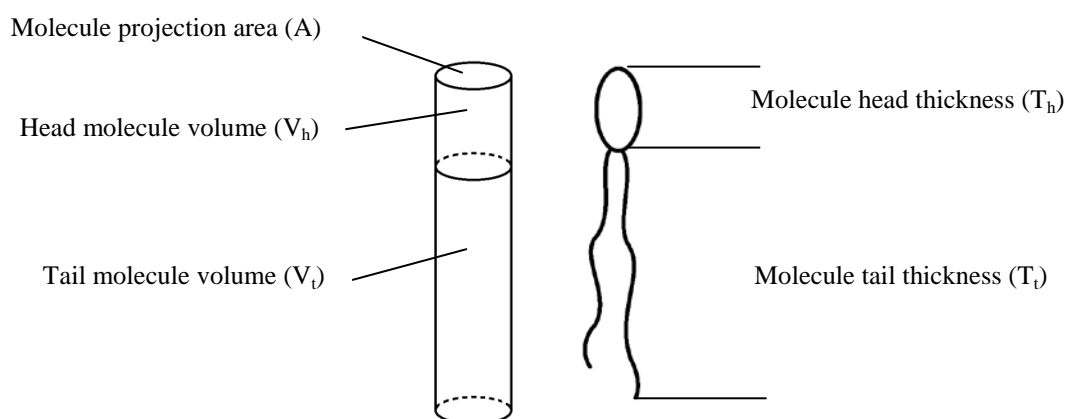


Figure 5.9. Schematic representation and related parameters of the molecule on the right and its approximation to a cylinder on the left.

With this model the number of parameters were reduced to the head and tail thickness, the layers roughness and the area per lipid, A . [165] By fitting more sets of data taken at different contrasts and applying the constraints imposed by the model described above, a precise description of the nanostructural details of the lipid systems used in the experiments was obtained.

5.5.3. Membrane model preparation

The first three lipid layers were deposited according to the Langmuir-Blodgett method. For the preparation of the floating lipid bilayer samples, a highly polished ($<3 \text{ \AA}$ roughness) silicon single 111 crystals of $8 \times 5 \text{ cm}^2$ surface and a 1 cm thickness were used as substrates. Prior to use, the substrates were sonicated in chloroform and acetone and then exposed to a continuous flow of ozone for 30 min to render the substrate surface highly hydrophilic. [15]

The previously prepared chloroform solution of DSPC and DSPG was spread onto the water subphase of a computer controlled NIMA 611 Langmuir-Blodgett (figure 5.10a) trough (surface area of 600 cm²; Nima Technology Ltd., Coventry, England) equipped with one barrier, an electronic pressure sensor with precut paper Wilhelmy plates (wet perimeter 20.6 mm; weight 80 mg m⁻²), and a dipper and well (63 × 180 mm²; 70 mm deep) at one end, until a slight change in surface pressure became measurable (0.2 mN m⁻¹).

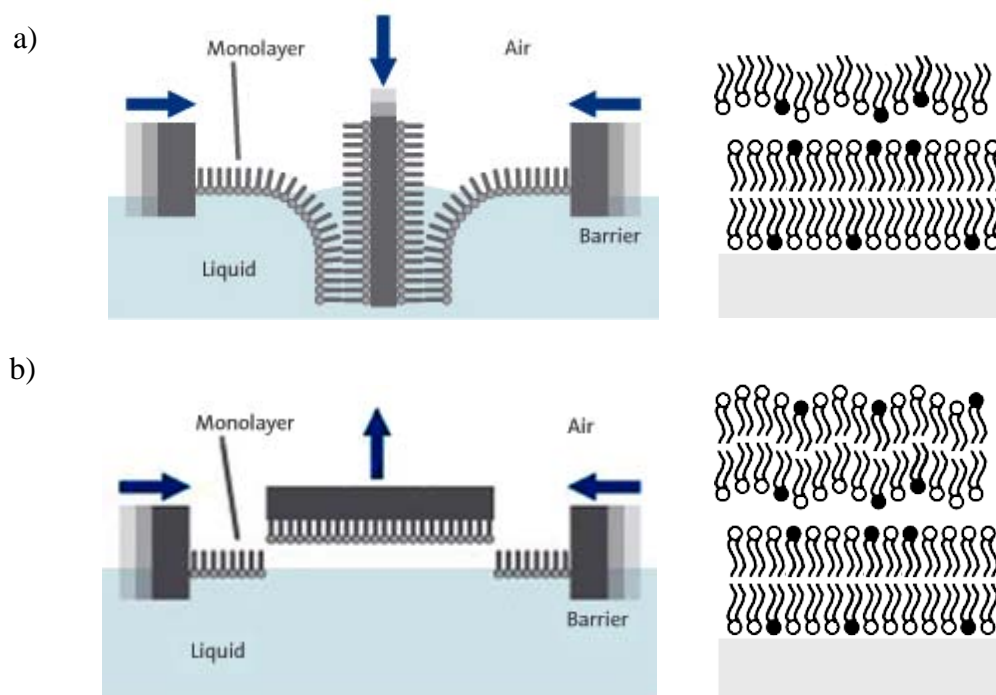


Figure 5.10. Representation of double bilayer formation with a) Langmuir-Blodgett method for the first three layers and b) Langmuir-Schaefer method for the last layer.

The temperature of the sub-phase water was held constant using a refrigerating/heating circulator (Fisher Scientific) set to 20 °C. After an equilibration time of ~30 min, the monolayer was compressed at a rate of 20 cm² min⁻¹ to a surface pressure of 40 ± 0.1 mN m⁻¹. Three vertical depositions onto the silicon substrate, beginning upward, resulted in an adsorbed lipid bilayer with a floating lipid monolayer resting on top. The floating lipid bilayer was completed by a final horizontal Langmuir-Schaefer (figure 5.10b) deposition of the same solution of DSPC and DSPG as the three first layers (see below). During this final step, the substrate with the floating bilayer was directly placed

onto a PTFE lid filled with ultrapure water. The sample cell was tightly closed and transferred to an aluminum holder. At the beam-line, the holder was connected to a water circulation bath (Haake) with a feedback in temperature from a PT100 resistance sensor placed close to the PTFE lid, in order to control the sample temperature. The samples were then annealed for one to two hours around 10 °C above the gel/liquid phase transition temperature (DSPC, DSPG: $T_m = 55$ °C). The PTFE lid included inlet and outlet holes that were used to rinse the sample with different sub-phases: : (i) Pure D₂O, (ii) a mixture of D₂O and H₂O having the same SLD of the silicon, silicon matched water (SMW), (iii) a mixture of D₂O and H₂O having SLD = 4 ($\times 10^{-6}$ Å⁻²), 4 matched water (4MW) (iv) pure H₂O, (v) and aqueous nanoparticle solution.

In each experiment, a measure of the pristine double bilayer was performed after annealing above the fluid-gel transition temperature in order to demonstrate the stability of the floating bilayer and to reduce the defects of the bilayers. Then, after solvent exchange, a measure was executed for each of the other three contrasts. The aqueous solution with AuNPs was injected at concentration of 0,01 mg/mL for all the experiments. A first measure was performed in order to collect data on the interaction of the pristine double bilayer with the NPs. After this step, the temperature was raised again at 55°C (just below DSPC and DSPG T_m) and then lowered again at room temperature. After one measure, the solvents were cyclically changed and the structure measure at each contrasts. The four collected data sets for each solvent were then fitted simultaneously.

The proportion of DSPC and DSPG were changed in the three experiments, as can be observed in Table 5-2. In the last experiment all the DSPC molecules were substituted with deuterated DSPC to have a different contrast especially in the tail regions richer of deuterium atoms.

Table 5-2. Percentage amount of different molecules used in the three experiments.

	DSPC	DSPG	Deuterated DSPC
Sample 1	90%	10%	/
Sample 2	75%	25%	/
Sample 3	/	25%	75%

5.6. Results and discussion

The lipid double bilayer of Sample 1 was obtained with a mixture of 10% DSPG and 90% DSPC. The first set of data is referred to a pristine lipid floating bilayer structure at 25°C after an annealing cycle. Annealing favors the re-organization and the removal of possible defects present in the structure. The data were analyzed according to the model described in section 5.2. It was further assumed symmetry of the bilayers.

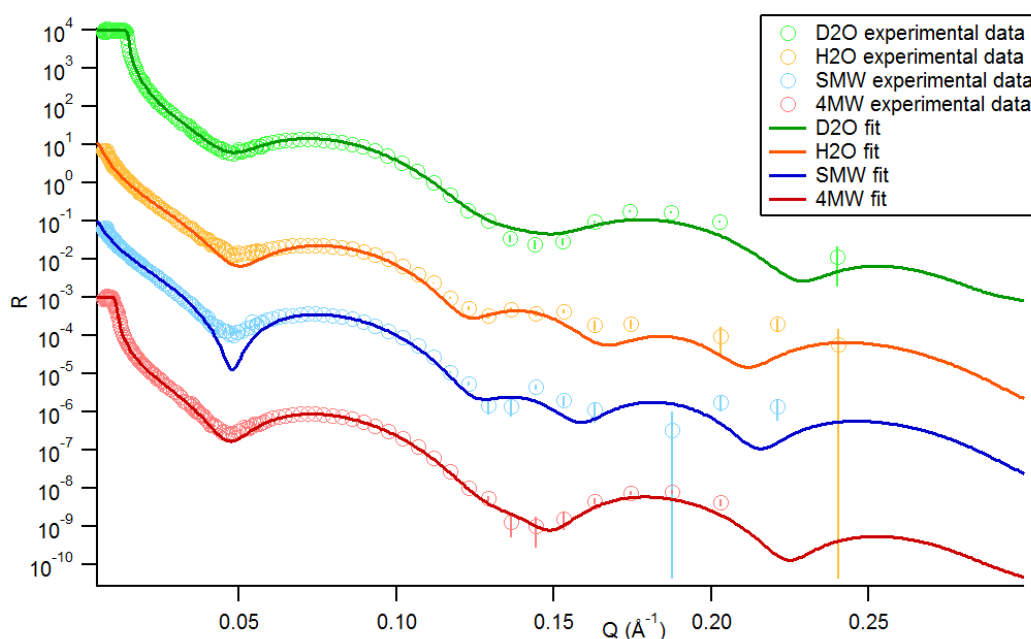


Figure 5.11. Reflectivity profiles of the pristine lipid double bilayer composed by 10% DSPG and 90% DSPC at four different contrasts: (*green curve*) pure D₂O, (*blue curve*) a mixture of D₂O and H₂O having the same SLD of the silicon, silicon matched water (SMW), (*red curve*) a mixture of D₂O and H₂O having SLD = $4 \times 10^{-6} \text{ \AA}^{-2}$, 4 matched water (4MW), (*orange curve*) pure H₂O. The reflectivity profiles are offset in order to better appreciate the curves behavior.

The data in Figure 5.11 were fitted with a layer sequences corresponding to two double bilayers one adsorbed directly on the substrate, one floating on top of it and separated by a layer of solvent. The precise parameters were obtained by fitting the data to the model and are reported in Table 5-3. The corresponding scattering length density profiles are displayed in Figure 5.12. The SLD of the liquid phase was set to $6,3 \times 10^{-6} \text{ \AA}^{-2}$ for D₂O, $-0,56 \times 10^{-6} \text{ \AA}^{-2}$ for H₂O, $4 \times 10^{-6} \text{ \AA}^{-2}$ for 4MW and $2,07 \times 10^{-6} \text{ \AA}^{-2}$ for SMW.

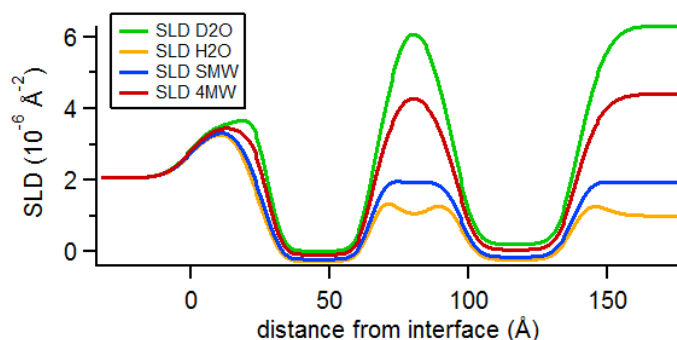


Figure 5.12. SLD profile of the pristine lipid double bilayer composed by 10% DSPG and 90% DSPC at four different contrasts: (*green curve*) pure D₂O, (*blue curve*) a mixture of D₂O and H₂O having the same SLD of the silicon, silicon matched water (SMW), (*red curve*) a mixture of D₂O and H₂O having SLD = 4 ($\times 10^{-6} \text{ \AA}^{-2}$), 4 matched water (4MW), (*orange curve*) pure H₂O.

Table 5-3. Structural parameters of the pristine double lipid bilayer composed by 10% DSPG and 90% DSPC.

Layer	Thickness [Å]	SLD [$\times 10^{-6} \text{ \AA}^{-2}$]	Solvent [%]	Roughness [Å]	Area per mol [Å ²]
Si	∞	2,07			
SiO ₂	19,5	3,47	4	7	
Heads	8,2	2,2	42,5	4	62
Tails	18,6	-0,33	5,3	4	
Tails	18,6	-0,33	5,3	4	
Heads	8,2	2,2	42,5	4	
Solvent	15,7	0	100	4	
Heads	8	2,2	57,4	5	62
Tails	20,5	-0,33	8,2	5	
Tails	20,5	-0,33	8,2	5	
Heads	8	2,2	57,4	5	
Backing	∞	6,3 (D ₂ O)		6,6	

The parameters of the pristine floating bilayer before the insertion of NPs are compatible to those obtained in the pristine layer of the previous work. [165] Afterwards a solution of 0,01 g/mL of AuNPs was injected inside the cell. No changes in the reflectivity profiles were observed, showing that the structure of the floating bilayer was not affected, in agreement with the previous experiments. [165] The temperature of

the bath was risen to 55°C, after that the reflectivity profile changed significantly (Figure 5.13). Only three contrasts are reported since a failure of solvent exchange prevent us from obtaining the H₂O contrast. At this point the configuration of the NP + lipid bilayers was stable since by performing the measurements at different times no changes in the reflectivity profiles were observed.

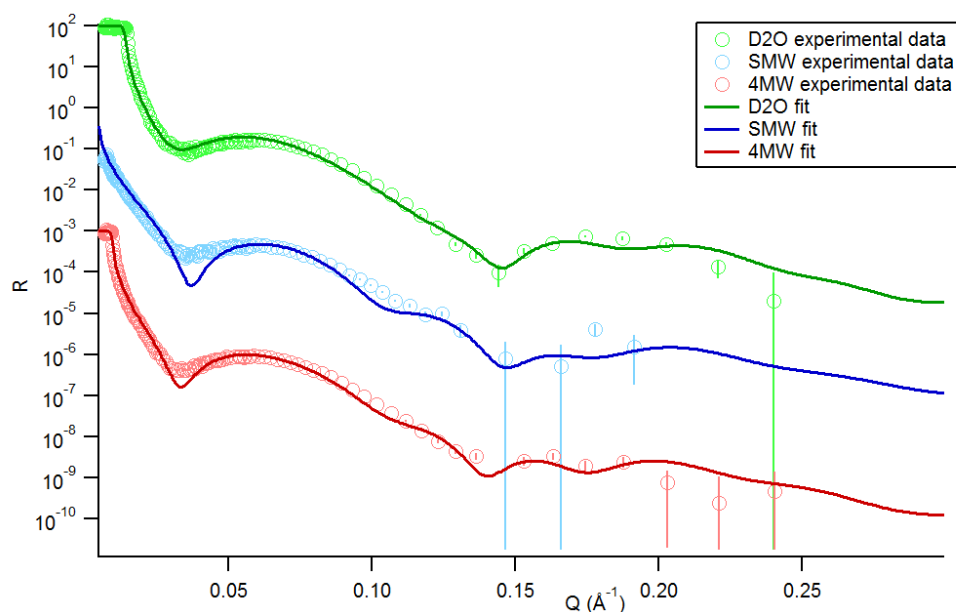


Figure 5.13. Reflectivity profiles of the lipid double bilayer composed by 10% DSPG and 90% DSPC + cationic AuNPs at three different contrasts: (*green curve*) pure D₂O, (*blue curve*) a mixture of D₂O and H₂O having the same SLD of the silicon, silicon matched water (SMW), (*red curve*) a mixture of D₂O and H₂O having SLD = 4 ($\times 10^{-6} \text{ \AA}^{-2}$), 4 matched water (4MW). The reflectivity profiles are offset in order to better appreciate the curves behavior.

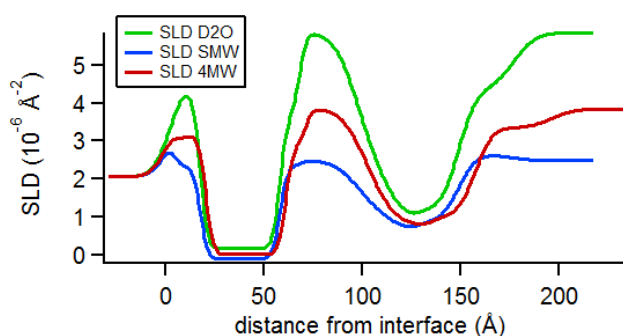


Figure 5.14. SLD profile of the lipid double bilayer composed by 10% DSPG and 90% DSPC + cationic AuNPs at three different contrasts: (*green curve*) pure D₂O, (*blue curve*) a mixture of D₂O and H₂O having the same SLD of the silicon, silicon matched water (SMW), (*red curve*) a mixture of D₂O and H₂O having SLD = 4 ($\times 10^{-6} \text{ \AA}^{-2}$), 4 matched water (4MW).

Table 5-4. Structural parameters of the double lipid bilayer composed by 10% DSPG and 90% DSPC + cationic AuNPs.

Layer	Thickness [Å]	SLD [$\times 10^{-6} \text{Å}^{-2}$]	Solvent [%]	Roughness [Å]	Area per mol [Å ²]
Si	∞	2,07			
SiO ₂	9	3,47	3,8	6	
Heads	12	2,2	58	3	65
Tails	20,3	-0,33	8	3	
Tails	20,3	-0,33	8	3	
Heads	12	2,2	58	3	
Solvent	25	0	100	3	
Heads	11,3	2,2	24	3	65
Tails	27	0,1	8,5	3	
Tails	13,7	2,7	9,5	4	
Heads	11	1,5	40	7	
Backing	∞	6,3 (D ₂ O)		9	

The comparison of the parameters before and after NPs injection and annealing evidences significant change in the floating bilayer structure, whereas only small changes are visible in the supported bilayer. The most relevant changes induced by the presences of the NPs in the structure of the membrane system is a strong asymmetry in the thicknesses, solvent % and SLDs of the inner and outer leaflet of the floating bilayer (Figure 5.14). One of the main advantage of performing reflectivity experiments at several isotopic composition of the solvent phase (contrast variation) is the ability to decouple the contribution of the water molecule to the SLD from the contribution of the membrane. Consequently the incorporation of water molecule in the membrane will affect only the parameter solvent %, but not the SLDs of the leaflets.

It is possible to see in Table 5-4 that the SLD of the hydrophobic tail regions increase significantly from the original value of $-0,33 \times 10^{-6} \text{Å}^{-2}$ to $0,1 \times 10^{-6} \text{Å}^{-2}$ (inner leaflet) and $2,7 \times 10^{-6} \text{Å}^{-2}$ (outer leaflet). The most likely explanation for this increase is the incorporation of AuNPs having an estimated SLD of $4,5 \times 10^{-6} \text{Å}^{-2}$. The size of the NPs of around 2 nm, and can well fit in the thickness of each membrane leaflet. The

analysis of our data is compatible with a differential incorporation of the NPs in the two leaflets, more pronounced on the outer one. The presence of the AuNPs inside the lipid bilayer probably increased the lateral pressure among the lipid molecules causing also a consistent dehydration of the lipid head groups, as can be seen in Table 5-4. This brings also another consequence that is the increase of the solvent layer between the two bilayer. Finally the presence of the NPs induce also an increased in the thickness of the solvent region between the two leaflets.

In order to understand if surface charge can play a fundamental role in the reorganization of the bilayers, another experiment was performed increasing the amount of DSPG to a ratio DSPG:DSPC= 25:75 (Sample 2).

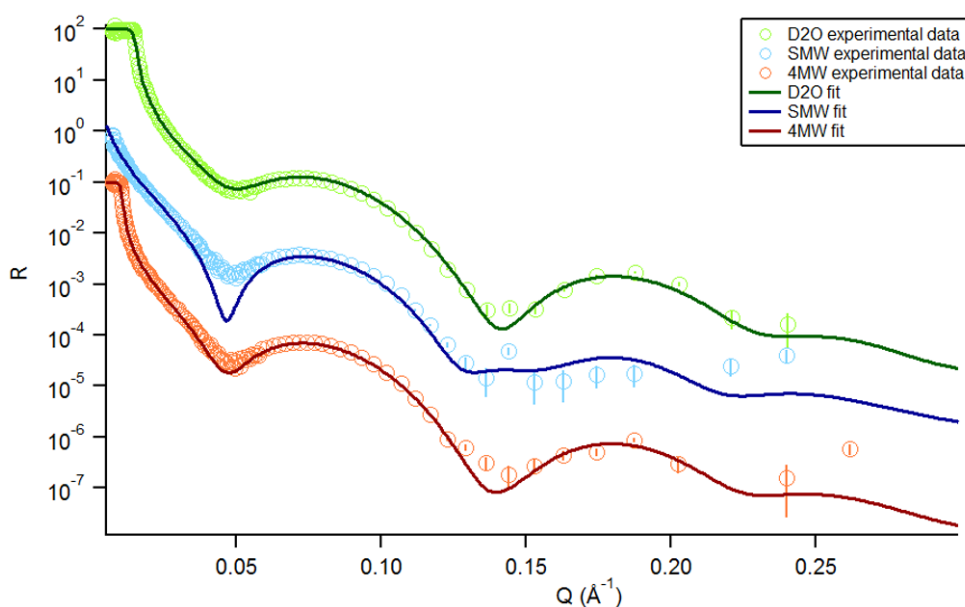


Figure 5.15. Reflectivity profiles of the pristine lipid double bilayer composed by 25% DSPG and 75% DSPC at three different contrasts: (*green curve*) pure D₂O, (*blue curve*) a mixture of D₂O and H₂O having the same SLD of the silicon, silicon matched water (SMW), (*red curve*) a mixture of D₂O and H₂O having SLD = $4 (\times 10^{-6} \text{ \AA}^{-2})$, 4 matched water (4MW). The reflectivity profiles are offset in order to better appreciate the curves behavior.

The measurements procedure was the same of the first sample: (*i*) floating lipid bilayer preparation, (*ii*) annealing (*iii*) reflectivity measurements at four different contrasts at 25°C (*iv*) injection AuNPs solution, (*v*) annealing, (*iv*) final characterization. Figure 5.15 displays the reflectivity curves of the pristine bilayer system at three contrasts. The model

represents well the data with the exception of a minimum at 0.05 \AA^{-1} for one of the contrasts probably due to a mismatch between the instrument resolution used in the fitting procedure and the real resolution which might be higher due to the undulation of the gold substrate at a length scale larger than the coherence length of the neutrons.

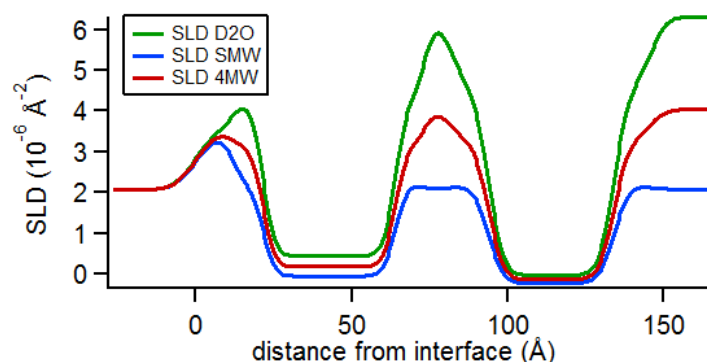


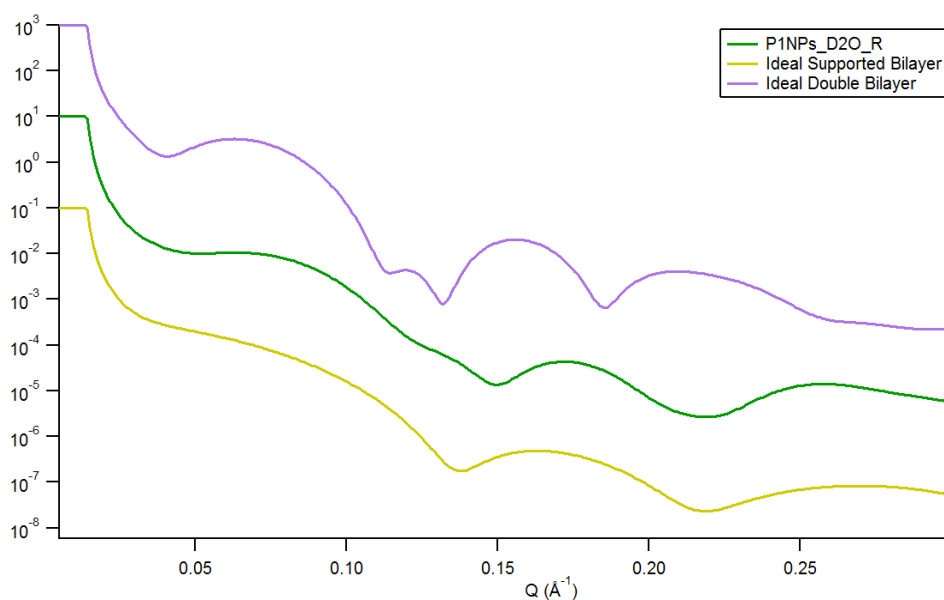
Figure 5.16. SLD profile of the pristine lipid double bilayer composed by 25% DSPG and 75% DSPC at three different contrasts: (*green curve*) pure D₂O, (*blue curve*) a mixture of D₂O and H₂O having the same SLD of the silicon, silicon matched water (SMW), (*red curve*) a mixture of D₂O and H₂O having SLD = 4 ($\times 10^{-6} \text{ \AA}^{-2}$), 4 matched water (4MW).

The SLD profiles corresponding to the fitting analysis are shown in Figure 5.16, and the corresponding structural parameters are reported in Table 5-5. The values obtained are comparable with those obtained for the 10% DSPG sample.

After injection of cationic AuNPs and one annealing cycle the measurements at different contrasts were significantly different with respect to the previous sample. The minimum at around 0.05 \AA^{-1} , characteristic fingerprint of the floating bilayers adsorbed on top of the supported bilayer, was considerably reduced, which is a sign of partial dissolution of the floating bilayer. On the other hand, a model that included only a supported bilayer did not describe correctly the reflectivity profile, as can be seen comparing the curves in figure 5.17. To properly fit the reflectivity profiles a model that includes a supported double bilayer plus a further layer on top of it was used. This floating layer is probably composed by a highly hydrated mixture of lipids and NPs.

Table 5-5. Structural parameters of the pristine double lipid bilayer composed by 25% DSPG and 75% DSPC.

Layer	Thickness [Å]	SLD [$\times 10^{-6} \text{Å}^{-2}$]	Solvent [%]	Roughness [Å]	Area per mol [Å ²]
Si	∞	2,07	/	/	/
SiO ₂	11	3,47	3,6	5,3	/
Heads	9,5	2,2	48,1	3	66
Tails	21,1	-0,33	11,8	3	/
Tails	21,1	-0,33	11,8	3	/
Heads	9,5	2,2	48,1	3	/
Solvent	8,4	0	100	3	/
Heads	11,8	2,2	57	3,7	66
Tails	20	-0,33	4,6	3,7	/
Tails	20	-0,33	4,6	3,7	/
Heads	11,8	2,2	57	3,7	/
Backing	∞	6,3 (D ₂ O)	/	3,9	/

**Figure 5.17.** Reflectivity profiles of an ideal double bilayer [purple curve], an ideal supported bilayer [yellow] and the lipid double bilayer composed by 25% DSPG and 75% DSPC + cationic AuNPs [green]

The reflectivity profiles are offset in order to better appreciate the curves behavior.

Even if this model worked well singularly for each contrast, it was difficult to find a set of common parameters that could fit globally the four contrasts. The best result that we could obtain was to use two sets of fitting parameters describing the measurements in H₂O and SMW (Figures 5.18 and 5.20a), and the measurements in D₂O and 4MW (Figures 5.19 and 5.20b), respectively. Table 5-6 shows the comparison between the data obtained with the fitting of H₂O and SMW (columns a) and those referred to 4MW and D₂O (columns b). The parameters corresponding to the supported lipid bilayer are very similar, as well as the thickness of the interstitial solvent layer between the supported bilayer and the floating layer. However, the characteristics of the floating layer are significantly different (see Table 5-6). The changes in the properties of the floating bilayer might be due to the exchange of solvent. This layer might not be as stable as a lipid bilayer and undergo dissolution or reorganization when the solvent is exchanged. Given the sequence of the solvent exchange being H₂O, SMW, 4MW and D₂O, it is possible that structural changes in the floating bilayer upon a single solvent exchange were negligible, but after multiple exchanges they became more pronounced. Hence, the reflectivity profiles corresponding to two subsequent solvent exchanges (H₂O-SMW and 4MW-D₂O) could still be modeled with a set of common parameters.

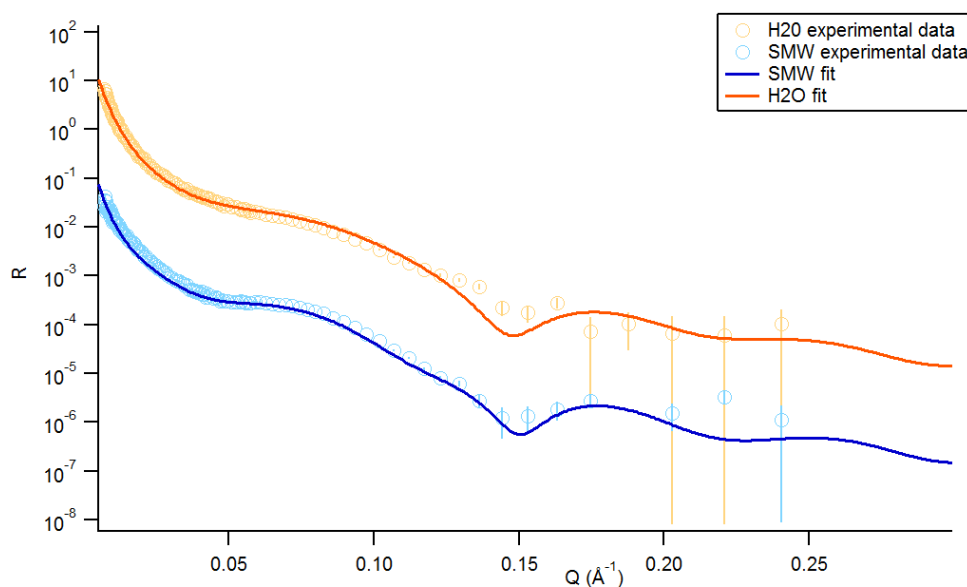


Figure 5.18. Reflectivity profiles of the lipid double bilayer composed by 25% DSPG and 75% DSPC + cationic AuNPs measured at two different contrasts: (*blue curve*) a mixture of D₂O and H₂O having the same SLD of the silicon, silicon matched water (SMW) and (*orange curve*) pure H₂O. The reflectivity profiles are offset in order to better appreciate the curves behavior.

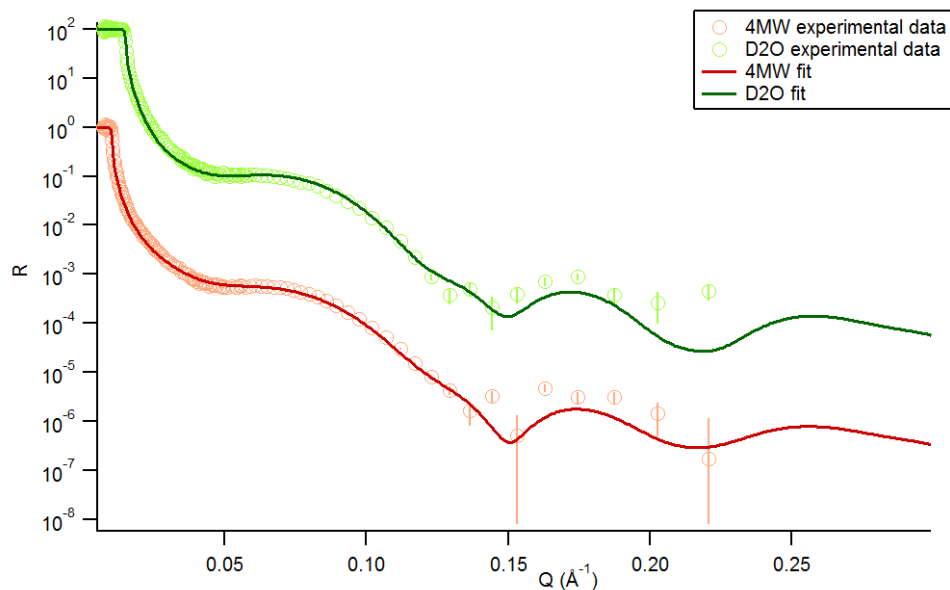


Figure 5.19. Reflectivity profiles of the lipid double bilayer composed by 25% DSPG and 75% DSPC + cationic AuNPs measured at two different contrasts: : (*green curve*) pure D₂O, and (*red curve*) a mixture of D₂O and H₂O having SLD = $4 (\times 10^{-6} \text{ \AA}^{-2})$, 4 matched water (4MW). The reflectivity profiles are offset in order to better appreciate the curves behavior.

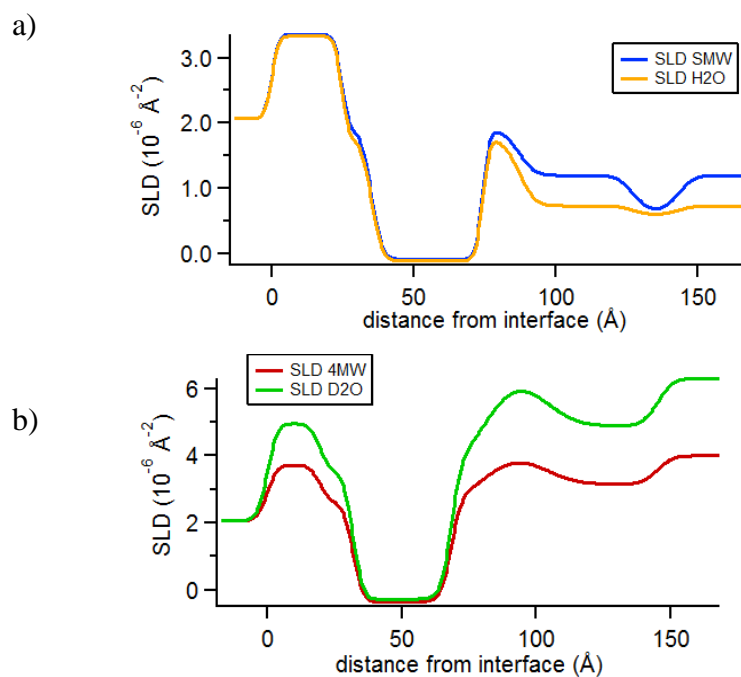


Figure 5.20. SLD profile of the lipid double bilayer composed by 25% DSPG and 75% DSPC + cationic AuNPs measured at four different contrasts: H₂O and SMW (a) and 4MW and D₂O (b).

To further investigate the instability of the floating bilayer composed by 25% of DSPG in the presence of NPs, the experiment with a lipid mixture of the same ratio of DSPG/DSPC was performed with a different isotopic composition (Sample 3). The DSPC used were fully deuterated (dDSPC). The effect of the NPs should be the same, but it was possible to obtain further information thanks to the contrast between the hydrogenated and deuterated components.

The measures were taken according to the previous procedure, before and after the annealing and the NPs injection. The reflectivity profiles and the fitted curves obtained for the pristine lipid bilayers are reported in Figure 5.21, the corresponding SLD and the fitting parameters are reported in Figures 5.22 and Table 5-7, respectively. Comparing the SLD profiles obtained with those of the previous experiments, it was noticed that in the D2O and 4MW measurement there is less contrast between the lipid bilayers and the solvent ($\sim 5,3 \times 10^{-6} \text{ \AA}^{-2}$, Table 5-7).

Table 5-6. Structural parameters of the structure composed by 25% DSPG and 75% DSPC + cationic AuNPs coupled by different contrasts: a) H₂O and SMW, b) 4MW and D₂O.

Layer	Thickness [Å]		SLD [$\times 10^{-6} \text{ \AA}^{-2}$]		Solvent [%]		Roughness [Å]		Area per mol [Å ²]	
	a	b	a	b	a	b	a	b	a	b
Si	∞	∞	2,07	2,07	/	/	/	/	/	/
SiO ₂	24,5	19,5	3,47	3,47	5	5,5	5	3	/	/
Heads	12,5	12,3	2,2	1,7	30	40	30	3	67	64
Tails	20	18,2	-0,15	-0,5	5	3,3	5	3	/	/
Tails	20	18,2	-0,15	-0,5	5	3,3	5	3	/	/
Heads	12,5	12,3	2,2	1,7	30	40	30	3	/	/
Solvent	40	41,4	0	0	100	100	100	9	/	/
Floating	16	23,3	0,6	2,8	10	30	10	9	/	/
Backing	∞	∞	2,07 (SMW)	4 (4MW)	/	/	/	4,5	/	/

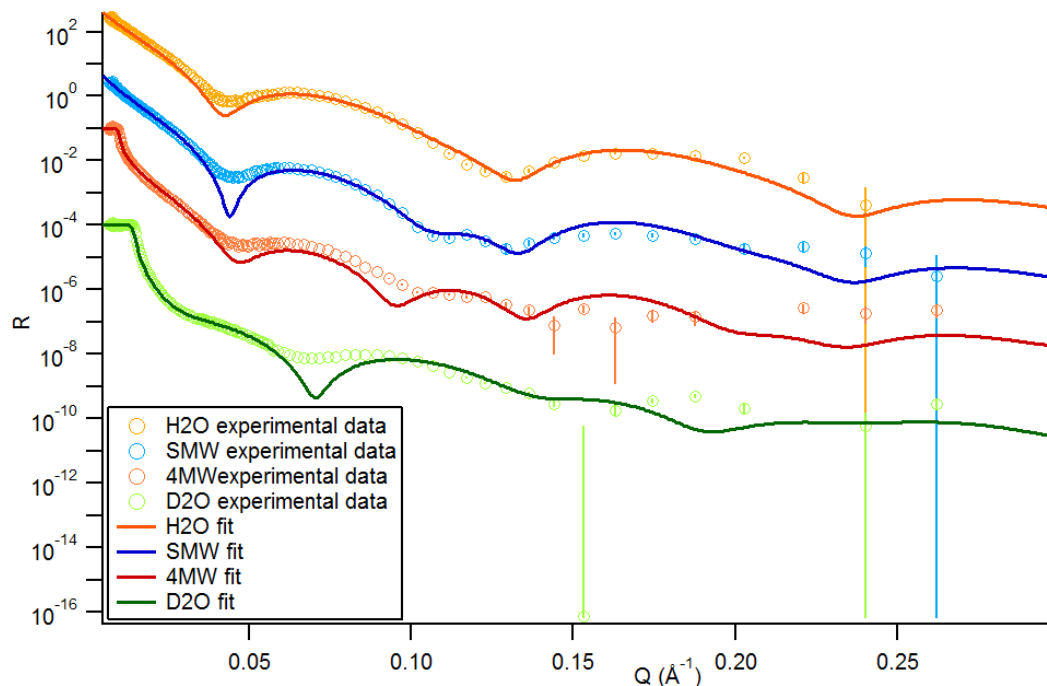


Figure 5.21. Reflectivity profiles of the pristine lipid double bilayer composed by 25% DSPG and 75% dDSPC at four different contrasts: (*green curve*) pure D₂O, (*blue curve*) a mixture of D₂O and H₂O having the same SLD of the silicon, silicon matched water (SMW), (*red curve*) a mixture of D₂O and H₂O having SLD = $4 (\times 10^{-6} \text{ \AA}^{-2})$, 4 matched water (4MW), (*orange curve*) pure H₂O. The reflectivity profiles are offset in order to better appreciate the curves behavior.

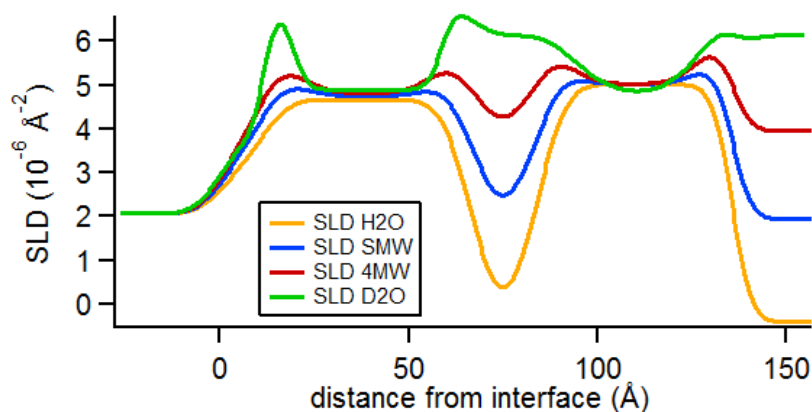


Figure 5.22. SLD profile of the pristine lipid double bilayer composed by 25% DSPG and 75% dDSPC at four different contrasts: (*green curve*) pure D₂O, (*blue curve*) a mixture of D₂O and H₂O having the same SLD of the silicon, silicon matched water (SMW), (*red curve*) a mixture of D₂O and H₂O having SLD = $4 (\times 10^{-6} \text{ \AA}^{-2})$, 4 matched water (4MW), (*orange curve*) pure H₂O.

The fits (see Figure 5.21) are reasonably good considering that four contrasts were fitted simultaneously. There are small discrepancies in the first minimum probably due to the mismatch between the instrumental resolution used in the fits, and the real resolution that is subjected to the characteristics of the sample (as described above). The structural parameters obtained by the fitting analysis are comparable to those obtained in the previous experiments. The significant differences in the SLDs of the lipids were due to a different isotopic composition.

Table 5-7. Structural parameters of the pristine double lipid bilayer composed by 25% DSPG and 75% dDSPC.

Layer	Thickness [Å]	SLD [$\times 10^{-6} \text{Å}^{-2}$]	Solvent [%]	Roughness [Å]	Area per mol [Å ²]
Si	∞	2,07			
SiO ₂	13	3,47	12	6	
Heads	9	7	32	6	67
Tails	23	5,3	5	6	
Tails	23	5,3	5	4	
Heads	9	7	32	2	
Solvent	15	0	100	12	
Heads	9	7	25	4	67
Tails	17	5	5	4,5	
Tails	17	5	5	4,5	
Heads	9	7	25	2	
Backing	∞	6,3 (D ₂ O)		4	

After AuNPs injection and annealing, the reflectivity profiles showed significant differences, although they were still compatible with the presence of a supported and a floating bilayers (Figure 5.23). This is in contrast with what observed in the previous experiment in which the annealing process in the presence of NPs induced the destabilization of the floating bilayer. The fitting analysis produced the structural parameters of Table 5-8 corresponding to the SLD profiles of Figure 5.24. The SLD of the tail region of the floating bilayer decreased from $5 \times 10^{-6} \text{Å}^{-2}$ to $4,5 \times 10^{-6} \text{Å}^{-2}$. This is compatible with the incorporation of some NPs in this region having a SLD lower of that

of the deuterated tails of the lipids. Only minor variations of hydration of the lipid bilayers were envisaged, whereas the thickness of the interstitial solvent layer between the two lipid bilayers increased. This was probably due to the redistribution of the charges at the surface of the bilayers causing a soft repulsion.

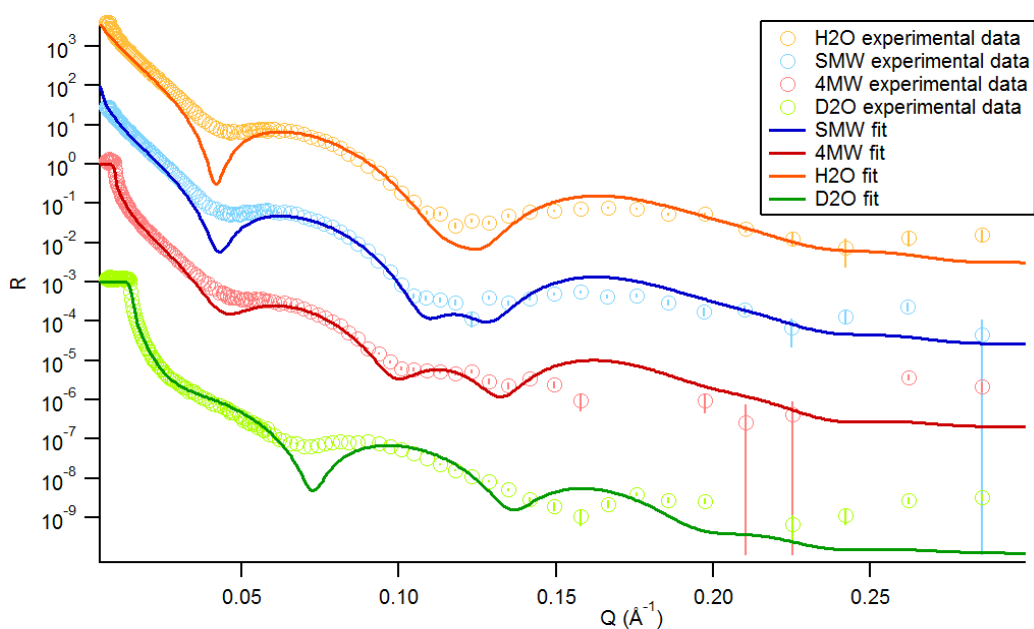


Figure 5.23. Reflectivity profiles of the lipid double bilayer composed by 25% DSPG and 75% dDSPC + cationic AuNPs at four different contrasts: (*green curve*) pure D₂O, (*blue curve*) a mixture of D₂O and H₂O having the same SLD of the silicon, silicon matched water (SMW), (*red curve*) a mixture of D₂O and H₂O having SLD = 4 ($\times 10^{-6} \text{ \AA}^{-2}$), 4 matched water (4MW), (*orange curve*) pure H₂O. The reflectivity profiles are offset in order to better appreciate the curves behavior.

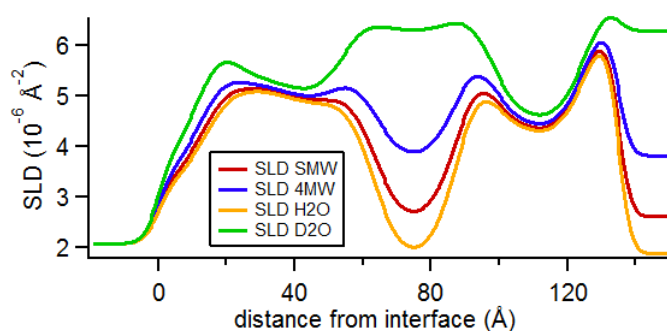


Figure 5.24. SLD profile of the lipid double bilayer composed by 25% DSPG and 75% dDSPC + cationic AuNPs at four different contrasts: (*green curve*) pure D₂O, (*blue curve*) a mixture of D₂O and H₂O having the same SLD of the silicon, silicon matched water (SMW), (*red curve*) a mixture of D₂O and H₂O having SLD = 4 ($\times 10^{-6} \text{ \AA}^{-2}$), 4 matched water (4MW), (*orange curve*) pure H₂O.

Table 5-8. Structural parameters of the double lipid bilayer composed by 25% DSPG and 75% dDSPC + cationic AuNPs.

Layer	Thickness [Å]	SLD [$\times 10^{-6} \text{Å}^{-2}$]	Solvent [%]	Roughness [Å]	Area per mol [Å ²]
Si	∞	2,07			
SiO ₂	13	3,47	13	3,5	
Heads	7,8	7	40	6	63
Tails	17,7	5,3	5	6	
Tails	17,3	5	5	6	
Heads	8	7	40	6	
Solvent	21	0	100	6	
Heads	9,5	7	22	6	63
Tails	15	4,5	7	6	
Tails	15,7	4,5	7	4	
Heads	7,3	7	22	6	
Backing	∞	3,8 (4MW)		3	

5.7. Conclusions

In this work the interaction of cationic AuNPs with a lipid system composed by a floating bilayer adsorbed onto a supported bilayer was described. The floating bilayer remains at least 1 nm above the supported bilayer and retains a level of hydration and of fluctuations of a typical biological membrane. This model system is therefore relevant for performing studies on the effects of AuNPs on the structure and integrity of lipid membranes. In particular, the effect of the surface charge of the lipid membrane was investigated, by performing the experiments on model membrane obtained by mixing uncharged DSPC lipids with negatively charged DSPG lipids in different proportions. As in the previous study [16], the injection of cationic NPs in the solution did not have a significant effect at room temperature were the lipid bilayer is in the gel phase. The reflectivity profile did not show any significant changes. As it was shown in molecular dynamic simulations [34] it seems that the NPs have to cross a free energy barrier before being able to interact with the membrane.

Once the temperature of the bath was risen to 55°C (slightly below the T_m of DSPC and DSPG), significant effects occurred in the structure of the membrane depending on the surface charge.

In the sample composed by DSPG (10%) and the remaining part by DSPC (90%) the analysis of the reflectivity profiles showed that after the annealing at 55°C the cationic NPs were incorporated into the floating lipid bilayer. The supported bilayer remained relatively unaffected by the presence of the NPs. The distribution of the NPs in the floating bilayer was asymmetric with a higher concentration of NPs in the external lipid leaflet. This is different from what happened in uncharged pure DSPC lipid bilayers [165] in which no asymmetry in the distribution of the NPs was envisaged and it is a clear effect of the surface charge of the membrane. The incorporation of the NPs induced also an increase of the thickness of the interstitial solvent layer between the two lipid bilayers. The samples composed by 25% of DSPG and 75% of DSPC showed a less obvious behavior. In one case the exposure to NPs at 55°C caused a destabilization of the floating bilayer. The reflectivity profiles were compatible with the presence of a layer of unknown

composition probably composed by a mixture of lipids and NPs at distance of 40 Å above the supported bilayer. In another case, the destabilization of the floating bilayer was not observed, but a behavior more similar to that of the sample composed by 10% DSPG and 90% of DSPC. Probably the higher values of surface charge in the lipid bilayer reduced the stability of the membrane, and increased the probability that the floating bilayer was destabilized.

By comparing the results of reference [15] for uncharged membrane surfaces and the results obtained in this work, it appears that the uptake of cationic NP decreases with the increase of surface charge in the membrane. Moreover, a common effect involving the incorporation of cationic NP in the floating membrane is the increase of the thickness of the interstitial solvent layer between the floating and the supported lipid bilayer. This is probably due to the redistribution of the charges inside the bilayers that can induce a soft repulsion.

Overall the work presented here confirms the results obtained in reference [15], where the effect of the charge of the NP were assessed, and extend the analysis by including the influence of the surface charge of the lipid membrane on the interaction with cationic NPs. This knowledge is a further step forward to the understanding the way NPs affect the structure and the properties of biomimetic membranes, and provide crucial information to effectively design NPs for biomedical applications.

Even if these were the first steps of a long path, this initial knowledge is fundamental as first approach with this innovative technique to deeply understand the possible effects of NPs on cell membranes. This is crucial for the effective design of NPs aimed toteranostic purposes as well as the general handling of these structures with human body.

Chapter 6 - Conclusions

According to the objectives proposed in section 1.7, this work focused on the production, development and optimization of water-soluble SPIONs as MRI contrast agents and fluorinated Au NPs as ^{19}F MRI probes. Moreover, the interaction of cationic AuNPs with cell model systems composed of a floating lipid bilayer adsorbed onto a supported bilayer was studied by neutron reflectometry experiments.

The conclusions extracted from the experimental results will be now illustrated and listed in the three main experimental areas of the project. Overall, the project produced promising preliminary results that need further study towards the development of powerful theranostic drug-delivery nanosystems.

i) Development of SPIONs as possible theranostic agents

Monodispersed hydrophobic SPIONs, stabilized with oleic acid and dissolved in toluene, characterized by an average hydrodynamic size of 16.9 ± 0.5 nm were successfully synthesized following a known protocol.

Water-soluble SPIONs supraparticles coated by HPB-II protein were obtained. These supraparticles have an averaged hydrodynamic diameter (D_H) of 249 ± 12 nm with a Zeta-potential of -29 mV and were characterized by UV-Vis, FTIR and CD. In particular, CD analysis showed that the protein did not significantly change its secondary structure upon adsorption on to the NP surface.

The coating process with HPB was also performed in acetate buffer at acidic pH=4.5 but with the production of larger and less stable supraparticles.

The ability of SPIONs HPB coated supraparticles to encapsulate a hydrophobic molecule (Nile red) was also tested. No conclusive results were obtained to prove the encapsulation of the dye and fluorescence experiments showed fluorescence emission for empty and loaded supraparticles at 558 and 585 nm.

ii) Synthesis of fluorinated Au NPs as ^{19}F MRI probes

Totally and partially-fluorinated gold NPs were produced by ligands exchange reactions. The exchange was performed starting from two different surface functionalized NPs: oleylamine stabilized AuNPs ($12,7 \pm 2,4$ nm) and DT stabilized AuNPs ($4,0 \pm 1,7$ nm). In the first set of experiments, oleylamine was exchanged with PFDT ligands and the protocol was optimized changing two main parameters: reaction time and ligands amount. The exchange yield (i.e. the PFDT amount on the NPs) resulted proportional to the reaction time. Almost totally fluorinated Au NPs were obtained after 18h reaction. Fluorinated NPs produced by exchange reactions showed an average size, which was not consistently affected by the reaction time. After 3 hours the mean diameter was $8,8 \pm 4,6$ nm, whereas after 18 hours it was $9,1 \pm 3,4$ nm. In addition, totally fluorinated AuNPs were also obtained by exchange reaction starting from DT stabilized (instead of oleylamine stabilized) Au NPs with a size of $5,1 \pm 1,9$ nm.

A NP fragmentation phenomenon was also observed and investigated. Some molecules with peculiar electronic properties in fact, could promote the fragmentation of NPs, giving rise to a small population of nanoclusters, as described in literature. [209], [208] This phenomenon was not completely elucidated with these experiments, but it is envisaged that it is caused by the presence of an excess of PFDT ligands. Increasing the reaction times or using triple amount of PFDT compared to the initial experiments, did not bring to any fragmentation of AuNPs. Also in the other samples, with different ligands and different stabilized AuNPs, no nanoclusters were found. Therefore it has been deduced that these ligands under these conditions cannot promote fragmentation. On the other hand, other experiments under different conditions should be performed to investigate if this phenomenon could still take place.

Totally fluorinated monodispersed Au NPs via Brust direct method were synthesized with a small size ($1,8 \pm 0,9$ nm). Fluorinated Au NPs were successfully coated by HPB II protein and turned water-soluble with the same protocol used for Magnetite

NPs. The so-produced supraparticles (size $127,1 \pm 1,08$ nm) were stable in aqueous solution but further investigation is needed for a full characterization.

iii) Analysis of Neutron Reflectometry experiments to study Au NPs interaction with cell membranes

The work performed at ILL focused on the NP interaction with cell membrane model system by Neutron Reflectometry. In particular, a previous work already reported in the literature was here extended including the influence of the surface charge of the lipid membrane on the interaction with cationic NPs.

The model system used in this work is relevant in the study of the effects of AuNPs on the structure and integrity of lipid membranes. In particular, the effect of the surface charge of the lipid membrane was investigated by performing the experiments on model membrane obtained by mixing uncharged DSPC lipids with negatively charged DSPG lipids at different proportion.

The injection of cationic NPs in the solution did not have a significant effect at room temperature were the lipid bilayer is in the gel phase. The reflectivity profile did not show any significant changes. It seems that the NPs have to cross a free energy barrier before being able to interact with the membrane.

If the temperature is increased, the situation is different. Once the temperature of the bath was risen to 55°C (slightly below the T_m of DSPC and DSPG), significant effects occurred in the structure of the membrane depending on the surface charge. The uptake of cationic NP was, then, observed but it decreases with the increase of surface charge in the membrane. Moreover, a common effect involving the incorporation of cationic NP in the floating membrane was the increase of the thickness of the interstitial solvent layer between the floating and the supported lipid bilayer. This was probably due to the redistribution of the charges inside the bilayers that may induce a soft repulsion. The best results have been collected for the sample composed by 10% of DSPG and 90% of DSPC. In this case the reflectivity profiles showed that after the annealing at 55°C the cationic

NPs were incorporated into the floating lipid bilayer and the supported bilayer remained relatively unaffected by the presence of the NPs.

Bibliography

- [1] H. Boulaiz, P. J. Alvarez, A. Ramirez, J. a Marchal, J. Prados, F. Rodríguez-Serrano, M. Perán, C. Melguizo, and A. Aranega, “Nanomedicine: application areas and development prospects.,” *Int. J. Mol. Sci.*, vol. 12, no. 5, pp. 3303–3321, 2011.
- [2] M. a. Albrecht, C. W. Evans, and C. L. Raston, “Green chemistry and the health implications of nanoparticles,” *Green Chem.*, vol. 8, no. 5, p. 417, 2006.
- [3] J. A. Akin, “Homeostatic process of thermoregulation,” *Nat. Educ. Knowl.*, vol. 3, no. 10, p. 7, 2011.
- [4] Y. Liu, H. Miyoshi, and M. Nakamura, “Nanomedicine for drug delivery and imaging: a promising avenue for cancer therapy and diagnosis using targeted functional nanoparticles.,” *Int. J. Cancer*, vol. 120, no. 12, pp. 2527–2537, 2007.
- [5] N. Desai, “Challenges in development of nanoparticle-based therapeutics.,” *AAPS J.*, vol. 14, no. 2, pp. 282–295, 2012.
- [6] K. K. Y. Wong and X. L. Liu, “Nanomedicine: a primer for surgeons.,” *Pediatr. Surg. Int.*, vol. 28, no. 10, pp. 943–951, 2012.
- [7] D. K. Kim and J. Dobson, “Nanomedicine for targeted drug delivery,” *J. Mater. Chem.*, vol. 19, no. 35, p. 6294, 2009.
- [8] V. V Mody, R. Siwale, A. Singh, and H. R. Mody, “Introduction to metallic nanoparticles,” *J. Pharm. Bioallied Sci.*, vol. 2, no. 4, pp. 282–289, Jun. 2010.
- [9] M. C. Garnett and P. Kallinteri, “Nanomedicines and nanotoxicology: some physiological principles.,” *Occup. Med. (Lond.)*, vol. 56, no. 5, pp. 307–311, 2006.
- [10] Z. R. Stephen, F. M. Kievit, and M. Zhang, “Magnetite Nanoparticles for Medical MR Imaging.,” *Mater. Today (Kidlington)*, vol. 14, no. 7–8, pp. 330–338, 2011.
- [11] M. Boccalon, P. Franchi, M. Lucarini, J. J. Delgado, F. Sousa, F. Stellacci, I. Zucca, A. Scotti, R. Spreafico, P. Pengo, and L. Pasquato, “Gold nanoparticles protected by fluorinated ligands for ¹⁹F MRI.,” *Chem. Commun. (Camb)*, vol. 49, no. 78, pp. 8794–8796, 2013.
- [12] K. Park, S. Lee, E. Kang, K. Kim, K. Choi, and I. C. Kwon, “New Generation of Multifunctional Nanoparticles for Cancer Imaging and Therapy,” *Adv. Funct. Mater.*, vol. 19, no. 10, pp. 1553–1566, 2009.
- [13] M. Mahmoudi, S. Sant, B. Wang, S. Laurent, and T. Sen, “Superparamagnetic iron oxide nanoparticles (SPIONs): development, surface modification and applications in chemotherapy.,” *Adv. Drug Deliv. Rev.*, vol. 63, no. 1–2, pp. 24–46, 2011.

- [14] O. C. Farokhzad and R. Langer, "Impact of Nanotechnology on Drug Delivery," *ACS Nano*, vol. 3, no. 1, pp. 16–20, 2009.
- [15] J. Ruiz-Cabello and B. P. Barnett, "Fluorine (^{19}F) MRS and MRI in biomedicine," *...in Biomed.*, no. September 2010, pp. 114–129, 2011.
- [16] P. Boisseau and B. Loubaton, "Nanomedicine, nanotechnology in medicine," *Comptes Rendus Phys.*, vol. 12, no. 7, pp. 620–636, 2011.
- [17] M. M. Janib, "Imaging and drug delivery using theranostic nanoparticles," *Natl. institutes Heal.*, vol. 62, no. 11, pp. 1052–1063, 2010.
- [18] A. Contero, E. Richer, A. Gondim, and R. P. Mason, "High throughput quantitative bioluminescence imaging for assessing tumor burden," vol. 574, no. 4, pp. 1–8, 2009.
- [19] R. Thomas, I.-K. Park, and Y. Y. Jeong, "Magnetic iron oxide nanoparticles for multimodal imaging and therapy of cancer.," *Int. J. Mol. Sci.*, vol. 14, no. 8, pp. 15910–15930, 2013.
- [20] C.-H. Lee, S.-H. Cheng, Y.-J. Wang, Y.-C. Chen, N.-T. Chen, J. Souris, C.-T. Chen, C.-Y. Mou, C.-S. Yang, and L.-W. Lo, "Near-Infrared Mesoporous Silica Nanoparticles for Optical Imaging: Characterization and In Vivo Biodistribution," *Adv. Funct. Mater.*, vol. 19, no. 2, pp. 215–222, 2009.
- [21] J. Frangioni, "In vivo near-infrared fluorescence imaging," *Curr. Opin. Chem. Biol.*, vol. 7, no. 5, pp. 626–634, 2003.
- [22] P. Sanchez Moreno, "Engineering lipid nanocapsule systems for intracellular delivery of anticancer drugs," Universidad de Granada, 2014.
- [23] Y. Il Park, J. H. Kim, K. T. Lee, K.-S. Jeon, H. Bin Na, J. H. Yu, H. M. Kim, N. Lee, S. H. Choi, S.-I. Baik, H. Kim, S. P. Park, B.-J. Park, Y. W. Kim, S. H. Lee, S.-Y. Yoon, I. C. Song, W. K. Moon, Y. D. Suh, and T. Hyeon, "Nonblinking and Nonbleaching Upconverting Nanoparticles as an Optical Imaging Nanoprobe and T1 Magnetic Resonance Imaging Contrast Agent," *Adv. Mater.*, vol. 21, no. 44, pp. 4467–4471, 2009.
- [24] L. Josephson, M. F. Kircher, U. Mahmood, Y. Tang, and R. Weissleder, "Near-Infrared Fluorescent Nanoparticles as Combined MR/Optical Imaging Probes," *Bioconjug. Chem.*, vol. 13, no. 3, pp. 554–560, 2002.
- [25] X.-F. Yu, L.-D. Chen, M. Li, M.-Y. Xie, L. Zhou, Y. Li, and Q.-Q. Wang, "Highly Efficient Fluorescence of NdF₃/SiO₂ Core/Shell Nanoparticles and the Applications for in vivo NIR Detection," *Adv. Mater.*, vol. 20, no. 21, pp. 4118–4123, 2008.

- [26] C. Richard, M. De Chermont, and D. Scherman, "Nanoparticles for imaging and tumor gene delivery," pp. 264–270, 2008.
- [27] D. Zhu, F. Liu, L. Ma, D. Liu, and Z. Wang, "Nanoparticle-based systems for t1-weighted magnetic resonance imaging contrast agents.," *Int. J. Mol. Sci.*, vol. 14, no. 5, pp. 10591–10607, 2013.
- [28] I. Tirotta, V. Dichiarante, C. Pigliacelli, G. Cavallo, G. Terraneo, F. B. Bombelli, P. Metrangolo, and G. Resnati, "F Magnetic Resonance Imaging (MRI): From Design of Materials to Clinical Applications," 2015.
- [29] W. Wolf, C. A. Presant, K. L. Servis, A. El-Tahtawy, M. J. Albright, P. B. Barker, R. Ring, D. Atkinson, R. Ong, and M. King, "Tumor trapping of 5-fluorouracil: in vivo ^{19}F NMR spectroscopic pharmacokinetics in tumor-bearing humans and rabbits.," *Proc. Natl. Acad. Sci. U. S. A.*, vol. 87, no. January, pp. 492–496, 1990.
- [30] K. Hayashi, M. Nakamura, W. Sakamoto, T. Yogo, H. Miki, S. Ozaki, M. Abe, T. Matsumoto, and K. Ishimura, "Superparamagnetic nanoparticle clusters for cancer theranostics combining magnetic resonance imaging and hyperthermia treatment.," *Theranostics*, vol. 3, no. 6, pp. 366–376, 2013.
- [31] S. a Wickline, A. M. Neubauer, P. M. Winter, S. D. Caruthers, and G. M. Lanza, "Molecular imaging and therapy of atherosclerosis with targeted nanoparticles.," *J. Magn. Reson. Imaging*, vol. 25, no. 4, pp. 667–680, Apr. 2007.
- [32] J. S. Weinstein, C. G. Varallyay, E. Dosa, S. Gahramanov, B. Hamilton, W. D. Rooney, L. L. Muldoon, and E. a Neuwelt, "Superparamagnetic iron oxide nanoparticles: diagnostic magnetic resonance imaging and potential therapeutic applications in neurooncology and central nervous system inflammatory pathologies, a review.," *J. Cereb. Blood Flow Metab.*, vol. 30, no. 1, pp. 15–35, 2010.
- [33] S. Prijic, J. Scancar, R. Romih, M. Cemazar, V. B. Bregar, A. Znidarsic, and G. Sersa, "Increased cellular uptake of biocompatible superparamagnetic iron oxide nanoparticles into malignant cells by an external magnetic field.," *J. Membr. Biol.*, vol. 236, no. 1, pp. 167–179, 2010.
- [34] E. Boisselier and D. Astruc, "Gold nanoparticles in nanomedicine: preparations, imaging, diagnostics, therapies and toxicity.," *Chem. Soc. Rev.*, vol. 38, no. 6, pp. 1759–1782, 2009.
- [35] M. Port, J.-M. Idée, C. Medina, C. Robic, M. Sabatou, and C. Corot, "Efficiency, thermodynamic and kinetic stability of marketed gadolinium chelates and their possible clinical consequences: a critical review," *BioMetals*, vol. 21, no. 4, pp. 469–490, 2008.

- [36] L. Gentilini, Cristina; Evangelista, Fabrizio; Rudolf, Petra; Franchi, Paola; Lucarini, Marco; Pasquato, "Water-Soluble Gold Nanoparticles Protected by Fluorinated Amphiphilic Thiolates," *J. CHEM. SOC.*, vol. 130, pp. 15678–15682, 2008.
- [37] B. Daglar and N. Aydogan, "Fluorocarbon–hydrocarbon hybrid gold NPs synthesized by bulk exchange reactions and surface coatings of fluorocarbon coated gold NPs are increased," *Colloids Surfaces A Physicochem. Eng. Asp.*, vol. 419, pp. 257–262, 2013.
- [38] S. K. Yen, P. Padmanabhan, and S. T. Selvan, "Multifunctional iron oxide nanoparticles for diagnostics, therapy and macromolecule delivery.," *Theranostics*, vol. 3, no. 12, pp. 986–1003, 2013.
- [39] J. H. Park, S. Lee, J.-H. Kim, K. Park, K. Kim, and I. C. Kwon, "Polymeric nanomedicine for cancer therapy," *Prog. Polym. Sci.*, vol. 33, no. 1, pp. 113–137, 2008.
- [40] V. V Mody, M. I. Nounou, and M. Bikram, "Novel nanomedicine-based MRI contrast agents for gynecological malignancies.," *Adv. Drug Deliv. Rev.*, vol. 61, no. 10, pp. 795–807, 2009.
- [41] J.-H. Lee, M. a Smith, W. Liu, E. M. Gold, B. Lewis, H.-T. Song, and J. a Frank, "Enhanced stem cell tracking via electrostatically assembled fluorescent SPION-peptide complexes.," *Nanotechnology*, vol. 20, no. 35, p. 355102, 2009.
- [42] V. J. Mohanraj and Y. Chen, "Nanoparticles-a review," *Trop. J. Pharm. Res.*, vol. 5, no. June, pp. 561–573, 2007.
- [43] C. Dubernet and P. Couvreur, "Nanoparticles in cancer therapy and diagnosis," vol. 54, pp. 631–651, 2002.
- [44] "Colorectal cancer biomarker panel," 2011. [Online] Available: http://www.ogt.co.uk/diagnostic_biomarkers/colorectal_cancer. [Accessed: 13-Jan-2015]
- [45] T. L. Doane and C. Burda, "The unique role of nanoparticles in nanomedicine: imaging, drug delivery and therapy.," *Chem. Soc. Rev.*, vol. 41, no. 7, pp. 2885–2911, Apr. 2012.
- [46] N. Praetorius and T. Mandal, "Engineered Nanoparticles in Cancer Therapy," *Recent Pat. Drug Deliv. Formul.*, vol. 1, no. 1, pp. 37–51, 2007.
- [47] C. L. Ventola, "The nanomedicine revolution: part 2: current and future clinical applications.," *P T*, vol. 37, no. 10, pp. 582–91, 2012.
- [48] M. J. Hawkins, P. Soon-Shiong, and N. Desai, "Protein nanoparticles as drug carriers in clinical medicine," *Adv. Drug Deliv. Rev.*, vol. 60, pp. 876–885, 2008.

- [49] H. Gelderblom, J. Verweij, K. Nooter, and a. Sparreboom, “Cremophor EL: The drawbacks and advantages of vehicle selection for drug formulation,” *Eur. J. Cancer*, vol. 37, pp. 1590–1598, 2001.
- [50] F. Kratz, “Albumin as a drug carrier: Design of prodrugs, drug conjugates and nanoparticles,” *J. Control. Release*, vol. 132, no. 3, pp. 171–183, 2008.
- [51] R. Wang, P. S. Billone, and W. M. Mullett, “Nanomedicine in action: An overview of cancer nanomedicine on the market and in clinical trials,” *Journal of Nanomaterials*, vol. 2013. 2013.
- [52] D. D. Von Hoff, T. Ervin, F. P. Arena, E. G. Chiorean, J. Infante, M. Moore, T. Seay, S. a Tjulandin, W. W. Ma, M. N. Saleh, M. Harris, M. Reni, S. Dowden, D. Laheru, N. Bahary, R. K. Ramanathan, J. Taberner, M. Hidalgo, D. Goldstein, E. Van Cutsem, X. Wei, J. Iglesias, and M. F. Renschler, “Increased survival in pancreatic cancer with nab-paclitaxel plus gemcitabine.,” *N. Engl. J. Med.*, vol. 369, pp. 1691–703, 2013.
- [53] J.-H. Lee, K. Lee, S. H. Moon, Y. Lee, T. G. Park, and J. Cheon, “All-in-One Target-Cell-Specific Magnetic Nanoparticles for Simultaneous Molecular Imaging and siRNA Delivery,” *Angew. Chemie*, vol. 121, no. 23, pp. 4238–4243, 2009.
- [54] C. Choi, Liu, lee, “Theranostic nanoplatforams for simultaneous cancer imaging and therapy: current approaches and future perspectives,” *Natl. institutes Heal.*, vol. 4, no. 2, pp. 330–342, 2012.
- [55] X. S. Chen, “Introducing theranostics journal-from the editor-in-chief,” *Theranostics*, pp. 1–2, 2011.
- [56] W. R. Sanhai, J. H. Sakamoto, R. Canady, and M. Ferrari, “Seven challenges for nanomedicine.,” *Nat. Nanotechnol.*, vol. 3, no. 5, pp. 242–244, 2008.
- [57] V. P. Torchilin, “Targeted pharmaceutical nanocarriers for cancer therapy and imaging.,” *AAPS J.*, vol. 9, no. 2, pp. E128–47, 2007.
- [58] F. RE, “Nanomedicine, Dr. Francesca RE,” *Education*, 2014. .
- [59] J. Y. Ljubimova and E. Holler, “Biocompatible nanopolymers: the next generation of breast cancer treatment?,” *Nanomedicine (Lond)*, vol. 7, no. 10, pp. 1467–1470, 2012.
- [60] R. Duncan, “Polymer conjugates as anticancer nanomedicines,” *Nat Rev Cancer*, vol. 6, no. 9, pp. 688–701, Sep. 2006.
- [61] J. a Hubbell, S. N. Thomas, and M. a Swartz, “Materials engineering for immunomodulation.,” *Nature*, vol. 462, no. 7272, pp. 449–460, 2009.

- [62] “HAK-FUN CHOW’S RESEARCH GROUP; Dendrimer Chemistry,” 2012.
[Online] Available:
http://www.cuhk.edu.hk/research/hfchow/HFC_NewWeb/Research_Dendrimer.htm.
- [63] J. F. Gohy, “Block copolymer micelles,” *Adv Polym Sci*, vol. 190, no. October, pp. 65–136, 2005.
- [64] S. M. Moghimi, A. C. Hunter, and J. C. Murray, “Long-Circulating and Target-Specific Nanoparticles : Theory to Practice,” vol. 53, no. 2, pp. 283–318, 2001.
- [65] C. C. Lee, E. R. Gillies, M. E. Fox, S. J. Guillaudeu, J. M. J. Fréchet, E. E. Dy, and F. C. Szoka, “A single dose of doxorubicin-functionalized bow-tie dendrimer cures mice bearing C-26 colon carcinomas.,” *Proc. Natl. Acad. Sci. U. S. A.*, vol. 103, no. 45, pp. 16649–16654, 2006.
- [66] H. M. Mansour, Y. S. Rhee, and X. Wu, “Nanomedicine in pulmonary delivery.,” *International journal of nanomedicine*, vol. 4, pp. 299–319, 2009.
- [67] P. Wiener, EC; Brechbiel, MW; Brothers, H; Magin, RL; Gansow, OA; Tomalia, DA; Lauterbur, “Dendrimer-based metal chelates: a new class of magnetic resonance imaging contrast agents.,” *Off. J. Scociety Magn. Reson. Med.*, vol. 31, no. 1, pp. 1–8, 1994.
- [68] S. C. Kim, D. W. Kim, Y. H. Shim, J. S. Bang, H. S. Oh, S. W. Kim, and M. H. Seo, “In vivo evaluation of polymeric micellar paclitaxel formulation: toxicity and efficacy,” *J. Control. Release*, vol. 72, no. 1–3, pp. 191–202, 2001.
- [69] Y. Barenholz, “Doxil - The first FDA-approved nano-drug: Lessons learned,” *J. Control. Release*, vol. 160, no. 2, pp. 117–134, 2012.
- [70] B. Čeh, M. Winterhalter, P. M. Frederik, J. J. Vallner, and D. D. Lasic, “Stealth liposomes: From theory to product,” *Adv. Drug Deliv. Rev.*, vol. 24, pp. 165–177, 1997.
- [71] A. Gabizon, R. Catane, B. Uziely, B. Kaufman, T. Safra, R. Cohen, F. Martin, A. Huang, and Y. Barenholz, “Prolonged circulation time and enhanced accumulation in malignant exudates of doxorubicin encapsulated in polyethylene-glycol coated liposomes,” *Cancer Res.*, vol. 54, pp. 987–992, 1994.
- [72] “Chemguide: CIE A level chemistry support: Learning outcome 11.3(b).” .
- [73] “New Method for Analysing Liposome Aggregation and Polydispersity. | Izon | Particle Analysis.” .
- [74] K. Sahithi, M. Swetha, K. Ramasamy, N. Srinivasan, and N. Selvamurugan, “Polymeric composites containing carbon nanotubes for bone tissue engineering.,” *Int. J. Biol. Macromol.*, vol. 46, no. 3, pp. 281–283, Apr. 2010.

- [75] A. Bianco, K. Kostarelos, and M. Prato, "Applications of carbon nanotubes in drug delivery.," *Curr. Opin. Chem. Biol.*, vol. 9, no. 6, pp. 674–679, 2005.
- [76] C. L. Zavaleta, B. R. Smith, I. Walton, W. Doering, G. Davis, B. Shojaei, M. J. Natan, and S. S. Gambhir, "Multiplexed imaging of surface enhanced Raman scattering nanotags in living mice using noninvasive Raman spectroscopy.," *Proc. Natl. Acad. Sci. U. S. A.*, vol. 106, no. 32, pp. 13511–13516, 2009.
- [77] M. R. McDevitt, D. Chattopadhyay, B. J. Kappel, J. S. Jaggi, S. R. Schiffman, C. Antczak, J. T. Njardarson, R. Brentjens, and D. a Scheinberg, "Tumor targeting with antibody-functionalized, radiolabeled carbon nanotubes.," *J. Nucl. Med.*, vol. 48, no. 7, pp. 1180–1189, 2007.
- [78] V. Choudhary and A. Gupta, "Polymer / Carbon Nanotube Nanocomposites," 2001.
- [79] V. S. Kulikova and a. F. Shestakov, "Functionalization of alkanes by gold nanoparticles stabilized by 1-dodecanethiol in organic media," *Russ. J. Phys. Chem. B*, vol. 2, no. 5, pp. 507–511, 2007.
- [80] K. K. Y. Wong and X. Liu, "Silver nanoparticles—the real 'silver bullet' in clinical medicine?," *Medchemcomm*, vol. 1, no. 2, p. 125, 2010.
- [81] C. Loo, A. Lin, L. Hirsch, M. Lee, J. Barton, N. Halas, J. West, and R. Drezek, "Nanoshell-enabled photonics-based imaging and therapy of cancer.," *Technol. Cancer Res. Treat.*, 2004.
- [82] A. K. Gupta and M. Gupta, "Synthesis and surface engineering of iron oxide nanoparticles for biomedical applications.," *Biomaterials*, vol. 26, no. 18, pp. 3995–4021, 2005.
- [83] K. B. Vargo, A. Al Zaki, R. Warden-Rothman, A. Tsourkas, and D. a Hammer, "Superparamagnetic Iron Oxide Nanoparticle Micelles Stabilized by Recombinant Oleosin for Targeted Magnetic Resonance Imaging.," *Small*, pp. 1–5, 2014.
- [84] a S. Thakor, J. Jokerst, C. Zavaleta, T. F. Massoud, and S. S. Gambhir, "Gold nanoparticles: a revival in precious metal administration to patients.," *Nano Lett.*, vol. 11, no. 10, pp. 4029–4036, 2011.
- [85] W. J. Rieter, K. M. Pott, K. M. L. Taylor, and W. Lin, "Nanoscale coordination polymers for platinum-based anticancer drug delivery.," *J. Am. Chem. Soc.*, vol. 130, no. 35, pp. 11584–11585, 2008.
- [86] X. Sun and Y. Li, "Colloidal Carbon Spheres and Their Core/Shell Structures with Noble-Metal Nanoparticles," *Angew. Chemie Int. Ed.*, vol. 43, no. 5, pp. 597–601, Jan. 2004.
- [87] J.-H. Lee, B. Schneider, E. K. Jordan, W. Liu, and J. a Frank, "Synthesis of Complexable Fluorescent Superparamagnetic Iron Oxide Nanoparticles (FL

- SPIONs) and Cell Labeling for Clinical Application.,” *Adv. Mater.*, vol. 20, no. 13, pp. 2512–2516, 2008.
- [88] D. Levy, R. Giustetto, and A. Hoser, “Structure of magnetite (Fe₃O₄) above the Curie temperature: a cation ordering study,” *Phys. Chem. Miner.*, vol. 39, no. 2, pp. 169–176, 2011.
- [89] G. Goya and T. Berquo, “Static and dynamic magnetic properties of spherical magnetite nanoparticles,” *J. Appl. ...*, vol. 94, no. 5, p. 3520, 2003.
- [90] a P. Reena Mary, T. N. Narayanan, V. Sunny, D. Sakthikumar, Y. Yoshida, P. a Joy, and M. R. Anantharaman, “Synthesis of Bio-Compatible SPION-based Aqueous Ferrofluids and Evaluation of RadioFrequency Power Loss for Magnetic Hyperthermia.,” *Nanoscale Res. Lett.*, vol. 5, no. 10, pp. 1706–1711, 2010.
- [91] V. I. Shubayev, T. R. P. II, and S. Jin, “Magnetic nanoparticles for theragnostics,” *Adv. Drug Deliv. Rev.*, vol. 61, no. 6, pp. 467–477, 2009.
- [92] S. Sun and H. Zeng, “Size-Controlled Synthesis of Magnetite Nanoparticles Size-Controlled Synthesis of Magnetite Nanoparticles,” vol. 124, no. 31, pp. 8204–8205, 2002.
- [93] S. L. Iconaru, A. M. Prodan, M. Motelica-Heino, S. Sizaret, and D. Predoi, “Synthesis and characterization of polysaccharide-maghemite composite nanoparticles and their antibacterial properties,” *Nanoscale Res. Lett.*, vol. 7, no. 1, p. 576, 2012.
- [94] W. W. Yu, J. C. Falkner, C. T. Yavuz, and V. L. Colvin, “Synthesis of monodisperse iron oxide nanocrystals by thermal decomposition of iron carboxylate salts.,” *Chem. Commun. (Camb)*, pp. 2306–2307, 2004.
- [95] S. Sun, H. Zeng, and D. Robinson, “Monodisperse MFe₂O₄ (M= Fe, Co, Mn) nanoparticles,” *J. ...*, vol. 4, no. 1, pp. 126–132, 2003.
- [96] A. Petri-Fink, B. Steitz, A. Finka, J. Salaklang, and H. Hofmann, “Effect of cell media on polymer coated superparamagnetic iron oxide nanoparticles (SPIONs): colloidal stability, cytotoxicity, and cellular uptake studies.,” *Eur. J. Pharm. Biopharm.*, vol. 68, no. 1, pp. 129–137, 2008.
- [97] R. a. Wassel, B. Grady, R. D. Kopke, and K. J. Dormer, “Dispersion of super paramagnetic iron oxide nanoparticles in poly(d,l-lactide-co-glycolide) microparticles,” *Colloids Surfaces A Physicochem. Eng. Asp.*, vol. 292, no. 2–3, pp. 125–130, 2007.
- [98] E. D. Smolensky and H. Y. E. Park, “Surface functionalization of magnetic iron oxide nanoparticles for MRI applications—effect of anchoring group and ligand exchange protocol,” *Contrast media ...*, vol. 6, no. 4, pp. 189–199, 2011.

- [99] L. Zhang, R. He, and H.-C. Gu, "Oleic acid coating on the monodisperse magnetite nanoparticles," *Appl. Surf. Sci.*, vol. 253, no. 5, pp. 2611–2617, 2006.
- [100] M. M. Lin, D. K. Kim, A. J. El Haj, and J. Dobson, "Development of superparamagnetic iron oxide nanoparticles (SPIONS) for translation to clinical applications," *IEEE Transactions on Nanobioscience*, vol. 7, no. 4, pp. 298–305, 2008.
- [101] C. W. V. Gmbh and C. Kga, "Design of an amphiphilic polymer for nanoparticle coating and functionalization," 2007.
- [102] Y. S. J. Chang-Moon, Lee; Cheong; Kim; Lim; Jeong, "Nonpolymeric Surface-Coated Iron Oxide Nanoparticles for In Vivo Molecular Imaging: Biodegradation, Biocompatibility, and Multiplatform," *J. Nucl. Med.*, vol. 54, no. 11, pp. 1974–1980, 2013.
- [103] M. F. Silva and M. A. Ciciliatti, "Superparamagnetic maghemite loaded poly (ϵ -caprolactone) nanocapsules: characterization and synthesis optimization," *Matéria (Rio ...)*, pp. 40–52, 2014.
- [104] H. Lee, M. K. Yu, S. Park, and S. Moon, "Thermally cross-linked superparamagnetic iron oxide nanoparticles: synthesis and application as a dual imaging probe for cancer in vivo," *J. ...*, no. 12, pp. 12739–12745, 2007.
- [105] S. Sulek, B. Mammadov, D. I. Mahcicek, H. Sozeri, E. Atalar, A. B. Tekinay, and M. O. Guler, "Peptide functionalized superparamagnetic iron oxide nanoparticles as MRI contrast agents," *J. Mater. Chem.*, vol. 21, p. 15157, 2011.
- [106] a. Carvalho, M. B. F. Martins, M. L. Corvo, and G. Feio, "Enhanced contrast efficiency in MRI by PEGylated magnetoliposomes loaded with PEGylated SPION: Effect of SPION coating and micro-environment," *Mater. Sci. Eng. C*, vol. 43, pp. 521–526, 2014.
- [107] M. K. Yu, D. Kim, I.-H. Lee, J.-S. So, Y. Y. Jeong, and S. Jon, "Image-guided prostate cancer therapy using aptamer-functionalized thermally cross-linked superparamagnetic iron oxide nanoparticles," *Small*, vol. 7, no. 15, pp. 2241–2249, 2011.
- [108] T. Neuberger, B. Schöpf, H. Hofmann, M. Hofmann, and B. von Rechenberg, "Superparamagnetic nanoparticles for biomedical applications: Possibilities and limitations of a new drug delivery system," *J. Magn. Magn. Mater.*, vol. 293, no. 1, pp. 483–496, 2005.
- [109] A. Patricia, H. Barros, and A. P. H. Barros, "Synthesis of Multifunctional Magnetic Nanoparticles for Biomedical Applications," Universidad de zaragoza, 2009.
- [110] M. Mahmoudi, A. Simchi, M. Imani, and U. O. Ha, "Superparamagnetic Iron Oxide Nanoparticles with Rigid Cross-linked Polyethylene Glycol Fumarate Coating for

- Application in Imaging and Drug Delivery Superparamagnetic Iron Oxide Nanoparticles with Rigid Cross-linked Polyethylene Glycol Fumarate Coating fo,” pp. 8124–8131, 2009.
- [111] A. J. Cole, A. E. David, J. Wang, C. J. Galbán, and V. C. Yang, “Magnetic brain tumor targeting and biodistribution of long-circulating PEG-modified, cross-linked starch-coated iron oxide nanoparticles.,” *Biomaterials*, vol. 32, no. 26, pp. 6291–6301, 2011.
- [112] K. Pervushin and R. Riek, “mutual cancellation of dipole–dipole coupling and chemical shift anisotropy indicates an avenue to NMR structures of very large biological macromolecules in solution,” *Proc. ...*, vol. 94, no. November, pp. 12366–12371, 1997.
- [113] K. H. Bae, Y. B. Kim, Y. Lee, J. Hwang, H. Park, and T. G. Park, “Bioinspired Synthesis and Characterization of Gadolinium-Labeled Magnetite Nanoparticles for Dual Contrast T₁ - and T₂ -Weighted Magnetic Resonance Imaging,” *Society*, pp. 505–512, 2010.
- [114] F. Prof, C. Royal, and I. Acadd, “pour le Institution , Foreign Associate of the Acad . Sciences , Paris , Ord . Bortuss . Modena , Stockholm , Munich , Bruxelles , Vienna , Bologna , of the Legion of Honour , & c . & c .,” *Society*, vol. 147, no. 1857, pp. 145–181, 2012.
- [115] M. C. Daniel and D. Astruc, “Gold nanoparticles: assembly, supramolecular chemistry, quantum-size-related properties, and applications toward biology, catalysis, and nanotechnology,” *Chem. Rev.*, vol. 104, no. 1, pp. 293–346, 2004.
- [116] J. Turkevich, P. C. Stevenson, and J. Hillier, “A study of the nucleation and growth processes in the synthesis of colloidal gold,” *Discuss. Faraday Soc.*, no. c, p. 55, 1951.
- [117] W. Cai, T. Gao, H. Hong, and J. Sun, “Applications of gold nanoparticles in cancer nanotechnology.,” *Nanotechnol. Sci. Appl.*, vol. 2008, pp. 17–32, 2008.
- [118] P. Mulvaney, M. Giersig, and A. Henglein, “Electrochemistry of Multilayer Colloids: Preparation and Absorption Spectrum of Gold-Coated Silver Particles,” *J. Phys. Chem.*, vol. 97, no. 2, pp. 7061–7064, 1993.
- [119] M. Brust, M. Walker, D. Bethell, D. J. Schiffrin, and R. Whyman, “Synthesis of Thiol-derivatised Gold Nanoparticles in a two-phase Liquid-Liquid System,” pp. 801–802, 1994.
- [120] C. a Waters, A. J. Mills, K. a Johnson, and D. J. Schiffrin, “Purification of dodecanethiol derivatised gold nanoparticles.,” *Chem. Commun. (Camb)*, no. January, pp. 540–541, 2003.

- [121] M. Brust, J. Fink, D. Bethell, D. J. Schiffrin, and C. Kiely, "Synthesis and reactions of functionalised gold nanoparticles," *J. Chem. Soc. Chem. Commun.*, p. 1655, 1995.
- [122] N. R. Jana and X. Peng, "Single-Phase and Gram-Scale Routes toward Nearly Monodisperse Au and Other Noble Metal Nanocrystals," *J. Am. Chem. Soc.*, vol. 125, no. Figure 2, pp. 14280–14281, 2003.
- [123] C. K. Yee, R. Jordan, A. Ulman, H. White, A. King, M. Rafailovich, and J. Sokolov, "Novel one-phase synthesis of thiol-functionalized gold, palladium, and iridium nanoparticles using superhydride," *Langmuir*, vol. 15, no. d, pp. 3486–3491, 1999.
- [124] M. P. Rowe, K. E. Plass, K. Kim, C. Kurdak, E. T. Zellers, and a J. Matzger, "Single-phase synthesis of functionalized gold nanoparticles," *Chem. Mater.*, vol. 16, no. 18, pp. 3513–3517, 2004.
- [125] D. S. Nanoparticles, T. Systems, and E. Section, "Comparative Study of," vol. 7463, no. 14, pp. 226–230, 1998.
- [126] Z. Xu, C. Shen, Y. Hou, H. Gao, and S. Sun, "Oleylamine as Both Reducing Agent and Stabilizer in a Facile Synthesis of Magnetite Nanoparticles Oleylamine as Both Reducing Agent and Stabilizer in a Facile Synthesis of Magnetite Nanoparticles," *Communications*, no. 7, pp. 1778–1780, 2009.
- [127] T. Yonezawa, S. Onoue, and N. Kimizuka, "Formation of Uniform Fluorinated Gold Nanoparticles and Their Highly Ordered Hexagonally Packed Monolayer," *Langmuir*, vol. 17, no. 8, pp. 2291–2293, Apr. 2001.
- [128] P. Pengo, S. Polizzi, M. Battagliarin, L. Pasquato, and P. Scrimin, "Synthesis, characterization and properties of water-soluble gold nanoparticles with tunable core size Part of this work was presented at the ISOCS XX, Flagstaff, Arizona, USA, July 14?19, 2002.," *J. Mater. Chem.*, vol. 13, no. 10, p. 2471, 2003.
- [129] J. Simard, C. Briggs, A. K. Boal, and V. M. Rotello, "Formation and pH-controlled assembly of amphiphilic gold nanoparticles," *Chem. Commun.*, no. 19, pp. 1943–1944, 2000.
- [130] C. J. Murphy, A. M. Gole, S. E. Hunyadi, J. W. Stone, P. N. Sisco, A. Alkilany, B. E. Kinard, and P. Hankins, "Chemical sensing and imaging with metallic nanorods.," *Chem. Commun. (Camb)*, no. 5, pp. 544–557, 2008.
- [131] T. Pham, J. B. Jackson, N. J. Halas, and T. R. Lee, "Preparation and characterization of gold nanoshells coated with self-assembled monolayers," *Langmuir*, vol. 18, no. 10, pp. 4915–4920, 2002.
- [132] S. K. Ghosh and T. Pal, "Interparticle Coupling Effect on the Surface Plasmon Resonance of Gold Nanoparticles : From Theory to Applications," 2007.

- [133] S. Link and M. a. El-Sayed, "Size and Temperature Dependence of the Plasmon Absorption of Colloidal Gold Nanoparticles," *J. Phys. Chem. B*, vol. 103, no. 21, pp. 4212–4217, 1999.
- [134] J. Zheng, C. Zhang, and R. M. Dickson, "Highly fluorescent, water-soluble, size-tunable gold quantum dots," *Phys. Rev. Lett.*, vol. 93, no. August, pp. 5–8, 2004.
- [135] M. M. Alvarez, J. T. Khoury, T. G. Schaaff, M. N. Shafigullin, R. L. Whetten, and I. Vezmar, "Optical Absorption Spectra of Nanocrystal Gold Molecules," *J. Phys. Chem. B*, vol. 101, no. 19, pp. 3706–3712, 1997.
- [136] X. Huang, I. H. El-Sayed, W. Qian, and M. a El-Sayed, "Cancer cell imaging and photothermal therapy in the near-infrared region by using gold nanorods.," *J. Am. Chem. Soc.*, vol. 128, no. 6, pp. 2115–2120, 2006.
- [137] S. Lee, E. J. Cha, K. Park, S. Y. Lee, J. K. Hong, I. C. Sun, S. Y. Kim, K. Choi, I. C. Kwon, K. Kim, and C. H. Ahn, "A near-infrared-fluorescence-quenched gold-nanoparticle imaging probe for in vivo drug screening and protease activity determination," *Angew. Chemie - Int. Ed.*, vol. 47, pp. 2804–2807, 2008.
- [138] C. Loo, A. Lowery, N. Halas, J. West, and R. Drezek, "Immunotargeted nanoshells for integrated cancer imaging and therapy," *Nano Lett.*, vol. 5, pp. 709–711, 2005.
- [139] and M. D. B. Harris, D. C., "Symmetry and Spectroscopy: an introduction to vibrational and electronic spectroscopy.," *Dover Publ.*, vol. Mineola, N, 1989.
- [140] E. C. Le Ru, E. J. Blackie, M. Meyer, and P. G. Etchegoin, "Surface Enhanced Raman Scattering Enhancement Factors: A Comprehensive Study," *J. Phys. Chem. C*, vol. 111, no. i, pp. 13794–13803, 2007.
- [141] E. J. Blackie, E. C. Le Ru, and P. G. Etchegoin, "Single-molecule surface-enhanced raman spectroscopy of nonresonant molecules," *J. Am. Chem. Soc.*, vol. 131, no. 20, pp. 14466–14472, 2009.
- [142] S. Nie, "Probing Single Molecules and Single Nanoparticles by Surface-Enhanced Raman Scattering," *Science (80-.)*, vol. 275, no. February, pp. 1102–1106, 1997.
- [143] A. Campion, P. Kambhampati, A. Campion, and C. Harris, "Surface-enhanced Raman scattering," vol. 27, pp. 241–250, 1998.
- [144] V. I. Kukushkin, a. B. Van'kov, and I. V. Kukushkin, "Long-range manifestation of surface-enhanced Raman scattering," *JETP Lett.*, vol. 98, no. 2, pp. 64–69, 2013.
- [145] D. L. Stokes and T. Vo-Dinh, "Development of an integrated single-fiber SERS sensor," *Sensors Actuators, B Chem.*, vol. 69, pp. 28–36, 2000.
- [146] and M. S. No TitleKak, Avinash C., "Principles of computerized tomographic imaging.," *Inst. Electr. Electron. Eng. Inc.*

- [147] J. S. Kim D, Park S, Lee J H, Jeong Y Y, “Antibiofouling polymer coated gold nanoparticles as a contrast agent for in vivo X-ray computed tomography imaging,” *J. Am. Chem. Soc.*, vol. 129, no. 19, pp. 7661–7665, 2007.
- [148] J. a. Copland, M. Eghtedari, V. L. Popov, N. Kotov, N. Mamedova, M. Motamedi, and A. a. Oraevsky, “Bioconjugated gold nanoparticles as a molecular based contrast agent: Implications for imaging of deep tumors using optoacoustic tomography,” *Mol. Imaging Biol.*, vol. 6, no. 5, pp. 341–349, 2004.
- [149] A. Manuscript, I. Disorders, and A. R. Technology, “NIH Public Access,” vol. 27, no. 12, pp. 417–428, 2009.
- [150] J. Xie, K. Chen, J. Huang, S. Lee, J. Wang, J. Gao, X. Li, and X. Chen, “PET/NIRF/MRI triple functional iron oxide nanoparticles.,” *Biomaterials*, vol. 31, no. 11, pp. 3016–3022, Apr. 2010.
- [151] M. Nahrendorf, H. Zhang, S. Hembrador, P. Panizzi, D. E. Sosnovik, E. Aikawa, P. Libby, F. K. Swirski, and R. Weissleder, “Nanoparticle PET-CT imaging of macrophages in inflammatory atherosclerosis,” *Circulation*, vol. 117, pp. 379–387, 2008.
- [152] N. K. Devaraj, E. J. Keliher, G. M. Thurber, M. Nahrendorf, and R. Weissleder, “¹⁸F labeled nanoparticles for in Vivo PET-CT imaging,” *Bioconjug. Chem.*, vol. 20, pp. 397–401, 2009.
- [153] M. P. Krafft and J. G. Riess, “Perfluorocarbons : Life Sciences and Biomedical Uses,” vol. 45, pp. 1185–1198, 2007.
- [154] N. Lewinski, V. Colvin, and R. Drezek, “Cytotoxicity of nanoparticles.,” *Small*, vol. 4, no. 1, pp. 26–49, 2008.
- [155] M. Sartor, “Dynamic Light Scattering,” San Diego, 2003.
- [156] B. J. Berne and R. Pecora, *Dynamic light scattering*, 2nd ed. Toronto: General Publishing Company Ltd., 2000.
- [157] J. Lyklema, *Fundamentals of Interface and Colloid Science: Particulate Colloids, Volume 4*, 1st ed. Elsevier B.V., 2005.
- [158] “Characterization Techniques.” .
- [159] L. Reimer and H. Kohl, *Transmission Electron Microscopy: Physics of Image Formation*, 5th ed. Springer, 2008.
- [160] T. Owen, *Fundamentals of Modern UV-Visible Spectroscopy: A Primer*. 2000.
- [161] “Nano Composix Europe - Plasmonics,” 2015. .

- [162] S. M. Kelly and N. C. Price, "The use of circular dichroism in the investigation of protein structure and function.," *Curr. Protein Pept. Sci.*, vol. 1, no. 4, pp. 349–384, 2000.
- [163] X. Hou and B. T. Jones, "Inductively Coupled Plasma/Optical Emission Spectrometry," *Encyclopedia of Analytical Chemistry*, vol. 42, no. 1. John Wiley & Sons Ltd, Chichester, pp. 9468–9485, 2000.
- [164] "ILL: Neutrons for science - Neutron reflectometry." .
- [165] S. Tatur, M. MacCarini, R. Barker, A. Nelson, and G. Fragneto, "Effect of functionalized gold nanoparticles on floating lipid bilayers," *Langmuir*, vol. 29, pp. 6606–6614, 2013.
- [166] M. L. Etheridge, S. a. Campbell, A. G. Erdman, C. L. Haynes, S. M. Wolf, and J. McCullough, "The big picture on nanomedicine: The state of investigational and approved nanomedicine products," *Nanomedicine Nanotechnology, Biol. Med.*, vol. 9, no. 1, pp. 1–14, 2013.
- [167] R. Weissleder, D. D. Stark, B. L. Engelstad, B. a Bacon, D. L. White, P. Jacobs, and J. Lewis, "Superparamagnetic Pharmacokinetics Iron Oxide : and Toxicity," *Ajr*, vol. 152, pp. 167–173, 1989.
- [168] P. Kocbek, S. Kralj, M. E. Kreft, and J. Kristl, "Targeting intracellular compartments by magnetic polymeric nanoparticles.," *Eur. J. Pharm. Sci.*, vol. 50, no. 1, pp. 130–138, 2013.
- [169] Y. Chang, Y. Li, X. Meng, N. Liu, D. Sun, H. Liu, and J. Wang, "Dendrimer functionalized water soluble magnetic iron oxide conjugates as dual imaging probe for tumor targeting and drug delivery," *Polym. Chem.*, vol. 4, no. 3, p. 789, 2013.
- [170] S. Mahajan, V. Koul, V. Choudhary, G. Shishodia, and A. C. Bharti, "Preparation and in vitro evaluation of folate-receptor-targeted SPION-polymer micelle hybrids for MRI contrast enhancement in cancer imaging.," *Nanotechnology*, vol. 24, no. 1, p. 15603, 2013.
- [171] K. Li and B. Liu, "Polymer encapsulated conjugated polymer nanoparticles for fluorescence bioimaging," *J. Mater. Chem.*, vol. 22, no. 4, p. 1257, 2012.
- [172] J.-J. Lin, J.-S. Chen, S.-J. Huang, J.-H. Ko, Y.-M. Wang, T.-L. Chen, and L.-F. Wang, "Folic acid-Pluronic F127 magnetic nanoparticle clusters for combined targeting, diagnosis, and therapy applications.," *Biomaterials*, vol. 30, no. 28, pp. 5114–24, Oct. 2009.
- [173] H. Rezvani Alanagh, M. E. Khosroshahi, M. Tajabadi, and H. Keshvari, "The Effect of pH and Magnetic Field on the Fluorescence Spectra of Fluorescein Isothiocyanate Conjugated SPION- Dendrimer Nanocomposites," *J. Supercond. Nov. Magn.*, vol. 27, no. 10, pp. 2337–2345, 2014.

- [174] K. Jores, A. Haberland, S. Wartewig, K. Mäder, and W. Mehnert, "Solid Lipid Nanoparticles (SLN) and oil-loaded SLN studied by spectrofluorometry and raman spectroscopy," *Pharm. Res.*, vol. 22, no. 11, pp. 1887–1897, 2005.
- [175] P. Greenspan and S. D. Fowler, "Spectrofluorometric studies of the lipid probe, Nile red," *J. Lipid Res.*, vol. 26, pp. 781–789, 1985.
- [176] M. B. Linder, "Hydrophobins: Proteins that self assemble at interfaces," *Curr. Opin. Colloid Interface Sci.*, vol. 14, no. 5, pp. 356–363, 2009.
- [177] J. Hakanpää, A. Paananen, S. Askolin, T. Nakari-Setälä, T. Parkkinen, M. Penttilä, M. B. Linder, and J. Rouvinen, "Atomic resolution structure of the HFBII hydrophobin, a self-assembling amphiphile," *J. Biol. Chem.*, vol. 279, no. 1, pp. 534–539, 2004.
- [178] J. Bayry, V. Aïmanianda, J. I. Guijarro, M. Sunde, and J.-P. Latgé, "Hydrophobins--unique fungal proteins," *PLoS Pathog.*, vol. 8, no. 5, p. e1002700, 2012.
- [179] Z. Wang, Y. Wang, Y. Huang, S. Li, S. Feng, H. Xu, and M. Qiao, "Characterization and application of hydrophobin-dispersed multi-walled carbon nanotubes," *Carbon N. Y.*, vol. 48, no. 10, pp. 2890–2898, 2010.
- [180] J. G. H. Wessels, "Hydrophobins, unique fungal proteins," *Mycologist*, vol. 14, no. 4, pp. 153–159, 2000.
- [181] S. Askolin, M. Linder, K. Scholtmeijer, M. Tenkanen, M. Penttilä, M. L. de Vocht, and H. a. B. Wösten, "Interaction and comparison of a class I hydrophobin from *Schizophyllum commune* and class II Hydrophobins *Trichoderma reesei*," *Biomacromolecules*, vol. 7, pp. 1295–1301, 2006.
- [182] C. Pigliacelli, A. D'Elcio, R. Milani, G. Terraneo, G. Resnati, F. Baldelli Bombelli, and P. Metrangolo, "Hydrophobin-stabilized dispersions of PVDF nanoparticles in water," *J. Fluor. Chem.*, 2015.
- [183] M. L. de Vocht, K. Scholtmeijer, E. W. van der Vegte, O. M. H. de Vries, N. Sonveaux, H. a. B. Wösten, J.-M. Ruyschaert, G. Hadziioannou, J. G. H. Wessels, and G. T. Robillard, "Structural Characterization of the Hydrophobin SC3, as a Monomer and after Self-Assembly at Hydrophobic/Hydrophilic Interfaces," *Biophys. J.*, vol. 74, no. 4, pp. 2059–2068, Apr. 1998.
- [184] A. R. Cox, F. Cagnol, A. B. Russell, and M. J. Izzard, "Surface properties of class II hydrophobins from *Trichoderma reesei* and influence on bubble stability," *Langmuir*, vol. 23, no. 15, pp. 7995–8002, 2007.
- [185] M. S. Grunér, G. R. Szilvay, M. Berglin, M. Lienemann, P. Laaksonen, and M. B. Linder, "Self-assembly of class II hydrophobins on polar surfaces," *Langmuir*, vol. 28, pp. 4293–4300, 2012.

- [186] M. Lienemann, J. A. Gandier, J. J. Joensuu, A. Iwanaga, Y. Takatsuji, T. Haruyama, E. Master, M. Tenkanen, and M. B. Linder, "Structure-function relationships in hydrophobins: Probing the role of charged side chains," *Appl. Environ. Microbiol.*, vol. 79, no. 18, pp. 5533–5538, 2013.
- [187] S. M. Moghimi, a C. Hunter, and J. C. Murray, "Nanomedicine: current status and future prospects.," *FASEB J.*, vol. 19, no. 3, pp. 311–330, 2005.
- [188] C. Lu, L. R. Bhatt, H. Y. Jun, S. H. Park, and K. Y. Chai, "Carboxyl–polyethylene glycol–phosphoric acid: a ligand for highly stabilized iron oxide nanoparticles," *J. Mater. Chem.*, vol. 22, p. 19806, 2012.
- [189] L. J. Bellamy, *The infra-red spectra of complex molecules*, 3rd ed. New York: Chapan and Hall Ltd., 1954.
- [190] M. Jackson and H. H. Mantsch, "The use and misuse of FTIR spectroscopy in the determination of protein structure.," *Crit. Rev. Biochem. Mol. Biol.*, vol. 30, no. 2, pp. 95–120, 1995.
- [191] Heacock and Marion, "The Infrared Spectra of Secondary Amines," 1956.
- [192] G. Cárdenas and V. Delgado, "Iron colloids prepared by chemical liquid," *J. Chil. Chem. Soc.*, vol. 3, no. 55, pp. 301–303, 2010.
- [193] J. A. Creighton and D. G. Eadon, "Ultraviolet-visible absorption spectra of the colloidal metallic elements," *J. Chem. Soc. Faraday Trans.*, vol. 87, no. 24, p. 3881, 1991.
- [194] and P. K. L. Christina H. Liu, Young R. Kim, Jia Q. Ren, Florian Eichler, Bruce R. Rosen, "Imaging Cerebral Gene Transcripts in Live Animals," vol. 27, no. 5, pp. 417–428, 2009.
- [195] F. Chen, W. Bu, L. Zhang, Y. Fan, and J. Shi, "Is black iron oxide nanoparticle always a light absorber?," *J. Mater. Chem.*, vol. 21, no. 22, p. 7990, 2011.
- [196] P. Greenspan, E. P. Mayer, and S. D. Fowler, "Nile red: A selective fluorescent stain for intracellular lipid droplets," *J. Cell Biol.*, vol. 100, no. 3, pp. 965–973, 1985.
- [197] T. Furuya, A. S. Kamlet, and T. Ritter, "Catalysis for fluorination and trifluoromethylation.," *Nature*, vol. 473, no. 7348, pp. 470–477, 2011.
- [198] K. L. Kirk, "Fluorine in medicinal chemistry: Recent therapeutic applications of fluorinated small molecules," *J. Fluor. Chem.*, vol. 127, pp. 1013–1029, 2006.
- [199] K. Müller, C. Faeh, and F. Diederich, "Fluorine in pharmaceuticals: looking beyond intuition.," *Science*, vol. 317, no. September, pp. 1881–1886, 2007.

- [200] W. K. Hagmann, "The many roles for fluorine in medicinal chemistry," *J. Med. Chem.*, vol. 51, no. 15, pp. 4359–4369, 2008.
- [201] M. a. Walling, J. a. Novak, and J. R. E. Shepard, "Quantum dots for live cell and in vivo imaging," *Int. J. Mol. Sci.*, vol. 10, pp. 441–491, 2009.
- [202] H. Hiramatsu and F. E. Osterloh, "Communications A Simple Large-Scale Synthesis of Nearly with Exchangeable Surfactants," *Chem. Mater.*, vol. 16, no. 13, pp. 2509–2511, 2004.
- [203] R. L. Wilson, J. F. Frisz, W. P. Hanafin, K. J. Carpenter, I. D. Hutcheon, P. K. Weber, and M. L. Kraft, "Fluorinated colloidal gold immunolabels for imaging select proteins in parallel with lipids using high-resolution secondary ion mass spectrometry," *Bioconjug. Chem.*, vol. 23, pp. 450–460, 2012.
- [204] A. Dass, R. Guo, and J. B. Tracy, "Gold nanoparticles with perfluorothiolate ligands," *Langmuir*, vol. 1995, no. 5, pp. 310–315, 2008.
- [205] Y. Jin and X. Gao, "Plasmonic fluorescent quantum dots.," *Nat. Nanotechnol.*, vol. 4, no. July, pp. 571–576, 2009.
- [206] M. Hu, J. Chen, Z.-Y. Li, L. Au, G. V Hartland, X. Li, M. Marquez, and Y. Xia, "Gold nanostructures: engineering their plasmonic properties for biomedical applications.," *Chem. Soc. Rev.*, vol. 35, pp. 1084–1094, 2006.
- [207] C. C. Huang, Z. Yang, K. H. Lee, and H. T. Chang, "Synthesis of highly fluorescent gold nanoparticles for sensing mercury(II)," *Angew. Chemie - Int. Ed.*, vol. 46, no. li, pp. 6824–6828, 2007.
- [208] T. Wang, X. Hu, and S. Dong, "The fragmentation of gold nanoparticles induced by small biomolecules.," *Chem. Commun. (Camb)*, pp. 4625–4627, 2008.
- [209] S. Riaz, L. Qu, E. K. Fodjo, W. Ma, and Y.-T. Long, "Thioanisole induced size-selective fragmentation of gold nanoparticles," *RSC Adv.*, vol. 4, p. 14031, 2014.
- [210] W. Cheng, S. Dong, and E. Wang, "Iodine-induced gold-nanoparticle fusion/fragmentation/aggregation and iodine-linked nanostructured assemblies on a glass substrate," *Angew. Chemie - Int. Ed.*, vol. 42, no. 29835120, pp. 449–452, 2003.
- [211] S. Riaz, W. Ma, C. Jing, M. H. Nawaz, D.-W. Li, and Y.-T. Long, "Thiol-ubiquinone assisted fragmentation of gold nanoparticles.," *Chem. Commun. (Camb)*, vol. 49, pp. 1738–40, 2013.
- [212] T. Wang, X. Hu, and S. Dong, "The fragmentation of gold nanoparticles induced by small biomolecules.," *Chem. Commun. (Camb)*, no. c, pp. 4625–4627, 2008.

- [213] M. Brust, M. Walker, D. Bethell, D. J. Schiffrin, and R. Whyman, "Synthesis of Thiol-derivatised Gold Nanoparticles in," pp. 801–802, 2000.
- [214] K. a Willets and R. P. Van Duyne, "Localized surface plasmon resonance spectroscopy and sensing.," *Annu. Rev. Phys. Chem.*, vol. 58, pp. 267–297, 2007.
- [215] S. Mourdikoudis and L. M. Liz-Marzán, "Oleylamine in nanoparticle synthesis," *Chem. Mater.*, vol. 25, pp. 1465–1476, 2013.
- [216] T. Yang, P. Li, M. Zanella, and W. H. Chang, "3/2008," vol. 4, no. 3, 2008.
- [217] N. Water-dispersible, R. De Palma, S. Peeters, M. J. Van Bael, H. Van Den Rul, K. Bonroy, W. Laureyn, J. Mullens, G. Borghs, and G. Maes, "Silane Ligand Exchange to Make Hydrophobic Superparamagnetic," no. 10, pp. 1821–1831, 2007.
- [218] L. O. Brown and J. E. Hutchison, "Controlled Growth of Gold Nanoparticles during Ligand Exchange," no. 9, pp. 882–883, 1999.
- [219] P. Ionita, A. Caragheorghopol, B. C. Gilbert, and V. Chechik, "EPR study of a place-exchange reaction on Au nanoparticles: Two branches of a disulfide molecule do not adsorb adjacent to each other," *J. Am. Chem. Soc.*, vol. 124, pp. 9048–9049, 2002.
- [220] R. Jin, "Quantum sized, thiolate-protected gold nanoclusters.," *Nanoscale*, vol. 2, pp. 343–362, 2010.
- [221] G. a. Rance, D. H. Marsh, and A. N. Khlobystov, "Extinction coefficient analysis of small alkanethiolate-stabilised gold nanoparticles," *Chem. Phys. Lett.*, vol. 460, pp. 230–236, 2008.
- [222] T. Ung, L. M. Liz-Marzán, and P. Mulvaney, "Gold nanoparticle thin films," *Colloids Surfaces A Physicochem. Eng. Asp.*, vol. 202, pp. 119–126, 2002.
- [223] F. Swinehart, "The Beer-Lambert," vol. 39, no. 7, pp. 333–335, 1962.
- [224] Keiichiro. Fuwa and B. L. Valle, "The Physical Basis of Analytical Atomic Absorption Spectrometry," *Anal. Chem.*, no. Figure 1, pp. 942–946, 1963.
- [225] J. Choi, S. Park, Z. Stojanović, H. S. Han, J. Lee, H. K. Seok, D. Uskoković, and K. H. Lee, "Facile solvothermal preparation of monodisperse gold nanoparticles and their engineered assembly of ferritin-gold nanoclusters," *Langmuir*, vol. 29, pp. 15698–15703, 2013.
- [226] S. Han, Y. Kim, and K. Kim, "Dodecanethiol-Derivatized Au/Ag Bimetallic Nanoparticles: TEM, UV/VIS, XPS, and FTIR Analysis.," *J. Colloid Interface Sci.*, vol. 208, pp. 272–278, 1998.

- [227] S. Coluccia, L. Marchese, and G. Martra, "Characterisation of microporous and mesoporous materials by the adsorption of molecular probes: FTIR and UV-Vis studies," *Microporous Mesoporous Mater.*, vol. 30, pp. 43-56, 1999.
- [228] C. Vilain, F. Goettmann, A. Moores, P. Le Floch, and C. Sanchez, "Study of metal nanoparticles stabilised by mixed ligand shell: a striking blue shift of the surface-plasmon band evidencing the formation of Janus nanoparticles," *J. Mater. Chem.*, vol. 17, p. 3509, 2007.
- [229] W. Haiss, N. T. K. Thanh, J. Aveyard, and D. G. Fernig, "Determination of Size and Concentration of Gold Nanoparticles from UV - Vis Spectra," vol. 79, no. 11, pp. 4215-4221, 2007.
- [230] S. K. Ghosh, S. Nath, S. Kundu, K. Esumi, and T. Pal, "Solvent and Ligand Effects on the Localized Surface Plasmon Resonance (LSPR) of Gold Colloids," *J. Phys. Chem B*, vol. 108, p. 13963, 2004.
- [231] T. H. F. Thake, J. R. Webb, A. Nash, J. Z. Rappoport, and R. Notman, "Permeation of polystyrene nanoparticles across model lipid bilayer membranes," *Soft Matter*, vol. 9, p. 10265, 2013.
- [232] B. D. Chithrani, A. a. Ghazani, and W. C. W. Chan, "Determining the size and shape dependence of gold nanoparticle uptake into mammalian cells," *Nano Lett.*, vol. 6, pp. 662-668, 2006.
- [233] "Gold Nanoparticles Cytotoxicity," 2011.
- [234] Y. Pan, S. Neuss, A. Leifert, M. Fischler, F. Wen, U. Simon, G. Schmid, W. Brandau, and W. Jahnke-Dechent, "Size-dependent cytotoxicity of gold nanoparticles," *Small*, vol. 3, pp. 1941-1949, 2007.
- [235] A. M. Alkilany, P. K. Nagaria, C. R. Hexel, T. J. Shaw, C. J. Murphy, and M. D. Wyatt, "Cellular uptake and cytotoxicity of gold nanorods: Molecular origin of cytotoxicity and surface effects," *Small*, vol. 5, pp. 701-708, 2009.
- [236] A. Hirano, H. Yoshikawa, S. Matsushita, Y. Yamada, and K. Shiraki, "Adsorption and disruption of lipid bilayers by nanoscale protein aggregates," *Langmuir*, vol. 28, pp. 3887-3895, 2012.
- [237] C. J. Murphy, A. M. Gole, J. W. Stone, P. N. Sisco, A. M. Alkilany, E. C. Goldsmith, and S. C. Baxter, "Gold Nanoparticles in Biology: Beyond Toxicity to Cellular Imaging," *Acc. Chem. Res.*, vol. 41, no. 12, 2008.
- [238] N. Pernodet, X. Fang, Y. Sun, A. Bakhtina, A. Ramakrishnan, J. Sokolov, A. Ulman, and M. Rafailovich, "Adverse effects of citrate/gold nanoparticles on human dermal fibroblasts," *Small*, vol. 2, no. 6, pp. 766-773, 2006.

- [239] M. Tsoli, H. Kuhn, W. Brandau, H. Esche, and G. Schmid, "Cellular uptake and toxicity of Au55 clusters," *Small*, vol. 1, pp. 841–844, 2005.
- [240] M. M. B. Holl, "Nanotoxicology : a personal perspective," 2009.
- [241] J. Kattan, J. P. Droz, P. Couvreur, J. P. Marino, A. Boutan-Laroze, P. Rougier, P. Brault, H. Vranckx, J. M. Grognet, X. Morge, and H. Sancho-Garnier, "Phase I clinical trial and pharmacokinetic evaluation of doxorubicin carried by polyisohexylcyanoacrylate nanoparticles," *Invest. New Drugs*, vol. 10, pp. 191–199, 1992.
- [242] N. K. Ibrahim, N. Desai, S. Legha, N. Formulation, P. Soon-shiong, R. L. Theriault, E. Rivera, B. Esmaeli, S. E. Ring, A. Bedikian, and G. N. Hortobagyi, "Phase I and Pharmacokinetic Study of ABI-007 , a of Paclitaxel Phase I and Pharmacokinetic Study of ABI-007 , a Cremophor-free ," *Clin. Cancer Res.*, vol. 8, no. May, pp. 1038–1044, 2002.
- [243] J. Penfold and R. K. Thomas, "The application of the specular reflection of neutrons to the study of surfaces and interfaces," *J. Phys. Condens. Matter*, vol. 2, pp. 1369–1412, 1999.
- [244] R. K. Heenan, J. Penfold, and S. M. King, "SANS at Pulsed Neutron Sources: Present and Future Prospects," *J. Appl. Cryst.*, vol. 30, pp. 1140–1147, 1997.
- [245] R.-J. Roe, *Methods of X-Ray and Neutron Scattering in Polymer Science*. Oxford University Press, 2000.
- [246] N. Torikai, N. L. Yamada, A. Noro, M. Harada, D. Kawaguchi, A. Takano, and Y. Matsushita, "Neutron Reflectometry on Interfacial Structures of the Thin Films of Polymer and Lipid," *Polym. J.*, vol. 39, no. 12, pp. 1238–1246, 2007.
- [247] B. T. M. W. and C. J. Carlile, *Experimental Neutron Scattering*. Oxford University Press, 2009.
- [248] P. Croce, "L. N´ evot, P. Croce To cite this version:," 1980.
- [249] A. Nelson, "Co-refinement of multiple-contrast neutron/X-ray reflectivity data using MOTOFIT," *J. Appl. Crystallogr.*, vol. 39, pp. 273–276, 2006.
- [250] R. Pynn and R. Pynn, "Neutron-Scattering By Rough Surfaces At Grazing-Incidence," *Physical Review B*, vol. 45. pp. 602–612, 1992.
- [251] C. M. McIntosh, E. a. Esposito, a. K. Boal, J. M. Simard, C. T. Martin, and V. M. Rotello, "Inhibition of DNA transcription using cationic mixed monolayer protected gold clusters," *J. Am. Chem. Soc.*, vol. 123, pp. 7626–7629, 2001.
- [252] M. J. Hostetler, S. J. Green, J. J. Stokes, and R. W. Murray, "Monolayers in three dimensions: Synthesis and electrochemistry of ω -functionalized alkanethiolate-

- stabilized gold cluster compounds,” *J. Am. Chem. Soc.*, vol. 118, no. 7, pp. 4212–4213, 1996.
- [253] J. Tien, A. Terfort, and G. M. Whitesides, “Microfabrication through Electrostatic Self-Assembly,” *Langmuir*, vol. 13, no. 20, pp. 5349–5355, 1997.
- [254] G. Fragneto, T. Charitat, E. Bellet-Amalric, R. Cubitt, and F. Graner, “Swelling of phospholipid floating bilayers: The effect of chain length,” *Langmuir*, vol. 19, pp. 7695–7702, 2003.
- [255] R. S. Armen, O. D. Uitto, and S. E. Feller, “Phospholipid component volumes: determination and application to bilayer structure calculations,” *Biophys. J.*, vol. 75, no. 2, pp. 734–744, 1998.